



Development of Nanostructured Materials for PEM Fuel Cells Application

A Dissertation

Submitted to

The Faculty of Natural Science II (Chemistry, Physics and Mathematics)

Martin Luther University Halle-Wittenberg

For

The Degree of Doctor of Science (Dr. rer. nat.)

Submitted by

Abu Bakr Ahmed Amine Nassr

born on 09.12.1978 in Sohag, Egypt

Reviewed by:

Prof. Dr. Michael Bron (MLU / Halle)

Prof. Dr. Christina Roth (FU/ Berlin)

Halle (Saale), 2014

„Gedruckt mit Unterstützung des Deutschen Akademischen Austauschdienstes (DAAD)“

*Dedicated to the memory
of my parents, to my sisters,
my brothers and my family.*

Declaration

I hereby declare that the thesis has not been handed in at any other university for reasons of graduation. I declare under penalty of perjury that this thesis is entirely my own work and has been written without any help of others. I only used the mentioned sources and indicated all kind of citations correctly.

Date of submission: 05.11.2013

Date of oral presentation: 30.01.2014

Halle/Saale

Abu Bakr Ahmed Amine Nassr

Table of Contents

Table of content.....	i
Table captions	v
Figure captions.....	vii
List of abbreviation.....	xiv
List of symbols.....	xvi
Motivation.....	xviii

1 Introduction and Basic Concepts

1.1	History of the fuel cells.....	1
1.2	Working principle of the fuel cells.....	3
1.3	Fuel cell types.....	4
1.4	Direct methanol fuel cell.....	7
1.4.1	Basic concepts of direct methanol fuel cells.....	7
1.4.2	Methanol electrooxidation mechanism.....	13
1.5	Electrocatalysts for methanol electrooxidation.....	16
1.5.1	Electrocatalyst supporting materials.....	16
1.5.2	Electrocatalyst preparation methods.....	22
1.5.2.1	Impregnation method.....	23
1.5.2.2	Carbonyl complex method.....	24
1.5.2.3	Colloidal method.....	24
1.5.3	Electrocatalyst systems (PtM).....	25
1.5.4	Electrocatalyst characterization methods.....	28
1.5.4.1	Structural characterization methods.....	29
1.5.4.2	Electrochemical characterization methods.....	32
1.6	Electrocatalysts evaluation in direct methanol fuel cells.....	34
1.7	Electrocatalysts for direct formic acid fuel cells.....	36
	References.....	37

2 Microwave Synthesis of PtRu/CNTs Electrocatalysts

2.1	Introduction.....	42
2.2	Experimental part.....	44
2.2.1	Electrocatalyst preparation.....	44
2.2.2	Electrocatalyst characterization.....	45
2.2.2.1	Structural characterization.....	45
2.2.2.2	Electrochemical characterization.....	45
2.3	Results and discussion.....	46

Table of Contents

2.3.1	Electrocatalyst preparation.....	46
2.3.2	XRD and TEM characterization	49
2.3.3	Electrochemistry study.....	53
2.3.3.1	CO stripping.....	53
2.3.3.2	Methanol oxidation.....	56
2.4	Conclusion.....	59
	References.....	60
	Supporting information.....	63

3 Structural Characterization and Performance of PtRu/CNTs in DMFCs

3.1	Introduction	65
3.2	Experimental work	67
3.2.1	Electrocatalyst preparation.....	67
3.2.2	Electrocatalyst characterization.....	67
3.2.2.1	Structural characterization.....	67
3.2.2.2	Electrochemical characterization.....	69
3.2.2.3	Direct methanol fuel cell tests.....	69
3.3	Results.....	71
3.3.1	Structural characterization of the electrocatalysts.....	71
3.3.1.1	XPS analysis.....	71
3.3.1.2	X-ray Absorption Fine Structure Spectroscopy.....	73
3.3.2	Electrochemical characterization and fuel cell tests.....	77
3.4	Discussion.....	86
3.5	Conclusion.....	88
	References.....	90
	Supporting information.....	93

4 Polyol synthesis of PtNi/CNTs Electrocatalysts

4.1	Introduction	98
4.2	Experimental	100
4.2.1	Carbon nanotubes functionalization.....	100
4.2.2	Characterization of functionalized carbon nanotubes.....	100
4.2.3	Preparation of electrocatalysts.....	101
4.2.4	Characterization of electrocatalysts.....	101
4.2.4.1	Structural characterization.....	101
4.2.4.2	Electrochemical characterization.....	103
4.3	Results and discussion.....	104

Table of Contents

4.3.1	Characterization of the functionalized support.....	104
4.3.2	Characterization of electrocatalysts.....	105
4.3.2.1	Structural characterization.....	105
4.3.2.2	Electrochemical characterization.....	112
4.3.3	Structure of the catalysts.....	114
4.3.4	Methanol electrooxidation.....	117
4.4	Conclusion.....	122
	References.....	123
	Supporting information.....	127

5 Microwave-Assisted Polyol Synthesis of PtNi/CNTs Electrocatalysts

5.1	Introduction	136
5.2	Experimental work.....	138
5.2.1	Catalyst preparation.....	138
5.2.2	Structural catalyst characterization.....	139
5.2.3	Electrochemical measurements and electrode preparation.....	140
5.2.4	CO Stripping measurements.....	141
5.2.5	Methanol oxidation activity.....	141
5.3	Results and discussion.....	142
5.3.1	Structural characterization	142
5.3.1.1	Metal loading determination by ICP.....	142
5.3.1.2	XRD and TEM characterization.....	143
5.3.1.3	XPS and XAFS characterization.....	147
5.3.2	Electrochemical characterization.....	152
5.3.2.1	CO Stripping and surface area determination.....	152
5.3.2.2	Methanol oxidation activity.....	154
5.3.3	Origin of the activity enhancement in PtNi catalysts.....	157
5.4	Conclusions.....	159
	References.....	160
	Supporting information.....	163

6 Polyol Synthesis of Pd/CNTs Electrocatalysts

6.1	Introduction	169
6.2	Experimental work.....	170
6.2.1	Catalysts preparation.....	170
6.2.2	Catalysts characterization by TGA, XRD and TEM.....	172
6.2.3	Electrochemical characterization.....	173

Table of Contents

6.3	Results and discussion.....	174
6.3.1	TGA, TEM and XRD.....	174
6.3.2	Electrochemical characterization.....	179
6.3.2.1	Surface area determination.....	179
6.3.2.2	Formic acid oxidation.....	182
6.3.2.3	Electrocatalyst stability.....	185
6.4	Conclusion.....	187
	References.....	188
	Supporting information.....	191

7 Summary and outlook

Summery and outlook.....	199
--------------------------	-----

Appendix.....

Publications Contribution Statement.....

Acknowledgment.....

Curriculum Vita.....

Table captions

Chapter 1

Table 1.2	Theoretical properties of various liquid fuels and compared with hydrogen.....	7
-----------	--	---

Chapter 2

Table 2.1	Structural parameters from XRD and TEM analysis.....	53
Table 2.2	Electrochemical parameters from CO stripping.....	56
Table 2.3	Peak potential, surface specific activity, mass specific activity and I_f/I_b for methanol oxidation from cyclic voltammetry measurements.....	60

Chapter 3

Table 3.1	Ru: Pt and $Ru^{4+} : Ru^0$ ratios as seen by XPS.....	73
Table 3.2	EXAFS fit results together with pairing factors and alloying extents for PtRu/CNTs and PtRu/C catalysts.....	77
Table 3.3	Electrochemical activity evaluated from chronoamperometry measurements.....	81

Chapter 4

Table 4.1	Composition (from ICP) and particle size (from TEM) for Pt/C and PtNi/FCNTs.....	106
Table 4.2	Pt to Ni atomic ratios derived from XPS data.....	108
Table 4.3	Electrochemical parameters calculated from CO stripping measurements.....	114
Table 4.4	Pt L3 edge best-fit results within two shell model.....	116
Table 4.5	Ni K edge best-fit results within three shell model.....	117
Table 4.6	Electrochemical parameters calculated from cyclic voltammetry measurements.....	119
Table SI4.1	Textural properties for CNTs as obtained from BET surface area measurements.....	129

Chapter 5

Table 5.1	Details of the preparation conditions for PtNi/CNT catalysts under microwave irradiation.....	139
Table 5.2	Metal loading and atomic ratios as obtained from ICP and particle size form TEM.....	143
Table 5.3	Atomic ratios for PtNi/FCNTs as calculated from XPS.....	148

Table captions

Table 5.4	Pt L_3 EXAFS fitting parameters – coordination numbers and distances (in brackets, in Å) along with total coordination numbers CN _{total} and platinum pairing factors PPt.....	151
Table 5.5	Electrochemical parameters from CO Stripping and CV measurements.....	154
Table SI5.1	Pt L_3 -edge EXAFS fit results within three shell model.....	168

Chapter 6

Table 6.1	Structural properties of Pd nanocatalysts from TGA and XRD analyses.....	179
Table 6.2	Electrochemical parameters from CO-Stripping, cyclic voltammetry and chronoamperometry measurements.....	183

Figure captions

Chapter 1

Figure 1.1	Grove’s ‘gas battery’ (1839) produced a voltage of about 1 volt, shown left. Grove’s ‘gas chain’ powering an electrolyzer (1842).....	2
Figure 1.2	NASA Space Shuttle Orbiter alkaline fuel cell.....	3
Figure 1.3	Schematic diagram of the fuel cell principle working and its reactions...	4
Figure 1.4	Schematic diagram of different types of fuel cells.....	6
Figure 1.5	Schematic diagram of DMFCs, 1 metal end plate , 2 flow field carbon plate, 3 gas diffusion layers (GDL), 4 catalysts layer, 5 proton exchange membrane.....	7
Figure 1.6	An artificial i-V polarization curve for DMFCs.....	9
Figure 1.7	Schematic representation of possible pathways for oxidation of $-(\text{CHO})_{\text{ads}}$	14
Figure 1.8	Carbon ordered structures including (a) graphite, consisting of a stack of graphene layers, (b) diamond, and the new carbon allotropes (c) 0D, buckminsterfullerene (C60), consisting of graphene balled into a sphere, (d) 1D, nanotube, made of a rolled-up cylinder of graphene, and (e) 2D, graphene.....	18
Figure 1.9	Structure of SWCNT and MWCNT.....	19
Figure 1.10	Structural models of SWCNTs exhibiting different chiralities; (a) armchair, (b) zig-zag, and (c) chiral arrangement.....	19
Figure 1.11	Schematic representation of oxygen containing groups bonded to the carbon nanotubes surface	21
Figure 1.12	Schematic diagram of the synthesis of PtRu electrocatalysts on 1-AP-functionalized MWCNTs.....	22
Figure 1.13	Different chemical methods for preparation of PtM/C catalysts.....	24
Figure 1.14	schematic models for electronic mechanism (A) and bifunctional mechanism (B) in PtM catalyst system.....	26
Figure 1.15	a) Characteristic CV of PtRu catalysts in methanol/sulfuric acid scan rate 50 mVs^{-1} ; and b) CO-Stripping Voltammetry for PtRu in sulfuric acid scan rate 20 mVs^{-1}	33

Chapter 2

Figure 2.1	(A) Schematic diagram of microwave reactor and (B) temperature profile during the microwave preparation of PtRu/CNTs MW in ethanol water (1:1,v/v), irradiation time 4 min, microwave power 300 W.....	47
Figure 2.2	Filtrate of PtRu/CNTs prepared by microwave heating for 1 min (a), For 10 min (b), prepared by conventional reflux (c) in ethanol,	

Figure captions

	prepared by microwave heating for 4 min (d) and by conventional reflux (f) in an ethanol/water mixture (1:1) before (I) and after (II) addition of 0.1 M NaBH ₄ solution. The power for microwave heating was set to 300 W, and the temperature for conventional heating was set to 85 °C 48	48
Figure 2.3	TEM images and the corresponding histograms of (A) PtRu/CNTs CR, (B) PtRu/CNTs MW, (C) PtRu/CNTs MW 200, (D) PtRu/CNTs MW 400, (E) PtRu/CNTs MW 600, (F) PtRu/CNTs MW 800 50	50
Figure 2.4	XRD patterns of (a) PtRu/CNTs CR, (b) PtRu/CNTs MW, (c) PtRu/CNTs MW 200, (d) PtRu/CNTs MW 400, (e) PtRu/CNTs MW 600, (f) PtRu/CNTs MW 800 52	52
Figure 2.5	CO stripping voltammograms of a) PtRu/CNTs CR, b) PtRu/CNTs MW, c) PtRu/CNTs MW 200, d) PtRu/CNTs MW 400, e) PtRu/CNTs MW 600, f) PtRu/CNTs MW 800 in 0.5 M H ₂ SO ₄ (scan rate 20 mV s ⁻¹); the black lines represent the CO stripping peak and the grey ones the second cycle 55	55
Figure 2.6	Cyclic voltammograms of a) PtRu/CNTs CR and PtRu/CNTs MW, b) PtRu/CNTs MW 200, 400 600 and 800 °C in 1 M CH ₃ OH/0.5 M H ₂ SO ₄ (scan rate 50 mV s ⁻¹) and c) the variation of mass activity (mA mg ⁻¹ _{Pt}) with the cycle number as extracted from cyclic voltammetry measurements..... 58	58
Figure SI2.1	Cyclic voltammogram of PtRu/C (30 wt% Alfa Aesar) in 1 M CH ₃ OH/0.5 M H ₂ SO ₄ , scan rate 50 mV ⁻¹ 63	63
Figure SI2.2	Cyclic voltammogram of Pt/C (20 wt%, E-Tek) in 1 M CH ₃ OH/0.5 M H ₂ SO ₄ , scan rate 50 mV ⁻¹ 63	63
Figure SI2.3	Variation of relative current with cycle number as extracted from CV measurements for various catalysts used in this study. Values normalized to the activity during scan number 10..... 64	64

Chapter 3

Figure 3.1	Pt 4f X-ray photoelectron spectra of PtRu/CNTs and PtRu/C catalysts...72	72
Figure 3.2	Ru 3d _{5/2} photoelectron lines of PtRu/CNTs and PtRu/C catalysts..... 72	72
Figure 3.3	RuK XANES spectra of PtRu/CNTs, PtRu/C catalysts and Ru metal and RuO ₂ as reference..... 75	75
Figure 3.4	RuK FT-EXAFS spectra of PtRu/CNTs, PtRu/C catalysts and Ru metal and RuO ₂ as references..... 75	75
Figure 3.5	PtL ₃ XANES spectra of PtRu/CNTs, PtRu/C catalysts and Pt foil as reference..... 76	76
Figure 3.6	PtL ₃ FT-EXAFS spectra of PtRu/CNTs, PtRu/C catalysts and Pt foil as reference..... 76	76

Figure captions

Figure 3.7	CV of PtRu/CNTs and PtRu/C catalysts in 0.5 M H ₂ SO ₄ , scan rate 50 mV.s ⁻¹).....	78
Figure 3.8	CA of PtRu/CNTs and PtRu/C catalysts at 0.7 V in 1M CH ₃ OH/0.5 M H ₂ SO ₄ A) initial electrode, B) after MOR for 100 cycles in the same solution.....	79
Figure 3.9	CV of PtRu/CNTs and PtRu/C catalysts in 1M CH ₃ OH/0.5 M H ₂ SO ₄ (A,B,C) and variation of the mass current at cycles number 20 and 100 extracted at 0.5 V D) and at peak potential E).....	80
Figure 3.10	IR corrected CH ₃ OH/H ₂ polarization curves for MEA1, MEA2 and MEA3 A) before and B) after ADT.....	81
Figure 3.11	<i>i</i> -V performance curves for MEAs in direct methanol fuel cell A) before and B) after ADT, and performance and relative performance of MEAs at C) 0.3 V and at D) 0.4 V.....	83
Figure 3.12	In situ CV curves for MEA1, MEA2 and MEA3 measured after ADT.....	84
Figure 3.13	ORR polarization curves after ADT for MEA1 and MEA 2 obtained by subtracting curves of CH ₃ OH/H ₂ from CH ₃ OH/O ₂	85
Figure 3.14	Proposed model for the as-prepared PtRu/CNTs (A), the heat treated catalysts (B) and the heat treated catalyst under electrochemical stress (C).....	88
Figure SI3.1	Ru 3d _{5/2} photoelectron spectra of selected samples deconvoluted Ru ⁰ into (red) and Ru ⁴⁺ (blue) contributions.....	93
Figure SI3.2	PtL ₃ XANES spectra of PtRu/CNTs compared to Pt foil and PtO ₂ reference.....	93
Figure SI3.3	PtL ₃ k-space EXAFS spectra of platinum foil, PtRu/C and PtRu/CNT catalysts.	94
Figure SI3.4	In situ CV curves for MEA1A), MEA2 B) and MEA3 C) before and after ADT.....	94
Figure SI3.5	comparison of <i>i</i> -V curves for all MEAs before ADT and after ADT; A) MEA1, B) MEA2 and C) MEA3.....	95
Figure SI3.6	EIS spectra (Nyquist plots) for MEA1 A), MEA2 B) and MEA3 C) before and after ADT in CH ₃ OH/H ₂	96
Figure SI3.7	TEM image of PtRu/C (HiSPEC [®] 5000) catalyst (30 % wt) from Alfa Aesar (JM), inset is the corresponding histogram.....	97

Chapter 4

Figure 4.1	XRD patterns of Pt/C (ETEK) , Pt/FCNTs and PtNi/FCNTs electrocatalysts (A) , heat treated PtNi(3:1)/FCNTs (B) and PtNi(1:1)/FCNTs (C).....	107
Figure 4.2	XPS spectra. A – Pt 4f lines of corresponding samples; B – Ni 2p _{3/2} regions; C – Ni 2p _{3/2} lines with (PtNi (3:1)/FCNT 400) and without (PtNi (2:1)/FCNT) clearly detectable Ni ⁰ contribution.....	109

Figure captions

Figure 4.3	Ni K (A) and Pt L ₃ (B) edge XANES spectra of the PtNi(1:1)/FCNTs and catalyst reference compounds.....	110
Figure 4.4	A Ni K edge real space EXAFS spectra of PtNi(1:1)/FCNTs catalyst and reference compounds B Pt L ₃ real space EXAFS spectra of PtNi(1:1)/FCNTs catalyst, platinum foil and platinum oxide. Inset – the same spectra in k-space.....	111
Figure 4.5	CO stripping voltammograms of selected samples.....	113
Figure 4.6	Schematic sketch of bimetallic Pt-Ni nanoparticles demonstrating that Pt and Ni are not randomly distributed in the particle, but Ni is enriched near the support and Pt towards the gas phase. Model represents both as prepared and heat treated samples, which however differ in the amount of surface segregation.....	116
Figure 4.7	CV of Pt/C ETEK, Pt/FCNTs and PtNi/FCNTs electrocatalysts in 0.5 M H ₂ SO ₄ /1 M CH ₃ OH (scan rate 100 mV/s). The current was normalized to the mass of Pt in the electrode.....	118
Figure 4.8	CV of PtNi(3:1)/FCNTs 200 (A) and PtNi(3:1)/FCNTs 400 (B) electrocatalysts in 0.5 M H ₂ SO ₄ /1 M CH ₃ OH (scan rate 100 mV/s).....	120
Figure 4.9	Variation of mass activity (mA/mg _{Pt}) with the number of cycle during the cycling potential, the data obtained for all catalysts from CV in 0.5 M H ₂ SO ₄ /1 M CH ₃ OH, scan rate 0.1V/s for 200 cycle in potential window (-0.2 to 1 V, vs. Ag/AgCl).....	121
Figure S14.1	TPD of as received (A) and functionalized (B) CNTs.....	127
Figure S14.2	TGA of as received CNTs and functionalized carbon nanotubes O ₂ (FCNTs) in atmosphere.....	128
Figure S14.3	Cyclic voltammogram for as received CNTs and nitric acid functionalized CNTs in 0.5 M H ₂ SO ₄ (scan rate 100 mV/s).....	129
Figure S14.4	N ₂ adsorption desorption isotherm for as received CNTs and functionalized CNTs.....	130
Figure S14.5	TEM images of A) Pt/C (ETEK), B) Pt/FCNTs and C) PtNi(1:1)/FCNTs, D) PtNi(2:1)/FCNTs, E) PtNi(3:1)/FCNTs, F) PtNi(3:2)/FCNTs, G) PtNi(1:1)/FCNTs 200, H) PtNi(3:2)/FCNTs 400.....	130
Figure S14.6	CV of Pt/C ETEK, Pt/FCNTs and PtNi/FCNTs electrocatalysts in 0.5M H ₂ SO ₄ /1M CH ₃ OH (scan rate 100 mV/s). Current is normalized to electrochemical surface area of the electrode.....	133
Figure S14.7	Ni 2p X-ray photoelectron spectra of samples after He ⁺ sputtering.....	133
Figure S14.8	Ni 2p X-ray photoelectron spectra of PtNi(3:2)/FCNTs sample before and after He ⁺ sputtering.....	134
Figure S14.9	Pt 4f X-ray photoelectron spectra of PtNi(3:2)/FCNTs sample before and after He ⁺ sputtering.....	134

Figure captions

Figure SI4.10	Model fit of NiK-edge EXFAS spectrum of PtNi(1:1)/FCNTs.....	135
Figure SI4.11	Model fit of PtL ₃ -edge EXAFS spectrum of PtNi(1:1)/FCNTs.....	135

Chapter 5

Figure 5.1	XRD patterns of PtNi/CNT electrocatalysts, A) effect of aging condition, B) effect of continuous irradiation duration, C) effect of pulsed number.....	144
Figure 5.2	TEM images of PtNi/CNT_C catalysts, A) PtNi/CNT_C_90_na and B) PtNi/CNT_C_60.....	145
Figure 5.3	TEM images of PtNi/CNT_P catalysts, A) PtNi/CNT_P_6 and B) PtNi/CNT_P_18.....	146
Figure 5.4	XPS spectra of PtNi/CNTs samples. A) Pt 4f signals; B) Ni 2p signals. (Ni 2p spectrum of PtNi/CNT_C_90_acid sample is not shown due to lower signal to noise ratio) and C) Ni 2p deconvolution exemplified with PtNi/CNT_C_90 sample.....	147
Figure 5.5	Pt L ₃ -edge XANES spectra (A) of the PtNi/FCNTs together with Pt-foil and PtO ₂ references, Pt L ₃ -edge FT-EXAFS spectra (B) of the PtNi/FCNTs together with Pt-foil reference and their fit three shell model exemplified by PtNi/CNT_P_12 (C).....	149
Figure 5.6	CO Stripping voltammograms for PtNi/CNT catalysts A) effect of aging condition for PtNi/CNT_C catalysts compared with Pt/C ETEK catalyst and B) effect pulsed irradiation cycle for PtNi/CNT_P catalysts.....	154
Figure 5.7	CV of PtNi/CNT catalysts in 1 M CH ₃ OH/0.5 M H ₂ SO ₄ scan rate 100 mV.s ⁻¹ , the current normalized to the Pt loading in the electrode.....	156
Figure 5.8	CA curves of PtNi/CNT catalysts in comparison with Pt/C ETEK in 1 M CH ₃ OH/ 0.5 M H ₂ SO ₄ at 0.7 V; A) effect of irradiation time and B) effect of pulse number.....	157
Figure 5.9	Model structures of PtNi catalysts supported on oxygen functionalized CNTs for the as prepared catalyst (A) and the catalysts after chemical (B) and/or electrochemical treatment (C) and (D) in acid environment.....	158
Figure SI5.1	Temperature profile of A) PtNi/CNT_C prepared under continuous irradiation mode and of B) PtNi/CNT_P prepared under pulsed irradiation mode. Inset the behaviour of irradiation mode is shown.....	163
Figure SI5.2	TEM images of PtNi/CNT_C catalysts, A) PtNi/CNT_C_90_acid, B) PtNi/CNT_C_90.....	163
Figure SI5.3	TEM images of PtNi/CNT_P catalysts, A) PtNi/CNT_P_9, B) PtNi/CNT_P_12.....	164

Figure captions

Figure S15.4	CV of PtNi/CNT catalysts in 0.5 M H ₂ SO ₄ scan rate 100 mV.s ⁻¹ , A) aged PtNi/CNT_C catalysts, B) PtNi/CNT_C catalysts prepared at different irradiation time and C) PtNi/CNT_P catalysts.....	165
Figure S15.5	CV for PtNi/CNT catalysts in 1 M CH ₃ OH/0.5 M H ₂ SO ₄ scan rate 100 mV.s ⁻¹ , the current normalized to the electrochemical surface area.....	166
Figure S15.6	Variation of mass specific activity and relative current against cycle number for PtNi/CNT_C and PtNi/CNT_P catalysts.....	167
Figure S15.7	CA curves of the PtNi/CNT catalysts in comparison with Pt/C ETEK in 1 M CH ₃ OH/ 0.5 M H ₂ SO ₄ at 0.7 V; A) PtNi/CNT_C catalysts and B) PtNi/CNT_P catalysts, the current normalized to the electrochemical active surface area.....	167

Chapter 6

Figure 6.1	TGA curve of various CNT-supported Pd-catalysts in O ₂ /Ar atmosphere. Heating rate 5 °C min ⁻¹	175
Figure 6.2	TEM images of Pd nanocatalysts, A) Pd/FCNT, B) Pd/FCNT_CtA, C) Pd/FCNT_A, D) Pd/FCNT_CtA_A, E) Pd/CNT and F) Pd/C E-TEK.....	177
Figure 6.3	XRD patterns of the prepared Pd nanocatalysts and Pd/C ETEK.....	178
Figure 6.4	Cyclic Voltammograms of the prepared Pd nanocatalysts and Pd/C ETEK in 0.5 M H ₂ SO ₄ (scan rate 50 mVs ⁻¹) ($\omega = 0$ rpm). Current normalized to the geometrical surface area of the electrode.....	180
Figure 6.5	CO-Stripping voltammograms of the prepared Pd nanocatalysts and Pd/C ETEK in 0.5 M H ₂ SO ₄ (scan rate 20 mVs ⁻¹) ($\omega = 0$ rpm), the black line represents the first scan whereas the red line represents the second one.....	182
Figure 6.6	Cyclic voltammograms of the prepared Pd nanocatalysts and Pd/C ETEK in 0.5 M HCOOH/0.5 M H ₂ SO ₄ (scan rate 50 mVs ⁻¹ , $\omega = 900$ rpm).....	183
Figure 6.7	Relation between the average particle size of the Pd nanocatalysts and the surface specific activity (SSA).....	184
Figure 6.8	Chronoamperometric curves of the prepared Pd nanocatalysts and Pd/C ETEK in 0.5 M HCOOH/0.5 M H ₂ SO ₄ ($\omega = 900$ rpm). Current normalized to Pd loading in the electrode.....	186
Figure S16.1	A) TG curve of FCNTs, as-received CNTs, Pd/FCNT and, Pd/CNT B) TG-DTG curves of Pd/FCNT with heating up to 1100 °C.....	191
Figure S16.2	TEM image of Pd/FCNT_A nanocatalysts, higher magnifications.....	192
Figure S16.3	TEM images of Pd nanocatalysts after heat treatment A) Pd/FCNT_CtA_200, B) Pd/FCNT_CtA_400, C) Pd/FCNT_CtA_A_200, And D) Pd/FCNT_CtA_A_400.....	192

Figure captions

Figure SI6.4	XRD patterns of Pd nanocatalysts after heat treatment.....	193
Figure SI6.5	Cyclic Voltammograms of the heat treated Pd nanocatalysts in 0.5 M H ₂ SO ₄ (scan rate 50 mVs ⁻¹) ($\omega = 0$ rpm), Current normalized to the geometrical surface area of the electrode.....	194
Figure SI6.6	CO-Stripping voltammograms of the heat treated Pd nanocatalysts in 0.5 M H ₂ SO ₄ (scan rate 20 mV s ⁻¹) ($\omega = 0$ rpm), the black line represents the first scan whereas the red line represents the second one.....	195
Figure SI6.7	Cyclic voltammograms of the heat treated Pd nanocatalysts in 0.5 M HCOOH/0.5 M H ₂ SO ₄ (scan rate 50 mV s ⁻¹ , $\omega = 900$ rpm).....	196
Figure SI6.8	Chronoamperometric curves of the prepared Pd nanocatalysts and Pd/C ETEK in 0.5 M HCOOH/0.5 M H ₂ SO ₄ ($\omega = 900$ rpm), the current normalized to the electrochemical surface area of Pd.....	197
Figure SI6.9	Chronoamperometric curves of heat treated Pd nanocatalysts in 0.5 M HCOOH/0.5 M H ₂ SO ₄ ($\omega = 900$ rpm), A) Pd/FCNT_CtA, B) Pd/FCNT_CtA_A. Current normalized to Pd loading in the electrode..	198

Appendix

Figure A1	Schematic diagram of the set-up for the three electrodes electrochemical cell (A) and the photos for the glassy carbon working electrode and its holder (B)	
Figure A2	Electrochemical set-up for electrochemical characterization at MLU Halle	
Figure A3	The photos of MEA (A), the hard components of the fuel cell (B) and the photo of the flow field for both anode and cathode side (C).	
Figure A4	The photos of A) set-up for DMFC measurements, 1) methanol feed solution, 2) the peristaltic pump, 3) the cell hard components and connection, 4) connection of both anode and cathode to the potentiostat, 5) the waste of the anode, 6) the fuel cell test station and 7) PC for data acquisition and B) the details of 3). The fuel cell measurements step up is available at MPI for Dynamics of Complex Technical Systems, Magdeburg.	

List of Abbreviation

AFCs	Alkaline Fuel Cells
ADT	Accelerated Durability Test
AP	Aminopyrene
BE	Binding Energy
CA	Chronoamperometry
CCM	Coated Catalysts Membrane
CE	Counter Electrode
CHP	Combined Heat and Power
CL	Catalyst Layer
CN	Coordination Number
CNTs	Carbon Nanotubes
CR	Conventional Reflux
CV	Cyclic Voltammetry
DFAFCs	Direct Formic Acid Fuel Cells
DFT	Density Functional Theory
DHE	Dynamic Hydrogen Electrode
DMFCs	Direct Methanol Fuel Cells
DTA	Differential Thermal Analysis
ECSA	Electrochemical Surface Area
EDAX	Energy-Dispersive X-ray Analysis or Energy-Dispersive Analysis of X-ray
EG	Ethylene Glycol
EIS	Electrochemical Impedance Spectroscopy
EMF	Electromotive Force
EXAFS	Extended X-ray Absorption Fine Structure
FAO	Formic Acid Oxidation
FCNTs	Functionalized Carbon Nanotubes
FCs	Fuel Cells
FT	Fourier Transformed
FT-IR	Fourier Transform Infrared
FWHM	Full Width at Half Maximum
GC	Glassy Carbon
GDL	Gas Diffusion Layer
GHG	Greenhouse Gas
ICP-OES	Inductively Coupled Plasma Optical Emission Spectroscopy
LEIS	Low-Energy Ion Scattering
MCFCs	Molten Carbonate Fuel Cells
MEA	Membrane Electrode Assembly

MOR	Methanol Oxidation Reaction
MSA	Mass Specific Activity
MW	Microwave heating
MWCNTs	Multi- Walled Carbon Nanotubes
NHE	Normal Hydrogen Electrode
OCV	Open Circuit Voltage
ORR	Oxygen Reduction Reaction
PAFCS	Phosphoric Acid Fuel Cells
PAH	Poly (allylaminehydrochloride)
PANi	Polyaniline
PDDA	Poly-diallyldimethylammonium chloride
PE	Photon Energy
PEM	Polymer Electrolyte Membrane or Proton Exchange Membrane
PEMFCs	Polymer Electrolyte Membrane Fuel Cells or Proton Exchange Membrane Fuel Cells
PTFE	Polytetrafluoroethylene
RE	Reference Electrode
RHE	Reversible Hydrogen Electrode
RT	Room Temperature
SECSA	Specific Electrochemical Surface Area
SOFCs	Solid Oxide Fuel Cells
SSA	Surface Specific Activity
SSC	Silver /Silver Chloride electrode
SWCNTs	Single-Walled Carbon Nanotubes
TEM	Transmission Electron Microscopy
TGA	Thermogravimetric Analysis
TPD	Temperature-Programmed Desorption
UHV	Ultra-High Vacuum
WE	Working Electrode
WHO	World Health Organization
XAFS	X-ray Absorption Fine Structure
XANES	X-ray Absorption Near Edge Structure
XAS	X-ray Absorption Spectroscopy
XPS	X-ray Photoelectron Spectroscopy
XRD	X-ray Diffraction

List of Symbols

\AA	Angstrom
a	Lattice parameter
d	Particle size or crystalline size [nm]
E_e^0	Standard potential for the cell [V]
E_o	Standard Potential for half-cell reaction [V]
ΔE_{rev}	The total theoretical voltage [V]
ΔE	Muffin-tin zero
E_{rev}	The theoretical reversible potential [V]
F	Faraday constant
fcc	Face-centered cubic structure
ΔG^0	Total change in the Gibbs free energy [kJ mol ⁻¹]
ΔH^0	Total Enthalpy Change [kJ mol ⁻¹]
i	Absolute current [mA] or Mass current [mA.mg ⁻¹ _{Pt}] or Specific Current [mA.cm ⁻² _{Pt}]
I	Measured current [mA]
I_p	The peak current [mA]
$I_{0.5}$	The current at potential 0.5 V [mA]
I_b	The backward current [mA]
I_f	The forward current [mA]
I_{total}	Total current [mA]
J_i	The alloying extent of metal i with another metal [%]
j	Current Density [mA.cm ⁻²]
M_{Pt}	The Pt loading in the electrode [mg _{Pt}]
n	Number of electrons
P_i	The Pairing factor of an element i .
Q_{CO}	The charge consumed during CO oxidation [mC]
Q_0	The standard charge required for oxidation of adsorbed CO monolayer [mC.cm ⁻²]
r	Shell radius
R_{ct}	Charge transfer resistance
R_M	Membrane resistance
R_{ohm}	Ohmic resistance
T	Temperature [°C]
V	The cell voltage [V]
X_{Ru}	Ru atomic fraction
η	Total efficiency of the fuel cell [%] or (Overvoltage) [V]
η_f	Fuel efficiency [%]
η_{rev}	The thermodynamic efficiency of the fuel cell

η_v	Fuel cell efficiency
μ	Absorption coefficient
μ_0	Background absorption
σ^2	Debye-Waller factor
θ	The diffraction angle [°]
λ	The wavelength [nm]
χ^2	Interface function (EXAFS)

Motivation

Polymer electrolyte membrane fuel cells (PEMFCs) working with liquid fuels are promising power sources for electronic devices. As liquid fuels, methanol and formic acid received significant attention for application in PEMFCs resulting in fuel cells called direct methanol fuel cells (DMFCs) and direct formic acid fuel cells (DFACFs); respectively.

DMFCs are considered to be one of the most promising candidates to replace lithium ion batteries as power sources in small electronic devices. The performance of DMFC however currently is limited by various technical challenges like methanol crossover, low anode catalyst activity and insufficient durability for long term application. In this regard, improvement the catalytic activity of the anode catalysts and enhancement their durability are an important topic in current DMFCs research.

To address the issue of catalyst activity and stability, our aim is to employ chemical methods using microwave irradiation heating for the synthesis of highly active catalysts for the anode side in DMFCs. Two catalyst systems will be chosen, namely; PtRu and PtNi supported on CNTs. In order to manipulate the surface structure of these catalysts, heat treatment in inert or reductive atmosphere will be employed aiming to achieve highly active and stable catalysts for the methanol oxidation reaction. The electrochemical characterization will be carried out in half cell measurements, however to get insight into the behavior under practical conditions, selected samples will be examined in membrane electrode assemblies. In depth structural characterization will be carried out to unravel in detailed the features of the catalyst structure with the aim of correlating them with their electrochemical performance. These investigations will help to identify the most active catalysts and to identify the structural features responsible for high activity.

Similarly activity and stability issues are important factors for Pd catalyst at the anode of DFACFs that may limit its performance. In order to address this issue, a chemical synthesis approach of Pd catalysts supported on CNTs will be employed using different synthesis ways. The structural and electrochemical characterization will be carried out to unravel electrochemical performance of the catalysts and to relate structure, performance, and stability.

The global demand for energy is rapidly rising with the increase in human population, urbanization and modernization. The growth in global energy demand is indeed projected to rise sharply over the coming years. The world heavily relies on fossil fuels to meet its energy requirements—fossil fuels such as oil, gas and coal are providing almost 80 % of the global energy demand. Fossil fuels, the main source of energy, are inflicting enormous impacts on the environment. Climatic changes driven by human activities, in particular greenhouse gas emissions (GHG), directly impact the environment. According to World Health Organization (WHO) as many as 160,000 people die from the side-effects of climate change each year and the numbers could almost double by 2020 [1]. There is worldwide research into other reliable energy resources to replace fossil fuels, considering the growing threat of their depletion in the next years [2]. Renewable energy is the solution to the growing energy challenges. Renewable energy resources such as solar, wind, biomass, and wave and tidal energy, are abundant, inexhaustible and environmentally friendly. These resources have the potential to meet the present and future energy demands of the world [2,3]. The increase in energy consumption causing the depletion of fossil fuels and rising public awareness for environmental protection drive research work to focus more on alternative energy sources [2].

As a consequence, novel renewable and clean energy power sources ought to be considered. One of the prevalent alternative sources of electric power is the fuel cells (FCs) technology. The fuel cell is defined as an electrochemical cell which converts the chemical energy stored in a fuel directly into electrical energy with high efficiency and low pollution emission (near zero emission). It is similar to a battery but with the advantage of no need to be recharged [4,5].

1.1 History of the fuel cells

The discovery of the fuel cell principle was achieved by Sir William Robert Grove (1811-96), British lawyer and amateur scientist who introduced the concept of a hydrogen fuel cell in 1839 [6]. Grove discovered that by immersing two platinum electrodes on one end in a solution of sulphuric acid and the other two ends separately sealed in containers of oxygen and hydrogen a constant current was flowing between the electrodes. Sealed containers contained water together with the respective gas. Grove noted that the water level rose in both tubes as the current flowed. The next step was to realize that combining pairs of electrodes connected in series produced a higher voltage, creating what he called a gas battery, i.e. the first fuel cell (Figure 1.1) [7].

In early 1933, Bacon developed the first fuel cell using hydrogen and oxygen for practical use. The fuel cell produced electricity through electrochemical processes using air and hydrogen. He began his work on alkaline fuel cells. In 1939, he built a cell

Chapter 1: Introduction and Basic Concepts

with nickel electrodes working at high pressure (200 atm) to prevent the electrolyte to flood the pores of the electrodes. During World War II, Bacon developed a fuel cell to be used in submarines of the Royal Navy. The work of Bacon on alkaline fuel cells has been developed through Pratt & Whitney to be used in the Apollo spacecraft [7,8].

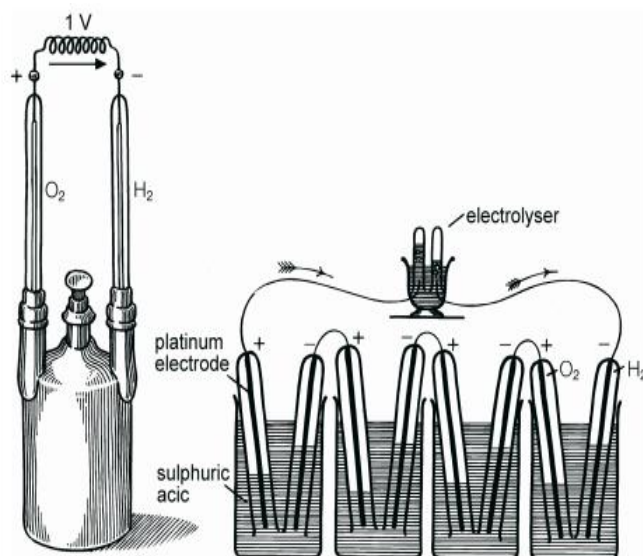


Figure 1.1: Grove's 'gas battery' (1839) produced a voltage of about 1 volt, shown left. Grove's 'gas chain' powering an electrolyzer (1842); Reprinted from Electrochemistry Encyclopedia, <http://electrochem.cwru.edu/encycl/art-f04-fuel-cells-pem.htm>, last access October 2013

In the 1970s, International Fuel Cells developed a more powerful alkaline fuel cell for NASA's Space Shuttle Orbiter (Figure 1.2). The Orbiter uses three fuel cell power plants to supply all of the electrical needs during flight [7,8].

In that regard, fuel cells have received increasing attention as power source with the advantage of producing very low emission and being a noiseless energy system. Currently fuel cell systems are widely employed in small scale applications such as portable computers and military communication equipment as well as in large scale applications such as combined heat and power (CHP) systems, mobile power systems, and vehicles. Prototype fuel cell automobiles are developed now by many companies like DaimlerChrysler, BMW, GM, Honda and Toyota [9].

In spite of the considerable advantages of the fuel cells technology as alternative power source, they still have serious technical drawbacks that limit their commercialization. One of these challenges is the high cost of the materials compared with other available technologies. Additional technical limitations of fuel cells are related to their durability issue, their operation at room temperature and their ability to reach a good performance after startup/shutdown cycles [10]. These constrains

limit the commercialization of the fuel cells technology, highlighting the importance of developing technological solutions that can overcome or solve these technical drawbacks.

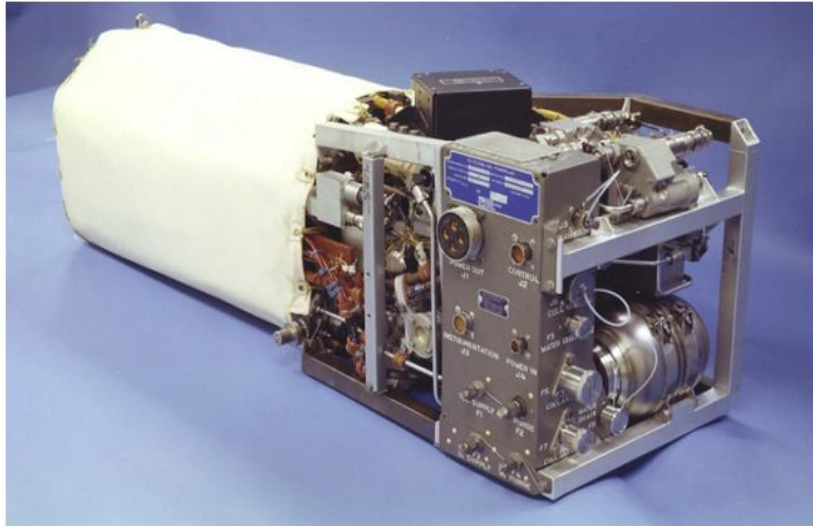


Figure 1.2: NASA Space Shuttle Orbiter alkaline fuel cell; Reprinted from Ref. [8].

1.2 Working principle of the fuel cells

Fuel cells supply electricity and heat through an electrochemical reaction between the fuel (i.e. Hydrogen, H_2) and an oxidant (Oxygen, O_2). The main products of these electrochemical reactions are electricity, water and heat. There are three main components for the fuel cell; the anode, the cathode and the electrolyte. There are different types of fuel cells which differ in their design which is based mainly on the electrolyte materials. The diverse fuel cells types will be discussed in the next section.

A typical reaction that occurs inside the fuel cell is the oxidation of hydrogen at the anode producing electrons and protons. The hydrogen ions then migrate through the electrolyte (ionic electrolyte) towards the cathode whereas the electrons pass through an electrical circuit to reach at the cathode where they combine with the oxygen (the oxidant) and with protons in the presence of the cathode catalyst producing water as a result of the reduction reaction. The electrochemical reactions which take place at the anode and cathode can be represented by the following equations (Equations 1.1 and 1.2) and are shown diagrammatically in Figure 1.3.

Chapter 1: Introduction and Basic Concepts

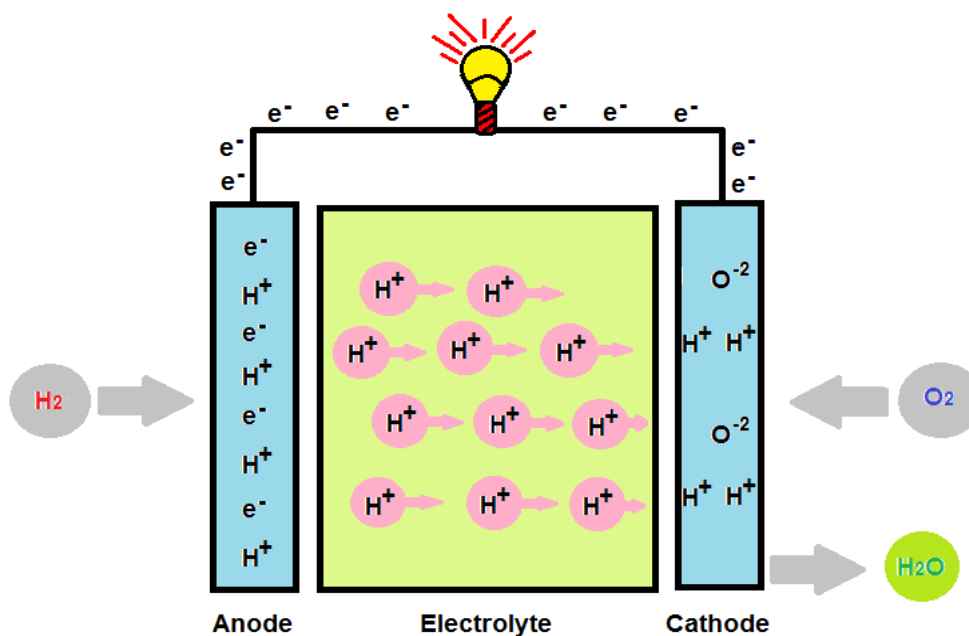
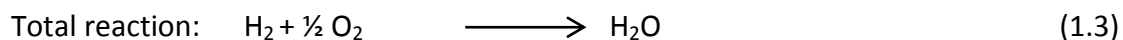
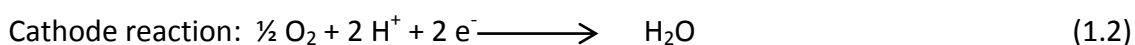
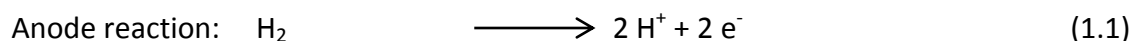


Figure 1.3: Schematic diagram of the fuel cell working principle and its reactions.

1.3 Fuel cell types

Fuel cell types are classified based on their working temperature and their applications but the most common classification is based on the electrolyte materials used in the fuel cell. According to this classification, fuel cells can be classified into five main types [7].

Alkaline Fuel Cells (AFC), where potassium hydroxide solution (KOH) is used as electrolyte. Since the AFCs are working with a liquid electrolyte (KOH), their operation temperature ranges from 60-100 °C, which classifies them as low operation temperature fuel cells. In AFCs, hydrogen is used as fuel and pure oxygen as oxidant to produce electricity, heat and water. AFCs have been used by NASA for the space mission programme to supply the spacecraft with electricity and drinking water.

Phosphoric Acid Fuel Cells (PAFCs) in which concentrated phosphoric acid is used as electrolyte. PAFCs work at temperatures in the range of 150 to 220 °C. Hydrogen and air oxygen are used as fuel and oxidant, respectively, in PAFCs while the noble metal platinum supported on carbon is used as electrode material. They are found suitable for stationary applications.

Molten Carbonate Fuel Cells (MCFCs), in which a molten carbonate immobilized inside a ceramic support is used as electrolyte. MCFCs are characterized by a higher operation temperature ranging from 600-700 °C. Hydrocarbons can be used as fuel where they are subjected to a reforming process under higher temperature. The electrodes kinetics is expected to be fast under this operation temperature. Thus, the usage of noble electrode materials is not required. The higher working temperatures make this type well suited for stationary applications.

Solid Oxide Fuel Cells (SOFCs) where a metallic solid oxide ceramic is used as an electrolyte i.e. Y_2O_3 -stabilized ZrO_2 . They are characterized by a high operating temperature in the range of 600-1000 °C and typically like MCFCs, hydrocarbons can be used as fuel. The stationary application is also the main applicable target for this type of fuel cells.

Proton Exchange Membrane Fuel Cells (PEMFCs), where a solid polymer exchange membrane is used as electrolyte. The usage of the solid polymer electrolyte membrane as electrolyte in PEMFCs limits the operating temperature of these cells in the range of 60-100 °C. PEMFC systems are usually used in portable and stationary applications. However, among the applications of PEMFCs, transportation seems to be the most suitable since they can provide continuous electrical energy supply at a high level of efficiency and power density at lower temperature. PEMFCs can be operated with different fuels such as H_2 (gas) and liquid fuels like methanol, ethanol, formic acid, or others, which make these fuel cells aside from their transportation application well suited for applications in portable and mobile electronic devices such as cell phones and laptops. The type of fuel cells, their working temperature, and the respective fuels are summarized below in Figure. 1.4 The above-mentioned types of fuel cells have been reviewed and their technologies have been the topic of several studies [11].

Among all types of fuel cells, PEMFCs received considerable attention as they are characterized by a high theoretical efficiency reaching up to 80 %. PEMFCs operate with hydrogen as fuel which can be used directly (direct hydrogen feed fuel cells) or being produced by on board steam reforming and partial oxidation of hydrocarbons (indirect hydrogen feed fuel cells). The hydrogen produced through these processes contains small quantities of CO which reduce the efficiency of the used catalyst materials in PEMFCs by catalyst CO-poisoning even at very low concentrations of CO (few ppm) resulting in reduced output power of the cell. The purification of hydrogen gas from CO add additional cost issues for PEMFCs and make the infrastructure more complex in addition to the difficulty of hydrogen handling and transportation. These technical obstacles of PEMFCs lead to the usage of hydrogen “stored” in liquid fuels as alternative fuels for further development of fuel cells [12].

Chapter 1: Introduction and Basic Concepts

Simple organic compounds, such as methanol, ethanol, and formic acid, have several advantages as liquid fuels to be used in fuel cells. Compared to hydrogen, they are easy to store and handle, possessing a high energy density in the order of 1 kWh/kg (Table 1.1). Furthermore, due to their simple structures they should have the simplest and most straightforward reaction mechanisms of all the possible organic fuels [13,14,15].

Ethanol is considered to be attractive due to its lower toxicity compared with methanol and its natural availability, produced as secondary product in many agriculture based industries. However its lower electrochemical activity reduces the performance of the ethanol feed direct fuel cells in comparison with methanol fuel cells [15].

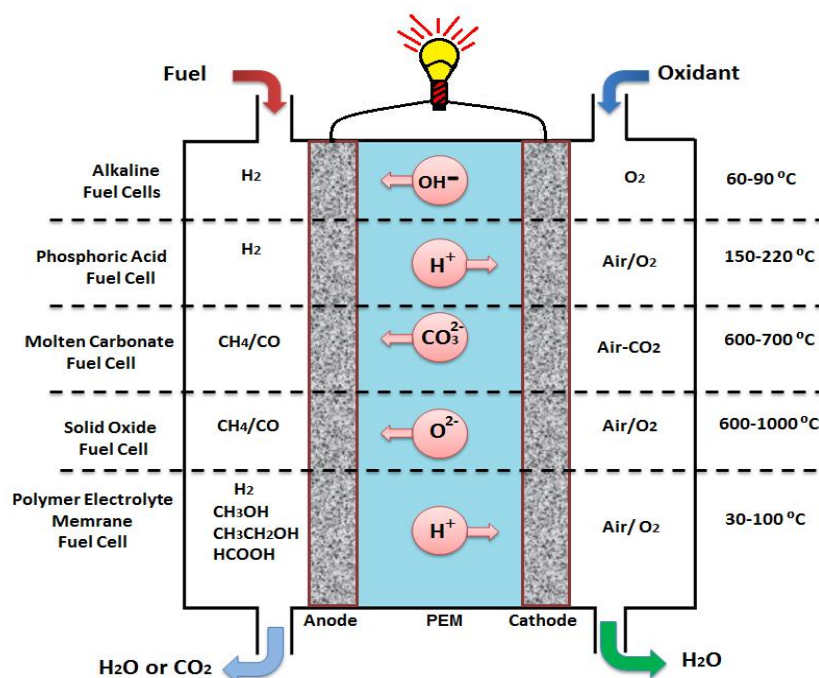


Figure 1.4: Schematic diagram of different types of fuel cells.

The direct oxidation of a liquid fuel in PEMFCs, in some cases called the direct oxidation fuel cells or direct liquid fuel cells, boasts this technology for small-scale applications particularly for cell phones, laptops and different types of small electronic devices. Among these liquid fuels suggested for this technology are methanol and formic acid. When methanol is used as direct fuel, the fuel cell is called direct methanol fuel cell (DMFC) whereas in case formic acid is used, the fuel cell is called direct formic acid fuel cell (DFAFC) [15].

Both of these types will be the topic of this thesis related to materials issues and particularly the electrocatalysts used in these types of fuel cells. In the following section the current status of these technologies in relation to the basic concepts and

Chapter 1: Introduction and Basic Concepts

the materials issues will be presented and discussed in view of the recent research work in this topic.

Table 1.1: Properties of various liquid fuels compared with hydrogen; Reprinted from Ref. [15] after modification.

Fuel	Energy Density (Wh/L) ^{a,b}	E_e^0 (V)	Reversible Energy Efficiency (%)
Hydrogen	180@ 1000 psi, 25 °C	1.23	83
Methanol	4820	1.21	97
Ethanol	6280	1.14	97
Formic Acid	1930	1.42	106

^a at standard condition and ^b Values for liquid fuels calculated with 100 wt. % fuel.

1.4 Direct methanol fuel cells

1.4.1 Basic concepts of direct methanol fuel cells

Methanol is a promising fuel for PEM fuel cells, which receives more attention than the other liquid fuels as a result of its higher electrochemical activity, high energy density and its lower cost compared to the other liquid fuels.

It exists as a liquid at room temperature and therefore it is easily handled and transported in addition to its production from biomass by fermentation of agriculture wastes [16,17].

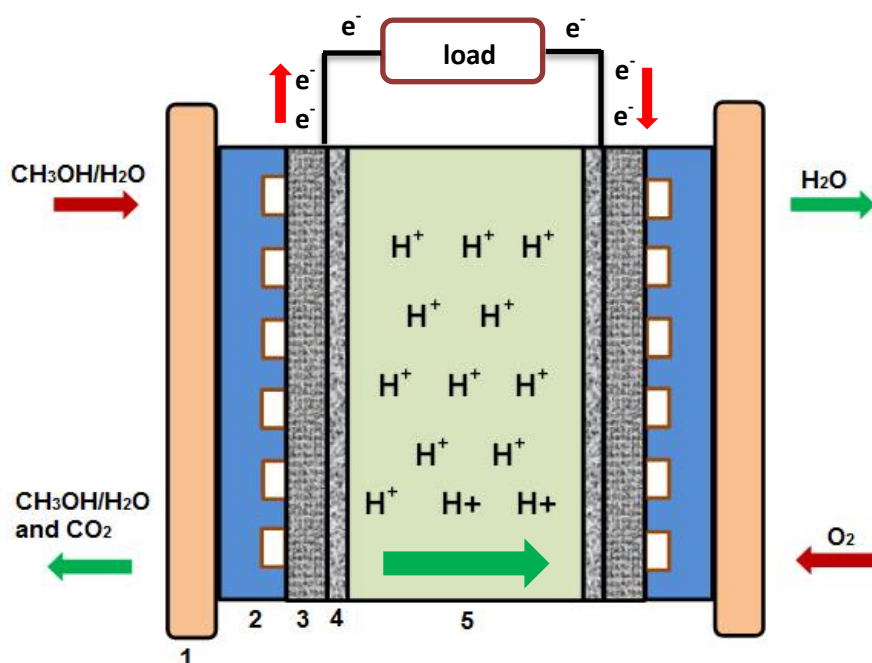
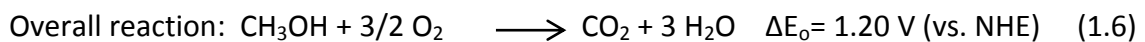
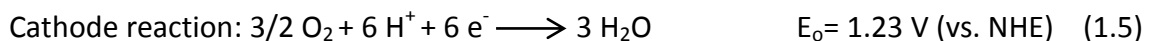
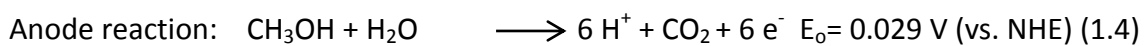


Figure 1.5: Schematic diagram of DMFCs, 1 metal end plate, 2 flow field carbon plate, 3 gas diffusion layers (GDL), 4 catalysts layer (CL), 5 proton exchange membrane.

Chapter 1: Introduction and Basic Concepts

In direct methanol fuel cells, the methanol aqueous solution is fed directly into the anode side to be oxidized at Pt based catalysts with the liberation of six electrons, and protons. As in hydrogen feed PEM fuel cells, in DMFCs oxygen is also used as the oxidant on the cathode. The heart of the DMFCs consists mainly of the membrane electrode assembly (MEA), which contains the two electrodes, anode and cathode separated by a polymer membrane. Every electrode structure has two layers called the gas diffusion layer (GDL) and the catalyst layer (CL). The gas diffusion layer consists of carbon cloth or carbon paper coated with carbon materials and contains a hydrophobic binder like polytetrafluoroethylene (PTFE). The catalyst layer consists of the corresponding catalyst material mixed with Nafion solution as binder and as proton conductor to facilitate the proton transfer inside the catalyst layer. The catalyst Nafion mixture is coated directly to the GDL. The MEA is mounted into the cell hard body by carbon plates, which serve as media to distribute the reactants (liquids and gases) into the electrode structure through the flow field while the carbon plates are in direct contact with metal end plates to fix the cell structure and serve as current collectors. In general, a Nafion membrane is used as polymer electrolyte membrane in DMFCs or other PEM fuel cell types. The function of the membrane is the proton exchange and to separate the reactants on both sides of the membrane. The Nafion membrane is a commercial membrane used in PEM fuel cells that has good protonic conductivity and good mechanical properties derived from its fluouopolymer backbone. However its high methanol permeability still represents a challenge for DMFCs commercialization. The schematic presentation of DMFCs is shown in Figure 1.5. The electrochemical reactions in DMFCs can be represented by the following equations: [17]



The total electrical work for the electrochemical reactions is calculated theoretically from the total change in the Gibbs free energy for the total reactions (methanol oxidation and oxygen reduction) which is related to the reversible voltage or electromotive force:

$$\Delta G^0 = -nF\Delta E_{rev} \quad (1.7)$$

Where n is the number of electrons transferred and F is the Faraday constant, 96485 C.mol^{-1} and ΔE_{rev} is the reversible voltage.

The ΔE_{rev} for the cell reactions can be calculated as follow:

$$\Delta E_{rev,cell} = E_{rev,cathode} - E_{rev,anode} \quad (1.8)$$

The reversible voltage of the direct methanol fuel cell, also called the Nernst potential, is equal to 1.2 V under standard condition (25 °C and 1 atm).

Since the fuel cell does not follow the Carnot efficiency which is related to the working temperature, the thermodynamic efficiency of the fuel cell is given by the ratio of the Gibbs free energy (ΔG°) to the enthalpy change (ΔH°).

$$\eta_{rev} = \frac{\Delta G^\circ}{\Delta H^\circ} \quad (1.9)$$

In practice, the voltage of a direct methanol fuel cell is not equal to the theoretical reversible voltage of the cell. This voltage loss results from the cell components behaviour under open circuit conditions such as corrosion of cell components in addition to the kinetic losses at the anode and the cathode under operating conditions. The cell voltage is related to the current density through the polarization curve (current-voltage curve) where the cell voltage is plotted against the current density. The polarization curve is overall a useful performance indicator which can account for the behavior of the cell voltage and current density obtained from the cell under certain conditions of temperature and pressure. An artificial polarization curve for a DMFC is shown in Figure 1.6.

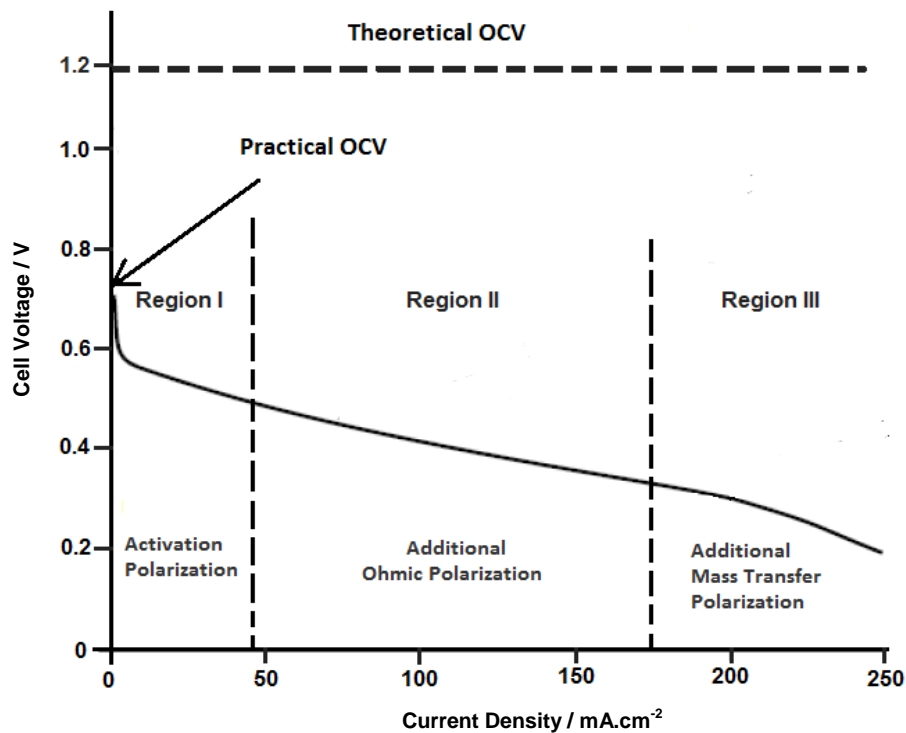


Figure 1.6: An artificial i-V polarization curve for a DMFC

The deviation of the practical cell voltage from the theoretical cell voltage is defined as the overvoltage or the polarization which results from different kinetics losses during the practical cell operation. The theoretical open circuit voltage for the DMFC is equal to 1.2 V while the practical open circuit voltage is about 0.7- 0.8 V which means that the DMFC has an overvoltage of 0.4-0.5 V at zero current.

In Figure 1.6, three different regions relevant to the three types of voltage losses can be distinguished as shown in the figure and described below:

The first region (I), the activation polarization region in which the voltage loss is a result of activation losses at lower current density.

The second region (II), the ohmic polarization region is characteristic of additional ohmic losses at medium current density.

The third region (III), the mass transport polarization region is characteristic of additional mass transfer limitations of the reactants and the polarization becomes more pronounced at higher current density and leads to steep decrease in the cell voltage.

From these regions, the types of the overpotential and their origins can be discussed as follows:

Activation Polarization: Activation polarization arises when the potential of the anode and cathode is shifted from their corresponding standard potential to some extent. This potential shift is known as activation overpotential and results from the slow reactions kinetics of the respective electrochemical reaction and depends on the activity of the catalyst materials. In the direct methanol fuel cell, the methanol oxidation reaction (MOR) is known to be a complex and multistep reaction which results in adsorption of some intermediates on the Pt catalyst surface. Consequently, the activity of the catalysts decreases resulting in an oxidation potential shift [18,19]. Also, the oxygen reduction reaction (ORR) on the cathode side is known to be a slow reaction with formation of intermediates and some processes of the multistep reaction cause the theoretical potential of the ORR to shift to some extent. Overall, the sluggishness of MOR and ORR kinetics at the anode and cathode of the DMFC, as a result of the lower activity of the anode and cathode materials causes the initial voltage loss of the cell at lower current density in the DMFC. It is well known that the sluggishness of the anode kinetics in DMFCs is more significant than on the cathode in comparison to PEMFCs working with hydrogen as a fuel where the kinetics of hydrogen oxidation is very fast and the more significant kinetic loss results from the sluggish cathode kinetics [17].

Ohmic Polarization: This type of overvoltage arise from the resistance of fuel cells components and mainly the resistance of ion transport through the ion conducting membrane. Additionally, the electron transfer in the electrode structure has some contribution.

Concentration Polarization (Mass Transfer Polarization): It is caused by the effect of mass transfer of the reactants at the electrode electrolyte interface. When the transfer of the reactants is slower than the rate of their consumption, a concentration gradient arises which decreases the cell voltage. This type of overvoltage is more pronounced at higher current density.

In addition to these different types of overvoltage which decrease the performance of the DMFCs, another serious effect is pronounced in direct methanol fuel cells. This effect results from the “methanol crossover” or “methanol permeation” from the anode into the cathode through the polymer membrane. The permeation of methanol in DMFCs causes two effects which decrease the cell performance. The first effect is the decrease of the fuel utilization, which means that a part of the methanol will be lost from the anode side and oxidized at the cathode. The current resulting from the oxidation of methanol at the cathode affects the total current density of the cell. The second effect of the methanol permeation is that the methanol permeating into the cathode will be oxidized at the cathode where the oxygen is reduced at the same time and hence the two opposite reactions will compete with each other leading to the formation of a mixed potential which in sequence decreases the cell voltage. Also, the adsorption of methanol on the cathode catalyst (methanol poisoning) will effect the activation of the cathode for ORR and decreases the ORR potential to about 0.9 V instead of 1.2 V (RHE).

From the discussion above, the actual voltage of a DMFC can be calculated from the theoretical open circuit voltage after subtraction of all other overvoltages as represented by the following equation (1.10):

$$V = \Delta E_{rev} - \eta_{act} - \eta_{ohm} - \eta_{trans} - \eta_{crossover} \quad (1.10)$$

Where ΔE_{rev} is the theoretical open circuit voltage, η_{act} is the activation overvoltage, η_{ohm} is the ohmic overvoltage, η_{trans} is the mass transfer overvoltage and $\eta_{crossover}$ is the fuel crossover overvoltage.

For calculation of the cell efficiency, the actual voltage efficiency for the DMFC at a defined current density ought to be calculated which is defined as the cell voltage divided by the theoretical voltage at the same temperature and pressure and given by the following equation (1.11):

$$\eta_v = \frac{V}{\Delta E_{rev}} \quad (1.11)$$

As a result of the methanol crossover, the current produced from the cell is smaller than that calculated based on the total methanol consumption. The ratio between the

Chapter 1: Introduction and Basic Concepts

measured current (I) and the theoretical current based on total methanol consumption and Faradays law (I_{total}) is known as fuel efficiency (η_f):

$$\eta_f = \frac{I}{I_{total}} \quad (1.12)$$

The total efficiency of DMFC is thus given by the following equation:

$$\eta = \eta_{rev} \times \eta_v \times \eta_f \quad (1.13)$$

The energy consumed by other accessories like pumps to deliver the fuel and blowers should be taken into consideration when the total efficiency of the system is calculated.

From equation 1.10, it's clear that the actual open circuit voltage of the direct methanol fuel cell is lower than the theoretical one (1.2 V) caused by the different types of overpotentials discussed above. This voltage loss is about 0.4-0.7 V under direct methanol fuel cell operation conditions and results mainly from the kinetic loss in the activation region. In that regard, decreasing the activation overpotential by the development of more active electrode materials for ORR and MOR is considered as an effective way to enhance the performance of direct methanol fuel cells which will make the wide application and commercialization of this type of fuel cells possible. The development of electrode materials for ORR and MOR is an active field of research for materials scientists interested in DMFCs and is currently being carried out by many different research groups [20].

The development of cathode catalyst materials for DMFCs is a hot area of this topic which deals with the preparation of highly active catalysts for ORR that fulfil the requirements for application in DMFCs such as higher methanol tolerance combined with higher activity towards ORR. Also, the decrease of Pt loading in the electrode materials through preparation of highly active bimetallic catalysts based on Pt alloyed with other transition metals such Cu, Co, Ni, Pd and Fe, is a promising target to decrease the cost of the fuel cells while maintaining its higher activity [21,22].

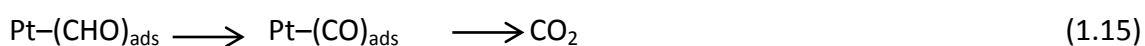
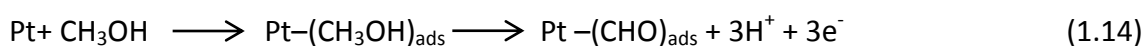
On the other hand, the highly catalytically active materials for MOR on the anode side represent an important venue for development and commercialization of DMFCs as the MOR is the main reaction on the anode side which has sluggish kinetics caused by adsorption of poisoning intermediate on the catalysts surface. In that regard, the preparation of catalyst materials with high poisoning tolerance and high activity toward MOR will be the main part of this thesis. In the next section an overview about the methanol electrooxidation mechanism will be given with a description of the properties of the required catalysts for MOR and how they can be prepared in a way

that could enhance their activities. It will also deal with the way of how they are characterized.

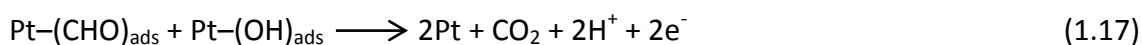
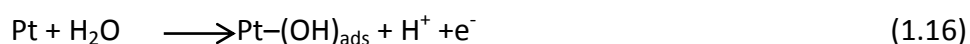
1.4.2 Methanol electrooxidation mechanism

For electrooxidation of methanol, Pt is well known as an active electrode material. Several studies on the mechanism of methanol electrooxidation on Pt have been done [19,23]. The availability of techniques by which the active intermediates and the final product can be identified and detected, assist to establish the mechanism for methanol electrooxidation [23-25]. According to the suggested mechanisms, methanol is dissociatively adsorbed through C-H cleavage at a Pt electrode forming a formyl-like species $-\text{CHO}$. These species can behave in different ways with the formation of strongly adsorbed CO species, which is responsible for the Pt electrode catalyst poisoning that decrease the electrode performance due to the higher potential required for oxidation of CO species into CO_2 .

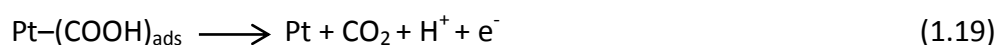
The total process can be written by the following equations (1.14 and 1.15):



In this process the formation of $-\text{CHO}_{\text{ads}}$ is the key step which controls the reaction mechanism. The oxidations of these species involve many pathways. The usual path is the oxidation of these species to CO_{ads} followed by formation of CO_2 as shown above. An alternative path is their direct oxidation by action of adsorbed OH_{ads} species formed from the dissociation of water according to the following equations (1.16 and 1.17)



Another parallel reaction combined with the above reaction is the formation of adsorbed formate which is further oxidized into CO_2 as follows :

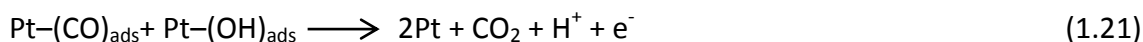


On the other hand, adsorbed CO_{ads} can be oxidized by the action of adsorbed OH_{ads} species into formate species followed by their oxidation into CO_2 according to reaction (1.20):



Chapter 1: Introduction and Basic Concepts

or oxidized directly by action of $(\text{OH})_{\text{ads}}$ into CO_2 according to equation (1.21):



The mechanism of methanol oxidation depends on the oxidative behavior of $-(\text{CHO})_{\text{ads}}$ species which undergo different pathways of oxidative removal according to the diagram in Figure 1.7.

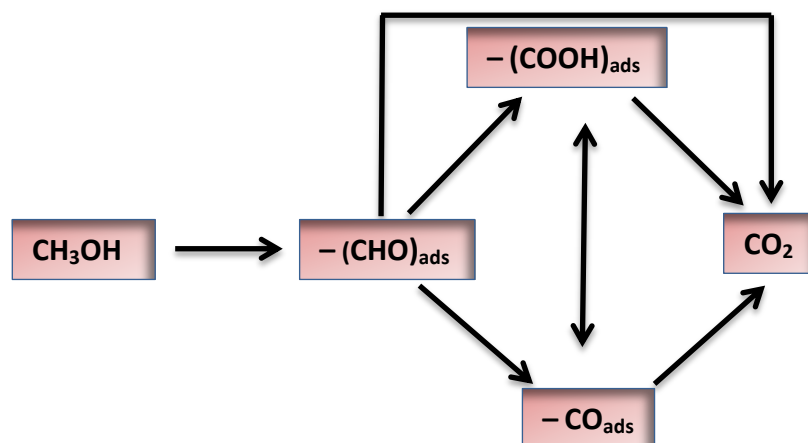


Figure 1.7: Schematic representation of possible pathways for oxidation of $-(\text{CHO})_{\text{ads}}$, Reprinted from Ref. [23].

The scheme shown above demonstrates the main challenge for methanol oxidation due to the formation of CO_{ads} on the Pt surface which is the fast step that leads to the blocking of the Pt surface by CO_{ads} causing what is called the poisoning effect. The removal of CO_{ads} can be achieved at potentials where oxygenated species are formed on the Pt surface by dissociation of water, this process occurs at potentials higher than 0.5-0.6 V vs. RHE [23,26].

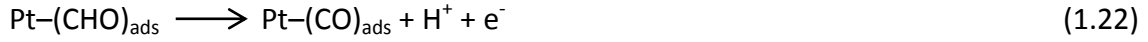
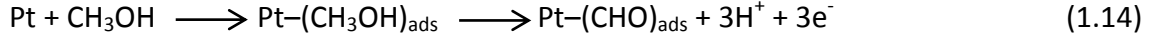
Another pathway is the oxidation of $-(\text{CHO})_{\text{ads}}$ into CO_2 through formation of $-(\text{COOH})_{\text{ads}}$ intermediates which also requires the presence of oxygenated species that can be derived from water dissociation on the Pt catalyst surface. In that regard, the bimetallic catalysts system (PtM) is considered as an attractive solution to overcome the poisoning of the Pt surface by adsorbed intermediates where the second metal M can supply the oxygenated species by water dissociation at a lower potential than Pt. A broad variety of PtM catalyst systems have been investigated for this purpose (M= Ru, Ni, Co, Mo, Sn, Pd, etc.) [19,23,25,27].

As reported in the literature, PtRu is the most active catalyst for methanol oxidation as confirmed by FT-IR spectroscopic studies. The $-(\text{OH})_{\text{ads}}$ species are formed on Ru sites at potentials much lower than on Pt leading to the oxidation of CO_{ads} at

Chapter 1: Introduction and Basic Concepts

lower potentials. The oxidation process of methanol on bimetallic systems with PtRu as an example can be summarized as follows [19,23,27]:

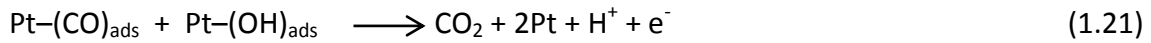
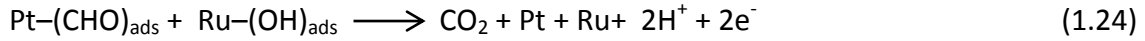
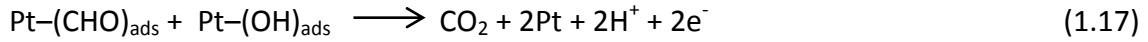
Step 1: adsorption, dissociation and dehydrogenation of the methanol molecule on the Pt catalyst forming formyl and/or the CO_{ads} intermediate:



Step 2: formation of $-(\text{OH})_{\text{ads}}$ on Pt and Ru



Step 3: oxidation of adsorbed intermediates by surface oxygenated species according to the following equations:



From the mechanism discussed above, the important role of the second metal as a promoter for adsorbed intermediates is evident from the formation of $(\text{OH})_{\text{ads}}$ due to the fact that it can oxidize them at lower potentials than on Pt [19]. In that regard, the development of bimetallic catalysts for methanol oxidation is considered as an important topic of research to improve the performance of DMFCs and speed up their commercialization [20].

Highly active catalyst materials should have a high number of active sites per mass unit which is difficult to produce with bulk materials. Consequently, attention has been paid to produce catalyst particles with small dimensions that provide more active sites per mass unit of catalyst. The ultimate goal is to prepare catalyst particles in the nanosize using nanotechnology. The materials in nanostructure form exhibit new properties which make them suitable for novel applications in different fields; in particular in fuel cells technology to enhance their wide application and commercialization.

The major goal of this work is the preparation of PtM (M= Ru, Ni) based nanostructured bimetallic catalysts for methanol oxidation. The methods of

preparation of these catalysts, their characterization and their electrochemical evaluation will be reviewed in view of recent literature.

1.5 Electrocatalysts for methanol electrooxidation

As discussed above in regard of the methanol oxidation mechanism, Pt is not an efficient catalyst for MOR and bimetallic catalyst systems are considered as an alternative strategy to overcome this technical obstacle and to decrease the poisoning effect of CO_{ads} on the Pt surface. The mechanism by which the second metal can affect the catalysis of methanol oxidation will be discussed in detail in the following sections.

The catalytic activity of an individual bimetallic catalyst depends on many factors that control its activity. Some of these properties include particle size, structure, surface composition, distribution of the catalytic constituents on the surface, and also on the type of supporting material. Most of the structural and surface properties of the catalyst can be controlled during the preparation process or by post treatment after the preparation. The first step of catalyst preparation involves the choice of support materials, considering its vital role in supporting the nanoparticle catalyst phase and allowing for the preparation of porous electrodes for the diffusion of reactants and liberation of products on the surface of the catalyst particles. More details about the supporting materials and their properties will be discussed in the next section.

1.5.1 Electrocatalyst supporting materials

Most of the electrocatalysts used for fuel cells technology, in particular PEMFCs, are Pt based catalysts. They are mostly used as supported catalysts where the active catalyst phase of Pt or its alloys with different metals is supported on porous conductive materials with high surface area. The role of the supporting materials is to maintain the high dispersion and homogenous distribution of the catalyst particles to obtain high catalytic activity. Also, the supporting materials are expected to play a role during the catalyst synthesis to control the morphology and the structure of the catalyst and even more the life time of the fuel cell [28,29].

Supporting materials are not only materials where the active catalyst particles can be supported on their surface to enhance their dispersion but they also provide a medium for reactants and products transport inside the fuel cells as expected from their electronic properties, their adsorption behavior and porous structure.

The requested properties for a catalyst support are high surface area for high catalyst loadings and good dispersion, suitable pore size for smooth mass transfer of the reactants and products inside the electrode, high electrical conductivity for good electron transport through the electrode, chemical and mechanical stability as well as electrochemical corrosion resistance in harsh fuel cell environments [28-30].

Among the materials that meet these criteria, carbon based materials are the most appropriate. Carbon black is the most common catalyst support used in fuel cell technology for Pt and Pt alloys for PEMFCs and PAFCs. The most widely used carbon black in research and commercial fuel cells (up to 80% in total) is the Vulcan XC-72 carbon black. It is produced via a furnace method using oil fractures as raw material. In addition to Vulcan XC-72 carbon, other carbon blacks are available commercially to be used in fuel cells, i.e. Black Pearl 2000, Ketjen EC series, and Denka Black [30].

Although they are highly used and show good performance during fuel cell application, carbon blacks suffer from their poorly defined porous structure and wide ranged particle size and pore size distributions. For example, in Vulcan XC-72 the half of its total pore volume is of macroporous or mesoporous size whereas the rest are micropores (< 1 nm) which limit the catalytic performance of catalysts supported on Vulcan XC-72 owing to their inaccessibility to reactants [21]. Additionally, the amorphous nature of carbon blacks makes them susceptible to electrochemical corrosion under fuel cell operation conditions, particularly in the presence of highly active metallic catalyst particles. The working conditions for carbon supports in fuel cells, even in the low-temperature types, are extremely harsh, especially at the cathode side where oxygen is reduced. In most cases, the electrochemical corrosion of carbon catalyst support can be referred to carbon oxidation or combustion [30,31].

As a result of carbon corrosion, the support loses its surface area leading to a catalyst detachment or agglomeration and therefore the performance of a fuel cell significantly decreases. The electrochemical corrosion of carbon blacks is accelerated with decreasing Pt particle size (3-8 nm), increasing Pt loadings, operation temperature, cathode potential, and amorphous nature of the carbon blacks. Hence, the search for more durable and stable substitutes for carbon blacks is of current research interest [30-32].

With increasing interest in carbon materials research, today different types of carbon or carbon-based materials have been developed, such as mesoporous carbon, carbon nanomaterial (graphitized carbon, carbon nanotubes, graphene, and carbon nanocoils) and heteroatom-doped carbons (nitrogen- and boron-doped carbons).

The carbon atom has six electrons and the hybridizations of the 2s orbital and two or three of the 2p orbitals can form a sp^2 or sp^3 hybrid, respectively, allowing carbon to build up different structures. For example the sp^2 orbital hybridization results in the hexagonal structure of graphite (Figure 1.8a), whereas the sp^3 hybridization status can form the tetrahedral bonded structure of diamond (Figure 1.8b).

Until the 1980s the only known carbon ordered structures were graphite and diamond. In 1985, the discovery of the buckyball structure (C_{60}) of carbon [29,33], which consists of a single layer of graphite containing pentagons and hexagons rings,

became the most famous among these structures (Figure 1.8c). The carbon structures can be divided into three groups, called zero-dimensional structures (0D) such as fullerenes, one-dimensional structures (1D) such as nanotubes, (Figure 1.8d), and two-dimensional structures (2D) such as graphene (i.e. a single sheet of graphite, Figure 1.8e) [29,33].

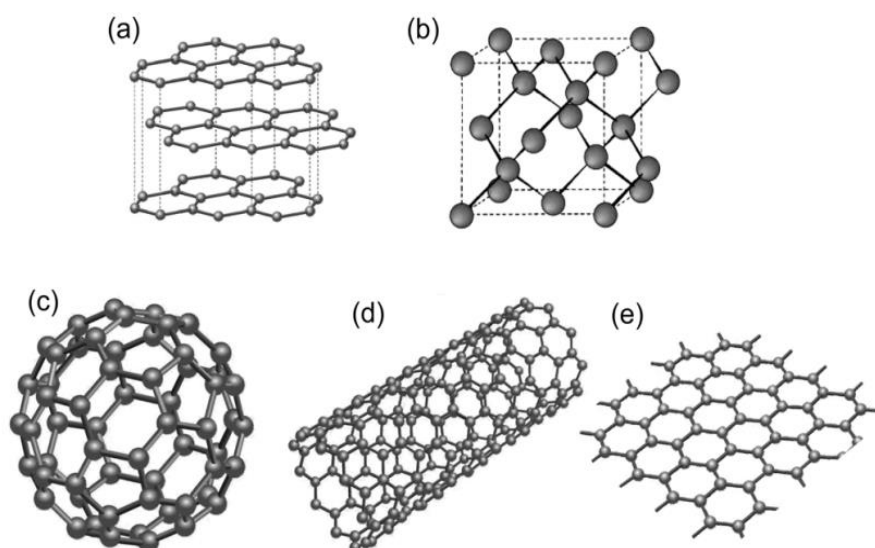


Figure 1.8: Carbon ordered structures including (a) graphite, consisting of a stack of graphene layers, (b) diamond, and the new carbon allotropes (c) 0D, buckminsterfullerene (C_{60}), consisting of graphene balled into a sphere, (d) 1D, nanotube, made of a rolled-up cylinder of graphene, and (e) 2D, graphene; Reprinted from Ref. [33].

Carbon nanotubes have been observed in 1976 and were defined at this time as hollow structure. However, the pioneering work by Iijima in the early 1990s on the discovery of multiwalled carbon nanotubes led to increasing attention and made them one of the most interesting materials in nanoscience and nanotechnology [34,35].

Carbon nanotubes have two defined structures. Single-walled carbon nanotubes (SWCNTs) consist of a sp^2 hybridized graphene sheet rolled up into a hollow cylinder (Figure 1.9). The SWCNTs have an internal diameter of 0.4-2.5 nm where their lengths varies from few micrometers to several millimeters. When the tube has several concentric cylinders, the structure is referred to as multiwall carbon nanotubes (MWCNTs), as shown in Figure 1.9. The MWCNTs have two or several walls, with an external diameter ranging from 5-30 nm with an interlayer spacing of 0.34 nm with the same range of the length as SWCNTs.

The physical properties of CNTs depend on variations of their microscopic structure. They have the ability to show semiconducting or metallic behavior

depending on their diameter and on the way *via* which the graphene sheet is rolled up around the tube axis. For example SWCNTs occur in three distinct geometries; namely armchair, zig-zag and chiral, as shown in Figure 1.10, where the armchair structure exhibits metallic characteristics, whereas the zig-zag structure acts as semiconductor [36].

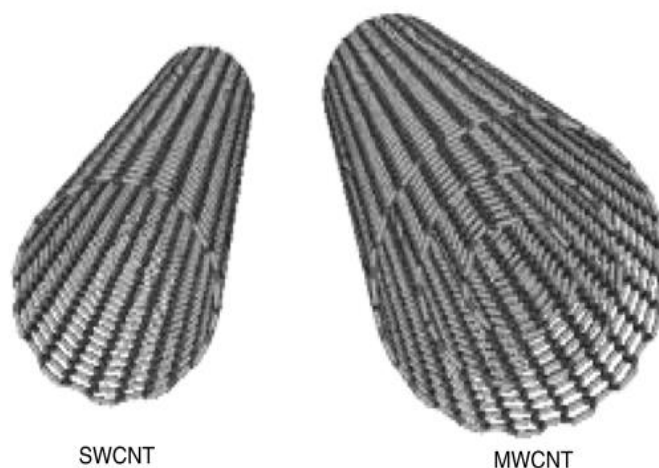


Figure 1.9: Structure of SWCNT and MWCNT; Reprinted from Ref. [33].

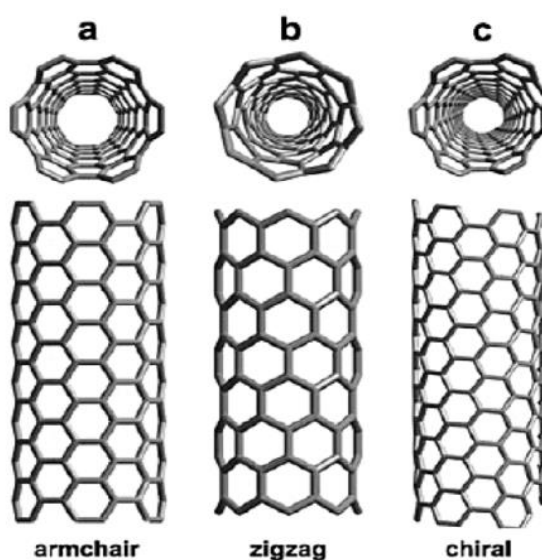


Figure 1.10: Structural models of SWCNTs exhibiting different chiralities; (a) armchair, (b) zig-zag, and (c) chiral arrangement; Reprinted from Ref. [33].

Compared with carbon black, carbon nanotubes (CNTs) have attracted increasing interest in fuel cell applications as a promising support material for metal catalysts, owing to their unique chemical stability, high surface to volume ratio, high electrical

conductivity (up to 10^4 S m^{-1} compared with carbon blacks 4 S m^{-1} [37]) and high electrochemical stability against corrosion [30].

Carbon nanotubes have indeed been used as catalyst support in many studies. As a result of the defect-free surface of CNTs and their chemical inertness, the catalyst nanoparticles are hindered from being deposited on their surface [38-41]. The lack of anchoring sites for nanoparticle deposition leads to the aggregation and low loading levels of metals on the support [42,43]. Several studies have shown that the introduction of surface groups into CNTs plays a key role in achieving high dispersion and a high loading level of the nanoparticle catalysts [32,41]. In that context, the functionalization of CNTs is a suitable approach to enhance the attachment of nanoparticle catalysts onto their surface for the preparation of nanoparticle catalysts in highly dispersed form. The most frequently adopted methods for CNT surface modification can be divided into two methods of functionalization: namely covalent functionalization [32,44,45] and non-covalent functionalization [46-48]. In the covalent surface functionalization, the CNTs surface will be changed by attaching new surface groups or molecules forming covalent bonds between these new groups or molecules and the surface of CNTs. The most widely investigated covalent functionalization method is the chemical surface oxidation which involves the introduction of oxygen surface functional groups to the CNTs external walls. This is achieved by an oxidation process in presence of strong acids such as concentrated HNO_3 or a mixture of it and H_2SO_4 or strong oxidizing agents such as H_2O_2 and KMnO_4 to create oxygen containing functional groups such as carboxyl ($-\text{COOH}$), hydroxyl ($-\text{OH}$) and carbonyl ($>\text{C}=\text{O}$) groups and other oxygen containing groups [32,44,45,49]. The different oxygen containing groups that can be obtained upon the oxidation process are shown in Figure 1.11. Such groups can serve as suitable anchoring and nucleation sites for nanoparticles on the CNTs surface providing a more homogenous, uniform distribution and a high loading of nanoparticles on their surface compared to non-functionalized CNTs [45,50].

Chemical oxidation by acids could affect the CNTs by damaging the structure forming amorphous carbon and leading to the loss of electrical conductivity. In that regard, gentle oxidation conditions by using diluted acids [51] or the electrochemical oxidation [52] are favored as they can introduce the requested functionalized groups without causing severe damage to the CNTs.

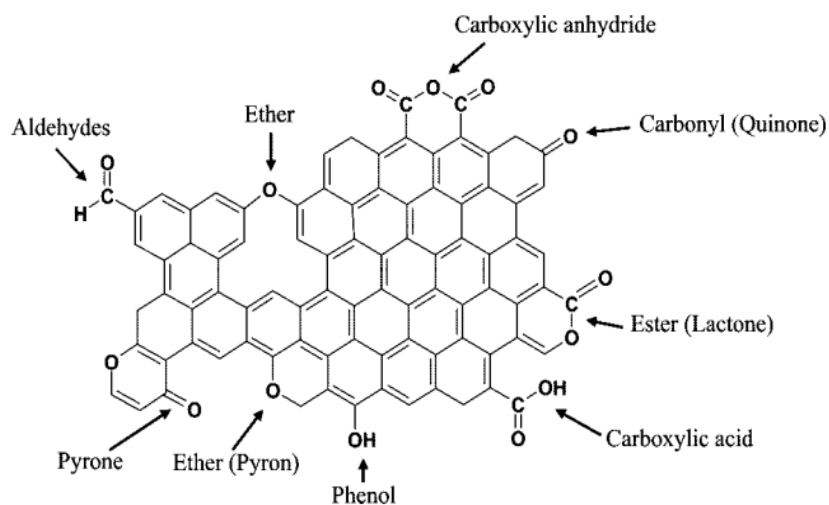


Figure 1.11: Schematic representation of oxygen containing groups bonded to the carbon nanotubes surface; Reprinted from Ref. [49]

In contrast, in non-covalent functionalization of CNTs, molecules bearing specific groups like carboxylic and amine groups can be physically attached to the surface of CNTs. These groups also can provide specific interaction with the metal precursors during the catalysts preparation. The advantage of this method is the possibility to attach a high density of functional groups with homogenous distribution on the surface of CNTs which makes the preparation of highly dispersed and homogenous nanoparticle catalysts more easily controllable. Also, the preservation of the intrinsic properties of CNTs, in particular the electrical conductivity is vital for electrocatalyst application as the initial properties of the CNTs will not be affected after the modification process. An example of these molecules used for non-covalent functionalization is 1-aminopyrene (1-AP) which is a bifunctional molecule with a pyrenyl group and an amino functional group. Since the pyrenyl group is highly aromatic in nature, it can interact strongly with the basal plane of graphite via π - π interaction. In the same way, the pyrenyl group of 1-AP could also strongly interact with the sidewalls of CNTs, attaching the 1-AP on the CNTs as shown in Figure 1.12 [47]. The amino groups on the CNTs surface play a vital role during the catalyst preparation as under slightly acidic conditions the surface of CNTs is weakly positively charged which can attract the negatively charged Pt precursors through a self-assembly process in case of Pt/CNTs preparation. In case PtRu/C is the targeted catalyst, the Ru precursor with its positive charge can be subsequently self-assembled after self-assembly of the Pt precursor on the CNTs surface which is followed by a reduction process forming the nanoparticles as shown in Figure 1.12.

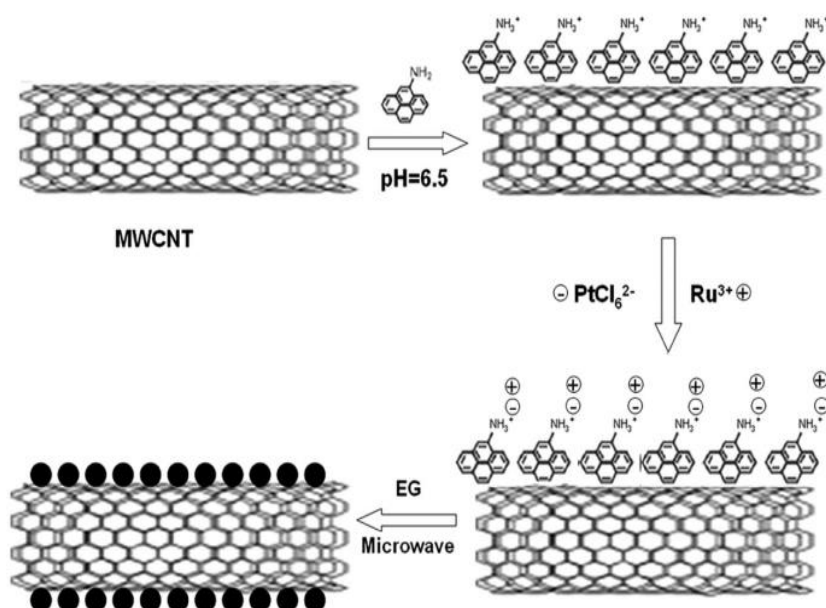


Figure 1.12: Schematic diagram of the synthesis of PtRu electrocatalysts on 1-AP-functionalized MWCNTs; Reprinted from Ref. [47].

Others molecules have been used for the non-covalent functionalization of CNTs, such as polymers or ionic liquid [53]. In this strategy, CNTs are wrapped with the polymer or ionic liquid bearing specific groups aiming to introduce surface functional groups on the CNTs with high density and uniform distribution for the anchoring and nucleation of nanoparticle catalysts. An example of these polymers compounds includes poly diallyldimethylammonium chloride (PDDA) [47,52,54] which is used as polymer for functionalization of CNTs and others carbon supports for electrocatalysis applications. It should be noted that other polymers i.e. polyallylaminehydrochloride (PAH) [55] and polyaniline (PANi) [56] have been used for functionalization of CNTs as electrocatalyst supports for fuel cells applications.

1.5.2 Electrocatalyst preparation methods

After choosing the supporting materials and the functionalization step, the next important step involves the selection of the preparation method. By choosing the preparation method and controlling the parameters of the process, the structural properties of the catalyst including the surface distribution of the metallic components, the atomic composition, the particle size distribution, the crystal phase and the alloying extent can be controlled.

Different methods were developed for the preparation of Pt based electrocatalysts for fuel cell applications including chemical and physical methods [23,57-59]. The chemical methods are considered as the most suitable methods for synthesis of Pt based

catalysts due to their simplicity and ease of application on a large scale for the preparation of large quantities of catalysts. The current research in electrocatalyst preparation is focused on the development of new methods for the cost-effective preparation of highly active catalysts to overcome the cost effect imposed by the use of noble catalysts in fuel cells and to enhance their commercialization [20,57]. In the following section the most important and recent chemical methods utilized for the preparation of carbon supported electrocatalysts will be summarized with special emphasis on PtM (M= Ru,Ni) catalysts for methanol oxidation in DMFCs. Figure 1.13 shows the different chemical methods used for the preparation of supported PtM catalysts.

1.5.2.1 Impregnation method

The impregnation method is the most common method for the preparation of monometallic and bimetallic electrocatalysts for methanol oxidation and oxygen reduction in fuel cells. In this process, a metal precursor is impregnated onto the carbon support material in aqueous or alcoholic media followed by reduction of the metal ions with reducing agents such as NaH_2PO_2 , $\text{Na}_2\text{S}_2\text{O}_3$, NaBH_4 , $\text{Na}_4\text{S}_2\text{O}_5$, N_2H_4 or formic acid. In the industrial process of catalyst preparation, after the impregnation step, the support with the impregnated metal ions is separated and dried. Thereafter it is subjected to thermal annealing in reductive atmosphere. In this case the process is called impregnation decomposition method and it has been used by many groups for the preparation of bimetallic supported catalysts such as PtRu/C or PtRu/MWCNTs [5,23,58].

Choosing the reducing agent is crucial because the reduction procedure is an important step for controlling the particle size and the alloying extent. For supported catalysts, it also affects particle distribution, in particular the distance between neighboring particles. Additionally, the reducing agent can affect the distribution of metallic components at the atomic level which plays a substantial role in the electrocatalytic activity of the catalysts; in particular for PtRu catalysts where the surface distribution of Pt and Ru on the catalyst surface is important for high catalytic activity.

In the impregnation step, different metal salts are used as metal precursors. It has been found that the usage of chloride containing precursors such as H_2PtCl_6 and RuCl_3 resulted in catalysts with high extent of agglomeration. In that regard, using other precursors such as organometallic compounds or non-chloride containing precursors is the best way for the preparation of catalysts with high dispersion of catalyst particles.

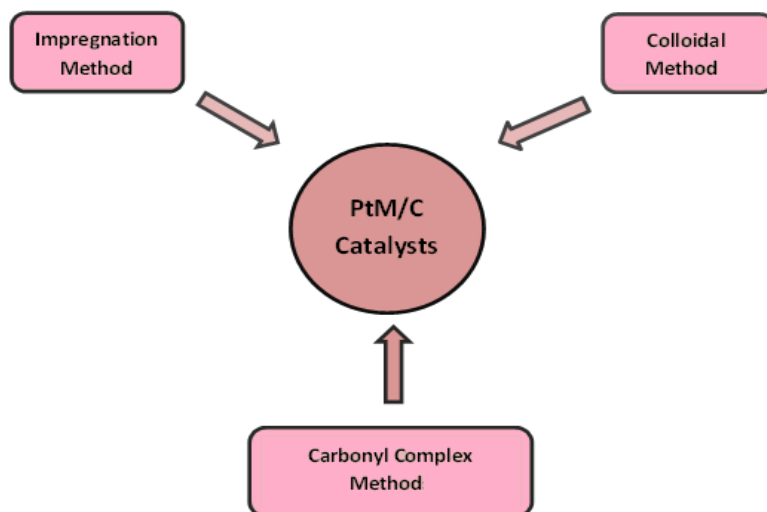


Figure 1.13: Different chemical methods for preparation of PtM/C catalysts.

1.5.2.2 Carbonyl complex method

In this method the carbonyl complexes of the prospective metals are prepared by reaction of their corresponding metal chloride salts with carbon monoxide at lower temperature under mechanical stirring. The prepared complexes afterward are adsorbed on the carbon support followed by a thermal decomposition step under reductive atmosphere. Using this method, catalysts with a controlled metal composition and a narrow particle size distribution can be prepared. PtRu/C [60] and PtNi/C [61] with high dispersion on the support were prepared using this method.

1.5.2.3 Colloidal method

The colloidal method is a common chemical method for the preparation of bimetallic catalysts. The colloidal method involves three main steps: 1) preparation of metal containing colloids; 2) deposition of the colloids onto the carbon support; and 3) chemical reduction of the mixture with reducing agents. In some procedures the reduction step is carried out before the deposition of the reduced nanoparticles. The stabilization of metal colloids is an important step in the colloidal method to prevent the aggregation of the colloids. Different stabilizing agents including polymers, block copolymers, solvents, long chain alcohols, surfactants and organometallics have been used for this purpose [23,57].

Different colloidal methods have been used for preparation of PtRu/C catalysts. One of these methods is the so called “Bönnemann method” which is based on the formation of organometallic colloids. More details about this method are reported elsewhere [62,63,64]. Using this method, PtRu catalysts with well-defined, alloyed particles and a

very narrow particle size distribution (<3 nm) can be prepared. Although highly dispersed catalysts can be obtained using colloidal methods, the colloidal method is complex and several chemicals are required. Additionally, the removal of the stabilizer after the reduction step is a crucial step which affects the electrochemical performance of the catalyst. In contrast, searching for an alternative route for preparing metal colloids without using stabilizing agents would be preferred. In that regard, colloidal nanoparticles are prepared using ethylene glycol as solvent, protecting and reducing agent at the same time. The glycol colloidal process is very attractive for large-scale synthesis of metal nanoparticle catalysts.

Using ethylene glycol as reducing agent for catalyst preparation is called "polyol method". The polyol method is widely used for the preparation of metal colloid catalysts by using the temperature-dependent reducing ability of a liquid polyol or diol such as ethylene glycol. Generally, ethylene glycol (EG) is used as both solvent to dissolve the metal precursors and reducing agent. The process involves the reduction of metal salts (the precursors) by the polyol at an elevated temperature, typically the boiling point of the solvent [57,59]. Recently, microwave heating is used to replace the conventional heating. Using microwave heating, Pt based supported catalysts are prepared in a few minutes providing a fast method for the preparation of highly dispersed catalysts with narrow particle size distribution [59,65-67].

1.5.3 Electrocatalyst systems (PtM)

In this part, electrocatalyst systems with emphasis on PtRu and PtNi systems will be discussed. It is well known that the catalytic activity of Pt catalysts towards methanol oxidation can be enhanced by addition of a second metal such as Ru, Mo, Sn Co, and Ni. The role of the second metal in enhancement of the catalytic activity and CO tolerance can be discussed by the most familiar two mechanisms, namely, the bifunctional mechanism and the electronic effect (ligand effect). According to the bifunctional mechanism, the second metal supplies the oxygen species which is formed at lower potential than on Pt through water dissociation and provides these oxygen species into adjacent Pt sites where the adsorbed poisoning intermediates can be oxidized [25,27,68,69].

In the electronic effect, it is assumed that the second metal modifies the electronic properties of the Pt surface and hence the adsorption of poisoning species on the Pt surface or even the dissociative adsorption of methanol itself can be changed. For a better understanding of the electronic effect, we consider the behavior of CO adsorption on the Pt surface. In this case the adsorption of CO on the Pt surface takes place by an electron donation/back donation mechanism stabilizing the adsorption of CO onto the Pt surface. The electron donation involves the electron transfer from the CO to the empty d band in Pt where the back donation involves the electron transfer

from a metal d orbital to the unoccupied $2\pi^*$ anti-bonding orbital of the CO molecule [27, 70-74].

In the PtM catalysts, the second metal modifies the electronic state of Pt by shifting the Fermi energy level with respect to the energy of CO molecular orbital resulting in the loss of bonding between the Pt surface and CO. A schematic diagram describing the two mechanisms is shown in Figure 1.14. It is also possible that the two mechanisms occur in the same catalyst system.

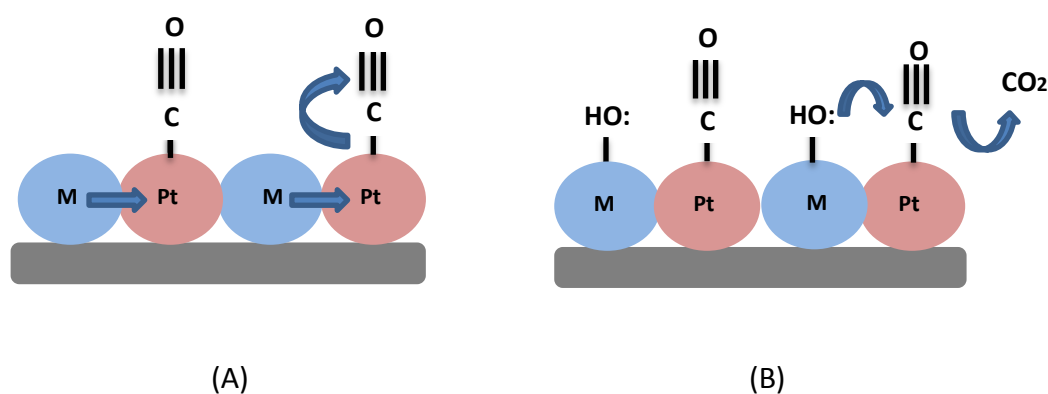


Figure 1.14: Schematic model for electronic mechanism (A) and bifunctional mechanism (B) in the PtM catalyst system.

One of the promising metals as a promoter for CO poisoning is Ru. Several studies have been established on the activity of the PtRu system for MOR [19,27]. The catalytic activity of PtRu depends on several factors such as the atomic ratio of Pt to Ru, Ru phases and the particle size. It has been reported that for supported PtRu catalysts, the Ru content in the range of 40–60 % gives the highest catalytic activity for MOR [75]. It should be noted that the surface metal composition in the PtRu catalyst may differ completely from the bulk composition. As electrocatalysis is a surface reaction, the catalytic activity depends effectively on the surface composition. It has been reported in several studies [24,76-78] that the highest activity for the PtRu system toward MOR is obtained with 20 % Ru on the surface. This ratio is based on the number of sites available for the adsorption of methanol and its intermediates which was detected by IR reflectance spectroscopy [24]. The number of active sites required for the adsorption of methanol and its intermediates is related to the surface composition of PtRu catalysts as the adsorption of methanol and the expected intermediates require four Pt surface sites; three for methanol adsorption and one for water adsorption with one Ru surface site for water activation and formation of OH_{ads} . Therefore the optimum surface atomic composition for the PtRu catalysts is Pt:Ru (4:1) [24,77,78]. Other adsorption species or multi-site adsorption should be taken into the account which could increase the number of the required Pt surface sites to 5 or 7 surface

atoms giving the surface composition of Ru to vary from 12.5 to 20 % [23]. Another study reported that the methanol adsorption process requires only three Pt surface sites where one Ru surface site is required for OH adsorption and therefore the optimum surface composition for PtRu in this case is Pt:Ru (3:1) [79].

The last point to comment on for the PtRu system is the Ru phase in this system. In the bifunctional mechanism, the Pt sites should be close enough to Ru sites to enhance the CO oxidation and hence the alloying of PtRu is not important. However, the alloy formation is necessary for the electronic effect between Pt and Ru which is important to reduce the bonding strength between Pt and CO molecules. It has been reported by Papageorgopoulos et al. [80] that the oxidation of CO on a PtRu surface requires the adsorbed CO to diffuse from Pt to Ru sites that ought to be close enough together but not necessarily in an alloyed state.

Several studies reported on the activity of the PtRu containing oxide phases, in particular the hydrous phase (RuO_xH_y or $\text{RuO}_2 \cdot (\text{H}_2\text{O})_x$) where these oxides are considered as good promoters for methanol oxidation and provide electronic and protonic conductivity [81,82]. The stability of these species is an important factor as they showed lower stability and their activity deteriorated by potential cycling in a potential range similar to the DMFC operation range [83]. However, other studies concluded that the presence of Ru oxides species has an inhibiting effect on the catalytic activity of PtRu catalysts for MOR by blocking the active metal alloy sites whereas PtRu alloys show the higher activity as anode catalyst in DMFCs [27].

The instability of catalysts containing Ru oxides could be attributed to Ru dissolution in acidic environment at higher potential. In contrast, the PtRu alloy structure is reported to be the most suitable and preferred catalyst for methanol oxidation in DMFCs due to their stability resulting from the alloy formation preventing the Ru dissolution under the operational conditions in DMFCs [84].

Another system of PtM catalysts for MOR is the PtNi system which is considered as a promising system for MOR. From a commercial point of view, the PtNi system is cheaper than PtRu due to Ni is a non-noble transition metal and much cheaper than Ru. PtNi catalysts showed higher catalytic activity towards methanol oxidation than Pt catalysts but lower than PtRu [27] whereas in another study PtNi catalysts showed higher catalytic activity than PtRu [85]. It is also reported that a low amount of Ni can reduce methanol adsorption by a dilution effect whereas higher amounts of Ni or its oxides enhance the methanol oxidation by an electronic effect. Recently PtNi catalysts supported on different carbon supports receive considerable attention as an alternative anode catalyst for MOR replacing the PtRu catalysts [27].

1.5.4 Electrocatalyst characterization methods

Electrocatalysts for methanol oxidation at the anode in DMFCs are required to have well-controlled nanostructure, dispersion and specific surface composition. The electrocatalytic activity of anode catalysts depends generally on several factors such as particle size, particle size distribution, morphology of the catalyst, catalyst surface composition, oxidation state of the second metal and microstructure of the electrocatalysts [86-91]. Characterization techniques are required to provide information about the nanoscale properties of the catalysts aiming to correlate these properties with their catalytic activity. In that regard, parameters such as particle size, alloying extent and variation in surface composition have an important effect on catalytic activity as both the composition and the actual atom distribution on the atomic scale will determine the obtained catalytic activity. Hence, surface structure, atomic distribution and composition are dominant nanostructure properties that require both control and careful characterization [99,100].

Regarding the electrocatalyst research, characterization methods play an important role to select and evaluate the proper catalysts for a specific application. The results of characterization ought to provide an overview based on which the researchers can decide on the applicability of the catalytic materials.

Several characterization techniques are used in electrocatalyst research for DMFCs. These techniques can be divided into two main groups: the first is the structural techniques including microscopic and spectroscopic techniques which can provide details concerning the structural aspects of the electrocatalysts such as particle size, morphology, size distribution, alloying degree, surface composition and surface atomic distribution. The second group of electrocatalyst characterization techniques is the electrochemical techniques such as cyclic voltammetry, CO-stripping technique and current potential techniques which can provide details about the active surface area, the catalytic activity of the catalysts towards methanol oxidation and finally electrochemical performance of the electrocatalysts in DMFCs.

In this section the two groups of characterization techniques of the electrocatalysts for DMFCs with special emphasis on anode catalysts will be presented. The basics of the characterization techniques and interpretation of the obtained results will be given.

1.5.4.1 Structural characterization methods

X-ray diffraction (XRD)

XRD is a very simple and fast technique used for studying Pt and PtM catalysts. This technique provides information about the structural phase, grain size, crystallinity and unit cell dimensions. The average grain size (in some references called average particle size) of the catalyst is calculated from the broadening of the diffraction peak using Scherrer's equation (Equation 1.26).

$$d = \frac{0.9 \lambda_{k\alpha 1}}{B_{2\theta} \times \cos \theta_B} \quad (1.26)$$

where d is the average grain diameter, 0.9 is a shape factor, $\lambda_{k\alpha 1}$ is the wavelength of X-ray radiation, θ_B is the angle of the diffraction peak, and $B_{2\theta}$ is the full width at half maximum (FWHM) in radians. Normally, the determination of the average grain diameter from the (220) peak broadening is used particularly for carbon supported PtM catalysts to avoid interference with the reflection signals associated with the carbon support.

Based on XRD measurements and according to the developed relationship by Antolini and co-workers, the alloying degree can be obtained from the detection of the change in the lattice upon alloying with the second metal. For example the atomic fraction of Ru alloyed in PtRu can be determined by the following equation (1.27).

$$a_{fcc} = a_0 - kX_{Ru} \quad (1.27)$$

Where a is the lattice constant for PtRu obtained from XRD analysis, a_0 is the lattice constant of pure Pt/C with a value of 0.39155 nm, k is a constant and equal to 0.124 and related to the unsupported alloy and X_{Ru} is the Ru atomic fraction [91].

Transmission electron microscopy (TEM)

TEM is a very important microscopic tool used for morphological characterization of nanoscaled catalysts. In this case, the catalyst particles are dispersed onto an electron-transparent substrate such as a thin copper-coated grid and subjected for investigation. TEM analysis gives information about the size, size distribution and the dispersion of the nanoparticle catalysts on the supporting materials. In some microscope set-ups, TEM is combined with other spectroscopic analysis such as energy-dispersive X-ray analysis (EDAX) and low-energy ion scattering (LEIS) to obtain more information about the real surface structure and surface metal composition and distribution of the bimetallic system.

X-ray photoelectron spectroscopy (XPS)

XPS is an important technique in electrocatalyst characterization. It is a surface technique based on the photoelectric effect. The technique measures core-level binding energies (BEs) of ejected photoelectrons from atoms at or near the surface of the catalyst sample upon X-ray absorption. Both valence and core electrons can be ejected by X-ray radiation.

XPS can provide information related to the identification of the elements and compounds present at or near the surface based on the relative binding energies (BE) and the peak area. Furthermore, estimation of their relative concentration is possible. The chemical composition of the catalyst can be determined using the peak area corresponding for each constituent. Additionally, the oxidation state of the chemical constituents can be determined where the binding energy depends on the oxidation state.

X-ray absorption spectroscopy (XAS)

X-ray absorption spectroscopy (XAS) refers to the details of how X-ray radiation is absorbed by an atom at energies near and above the core-level binding energies of that atom. XAS is a structural technique that is used to study the structural properties of bimetallic electrocatalyst. XAS spectra can be divided into two regions, the near edge structure (XANES) region (0–50 eV above the absorption edge) and extended X-ray absorption fine structure (EXAFS) region (>50 eV above the absorption edge).

XANES spectra can provide information about the oxidation state, d-electron density and the electronic environment of the absorbing atom, whereas EXAFS can provide information about the environment of a particular atom. In particular for bimetallic systems, analyzing the EXAFS spectrum of each metal gives valuable structural and chemical information about the nanostructure (e.g., interatomic distance, coordination number and oxidation state of chemical species) [89-91].

In bimetallic catalyst systems XAS can provide information about distribution of atoms and their alloying extent. By collecting the XAS data at the absorption edges corresponding to each element in the bimetallic nanoparticles under investigation, the alloying extent and atomic distribution of bimetallic nanoparticles can be determined [93]. In general, for a bimetallic particle containing **A** and **B** atoms, there are different types of structures, depending on the distribution and the alloying of **A** and **B** atoms in the clusters. If **A** and **B** are mixed statistically, in accordance with the overall concentration, a random alloy structure is obtained, where the total coordination number of **A** and **B** around **A**, that is, $\sum CN_{A-i} = CN_{A-A} + CN_{A-B}$, is almost equal to the total coordination number of **A** and **B** around **B**, $\sum CN_{B-i} = CN_{B-B} + CN_{B-A}$ and the extent of alloying of **A** atoms (J_A) is equal to the extent of alloying of **B** atoms (J_B).

Chapter 1: Introduction and Basic Concepts

In contrast, if **A** and **B** atoms are mixed nonstatistically then segregation of atoms of different elements results in a core-shell type structure where the coordination number of one type is larger than that of the other [90,91].

The quantitative extent of alloying or atomic distribution in bimetallic nanoparticles can be evaluated by deriving the EXAFS structural parameters. The needed parameters to derive the extent of alloying are the pairing factors for each atoms **A** and **B** and represented as $P_{A \text{ observed}}$, $P_{B \text{ observed}}$, $P_{A \text{ random}}$, and $P_{B \text{ random}}$. The pairing factor is a measure of the probability of atoms **A** to bind to other atoms of **B**.

The pairing factor $P_{A \text{ observed}}$ can be defined as the ratio of the coordination number of the scattering atoms **B** around absorbing **A** atoms (CN_{A-B}) to the total coordination number of the absorbing atoms ($\sum CN_{A-i}$) and is given by equation (1.28)

$$P_{A \text{ observed}} = CN_{A-B} / (CN_{A-A} + CN_{A-B}) \quad (1.28)$$

Similarly, $P_{B \text{ observed}}$ is defined as the ratio of the scattering atoms **A** coordination number around absorbing **B** atoms (CN_{B-A}) to the total coordination number of absorbing atoms ($\sum CN_{B-i}$) and given by equation (1.29)

$$P_{B \text{ observed}} = CN_{B-A} / (CN_{B-B} + CN_{B-A}) \quad (1.29)$$

The parameters, $P_{A \text{ random}}$ and $P_{B \text{ random}}$ are calculated theoretically based on the atomic composition of the bimetallic system under investigation. For example, the bimetallic system **AB** with an atomic composition of 1:1, assuming that $CN_{A-A} = CN_{A-B}$ and $CN_{B-B} = CN_{B-A}$ gives values of $P_{A \text{ random}}$ and $P_{B \text{ random}}$ equal to 0.5. This procedure is extended to other bimetallic systems with different atomic compositions.

Based on the calculated pairing factors, the extent of alloying for each element **A** and **B** in the particle can be determined by the following equations (1.30 and 1.31)

$$J_A = \frac{P_{A \text{ observed}}}{P_{A \text{ random}}} \times 100 \% \quad (1.30)$$

$$J_B = \frac{P_{B \text{ observed}}}{P_{B \text{ random}}} \times 100 \% \quad (1.31)$$

From the alloying extent and the coordination numbers for each element from EXAFS fitting, the structure model for the bimetallic system can be predicted [90,91,93].

1.5.4.2 Electrochemical characterization methods

In this part the electrochemical methods utilized for the characterization of the electrocatalysts, mainly the bimetallic system, and their evaluation for MOR will be shortly presented.

Cyclic voltammetry (CV)

CV is an electrochemical technique used to study the basic characteristics of an electrochemical system including the mechanism of electrode reactions and their kinetic behavior. In CV measurements, a three electrodes electrochemical cell setup is needed, in which three electrodes, namely working electrode (WE), reference electrode (RE) and counter electrode (CE) are used. The WE is the electrode at which the main electrochemical reaction takes place. The WE potential is controlled in reference to the RE and the current produced at the WE flows between the WE and CE which is used as indicator for the current. During CV measurements, the working electrode potential is swept from an initial potential limit to a final potential limit and back to the initial potential while recording the current. The sweeping of the potential is carried out linearly and the sweep rate can be controlled in a wide range. By plotting the measured current against the applied potential, the voltammogram is obtained [94].

In electrocatalyst characterization, CV is used for the determination of the electrochemical surface area (ECSA) from the voltammogram of the catalyst in acid solution where the hydrogen adsorption desorption region is used for this purpose. This method is valid only for Pt catalyst. Other methods for the bimetallic catalyst can be used, such as CO stripping voltammetry which will be discussed below.

Additionally, CV can be used for quantification of the catalytic activity of the catalyst toward MOR. The catalytic activity is expressed in different parameters that can be extracted from the voltammogram. For example, Figure 1.15a shows the characteristic CV of PtRu in 1 M methanol / 0.5 M sulfuric acid solution.

From the figure, parameters such as the current at the peak potential (I_p) can be determined. It is used to calculate the mass specific activity (MSA) where the current is expressed with respect to the metal loading in the electrode or the surface specific activity (SSA) where the current is expressed with respect to the surface area of the catalysts. The current at a specific potential is also used as indicator for the catalytic activity, e.g. ($I_{0.5}$). Another important parameter that can be obtained from CV of methanol oxidation is the ratio between the values of the current peak in the forward scan and the current in the backward scan (I_f/I_b) which is used as an indication for the CO-tolerance of the catalysts under investigation [95-97].

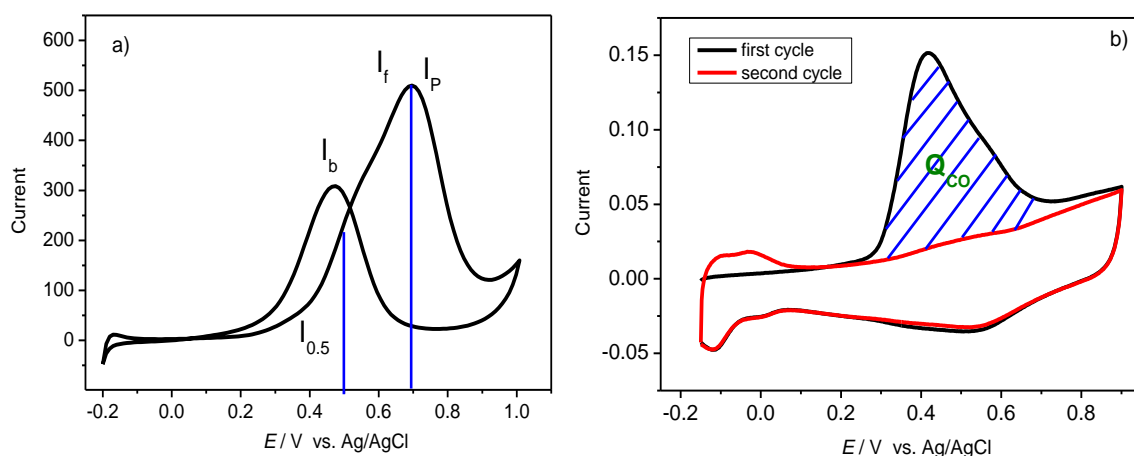


Figure 1.15: a) Characteristic CV of PtRu catalysts in 1 M methanol/0.5 M sulfuric acid, scan rate 50 mVs⁻¹ and b) CO-stripping voltammetry for PtRu in 0.5M sulfuric acid, scan rate 20 mVs⁻¹.

CO-Stripping voltammetry

CO-stripping voltammetry is an ideal technique for the determination of the electrochemical surface area (ECSA) of bimetallic catalyst systems. As mentioned above, determination of ECSA using the hydrogen adsorption/desorption region from the voltammogram of the catalysts in acid solution is not the accurate way to be used for bimetallic catalysts because of the overlapping of the potentials for hydrogen adsorption with the one for oxygen adsorption. Additionally, the hydrogen adsorption on the bimetallic catalyst surface is combined sometimes with hydrogen absorption in particular in the PtRu system where H absorption by Ru is expected. This behavior hinders the determination of the accurate value for ECSA using the charge in the hydrogen adsorption/desorption region. In contrast, the adsorptive CO-stripping voltammetry represents an alternative method for the determination of the ECSA of Pt based bimetallic catalysts.

In this method a monolayer of CO molecules will be adsorbed on the electrocatalyst surface under potential control. Then the adsorbed CO_{ads} is oxidized at higher potential during a potential cycle. As it is shown above (Figure 1.15 b) in the CO-stripping voltammogram of PtRu catalysts in sulfuric acid, during the first cycle the voltammogram shows a strong peak for the oxidation of CO_{ads} where the hydrogen adsorption is suppressed completely at lower potential as a result of the CO blocking of the sites for hydrogen adsorption. In the second cycle, the hydrogen adsorption is developed at lower potential without appearance of any peak for CO oxidation at higher potential owing to the CO free surface indicating the complete oxidation of CO_{ads} in the first cycle. Integration of the charge consumed during CO_{ads} oxidation (the charge under the CO_{ads} oxidation peak (Q_{CO})) is used for the determination of the

electrochemical surface area of the catalyst according to the following equation (1.32) [51,81,98,99]:

$$ECSA(cm^2) = \frac{Q_{CO}(mC)}{Q_0(mC.cm^{-2})} \quad (1.32)$$

Where Q_{CO} is the charge consumed during CO_{ads} oxidation in mC and Q_0 is the standard value of the charge required for oxidation of an adsorbed monolayer of CO_{ads} on Pt surface which is equal to $420 (\mu C.cm^{-2})$.

Dividing the obtained $ECSA$ by the Pt loading in the electrode (M_{Pt}), the specific electrochemical surface area ($SECSA$) ($m^2.g^{-1}$) can be calculated according to the following equation (1.33):

$$SECSA (m^2 g^{-1}) = \frac{ECSA}{M_{Pt}} \quad (1.33)$$

Chronoamperometry

In this technique the working electrode potential is fixed at a specific value at which an electrochemical reaction takes place. In MOR, recording the current response versus time (I-t curve, chronoamperometric curve) at the specific potential, the catalytic activity of the catalysts at this potential can be determined. This technique is used in electrocatalyst research for MOR to check the stability of the catalyst at specific a potential and also to differentiate the catalytic activity of different catalysts under identical conditions [94].

1.6 Electrocatalysts evaluation in direct methanol fuel cells

After the characterization of the catalysts using structural characterization techniques and studying the electrochemical behavior, the next step is the evaluation of the catalysts in a real fuel cell. It is important to mention that not all the electrocatalysts that show high activity in the electrochemical testing can show the same activity in the real fuel cell. So, evaluation of the electrocatalysts in real fuel cells is an important step to confirm their applicability in fuel cells.

The first step for testing the electrocatalysts in direct methanol fuel cells is the preparation the membrane electrode assemblies (MEAs). In this step the electrocatalyst ink is prepared by mixing the catalyst with a solvent (i.e water and isopropanol) and binding material (i.e. Nafion solution). This catalyst ink is applied onto a gas diffusion medium called gas diffusion layer (GDL) which consists of carbon material and a hydrophobic region to form a catalyst layer (CL). Different techniques are used for application of the catalyst ink on the GDL such as hand painting (also called hand brush) or the air brush technique. After the preparation of the catalyst

layers, both electrodes are applied to a polymer electrolyte membrane (PEM) as proton conductor by means of a hot press and the MEA is ready to be evaluated in fuel cells. Alternatively, the catalyst layer is applied directly to the membrane to yield a catalyst coated membrane (CCM). The prepared CCM is sandwiched between two GDLs in a single fuel cell setup as the hot press step is not required. During the CCM preparation, the air brush technique is more practical compared to the hand brush technique [100].

The prepared MEA is mounted into the fuel cell and first activated before recording its I-V curve. Different activation methods have been reported for the MEA. From I-V curves different parameters can be determined such as the open circuit voltage of the cell (OCV) and the value of the current per electrode area ($\text{mA}\cdot\text{cm}^{-2}$) known as the current density or the mass specific current at a specific potential and therefore the performance of the catalysts material can be evaluated. These parameters are also often used to characterize and differentiate different MEAs prepared from different catalysts.

Another important issue concerning the direct methanol fuel cells is the durability. In particular, the problem of Ru dissolution has been reported for the PtRu system in many studies as the Ru dissolves out of the catalyst under fuel cell operation conditions leading to a decline in the cell performance and a decrease in cell life time. To address the durability issue, several protocols such as the discharge at a specific current density or at a specific potential for long time have been suggested to investigate the durability of the DMFCs [101]. Testing the durability behavior of an individual electrode (anode or cathode) can be carried out using potential cycling or fixed potential protocols which are fast and can provide information about the degradation behavior of the electrode under investigation [102,103].

The potential of the anode in DMFCs during the fuel cell operation reaches a value of 0.3-0.5 V but during the operation fuel starvation or short circuits might occur and the anode exhibits a high potential that could reach up to 0.7 V. In that regard, selecting the potential limit for the durability test is important to obtain information about the stability of the electrode catalyst [102,103].

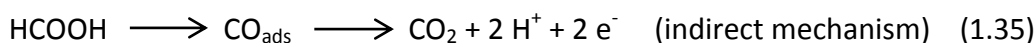
To evaluate the degradation behavior and hence the stability of MEAs, various techniques are used to evaluate the MEA performance before and after the durability test, such as I-V polarization curves, *in-situ* cyclic voltammetry, *in-situ* CO stripping and electrochemical impedance. All of these techniques can assist to get information about degradation behavior of the catalysts after the durability test, their stabilities and the effect of the degradation on the individual electrode and the cell performance [102,103].

1.7 Electrocatalysts for direct formic acid fuel cells

The direct formic acid fuel cell is a promising direct liquid fuel cell working on liquid formic acid as a fuel. Formic acid has several advantages compared to others liquid fuels like methanol and ethanol. It has lower toxicity than methanol and hence it is safer. It can also be produced from environmental waste and biomass.

Theoretically, the electromotive force (*EMF*) of direct formic acid fuel cell is 1.45 V, that is higher compared to DMFC (1.19 V) and H₂-PEMFC (1.23 V) [104], and therefore a better performance of DFAFC is expected. Additionally, the fuel crossover through the polymer membrane is limited in DFAFC as a result of the electrostatic repulsion between HCOO⁻ and the -SO₃ groups in the Nafion membrane that give the possibility for using higher concentrations of the fuel [105,106].

Despite the fast oxidation kinetics of formic acid on Pt anode catalysts, its oxidation is also associated with formation of CO_{ads} as adsorbed intermediates decreasing the efficiency of the catalyst. The mechanism of formic acid oxidation on Pt catalyst proceeds according to the dual path mechanism (direct mechanism and indirect mechanism) which involves two steps; namely, the dehydrogenation step (direct mechanism) and the dehydration step (indirect mechanism) as shown by the following equations (1.34 and 1.35) [15, 107].



In that regard, Pt is not the best catalyst for formic acid oxidation. Pd represents an alternative catalyst for formic acid oxidation (FAO) on which the oxidation proceeds according to the direct mechanism and hence avoiding the poisoning by CO_{ads} intermediate. Several studies have been reported on the electrocatalytic activity of Pd/C catalysts and their application for direct formic acid fuel cells [108-112] where they showed higher cell performance compared to other catalysts such as Pt and PtRu [113]. The deactivation of Pd catalysts has been recently reported after long time operation and therefore developing of high active and stable Pd catalysts is an important topic in electrocatalysis research [114].

Selecting the method of the preparation and choosing the support material could assist for the preparation of catalysts with desired electrocatalytic activity and therefore enhancing the direct formic acid fuel cells performance. In the last chapter of this thesis, a systematic study on the preparation of Pd catalysts supported on multiwalled carbon nanotubes by the polyol method will be presented. It is expected that with manipulation of the preparation conditions and support functionalization, high catalytic activity and stability can be achieved which will be discussed in details in this chapter.

References

- [1] M. Asif, T. Muneer, *Renewable & Sustainable Energy Reviews* 11 (2007) 1388.
- [2] H. Benli, *Renewable Energy* 50 (2013) 33.
- [3] S. Shafiee, E. Topal, *Energy Policy* 37 (2009) 181.
- [4] S.M. Haile, *Acta Materialia* 51 (2003) 5981.
- [5] O. Erdinc, M. Uzunoglu, *Renewable & Sustainable Energy Reviews* 14 (2010) 2874.
- [6] P.G. Grimes, *EEE Trans. Aerosp. Electron. Syst.* 15 (2000) 1.
- [7] J.M. Andújar, F. Segura, *Renewable & Sustainable Energy Reviews* 13 (2009) 2309.
- [8] N.H. Behling, Chapter 3: *History of Alkaline Fuel Cells*, in *Fuel Cells Current Technology Challenges and Future Research Needs*, Elsevier, 2013, pp. 37-51.
- [9] S. Mekhilef, R.S. Safari, *Renewable & Sustainable Energy Reviews* 16 (2012) 981.
- [10] X.-Z. Yuan, H. Li, S. Zhang, J. Martin, H. Wang, *J. Power Sources* 196 (2011) 9107.
- [11] G. Weaver, Chapter 5: *Fuel Cell Technology Review*, *World Fuel cells*, Elsevier, 2002. pp. 81-96.
- [12] X.-Z. Yuan, H. Wang, in: J. Zhang (Ed.), *PEM Fuel Cell Electrocatalysts and Catalyst Layers: Fundamentals and Applications*, Springer, New York, 2008, pp.1-87.
- [13] W. Qian, D.P. Wilkinson, J. Shen, H. Wang, J. Zhang, *J. Power Sources* 154 (2006) 202.
- [14] T.V. Parsons, *J. Electroanal. Chem.* 257 (1988) 9.
- [15] S.L. Blair, W.L. (Simon) Law, in: H. Liu, J. Zhang (Eds.), *Electrocatalysis of Direct Methanol Fuel Cells: From Fundamentals to Applications*, Wiley-VCH, Weinheim 2009, pp. 527-566.
- [16] K. Vogt, D. Vogt, T. Patel, R. Upadhye, D. Edlund, R. Edmonds, J. Gordon, A. Suntana, R. Sigurdardottir, M. Miller, A. Roads, M. Andreu, *Renewable Energy* 34 (2009) 233.
- [17] A.S. Aricò, V. Baglio, V. Antonucci, in: H. Liu, J. Zhang (Eds.), *Electrocatalysis of Direct Methanol Fuel Cells: From Fundamentals to Applications*, Wiley-VCH, Weinheim, 2009, pp. 1-77.
- [18] R. Dillon, S. Srinivasan, A.S. Aricò, V. Antonucci, *J. Power Sources* 127 (2004) 112.
- [19] A. Hamnett, *Catal. Today*, 38 (1997) 445.
- [20] X. Zhao, M. Yin, L. Ma, L. Liang, C. Liu, J. Liao, T. Lu, W. Xing, *Energy Environ. Sci.* 4 (2011) 2736.
- [21] V. Baglio, A. Stassi, A. Di Blasi, C. D'Urso, V. Antonucci, A.S. Aricò, *Electrochim. Acta* 53 (2007) 1360.
- [22] V.E. Guterman, A.Y. Pakharev, N.Y. Tabachkova, *Applied Catalysis A*: 453 (2013) 113.

Chapter 1: Introduction and Basic Concepts

- [23] C. Lamy, C. Coutanceau, in: Z.-X. Liang, T.S. Zhao (Eds), *Catalysts for Alcohol-Fuelled Direct Oxidation Fuel Cells*, RSC, UK, **2012**, pp. 1-70.
- [24] A. Kabbabi, R. Faure, R. Durand, B. Beden, F. Hahn, J.-M. Léger, C. Lamy, *J. Electroanal. Chem.* 444 (**1992**) 41.
- [25] T. Iwasita in: W. Vielstich, H. A. Gasteiger, A. Lamm (Eds), *Handbook of Fuel Cells – Fundamentals, Technology and Applications*, volume 2, John Wiley & Sons, Ltd **2003**, pp. 1-22.
- [26] N.H. Li, S.G. Sun, S.P. Chen, *J. Electroanal. Chem.* 430 (**1997**) 57.
- [27] E. Antolini, in: H. Liu, J. Zhang, (Eds.), *Electrocatalysis of Direct Methanol Fuel Cells: From Fundamentals to Applications*, Wiley-VCH, Weinheim, **2009**, pp. 227-255.
- [28] D.M. Gattia, M.V. Antisari, L. Giorgi, R. Marazzi, E. Piscopiello, A. Montone, S. Bellitto, S. Licocchia, E. Traversa *J. Power Sources* 194 (**2009**) 243.
- [29] A.L. Dicks, *J. Power Sources* 156 (**2006**) 128.
- [30] J. Liang, S.Z. Qiao, G.Q. (Max) Lu, D. Hulicova-Jurcakova, in: J.M.D. Tascón (Ed.) *Novel Carbon Adsorbents*, Elsevier **2012**, pp.549-581
- [31] L.M. Roen, C.H. Paik, T.D. Jarvi, *Electrochem. Solid State Lett.* 7 (**2004**) A19.
- [32] W. Zhang, P. Sherrell, A.I. Minett, J.M. Razal, J. Chen, *Energy Environ. Sci.* 3 (**2010**) 1286.
- [33] M. Scarselli, P. Castrucci, M. De. Crescenzi, *J. Phys.: Condens. Matter* 24 (**2012**) 313202
- [34] S. Iijima, *Nature* 354 (**1991**) 56.
- [35] S. Iijima, *Physica B*: 323 (**2002**) 1
- [36] J-C. Charlier, X. Blase, S. Roche, *Rev. Mod. Phys.* 79 (**2007**) 677.
- [37] W. Li, C. Liang, W. Zhou, J. Qiu, Z. Zhou, G. Sun, Q. Xin, *J. Phys. Chem. B* 107 (**2003**) 6292.
- [38] J. Lee, J. Kim, T. Hyeon, *Adv. Mater.* 18 (**2006**) 2073.
- [39] G.G. Wildgoose, C.E. Banks, R.G. Compton, *Small* 2 (**2006**) 182.
- [40] C.E. Banks, T.J. Davies, G.G. Wildgoose, R.G. Compton, *Chem. Commun.* 7 (**2005**) 829.
- [41] E. Antolini, *Appl. Catal. B*: 88 (**2009**) 1.
- [42] X.H. Peng, J.Y. Chen, J.A. Misewich, S.S. Wong, *Chem. Soc. Rev.* 38 (**2009**) 1076.
- [43] J. Prabhuram, T.S. Zhao, Z.K. Tang, R. Chen, Z.X. Liang, *J. Phys. Chem. B* 110 (**2006**) 5245.
- [44] D.-J. Guo, H.-L. Li, *J. Power Sources* 160 (**2006**) 44.
- [45] S.P. Somani, P.R. Somani, A. Sato, M. Umeno, *Diamond Relat. Mater.* 18 (**2009**) 497.
- [46] Y.Y. Ou, M.H. Huang, *J. Phys. Chem. B*: 110 (**2006**) 2031.
- [47] S.Y. Wang, X. Wang, S.P. Jiang, *Langmuir* 24 (**2008**) 10505.

Chapter 1: Introduction and Basic Concepts

- [48] D.-Q. Yang, B. Hennequin, E. Sacher, *Chem. Mater.* 18 (2006) 5033.
- [49] S. Kundu, Y. Wang, W. Xia, Martin Muhler, *J. Phys. Chem. C* 112 (2008) 16869.
- [50] H. Xu, L.P. Zeng, S.J. Xing, G.Y. Shi, Y.Z. Xian, L.T. Jin, *Electrochem. Commun.* 10 (2008) 1839.
- [51] AB.A.A. Nassr, I. Sinev, W. Grünert, M. Bron, *Applied Catalysis B*: 142 (2013) 849.
- [52] S. Wang, S.P. Jiang, X. Wang, *Nanotechnology* 19 (2008) 265601.
- [53] B.H. Wu, D. Hu, Y.J. Kuang, B. Liu, X.H. Zhang, J.H. Chen, *Angew. Chem. Int. Ed.* 48 (2009) 4751.
- [54] B. Luo, S. Xu, X. Yan, Q. Xue, *J. Electrochem. Soc.* 160 (2013) F262.
- [55] S. Zhang, Y.Y. Shao, G.P. Yin, Y.H. Lin, *J. Mater. Chem.* 20 (2010) 2826.
- [56] H.-Y. Lee, W. Vogel, P.P.-J. Chu, *Langmuir* 27 (2011) 14654.
- [57] H. Liu, C. Song, L. Zhang, J. Zhang, H. Wang, D.P. Wilkinson, *J. Power Sources* 155 (2006) 95.
- [58] O.A. Petrii, *J. Solid State Electrochem.* 12 (2008) 609.
- [59] N.C. Bagkar, H.M. Chen, H. Parab, R.-S. Liu in: H. Liu, J. Zhang (Eds.), *Electrocatalysis of Direct Methanol Fuel Cells: From Fundamentals to Applications*, Wiley-VCH, Weinheim, 2009, pp. 79-114.
- [60] A.J. Dickinson, L.P.L. Carrette, J.A. Collins, K.A. Friedrich, U. Stimming, *Electrochim. Acta* 47 (2002) 3733.
- [61] H. Yang, W. Vogel, C. Lamy, N. Alonso-Vante, *J. Phys. Chem. B*: 108 (2004) 11024.
- [62] H. Bönemann, R. Brinkmann, W. Brijoux, E. Dinjus, T. Jousen, B. Korall, *Angew. Chem.* 103 (1991) 1344.
- [63] T.J. Schmidt, M. Noeske, H.A. Gasteiger, R.J. Behm, P. Britz, W. Brijoux, H. Bönemann, *Langmuir* 14 (1997) 2591.
- [64] H. Bönemann, W. Brijoux, R. Brinkmann, R. Fretzen, T. Jousen, R. Köppler, B. Korall, P. Neiteler, J. Richter, *J. Mol. Catal.* 86 (1994) 129.
- [65] M. Tsuji, M. Kubokawa, R. Yano, N. Miyamae, T. Tsuji, M.-S. Jun, S. Hong, S. Lim, S.-H. Yoon, I. Mochida, *Langmuir* 23 (2007) 387.
- [66] D.-M. Gu, Y.-Y. Chu, Z.-B. Wang, Z.-Z. Jiang, G.-P. Yin, Y. Liu, *Appl. Catal. B*: 102 (2011) 9.
- [67] P.C. Sherrell, J. Chen, J.M. Razal, I.P. Nevirkovets, C. Crean, G.G. Wallace, A.I. Minett, *Energy Environ. Sci.* 3 (2010) 1979.
- [68] N.M. Markovic, H.A. Gasteiger, P.N. Ross, X. Jiang, I. Villegas, M.J. Weaver, *Electrochim. Acta* 40 (1995) 91.
- [69] S.L. Goikovic, T.R. Vidakovic, D.R. Durovic, *Electrochim. Acta* 48 (2003) 3607.
- [70] M. Watanabe, H. Igarashi, T. Fujino, *Electrochem. Commu.* 67 (1999) 1194.
- [71] T. Tada, H. Igarashi, H. Uchida, M. Watanabe, *J. Electrochem. Soc.* 146 (1999) 3750.

Chapter 1: Introduction and Basic Concepts

- [72] N.M. Markovic, H.A. Gasteiger, P.N. Ross, X. Jiang, I. Villegas, M.J. Weaver, *Electrochim. Acta* **40** (1995) 91.
- [73] T. Iwasita, *Electrochim. Acta* **47** (2002) 3663.
- [74] P.A. Christensen, A. Hamnett, G.L. Troughton, *J. Electroanal. Chem.* **362** (1993) 207.
- [75] D. Chu, S. Gilman, *J. Electrochem. Soc.* **143** (1996) 1685.
- [76] K.-W. Park, J.-H. Choi, K.-S. Ahn, Y.-E. Sung, *J. Phys. Chem. B* **108** (2004) 5989.
- [77] H.A. Gasteiger, N. Markovic, P.N. Ross, E.J. Cairns, *J. Electrochem. Soc.* **141** (1994) 1795.
- [78] W. Chrzanowski, A. Wieckowski, *Langmuir* **14** (1998) 1967.
- [79] H.A. Gasteiger, N. Marković, P.N. Ross Jr, E.J. Cairns, *Electrochimica Acta* **39** (1994) 1825.
- [80] D.C. Papageorgopoulos, M.P. de Heer, M.Keijzer, J.A.Z. Pieterse, F.A. de Bruijn, *J. Electrochem. Soc.* **151** (2004) A763.
- [81] R. Chetty, W. Xia, S. Kundu, M. Bron, T. Reinecke, W. Schuhmann, M. Muhler, *Langmuir* **25** (2009) 3853.
- [82] D.R. Rolison, P.L. Hagans, K.E. Swider, J.W. Long, *Langmuir* **15** (1999) 774.
- [83] J.-H. Ma, Y.-Y. Feng, J. Yu, D. Zhao, B.-Q. Xu, *J. Catal.* **275** (2010) 34.
- [84] E. Antolini, *J. Solid State Electrochem.* **15** (2011) 455.
- [85] K. Park, J. Choi, B. Kwon, S. Lee, Y. Sung, H. Ha, S. Hong, H. Kim, A. Wieckowski, *J. Phys. Chem. B* **106** (2002) 1869.
- [86] S. Mukerjee, J. McBreen, *J. Electroanal. Chem.* **448** (1998) 163.
- [87] Y. Takasu, T. Iwazaku, W. Sugimoto, Y. Murakami, *Electrochem. Commun.* **2** (2000) 671.
- [88] O.V. Cherstiouk, P.A. Simonov, E.R. Savinova, *Electrochim. Acta* **48** (2003) 3851.
- [89] B.-J. Hwang, L.S. Sarma, C.-H. Chen, C. Bock, F.-J. Lai, S.-H. Chang, S.-C. Yen, D.-G. Liu, H.-S. Sheu, J.-F. Lee, *J. Phys. Chem. C* **112** (2008) 19922.
- [90] C.-H. Chen, L.S. Sarma, D.-Y. Wang, F.-J. Lai, C.-C. Al Andra, S.-H. Chang, D.-G. Liu, C.-C. Chen, J.-F. Lee, B.-J. Hwang, *ChemCatChem* **2** (2010) 159.
- [91] F. Taufany, C.-J. Pan, F.-J. Lai, H.-L. Chou, L.S. Sarma, J. Rick, J.-M. Lin, J.-F. Lee, M.-T. Tang, B.-J. Hwang, *Chem. Eur. J.* **19** (2013) 905.
- [92] E. Antolini, F. Cardellini, *J. Alloys Compd.* **315** (2001) 118.
- [93] B.-J. Hwang, L.S. Sarma, J.M. Chen, C.H.Chen, S.C. Shih, *J. Am. Chem. Soc.* **127** (2005) 11140.
- [94] A.J. Bard, L.R. Faulkner, *Electrochemical Methods: Fundamentals and Applications*, 2nd edn, John Wiley & Sons, Inc., New York (2000).
- [95] H.-Y. Lee, W. Vogel, P.P.-J. Chu, *Langmuir* **27** (2011) 14654.
- [96] Z. Liu, F. Su, X. Zhang, S.W. Tay, *ACS Appl. Materials & Interfaces* **3** (2011) 3824.

- [97] L. Ma, X. Zhao, F. Si, C. Liua, J. Liaoa, L. Lianga, W. Xing, *Electrochim. Acta* 55 (2010) 9105.
- [98] A. Pozio, M. De Francesco, A. Cemmi, F. Cardellini, L. Giorgi, *J. Power Sources* 105 (2002) 13.
- [99] T. Vidakovic, M. Christov, K. Sundmacher, *Electrochim. Acta* 52 (2007) 5606.
- [100] L. Ma, Y. Huang, L. Feng, W. Xing, J. Zhang, in: H. Liu, J. Zhang (Eds.), *Electrocatalysis of Direct Methanol Fuel Cells: From Fundamentals to Applications*, Wiley-VCH, Weinheim, 2009, pp. 417-447.
- [101] M.K. Jeon, J.Y. Won, K.S. Oh, K.R. Lee, S.I. Woo, *Electrochim. Acta* 53 (2007) 447.
- [102] W. Chen, G. Sun, Z. Liang, Q. Mao, H. Li, G. Wang, Q. Xin, H. Chang, C. Pak, D. Seung, *J. Power Sources* 160 (2006) 933.
- [103] P. Joghee, S. Pylypenko, T. Olson, A. Dameron, A. Corpuz, H.N. Dinh, K. Wood, K. O'Neill, K. Hurst, G. Bender, T. Gennett, B. Pivovar, R. O'Hayre, *J. Electrochem. Soc.* 159 (2012) F768.
- [104] T.T. Cheng, E.L. Gyenge, *J. Appl. Electrochem.* 39 (2009) 1925.
- [105] X. Li, I.M. Hsing, *Electrochim. Acta* 51 (2006) 3477.
- [106] J.-H. Choi, K.-J. Jeong, Y. Dong, T.H.J. Han, T.-H. Lim, J.-S. Lee, Y.-E. Sung, *J. Power Sources* 163 (2006) 71.
- [107] J.L. Haan, R.I. Masel, *Electrochim. Acta* 54 (2009) 4073.
- [108] L. Lu, H. Li, Y. Hong, Y. Luo, Y. Tang, T. Lu, *J. Power Sources* 210 (2012) 154.
- [109] X. Yu, P.G. Pickup, *J. Power Sources* 182 (2008) 124.
- [110] S. Ha, R. Larsen, R.I. Masel, *J. Power Sources* 144 (2005) 28.
- [111] S. Uhm, H. J. Lee, J. Lee, *Phys. Chem. Chem. Phys.* 11 (2009) 9326.
- [112] H. Meng, F. Xie, J. Chen, P. K. Shen, *J. Mater. Chem.* 21 (2011) 11352.
- [113] C. Rice, S. Ha, R.I. Masel, A. Wieckowski, *J. Power Sources* 115 (2003) 229.
- [114] W. Yu, P.G. Pickup, *Electrochem Comm.* 11 (2009) 2012.

The content of this chapter has been published as
**Microwave-Assisted Ethanol Reduction as a New Method for the Preparation of
Highly Active and Stable CNT-Supported PtRu Electrocatalysts for Methanol
Oxidation**

Abu Bakr Ahmed Amine Nassr, Michael Bron, ChemCatChem 5 (2013) 1472 - 1480.

<http://onlinelibrary.wiley.com/doi/10.1002/cctc.201200742/abstract>

Reproduced with permission of WILEY-VCH Verlag GmbH & Co. KGaA, Weinheim Copyright
© 2013

2.1 Introduction

The electrooxidation of methanol is the anodic reaction in direct methanol fuel cells (DMFCs) that are considered as clean energy converters with low emission and high power density. Methanol is a promising fuel for fuel cells working with liquid energy carriers because of its ease of handling and storage. It is cheap and can be produced from fossil sources, such as natural gas or coal, as well as from sustainable sources through fermentation of agricultural products and from biomass [1,2].

The efficiency of the electrooxidation process depends mainly on the catalytic properties of the catalyst materials used [1,3,4]. Highly dispersed Pt catalysts supported on carbon demonstrate good catalytic activity for the methanol oxidation reaction (MOR) in which carbon provides the conductivity path and adsorption and desorption of the reactants and products play an important role [3,5]. The activity of the Pt catalysts is limited by CO poisoning, which formed as intermediate during the methanol oxidation. CO strongly adsorbs on Pt and hence blocks the catalysts surface, which prevents further methanol oxidation. The oxidation of CO on Pt proceeds only at higher potentials, at which oxygenated species form by the dissociation of water, causing a significant overpotential. To overcome this problem and to enhance methanol oxidation activity and CO tolerance, a second component that can form oxygenated species at lower potential other than Pt should be combined with Pt catalysts [6,7].

In this regard, new catalyst systems combining Pt with metal oxides, such as CeO₂, WO₃, TiO₂, NiO_x, and MoO_x [8-16] or with second a metal such as Ni, Co, Mo, Sn and Ru have been developed [17-21]. Up to now, PtRu bimetallic catalysts have been considered as one of the most active catalyst systems for MOR. PtRu electrocatalysts show higher CO tolerance and higher methanol activity compare to Pt catalysts [20]. The enhanced CO tolerance is probably due to the ability of Ru to dissociate water at lower potentials and thus form oxygenated species which can act as an oxidant of CO

species strongly adsorbed on the Pt surface [7,22,23]. This mechanism is called the bifunctional mechanism and was suggested by Wantabe and Motoo [23]. Another mechanism is the so-called ligand effect or electronic effect, according to which the second metal modifies the electronic properties of the Pt surface by electron donation into the d-band of Pt and thus weakens the CO bonding to Pt [24].

The electrocatalytic activity of supported PtRu electrocatalysts depends mainly on their preparation methods, compositions, surface properties and degree of alloying [7]. The active phase in PtRu bimetallic systems is still an issue of debate, in which some studies stress that it is the PtRu alloy [25-29]. Other studies postulate that Ru oxides, mainly the hydrous form, are responsible for high activity [30-34]. These chemical and surface properties can be controlled during the preparation or post treatment step to achieve a catalyst with desirable properties and high electrocatalytic activity.

Various techniques have been developed to prepare PtRu nanoparticle catalysts on carbon support, such as impregnation, colloidal syntheses and thermal decomposition methods [35]. The radiation-induced preparation of nanoparticles has been reported to be a simple and fast method for the preparation of supported catalysts for different applications. In radiation induced preparation methods, electromagnetic radiation is used to reduce metal ions to their metallic state through the generation of reduced species in the solution or through the action of the radiation on the reducing agent, which decomposes under the radiation effect to trigger the reduction process. Many sources of radiation have been used for this purpose, such as gamma rays, electron beam, ultrasonic radiation, laser radiation and microwave radiation [21,36-40].

Microwave-assisted syntheses have received significant attention as methods for the preparation of active PtRu catalysts for MOR because the nanoparticles prepared by this method are produced in very narrow particle size distribution and with good dispersion on the support, which yields systems with high electrocatalytic activity [21]. In the microwave-assisted synthesis, polyols such as ethylene glycol, are usually used as reducing agents. Under microwave heating (MW) conditions, polyols reduce the metal ions into their metallic state within a few minutes compared to conventional heating, which needs significantly longer time [21,41]. Because the interaction of microwaves with polyols is related to the dielectric constant and dielectric loss of the material, other alcohols with high dielectric constant and dielectric loss can also be used as reducing agents under microwave irradiation. Ethanol is one of those alcohols because it has a dielectric constant and dielectric loss of 24.3 and 22.8, respectively [42]. It has been used under microwave irradiation for the preparation of silver nanoparticles [43]. Furthermore, ethanol is a mild reducing agent for the preparation of metallic nanoparticles under conventional reflux conditions [49-51]. In the field of

catalysis for fuel cells, ethanol has been used as a reducing agent under conventional heating for the preparation of PtRu/C for methanol oxidation [44,45] and Pt/C [46] and PtAu/C [47] for oxygen reduction in fuel cells. To the best of our knowledge, there is no study on the use of ethanol under microwave irradiation for preparation of PtRu catalysts for MOR. Herein, we report the preparation of PtRu nanoparticles supported on multiwall carbon nanotubes (MWCNTs) with the reducing agent ethanol under microwave irradiation. The presence of water is necessary to achieve microwave-induced reduction. The structural characterization of the resulting materials was performed by using TEM and XRD analyses, whereas evaluation of their electrocatalytic activity for the MOR was done by using electrochemical methods.

2.2 Experimental part

2.2.1 Electrocatalyst preparation

Multiwalled carbon nanotubes (Baytubes C 150 P, Bayer MaterialScience AG, Germany) oxidized previously in nitric acid (5 M) at 100 °C for 6 h to introduce oxygen-containing surface groups were used as supporting material for the electrocatalysts. To oxidized CNTs (100 mg) dispersed in water (20 ml), H₂PtCl₆ ethanolic solution (10 mL; 8.44 mM) and of RuCl₃ ethanolic solution (10 mL; 8.44 mM), yielding a metal loading of 20 % and a Pt/Ru ratio of 1 were added dropwise with stirring. The solution was completed to total volume (100 mL) by maintaining the ratio of ethanol to water to 1:1 (v/v) and kept for 1 h under continuous stirring, followed by ultrasonication for 30 min under N₂ atmosphere. Then, the reaction mixture was transferred to a microwave reactor (START 1500, Microwave Extractor, Milestone Srl) and heated at a power for MW of 300 W for 4 min under reflux conditions and with stirring. The reaction temperature inside the reaction vessel was monitored with a thermocouple, whereas the temperature on the outside wall of the reaction vessel was monitored with an IR heat sensor. The schematic diagram of the microwave reactor and the temperature profile during the MW are shown in Figure 2.1 A and B. After the heating process, the reaction mixture was left to cool down to RT and then kept under stirring overnight to promote the deposition of nanoparticles onto the CNTs surface. Afterwards, the catalyst was separated through centrifugation (Centrifuge 4807, Eppendorf) at 5000 rpm for 15 min and subjected to five washing cycles with deionized water. Finally, the catalyst was dried at 80 °C in an oven overnight, crushed in a mortar into fine powder, and stored in a glass vial until used. This process was repeated several times, and the products were combined to obtain enough material for further experiments (see below).

For comparison, a PtRu/CNT catalyst was prepared by ethanol reduction using oil bath heating at 85 °C under conventional reflux (CR) conditions. This catalyst was labeled

PtRu/CNTs CR, whereas the samples prepared under MW conditions were labeled PtRu/CNTs MW.

Each 50 mg of the catalyst was heated under reductive atmosphere (5 % H₂/Ar, 50 ml min⁻¹); heating ramp rate: 20 °C min⁻¹) up to 200, 400, 600 and 800 °C and maintained there for 2 h. The heat-treated samples were labeled PtRu/CNTs MW X, where X represents the heat treatment temperature.

2.2.2 Electrocatalyst characterization

2.2.2.1 Structural characterization

The metal loading and composition of the catalysts were analyzed by using inductively coupled plasma optical emission spectroscopy (ICP-OES) (ULTIMA 2, HORIBA Jobin Yvon). The sample was subjected to microwave digestion in a mixture of HCl /nitric acid following the method described in Ref. [48]. Then, the metal solution was diluted and the amount of each metal was analyzed.

The crystal structure of the prepared catalysts was examined by using XRD; the data was collected on a D8 advanced X-ray diffractometer, (Bruker AXS GmbH), working with a Cu K α source ($\lambda = 0.15406$ nm) in the 2θ range of 20-90 ° at a scan rate of 2° min⁻¹. For calculating the crystallite size, the samples were scanned with a lower scan rate (0.5° min⁻¹) at the $2\theta = 62-75^\circ$. The data obtained were fitted with a Gaussian function by using Origin8 software to obtain the full width at half maximum (FWHM).

Morphological properties of the catalysts were examined with a LEO 912 transmission electron microscope operating at an acceleration voltage of 120 keV. Several milligrams of the catalyst were dispersed in ethanol under ultrasonication for 10 min, and then drops of the suspension were deposited on a carbon-coated copper grid and left until evaporation of the solvent; this was followed by TEM analysis. The mean particle size was calculated by determining the diameter for more than 100 particles.

2.2.2.2 Electrochemical characterization

The electrocatalytic activity of the catalysts for methanol electrooxidation was tested in a three-compartment electrochemical cell, in which a Pt wire, an Ag/AgCl/saturated KCl electrode, and a catalyst-coated glassy carbon electrode were used as counter electrode, reference electrode, and working electrode; respectively.

The working electrode was prepared by using a thin film coating technique. In detail, 2.5 mg of PtRu/CNTs catalyst were mixed with isopropanol (350 μ L) containing Nafion solution (50 μ L, 5 wt.% ; Aldrich) and sonicated for 1 h in an ultrasonic bath followed by stirring for 2 h to obtain a homogenous dispersion. Then, this dispersion (5 μ L) was coated on a glassy carbon electrode (4 mm in diameter, 0.125 cm²) and left to dry at RT. The glassy carbon electrode was cleaned before coating by polishing using alumina suspension (Leo Corp) of 1 and 0.3 μ m, respectively using a polishing cloth and

then cleaned ultrasonically in ethanol water solution (1:1, v/v) and in water; respectively, each for 10 min.

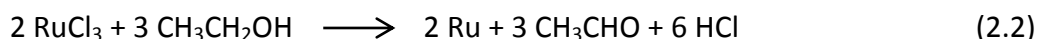
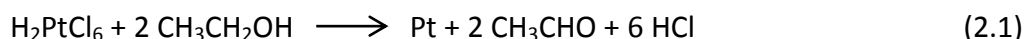
The catalytic activity was determined using cyclic voltammetry. First, the catalyst-coated electrode was cycled 50 times in N₂ purged 0.5 M H₂SO₄ between -0.2 and 1 V at a scan rate of 50 mV s⁻¹; this step was considered as surface cleaning of the working electrode and should be performed before each measurement. Then, the cleaned electrode was transferred to a cell containing N₂-purged solution of 1 M CH₃OH/0.5M H₂SO₄ and 100 cycles were recorded under the same conditions while purging the N₂ into the solution during the measurements. The twentieth cycle was selected to evaluate and compare the catalytic activity of all catalysts for the MOR.

For determination of the electrochemical surface area, CO stripping measurements were performed in 0.5 M H₂SO₄ solution. First, the electrode was cleaned as above, and then CO gas was purged into the solution for approximately 20 min while holding the electrode potential at -0.15 V to form an adsorbed CO layer on the catalyst surface. Next, the solution was purged with N₂ for 20 min to remove dissolved CO, and finally the CO stripping voltammogram was recorded for three consecutive cycles in the potential window -0.15 to 0.9 V at a scan rate of 20 mV s⁻¹.

2.3 Results and discussion

2.3.1 Electrocatalyst preparation

Ethanol was used as a reducing agent for the preparation of CNT-supported PtRu electrocatalysts under microwave irradiation. The reduction of Pt and Ru salts by ethanol can be represented by the Equations (2.1) and (2.2): [44,45]



In preliminary work, pure ethanol was used as a reducing agent for the preparation of PtRu/CNTs under MW conditions. A power of 300 W was applied for different heating times ranging from 1 min to 10 min (Figure 2.1). Each time the solid product was separated and the filtrate was investigated visually and by addition of 0.1 M NaBH₄. The filtrate displayed a yellow color, which, upon addition of 0.1 M NaBH₄ turned black as result of the reduction of Pt and Ru ions; this indicated that the filtrate still contains metal ions, which have not been reduced under MW conditions. Testing the solid product by using electrochemical methods did not show any features typical of the PtRu catalyst system, which confirms that Pt and Ru were not deposited on the CNTs supports. The same behavior was observed when the reduction was performed in ethanol by oil bath heating at 85°C for 2 h. The color of the filtrate before and after

addition of 0.1 M NaBH₄ solution for under different reaction conditions is shown in Figure 2.2.

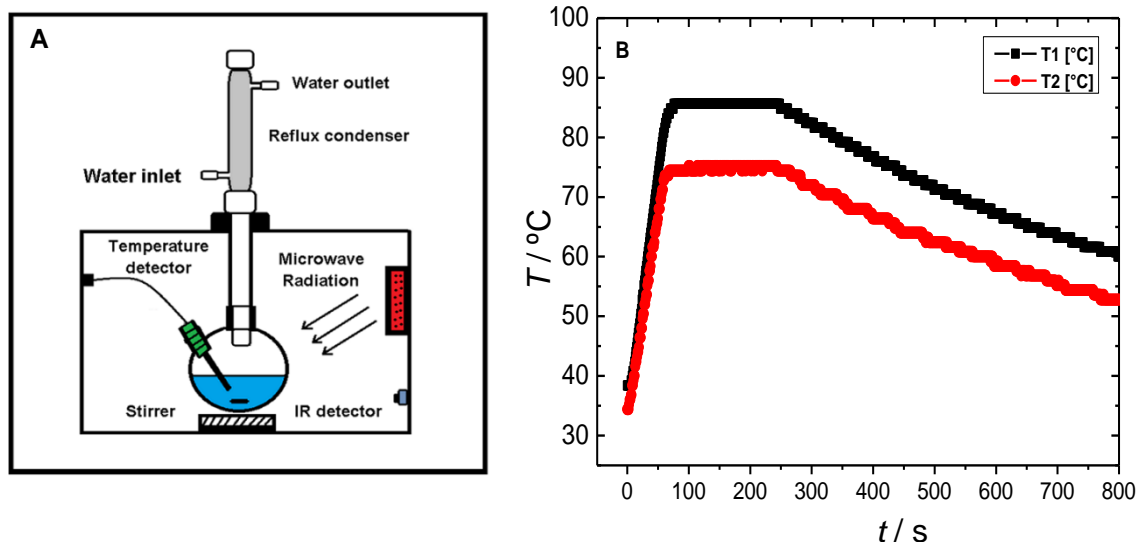


Figure 2.1: (A) Schematic diagram of microwave reactor and (B) temperature profile during the microwave preparation of PtRu/CNTs MW in ethanol water (1:1, v/v), irradiation time 4 min, microwave power 300 W.

However, on using an ethanol/water mixture (1:1, v/v) as solvent/reducing agent under the same MW conditions of for only 4 min (cf. Figure 2.1: the boiling temperature was reached after 1 min and held for 3 min), the filtrate was clear and did not show any changes upon addition of 0.1 M NaBH₄ solution. The same result was obtained when the reaction was performed under reflux at 85 °C for 2 h (Figure 2.2d and e). Obviously, the reduction of Pt and Ru salts to their metallic states can be achieved under these conditions. These results indicate that the ethanol/water mixture is a more powerful reducing agent than pure ethanol (i.e., a more negative redox potential, which means that it is more easily oxidized) [49,52]. It is, however, also possible that the presence of water opens a mechanistic pathway which does not work in pure ethanol.

Given these initial results, the samples prepared in an ethanol/water mixture have been analyzed as described in the experimental section. Inductively coupled plasma analysis indicated a Pt/Ru atomic ratio of 1 for PtRu/CNTs prepared under MW conditions, which corresponds to the nominal atomic ratio, whereas a ratio of 1.8 was found for PtRu/CNTs prepared by conventional heating (CR). Moreover, the metal loading for PtRu/CNTs MW (Pt = 10.37 wt.%, Ru = 5.12 wt.%, total loading 15.49 wt.%) was higher than that for PtRu/CNTs CR (Pt = 9.86 wt.%, Ru = 2.81 wt.%, total 12.67 wt.%). It can be concluded that microwave-assisted reduction, in addition to being very fast, is in our case much more efficient and leads to better results in terms of metal loading and atomic ratio compared to the conventional reduction.

Chapter 2: Microwave-Assisted Synthesis of PtRu/CNTs Electrocatalysts

The overall metal loading is lower than the nominal loading, which indicates that some metal is lost during the preparation. This is attributed to the loss of Pt and Ru species during the washing process because the filtrate of the preparation process seems to be free of metal ions and particles (Figure 2.2). It is not clear to us at the moment why the amount of Ru is significantly lower for the CR-derived catalysts. This is probably related to different reduction potentials of Pt and Ru (Pt^{4+}/Pt , $E^\circ \sim 0.74$ V, Ru^{3+}/Ru , $E^\circ \sim 0.62$ V) [53] which could lead to different deposition behavior during slower conventional reduction compared with faster microwave-assisted reduction.

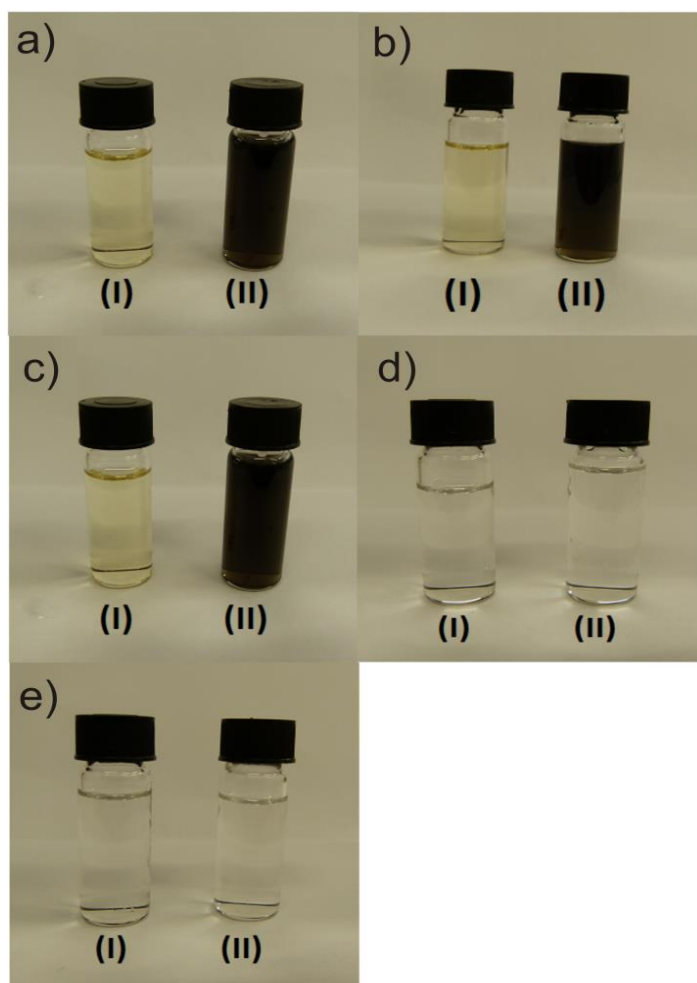


Figure 2.2: Filtrate of PtRu/CNTs prepared by microwave heating for 1 min (a), for 10 min (b), prepared by conventional reflux (c) in ethanol, prepared by microwave heating for 4 min (d) and by conventional reflux (e) in an ethanol/water mixture (1:1) before (I) and after (II) addition of 0.1 M NaBH_4 solution. The power for microwave heating was set to 300 W, and the temperature for conventional heating was set to 85 °C.

In summary, these results indicate that the microwave irradiation heating using ethanol/water mixtures is not only a fast method to prepare PtRu-supported catalysts

with high metal loading, but also facilitates the simultaneous reduction of Pt ions and Ru ions.

2.3.2 XRD and TEM characterization.

The TEM images of the prepared PtRu/CNTs catalysts before and after heat treatment (in hydrogen at different temperatures as indicated) and the corresponding histograms for particle size distribution are shown in Figure 2.3. For the as-prepared samples PtRu/CNTs CR and PtRu/CNTs MW, the nanoparticles are dispersed on the carbon support and the mean particle size is similar (3.1 nm and 3.2 nm; respectively). The sample prepared through microwave assisted reduction demonstrates a more homogenous dispersion than the sample prepared by conventional reduction which shows some agglomeration. This is attributed to the homogenous and fast heating by microwave irradiation. Notably, the catalysts were prepared without any stabilizing agents. On the other hand, for the heat-treated samples (Figure 2.3, c-f), the mean particle size increases with an increase in reduction temperature from 4.9 nm for the sample treated at 200 °C to 7.7 nm with heating at 800 °C. Furthermore, the samples heat treated at temperatures of 200-600 °C are still well dispersed on CNTs, whereas the sample treated at 800 °C shows a higher degree of agglomeration as well as the appearance of a few large particles (≈ 35 nm, not included in the particle size distribution; Figure 2.3).

The diffraction patterns for as-prepared and heat treated PtRu/CNTs catalysts are shown in Figure 2.4. Both as-prepared PtRu/CNTs CR and PtRu/CNTs MW demonstrate diffraction peaks at 2θ values of 39.7° and weak signals at 46.4° , 67.9° , and 81.1° corresponding to the Pt (fcc) structure planes (111), (200) (220) and (311), respectively. The peak at $2\theta = 26$ is assigned to the (002) plane of the graphite structure of the CNT. No indication for alloying or solid solution formation between Pt and Ru can be deduced, and at the same time the patterns do not show any peaks for Ru or its oxide, which reveals that Ru species could be present in an amorphous form [33,54].

With an increase in the heat treatment temperature, the diffraction peaks for Pt (fcc) become sharper and shift to a higher 2θ value, indicating the formation of PtRu solid solution [54,55] (see below). At 800 °C, a new but a very weak signal at $2\theta = 43.3^\circ$ assigned to the Ru (101) plane develops, which indicates the presence of a separated Ru phase [33].

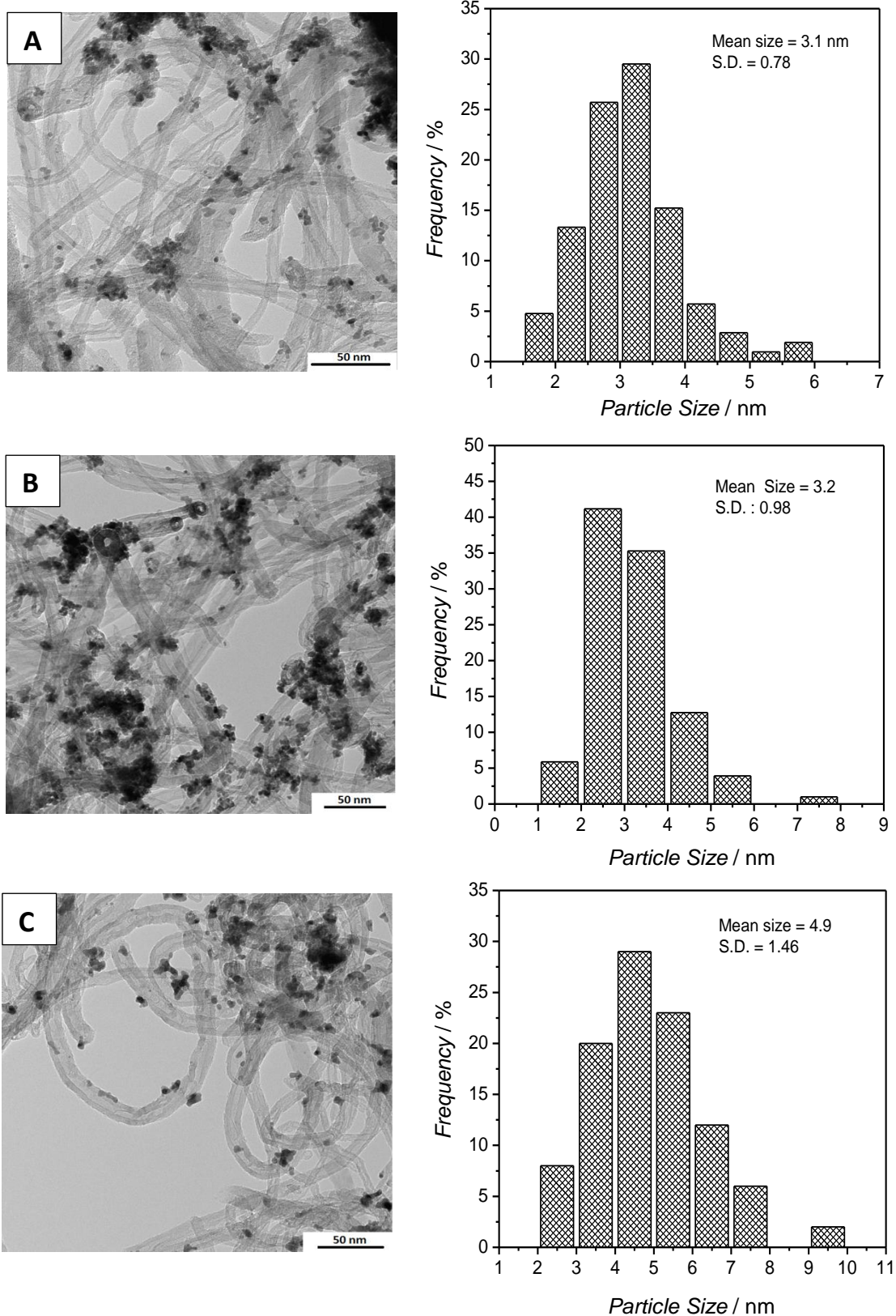


Figure 2.3: TEM images and the corresponding histograms of (A) PtRu/CNTs CR, (B) PtRu/CNTs MW, (C) PtRu/CNTs MW 200, (D) PtRu/CNTs MW 400, (E) PtRu/CNTs MW 600, (F) PtRu/CNTs MW 800.

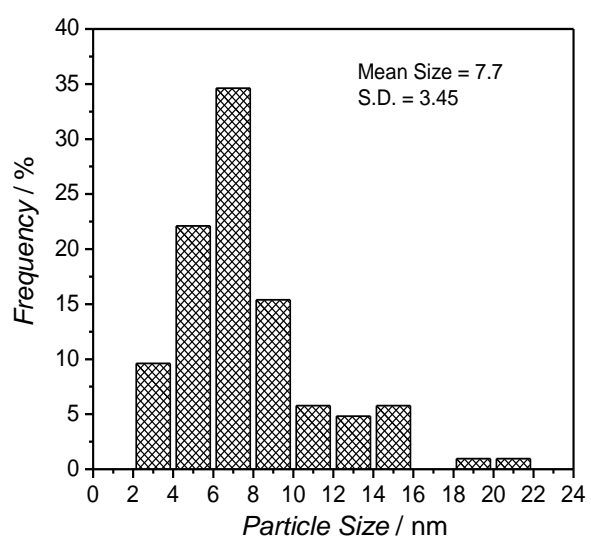
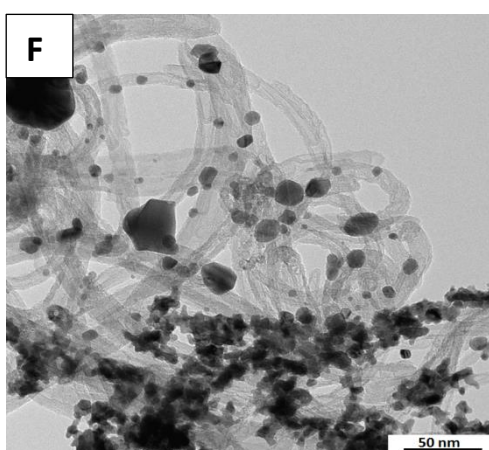
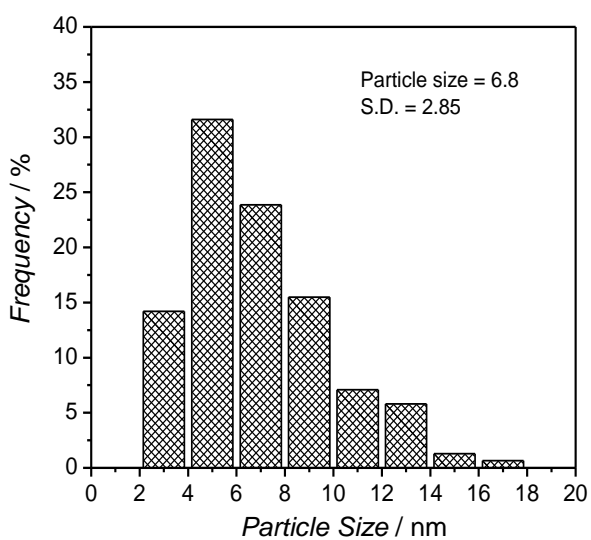
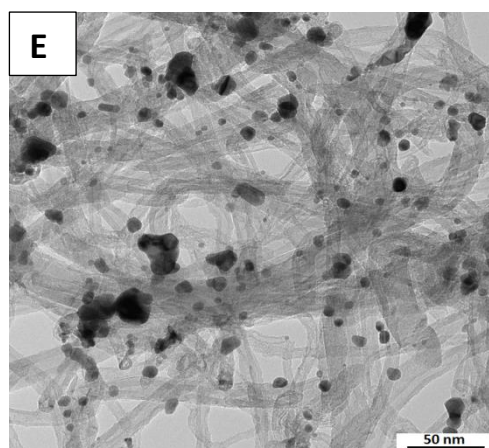
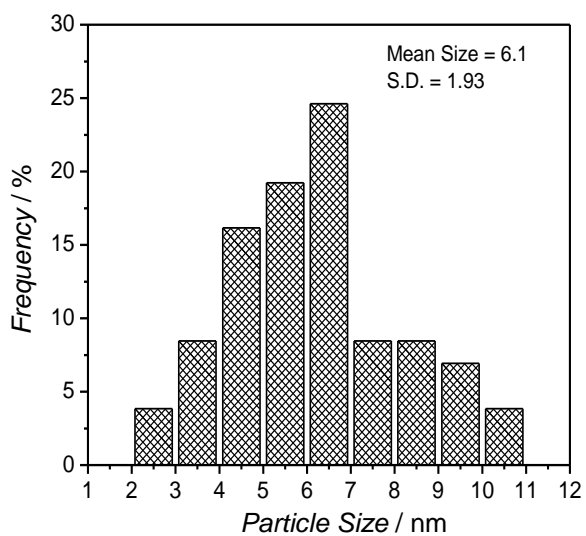
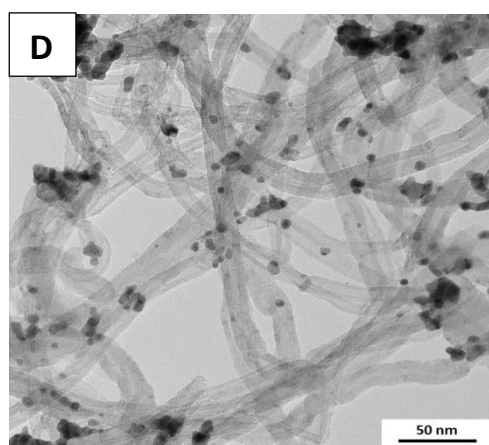


Figure 2.3: continued

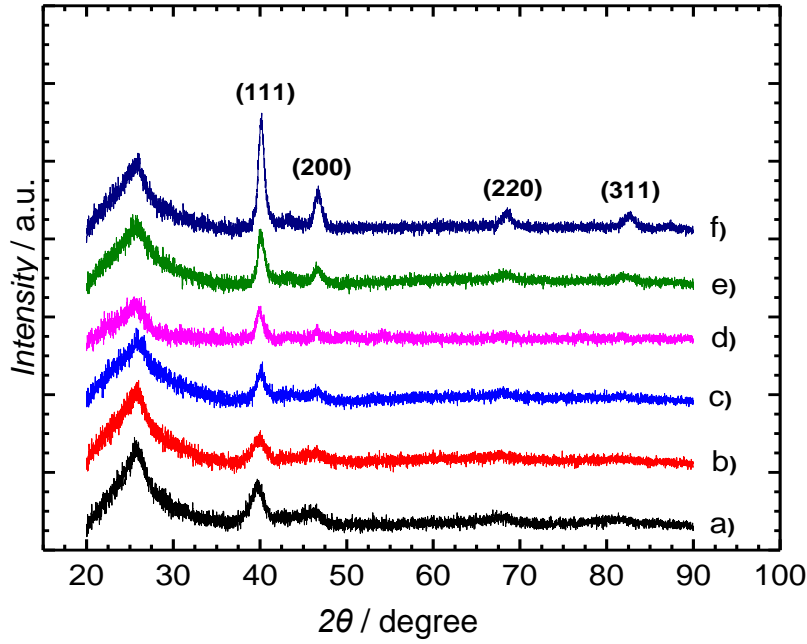


Figure 2.4: XRD patterns of (a) PtRu/CNTs CR, (b) PtRu/CNTs MW, (c) PtRu/CNTs MW 200, (d) PtRu/CNTs MW 400, (e) PtRu/CNTs MW 600, (f) PtRu/CNTs MW 800.

The mean crystallite size of the catalysts was determined from the (220) peak by using Scherrer's Equation:

$$d = \frac{0.9 \lambda}{B_{2\theta} \cos \theta_{max}} \quad (2.3)$$

In which d is the crystallite size in nm, λ is the wavelength (0.15406 nm), $B_{2\theta}$ is the full-width at half maximum (FWHM) in radians and θ_{max} is the 2θ angle at the maximum.

The calculated crystallite sizes are given in Table 2.1. The as-prepared catalysts show the same value, which indicates that the fast MW has no effect on the crystallite size, whereas the size increases with an increase in the heat treatment temperature. There is a slight dissimilarity between the particle sizes estimated from TEM and the crystallite size from XRD. While the former method can be used to visualize the whole particle, the latter detects only crystalline domains. Thus it might be that crystalline Pt particles are present, which are surrounded by amorphous layers of e.g. Ru oxides. In literature, the particle size estimated from TEM is considered as more precise [55,56]. To estimate the extent of solid solution/alloy formation of the heat-treated catalysts, the lattice parameter was calculated from Equation (2.4) [54,57]:

$$a_{fcc} = \frac{\sqrt{2} \lambda_{\kappa\alpha 1}}{\sin \theta_{max}} \quad (2.4)$$

Chapter 2: Microwave-Assisted Synthesis of PtRu/CNTs Electrocatalysts

The Ru atomic fraction and thus the extent of alloying can be calculated as suggested by Antolini et al. [58,59], by using Equation (2.5):

$$a_{fcc} = I_{oc} - kX_{Ru} \quad (2.5)$$

The lattice parameters and Ru atomic fractions X_{Ru} for all catalysts are given in Table 2.1. As expected, the catalysts prepared under conventional or MW conditions demonstrate a lattice parameter close to that of pure Pt [59]. The absence of any alloying or solid solution formation between Pt and Ru agrees with results reported for PtRu/C prepared through ethanol reduction under conventional reflux [44]. For the heat-treated catalysts, the lattice parameter decreases with an increase in temperature, which results from the incorporation of Ru with smaller atomic radius into the Pt lattice [54,55,59], and the atomic fraction increases with an increase in the temperature. However, even after heat treatment at 800 °C, not all Ru species are incorporated into the Pt lattice, which would lead to an X_{Ru} of 0.5 and points to separate Ru phases or still some amorphous Ru oxides; the latter, however are not expected under the reduction conditions used.

Table 2.1: Structural parameters from XRD and TEM analysis.

Catalysts	2 θ	FWHM ^[a]	Crystalline Size (nm) ^[b]	Particle Size (nm) ^[c]	Lattice parameter(nm)	X_{Ru}
PtRu/CNTs CR	67.41	3.502	2.7	3.1	0.3925	0
PtRu /CNTs MW	67.48	4.462	2.1	3.2	0.3922	0
PtRu/CNTs MW 200	68.04	2.978	3.2	4.9	0.3894	0.1733
PtRu /CNTs MW 400	68.05	2.242	4.2	6.7	0.3893	0.1814
PtRu /CNTs MW 600	68.31	1.778	5.4	6.8	0.3880	0.2862
PtRu /CNTs MW 800	68.44	1.444	6.6	7.7	0.3874	0.3346

^[a] FWHM= full-width at half-maximum, ^[b] Measured by XRD, ^[c] Measured by TEM

2.3.3 Electrochemistry study

2.3.3.1 CO Stripping

CO stripping voltammetry is a powerful and simple technique to obtain information about the electrochemical surface area of electrocatalysts and their tolerance to CO poisoning. The CO stripping voltammograms of all PtRu/CNTs electrocatalysts are shown in Figure 2.5. All voltammograms display an oxidation peak during the first scan at potentials close to 0.3 V, which is attributed to the oxidation of adsorbed CO layers. The absence of any peak in the second scan confirms the complete oxidation of adsorbed CO during the first scan. Hydrogen adsorption-desorption (H_{ad}/H_{des}) in the region of lower potentials is suppressed completely during the first scan as result of the blocking of Pt sites with adsorbed CO molecules. Only ill-defined H_{ad}/H_{des} features

develop during the second scan, which is characteristic for PtRu catalysts with higher Ru content [44,60].

The electrochemical surface area (ECSA) was determined by integrating the charge consumed during the oxidation of adsorbed CO after subtracting the base voltammogram [61]. The standard value of 420 $\mu\text{C cm}^{-2}$ for the oxidation of a monolayer of adsorbed CO on Pt surfaces was used as conversion factor. For the specific electrochemical surface area (SECSA), the electrochemical surface area was divided by the loading of Pt (mg) on the electrode [61,62]: according to the Equations (2.6) and (2.7):

$$ECSA(\text{cm}^2) = \frac{Q_{CO}(\text{mC})}{Q_0(\text{mC.cm}^{-2})} \quad (2.6)$$

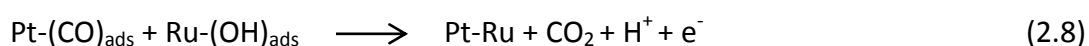
$$SECSA (\text{m}^2.\text{g}^{-1}) = \frac{ECSA}{M_{Pt}} \quad (2.7)$$

in which Q_{CO} is the CO oxidation charge in mC, Q_0 is the charge required for oxidation of an adsorbed monolayer of CO and equal to 420 ($\mu\text{C.cm}^{-2}$) and M_{Pt} is the Pt loading (mg) on the electrode.

The results are given in Table 2.2. The electrochemical surface area of the catalyst prepared with the help of MW decreases only slightly if heat treated at temperature up to 600 °C, whereas the decrease is much pronounced after 800 °C.

The decrease in surface area is less than that expected with the increase in particle size. This could be due to liberation of Pt surface sites from organic residues (which probably form in the course of the preparation process) during heat treatment. However, the XRD patterns indicate that Ru migrates into the Pt lattice during heat treatment. Thus, Ru species blocking the Pt surface after preparation are probably relocated during reduction, which leads to higher Pt surface area. The PtRu catalyst prepared through conventional reduction has a higher electrochemical surface area but the same particle size, which could be due to the different atomic ratios of Pt to Ru (1.8:1 for this catalyst vs. 1:1 for PtRu/CNTs prepared through microwave-assisted reduction). Thus, the blocking of the Pt surface by Ru species is less pronounced.

The onset potential for CO oxidation (Table 2.2) decreases with an increase in the heat treatment temperature, which could result from the increased extent of alloying in the heat-treated catalysts (XRD results Table 2.1). It is expected that Ru sites close to Pt sites facilitate the oxidation of adsorbed CO on the Pt sites according to the bifunctional mechanism [29]. This process can be represented by Equation (2.8):



Alternatively, Ru alloying could change the electronic properties of Pt in PtRu alloys and hence enhance the CO oxidation on PtRu by weakening the CO bonding (electronic effect). PtRu prepared under CR conditions shows higher onset and peak potentials for CO oxidation than does PtRu prepared under MW conditions. This can be due to lower Ru content in this catalyst or different surface properties. An increase in PtRu pairs on the surface of PtRu improves the onset potential and lowers the peak potential for CO oxidation on PtRu alloys [29]. These results indicate that the catalysts prepared by microwave-assisted reduction should be slightly less susceptible to CO poisoning than the catalysts prepared by conventional reduction.

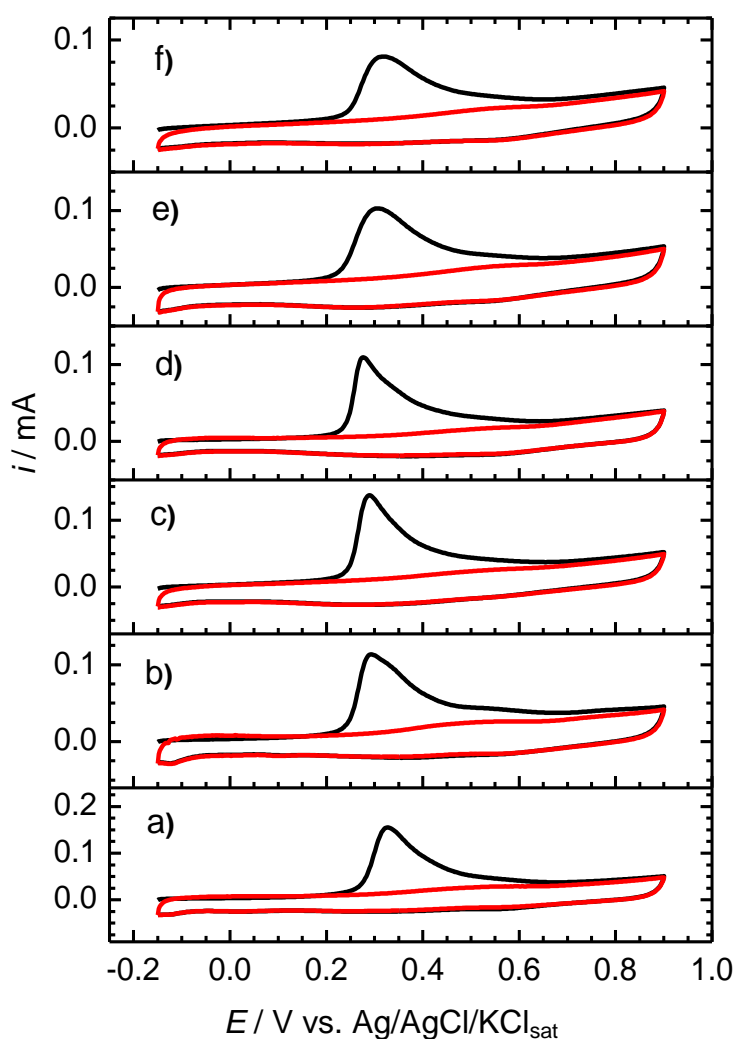


Figure 2.5: CO stripping voltammograms of a) PtRu/CNTs CR, b) PtRu/CNTs MW, c) PtRu/CNTs MW 200, d) PtRu/CNTs MW 400, e) PtRu/CNTs MW 600, f) PtRu/CNTs MW 800 in 0.5 M H_2SO_4 (scan rate 20 mV s^{-1}); the black lines represent the CO stripping peak and the red ones the second cycle.

Chapter 2: Microwave-Assisted Synthesis of PtRu/CNTs Electrocatalysts

Table 2.2: Electrochemical parameters from CO stripping.

Catalyst	Onset potential ^[a] [V]	Peak potential ^[a] [V]	Q [mC]	ECSA [cm ²]	SECSA [m ² g ⁻¹]
PtRu/CNTs CR	0.176	0.326	1.067	2.54	72.15
PtRu/CNTs MW	0.165	0.291	0.904	2.15	58.17
Pt Ru/CNTs MW 200	0.159	0.289	0.882	2.10	56.75
PtRu/CNTs MW 400	0.156	0.275	0.777	1.85	50.00
PtRu/CNTs MW 600	0.146	0.305	0.818	1.94	52.63
PtRu/CNTs MW 800	0.148	0.314	0.614	1.64	39.54

[a] for CO oxidation

2.3.3.2 Methanol oxidation

The methanol oxidation on the prepared electrocatalysts has been studied by using cyclic voltammetry in 1M CH₃OH/0.5M H₂SO₄ at a scan rate of 50 mV s⁻¹, as shown in Figure 2.6A and B, respectively. The as-prepared catalysts demonstrate a methanol oxidation behavior similar to that of pure platinum catalysts with two distinct current peaks: one in the forward scan for the oxidation of carbonaceous species formed at lower potentials and of methanol, with the current decreasing in the region of Pt-oxide formation; and one in the backward scan, typically higher in current value, for the oxidation of methanol on the Pt surface liberated from oxide and poisonous species. During methanol oxidation on heat-treated PtRu/CNTs MW, the current in forward peak (I_f) is more intense than that in the backward one (I_b), as typically reported for PtRu catalysts [21,29,44,54]. The I_f/I_b ratio is typically used to estimate the poisoning tolerance of a catalyst, with a high value indicating lower poisoning. As can be seen from the values in Table 2.3, the non-heat-treated catalysts show lower poisoning tolerance and the I_f/I_b value increases with an increase in temperature. The I_f/I_b values of our heat-treated samples and thus their poisoning resistance are higher than those of a commercial catalyst, which shows an I_f/I_b value of 1.17 (see, Figure SI2.1 in the Supporting Information) and those of a Pt/C catalyst (Figure SI2.2). The lowest poisoning tolerance is observed for the catalyst prepared under conventional heating conditions, as already suggested by CO stripping. Notably, the absolute current values are higher for the non-heat-treated samples.

The electrocatalytic activity of the catalysts was evaluated from the twentieth cycle in terms of mass-specific activity (peak current divided by Pt mass) and surface-specific activity (peak current divided by surface area (ECSA)), as listed in Table 2.3. There is no simple or linear dependence of both activity values from the heat treatment temperature. The highest surface-specific activity is obtained after treatment at 600 °C, which indicates that under these conditions the most favorable surface atomic arrangements are formed. As seen from XRD results, the alloy is formed with heat treatment. The mass-specific activity however is highest for the non-heat treated

catalyst; however, it is only slightly lower for the catalyst heat treated at 600 °C. The different orders in mass- and surface-specific activities are certainly related to the different particle sizes.

The catalytic activities are evaluated from the twentieth scan of continuous cycling, at which the non-heat-treated samples showed steady-state behavior in preliminary experiments. However, further cycling leads to a gradual decrease in activity, whereas for the heat-treated catalysts the activity increases with the cycle number. The plot of the mass-specific activity against the cycle number for all catalysts reveals this behavior (Figure 2.6C), in which activity of the non-heat-treated catalyst increases with potential cycling and reaches its maximum at the twentieth cycle, after which the catalysts activity start to deteriorate gradually. The same behavior is observed for the conventionally heated catalyst (data not included). The heat-treated catalysts, except PtRu/CNTs MW 800, similarly show a stronger increase in activity for 20 cycles and a slight increase thereafter. These results indicate that the as-prepared catalysts are less stable under dynamic electrochemical conditions, which could probably be attributed to the dissolution of Ru species during cycling. The initial increase in activity would then be attributed to the liberation of Pt sites from Ru. In contrast, the heat-treated catalysts show good stability under the same conditions, which suggests that the heat treatment-induced alloying of Ru in PtRu catalysts enhances their activities and stabilities as result of the formation of favorable active site on the surface of PtRu alloys. Notably, the stability of the heat-treated samples is better than that of a commercial PtRu/C catalyst (Figure SI2.3 in the Supporting information). Thus, although the initial activity of the commercial catalyst appears higher, after more than 100 cycles the activity of the heat treated samples prepared by microwave-assisted reduction is superior.

The increase in the metallic Ru species in PtRu catalysts in an alloy form enhances their activities and stabilities for the MOR, [28,29,63] whereas the presence of anhydrous RuO₂ which forms as the catalyst component during the catalyst preparation or heat treatment in oxygen atmosphere could decrease the activity of the PtRu catalysts [28,63]. Our preliminary results from XPS and X-ray absorption spectroscopy (XAS) characterization show that the Ru species in the as-prepared catalysts PtRu/CNTs CR and PtRu/CNTs MW are present mainly as anhydrous RuO₂, whereas in the heat-treated catalysts, the metallic Ru species are the major components among the Ru species. A detailed analysis of XPS and XAS parallel to performance testes of the catalysts in a real direct methanol fuel cell to establish a structure-activity relation is underway and will be presented in a separate article.

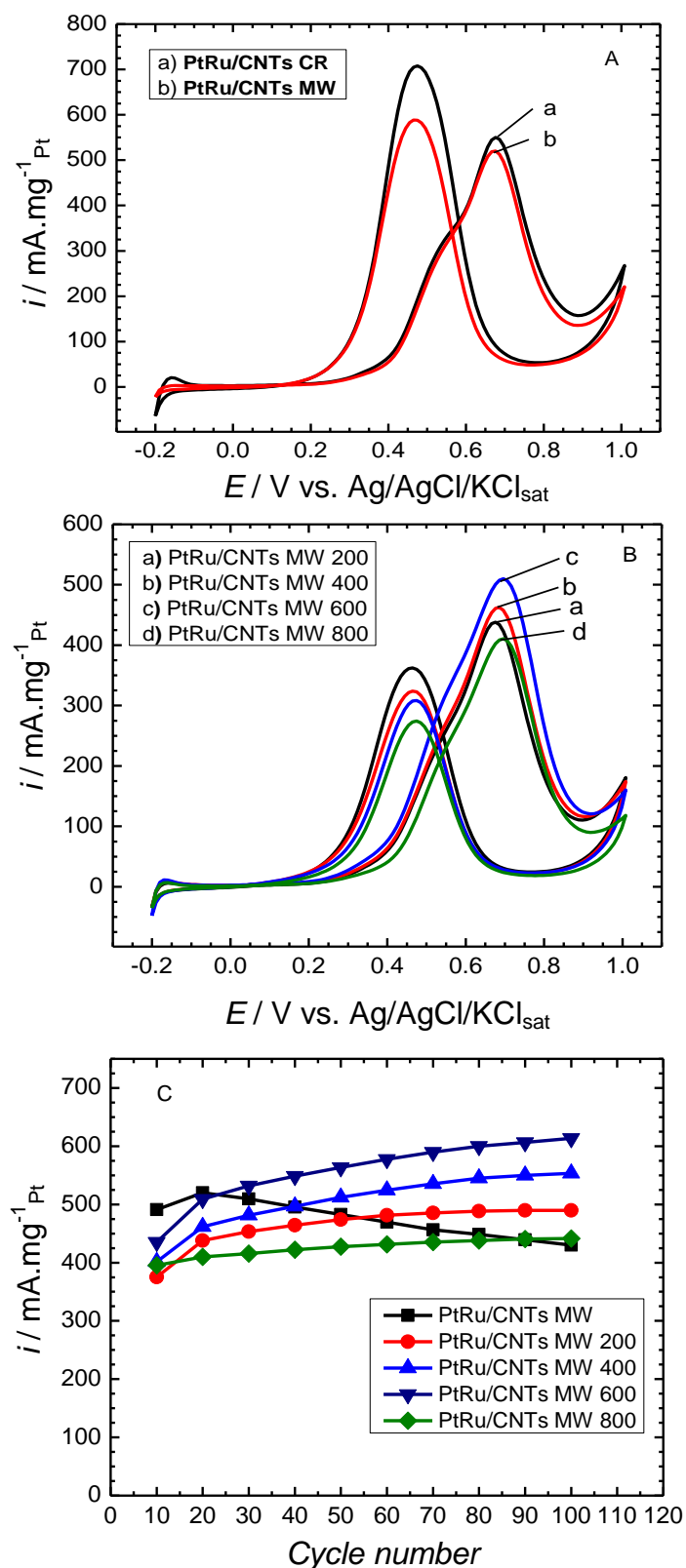


Figure 2.6: Cyclic voltammograms of a) PtRu/CNTs CR and PtRu/CNTs MW, b) PtRu/CNTs MW 200, 400 600 and 800 °C in 1 M $\text{CH}_3\text{OH}/0.5 \text{ M H}_2\text{SO}_4$ (scan rate 50 mV s^{-1}) and c) the variation of mass activity ($\text{mA} \cdot \text{mg}^{-1} \text{Pt}$) with the cycle number as extracted from cyclic voltammetry measurements.

Chapter 2: Microwave-Assisted Synthesis of PtRu/CNTs Electrocatalysts

Table 2.3: Peak potential, surface specific activity, mass specific activity and I_f/I_b for methanol oxidation from cyclic voltammetry measurements.

Catalysts	Peak Potential (V)	Surface specific activity ($\text{mA cm}^{-2}_{\text{Pt}}$)	Mass specific activity ($\text{mA mg}^{-1}_{\text{Pt}}$)	I_f/I_b
PtRu/CNTs CR	0.677	0.76	549.8	0.77
PtRu/CNTs MW	0.674	0.89	520.3	0.88
PtRu/CNTs MW 200	0.674	0.77	437.8	1.20
PtRu/CNTs MW 400	0.685	0.92	461.2	1.41
PtRu/CNTs MW 600	0.670	0.97	509.2	1.65
PtRu/CNTs MW 800	0.672	0.87	409.7	1.50

2.4 Conclusion

PtRu nanocatalysts supported on carbon nanotubes were prepared by microwave-assisted ethanol reduction in the presence of water. The results reveal that ethanol is not a powerful reducing agent for preparation of PtRu nanocatalysts, whereas the use of an ethanol/water mixture could reduce Pt and Ru ions to their metallic state under fast MW heating. The PtRu nanocatalysts prepared with this method were well dispersed on the CNTs, with particles in the nanometer range as determined from TEM analysis. XRD detected Pt face-centered cubic structure with no diffraction peaks for Ru or its oxide. After heat treatment in hydrogen at 200 - 600 °C, the formation of an alloy/solid solution was observed with an increasing Ru fraction in the lattices. Heat treatment higher than 600 °C leads to formation of a separate Ru phase as detected from XRD analysis.

Electrochemical characterization of the catalysts showed that heat treatment leads to enhanced stability while maintaining high activity and an optimum heat treatment temperature of 600 °C was found. The higher electrocatalytic activity and higher stabilities observed after heat treatment could be attributed to the formation of favorable active site on the catalyst surface as a result of the formation of a PtRu alloy surface, which is reported to be the active surface for the MOR.

Finally, more investigations are still needed to elucidate the active phases for the prepared catalyst in comparison with the heat-treated catalysts to clarify the origin of this higher activity and higher stability of the catalysts so as to apply them in direct methanol fuel cells.

References

- [1] A.S. Arico, S. Srinivasan, V. Antonucci, *Fuel Cells* 1 (2001) 133.
- [2] A.S. Arico, V. Baglio, V. Antonucci, in H. Liu, J. Zhang (Eds.), *Electrocatalysis of Direct Methanol Fuel Cells: From Fundamentals to Applications*, Wiley-VCH, Weinheim, 2009, pp. 1-77.
- [3] S. Wasmus, A. Küver, *J. Electroanal. Chem.* 461 (1999) 14.
- [4] S.K. Kamarudin, N. Hashim, *Renew. Sustain. Energy Review* 16 (2012) 2494.
- [5] Y. Chen, G. Zhang, J. Ma, Y. Zhou, Y. Tang, T. Lu, *Int. J. Hydrogen Energy*, 35 (2010) 10109.
- [6] H. Igarashi, T. Fujino, Y. Zhu, H. Uchida, M. Watanabe. *Phys. Chem. Chem. Phys.* 3 (2001) 306.
- [7] X. Zhao, M. Yin, L. Ma, L. Liang, C. Liu, J. Liao, T. Lu, W. Xing, *Energy Environ. Sci.* 4 (2011) 2736.
- [8] E. Lee, A. Manthiram, *J. Phys. Chem. C* 114 (2010) 21833.
- [9] M.A. Scibioh, S.-K. Kim, E.A. Cho, T.-H. Lim, S.-A. Hong, H.Y. Ha, *Appl. Catal. B*: 84 (2008) 773.
- [10] L. X. Yang, C. Bock, B. MacDougall, J. Park, *J. Appl. Electrochem.* 34 (2004) 427.
- [11] J. Ye, J. Liu, Z. Zou, J. Gu, T. Yu, *J. Power Sources* 195 (2010) 2633.
- [12] B. Abida, L. Chirchi, S. Baranton, T.W. Napporn, H. Kochkar, J.-M. Léger, A. Ghorbel, *Appl. Catal. B*: 106 (2011) 609.
- [13] R.S. Amin, R.M. Abdel Hameed, K.M. El-Khatib, M.E. Youssef, A.A. Elzatahry, *Electrochim. Acta* 59 (2012) 499.
- [14] D. B. Kim, H.-J. Chun, Y. K. Lee, H.-H. Kwon, H.-I. Lee, *Int. J. Hydrogen Energy* 35 (2010) 313.
- [15] Z.M. Cui, S.P. Jiang, C.M. Li, *Chem. Commun.* 47 (2011) 8418.
- [16] R. Vellacheri, S.M. Unni, S. Nahire, U.K. Kharul, S. Kurungot, *Electrochim. Acta* 55 (2010) 2878.
- [17] X-W. Zhou, R.-H. Zhan, Z.-Y. Zhou, S.-G. Sun, *J. Power Sources* 196 (2011) 5844.
- [18] Y. Hu, P. Wu, Y. Yin, H. Zhang, C. Cai, *Appl. Catal. B*: 111 (2012) 208.
- [19] Z. Ji, X. Shen, G. Zhu, K. Chen, G. Fu, L. Tong, *J. Electroanal. Chem.* 685 (2011) 95.
- [20] E. Lee, A. Murthy, A. Manthiram, *J. Electroanal. Chem.* 659 (2011) 168.
- [21] S. Wang, S.P. Jiang, X. Wang, *Electrochim. Acta* 56 (2011) 3338.
- [22] L. Ma, C. Liu, J. Liao, T. Lu, W. Xing, J. Zhang, *Electrochim. Acta* 54 (2009) 7274.
- [23] M. Watanabe, S. Motoo, *J. Electroanal. Chem.* 60 (1975) 275.
- [24] T. Frelink, W. Visscher, J.A.R. van Veen, *Surf. Sci.* 335 (1995) 353.
- [25] P. Waszczuk, G.U. Lu, A. Wieckowski, C. Lu, C. Rice, M.I. Masel, *Electrochim. Acta* 47 (2002) 3637.

- [26] P.K. Babu, H.S. Kim, S.T. Kuk, J.H. Chung, E. Oldfield, A. Wieckowski, E.S. Smotkin, *J. Phys. Chem. B* 109 (2005) 17192.
- [27] C. Roth, N. Benker, T. Buhrmester, M. Mazurek, M. Loster, H. Fuess, D.C. Koningsberger, D.E. Ramaker, *J. Am. Chem. Soc.* 127 (2005) 14607.
- [28] Y.-C. Wei, C.-W. Liu, K.-W. Wang, *ChemPhysChem* 10 (2009) 1230.
- [29] K.-S. Lee, T.-Y. Jeon, S.J. Yoo, I.-S. Park, Y.-H. Cho, S.H. Kang, K.H. Choi, Y.-E. Sung, *Appl. Catal. B*: 102 (2009) 334.
- [30] B. Yang, Q.Y. Lu, Y. Wang, L. Zhuang, J.T. Lu, P.F. Liu, *Chem. Mater.* 15 (2003) 3552.
- [31] J.W. Long, R.M. Stroud, K.E. Swider-Lyons, D.R. Rolison, *J. Phys. Chem. B* 104 (2000) 9772.
- [32] J.L. Gomez dela Fuente, M.V. Martinez-Huerta, S. Rojas, P. Hernandez-Fernandez, P. Terreros, J.L.G. Fierro, M.A. Pena, *Appl. Catal. B*: 88 (2009) 505.
- [33] R. Chetty, W. Xia, S. Kundu, M. Bron, T. Reinecke, W. Schuhmann, M. Muhler, *Langmuir* 25 (2009) 3853.
- [34] J.-H. Ma, Y.-Y. Feng, J. Yu, D. Zhao, A.-J. Wang, B.-Q. Xu, *J. Catal.* 275 (2010) 34.
- [35] H. Liu, C. Song, L. Zhang, J. Zhang, H. Wang, D.P. Wilkinson, *J. Power Sources* 155 (2006) 95.
- [36] T.A. Yamamoto, S. Kageyama, S. Seino, H. Nitani, T. Nakagawa, R. Horioka, Y. Honda, K. Ueno, H. Daimon, *Applied. Catal. A*: 396 (2011) 68.
- [37] S. Kageyama, A. Murakami, S. Ichikawa, S. Seino, T. Nakagawa, H. Daimon, Y. Ohkubo, J. Kugai, T.A. Yamamoto, *J. Mater. Res.* 27 (2012) 1037.
- [38] Md. Abdul Matin, J.-H. Jang, E. Lee, Y.-U. Kwon, *J. Appl. Electrochem.* 42 (2012) 827.
- [39] S. Moussa, A.R. Siamaki, B.F. Gupton, M.S. El-Shall, *ACS Catal.* 2 (2012) 145.
- [40] S. Moussa, V. Abdelsayed, M.S. El-Shall, *Chem. Phys. Lett.* 510 (2011) 179.
- [41] D.-M. Gu, Y.-Y. Chu, Z.-B. Wang, Z.-Z. Jiang, G.-P. Yin, Y. Liu, *Appl. Catal. B*: 102 (2011) 9.
- [42] S. Horikoshi, M. Abe, N. Serpone, *Appl. Catal. B*: 89 (2009) 284.
- [43] A. Pal, S. Shah, S. Devi, *Mater. Chem. Phys.* 114 (2009) 530.
- [44] A.B. Kashyout, A.B.A. Nassr, L. Giorgi, T. Maiyalagan, B.A.B. Youssef, *Int. J. Electrochem. Sci.* 6 (2011) 379.
- [45] J. Zeng, Jim Y. Lee, *J. Power Sources* 140 (2005) 268.
- [46] K. Leelarujji, M. Hunsom, *Renew. Energy* 35 (2010) 2422.
- [47] B.R. Camacho, M. T. Rodríguez, O. Solorza-Feria, *J. New. Mater. Electrochem. Systems* 12 (2009) 43.
- [48] M. Balcerzak, E. Swiecicka, E. Balukiewicz, *Talanta* 48 (1999) 39.
- [49] J.-M. Lee, D.-W. Kim, T.-H. Kim, S.-G. Oh, *Mater. Letters* 61 (2007) 1558.

- [50] T.-H. Kim, D.-W. Kim, J.-M. Lee, Y.-G. Lee, S.-G. Oh, *Mater. Resear. Bull.* 43 **(2008)** 1126.
- [51] S.-R. Wang, W. J. Tseng, *J. Nanopart. Res.* 11 **(2009)** 947.
- [52] F. Bonet, C. Guéry, D. Guyomard, R. Herrera-Urbina, K. Tekaiia-Elhsissen, J.-M. Tarascon, *Int.. J. Inorg. Mater.* 1 **(1999)** 47.
- [53] J. Guo, G. Sun, Q. Wang, Z. Zhou, S. Tang, L. Jiang, B. Zhou, Q. Xin, *Carbon* 44 **(2006)** 152.
- [54] J.W. Guo, T.S. Zhao, J. Prabhuram, R. Chen, C.W. Wong, *Electrochim. Acta* 51 **(2005)** 754.
- [55] R. Chetty, S. Kundu, W. Xia, M. Bron, W. Schuhmann, V. Chirila, W. Brandl, T. Reinecke, M. Muhler, *Electrochim. Acta* 54 **(2009)** 4208.
- [56] D. Ozkaya, *Platinum Met. Rev.* 52 **(2008)** 61.
- [57] V. Radmilovic, H.A. Gasteiger, P.N. Ross, *J. Catal.* 154 **(1995)** 98.
- [58] E. Antolini, F. Cardellini, L. Giorgi, *J. Mater. Sci. Lett.* 19 **(2000)** 2099.
- [59] E. Antolini, F. Cardellini, *J. Alloys Compd.* 315 **(2001)** 118.
- [60] T. Vidaković, M. Christov, K. Sundmacher, K.S. Nagabhushana, W. Fei, S. Kinge, H. Bönemann, *Electrochim. Acta* 52 **(2007)** 2277.
- [61] T. Vidaković, M. Christov, K. Sundmacher, *Electrochim. Acta* 52 **(2007)** 5606.
- [62] A. Rose, R. Bilsborrow, C.R. King, M.K. Ravikumar, Y. Qian, R.J.K. Wiltshire, E.M. Crabb, A.E. Russell, *Electrochim. Acta* 54 **(2009)** 5262.
- [63] Y.-C. Wei, C.-W. Liu, W.-J. Chang, K.-W. Wang, *J. Alloys Compd.* 509 **(2011)** 535.

Supporting information

As reference materials, commercially available catalysts (30 wt.% PtRu/C, Alfa Aesar, and 20 wt.% Pt/C E-Tek) have been tested by cyclic voltammetry in the same way as the catalysts prepared in this study as shown in Figures SI2.1 and SI2.2:

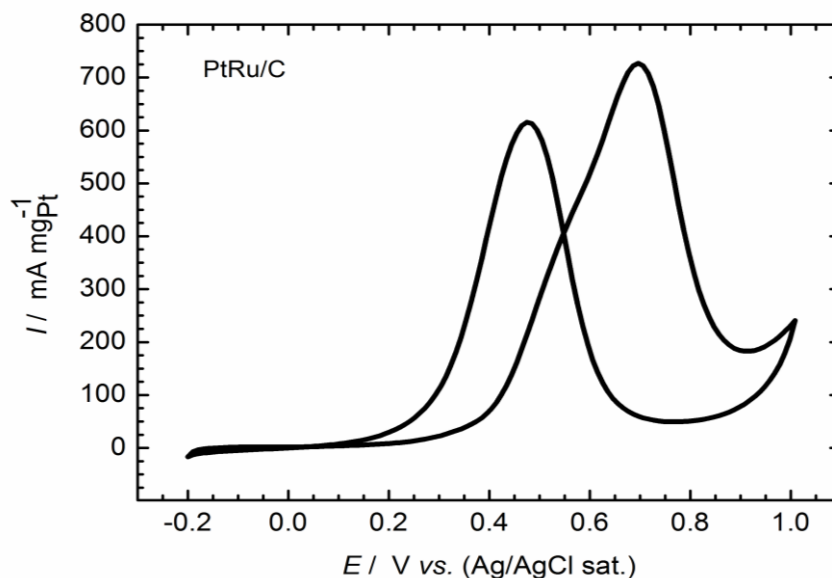


Figure SI2.1: Cyclic voltammogram of PtRu/C (30 wt% Alfa Aesar) in 1 M CH₃OH/0.5 M H₂SO₄, scan rate 50 mV⁻¹.

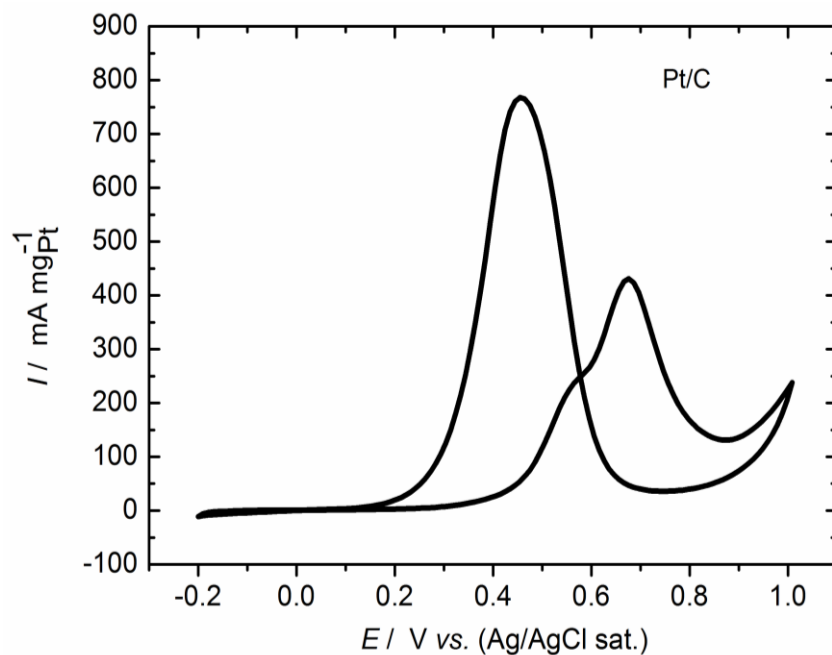


Figure SI2.2: Cyclic voltammogram of Pt/C (20 wt%, E-Tek) in 1 M CH₃OH/0.5 M H₂SO₄, scan rate 50 mV⁻¹.

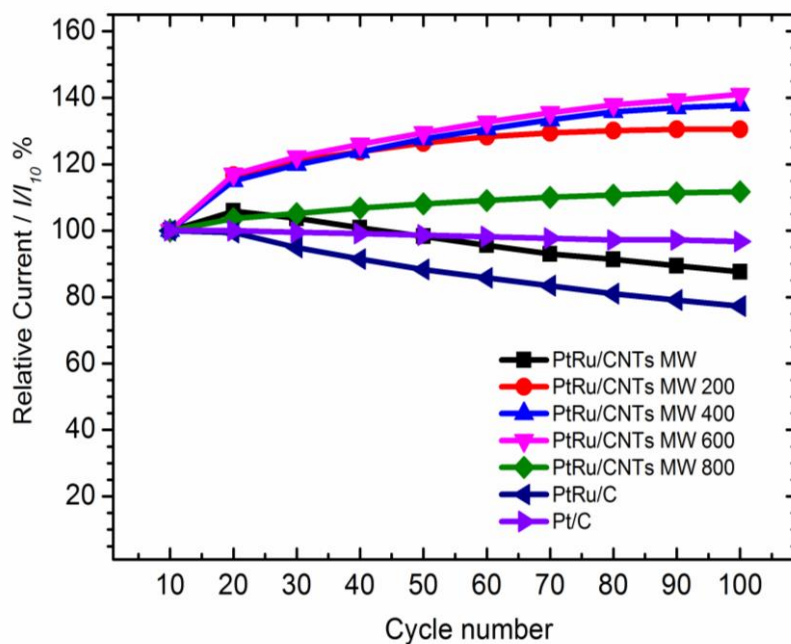


Figure S12.3: Variation of relative current with cycle number as extracted from CV measurements for various catalysts used in this study. Values normalized to the activity during scan number 10.

The content of this chapter prepared to be submitted for publications in Journal of Power Sources as

PtRu/CNTs as highly active and durable electrocatalysts: correlating structure with stability

Abu Bakr Ahmed Amine Nassr, Prashant Subhas Khadke, Ilya Sinev, Ulrike Krewer
Wolfgang Grünert, Michael Bron

3.1 Introduction

Carbon supported nanostructured bimetallic catalysts have attracted significant attention owing to their potential applications in many fields, including heterogeneous catalysis, environmental protection and energy conversion [1,2]. One prominent example is the polymer electrolyte membrane fuel cell (PEMFC) where bimetallic nanoparticles may be used as cathode or anode catalysts. The catalytic activity depends mainly on their size, structure, composition and surface properties [3-6]. In this regard, carbon supported PtRu catalysts are known to be an active catalyst material for the methanol oxidation reaction (MOR) at the anode of the direct methanol fuel cell (DMFC). The higher activity of bimetallic PtRu/C catalysts toward MOR compared to monometallic Pt/C catalysts is attributed to the higher tolerance against CO poisoning arising from the supply of oxygen species by Ru metal or its oxides on the catalyst surface and/or to the electronic modification of Pt by Ru, reducing the bonding energy between the Pt surface and the CO poisoning species [3,5-7]. The catalytic properties of PtRu/C mainly depend on the state of Ru in the catalyst, surface composition, alloying extent between Pt and Ru and their distribution on the atomic scale [7-10]. Tuning these structural properties would be highly desired to enhance catalytic activity and lower the loading of precious and costly PtRu catalyst in the DMFC electrode [11].

The stability of PtRu catalysts in direct methanol fuel cells under operation is an important issue since the dissolution of Ru from PtRu during the fuel cell operation leads to decreasing tolerance of PtRu catalysts against CO poisoning intermediates [12-15] and thus reduced cell performance. Also, the migration of dissolved Ru into the cathode side may cause cathode catalyst contamination with Ru resulting in decreased efficiency for oxygen reduction and hence decreased cell performance [15-17].

The issue of Ru dissolution in PtRu catalysts and the impact on fuel cell performance has been reviewed recently by Antolini [18] together with suggestions to overcome this problem. It has been postulated that Ru in its hydrous oxide form ($\text{RuO}_x \cdot \text{H}_2\text{O}$ or $\text{RuO}_x \text{H}_y$) is responsible for high activity of the PtRu system [19-21]

whereas other studies reported higher activities for PtRu containing anhydrous oxide (RuO₂) [22-24]. The post heat treatment under different atmosphere is suggested as a method for surface modification of PtRu/C catalysts to prepare a stable alloy structure and therefore to enhance their activity and stability as a result of increasing the bonding between Pt and Ru, increasing the alloying extent and alternation the population and distribution of the active metallic sites on the surface of the catalysts [27,29,34]. In contrast, some studies stress that the metallic form of Ru in PtRu is responsible for the higher activity and stability depending on the alloying extent [25-27]. Although the hydrous oxide of Ru exhibits higher activity for MOR, its stability is lower and it undergoes dissolution under repeated potential cycles in acid environment [21]. Heat treatment has been suggested as an option to enhance the stability of hydrous ruthenium oxide [28].

To overcome the problem of Ru dissolution in PtRu catalysts different solutions have been suggested such as the preparation of highly stable PtRu catalysts [21,25,26,29], the use of new or modified supports that can stabilize the Ru [14,15,30] and finally using additives (metals or metal oxides) that can also prevent Ru from dissolution. As one example of these additives, Au has been shown to stabilize PtRu catalysts and at the same time enhance their activities [31,32]. As another example, TiO₂ has been used as stabilizer for PtRu catalysts, increasing life time and stability of PtRu in extended potential regions and even in real direct methanol fuel cell environment [33].

So, for long term stability of PtRu catalysts in direct methanol fuel cells, the stable alloy structure seems to be the best choice than the oxide containing one. However the alloy structure is high stable structure of PtRu catalysts, as emphasized from different reports, than the oxides form of PtRu or non-alloyed PtRu, the investigation of the Ru phases in PtRu catalyst and their relation to the activity and stability of this system in methanol oxidation reaction and in real direct methanol fuel cell still an active point of research that required more detailed studies to address this issue well.

Surface segregation in bimetallic catalysts is a well-documented phenomenon related to thermodynamic considerations where the segregation of the individual metal depends on its surface energy and its atomic radius as the metal with a lower surface energy and a large atomic radius has the tendency to segregate towards the surface [35,36]. For PtRu alloys, under heat treatment conditions it is expected that Pt atoms with lower surface energy segregate to the surface of PtRu forming a catalyst surface with Pt enriched surface that could stabilize the PtRu structure and limit the process of Ru dissolution [27,36,37].

We have recently reported on the preparation of PtRu supported on functionalized carbon nanotubes using a novel microwave assisted reduction method employing an

ethanol/water mixture as solvent and reducing agent, achieving a Pt/Ru composition of 1:1 which was difficult to obtain under conventional heating [29]. In addition to the simultaneous reduction of Pt and Ru ions, the microwave approach is fast, simple and applicable on the industrial scale [6].

In this article, we report on the full structural characterization of the PtRu/CNTs catalysts with X-ray photoelectron spectroscopy (XPS) and X-ray absorption fine structure spectroscopy (XAFS) aiming to correlate the structural properties with electrochemical results. The performance and stability of selected catalysts was evaluated in a single direct methanol fuel cell including an accelerated durability test (ADT) and will be discussed in view of the spectroscopic results and the effect of heat treatment on the catalyst structure.

3.2 Experimental work

3.2.1 Electrocatalyst preparation

Preparation of the PtRu/CNT catalysts was done with microwave-assisted ethanol reduction preparation which has been recently introduced by us [29]. Briefly, the Pt and Ru precursors together with oxidized carbon nanotubes were dispersed in an ethanol-water mixture (1:1 v/v) which served as solvent and reducing agent. After stirring and sonication the dispersion was irradiated with microwave radiation for 4 min at 300 W in a microwave reactor (Microwave START 1500, Milestone) under reflux conditions followed by stirring overnight and finally the catalyst was separated and dried. The catalyst powder was subjected to heat treatment in reductive atmosphere (10 % H₂ in Ar) for 2 h at different temperatures of 200, 400, 600 and 800 °C. The catalysts were labeled PtRu/CNTs MWX, where X refers to the heat treatment temperature. For comparison, a commercial catalysts PtRu/C (HiSPEC® 5000) (20 wt% Pt and 10 wt% Ru with an atomic ratio of Pt:Ru = 1) from Alfa Aesar (JM) was used as benchmark catalyst and investigated in the same way as the prepared samples. Also, a PtRu/CNT catalyst was prepared using EtOH/water under conventional reflux, used as reference for structural characterization and labeled PtRu/CNTs CR.

3.2.2 Electrocatalyst characterization

3.2.2.1 Structural characterization

The catalysts were characterized with structural techniques such as X-ray photoelectron spectroscopy (XPS) and X-ray absorption fine structure spectroscopy (XAFS). XPS measurements were carried out in an ultra-high vacuum (UHV) setup equipped with a monochromatic Al K α X-ray source ($h\nu = 1486.6$ eV), operated at 14.5 kV and 35 mA, and a high resolution Gamdata-Scienta SES 2002 analyzer. The base pressure in the measurement chamber was maintained at about 7×10^{-10} bar. The measurements were carried out in the fixed transmission mode with pass energy of

200 eV resulting in an overall energy resolution of 0.25 eV. High-resolution spectra for C 1s (together with Ru 3d), O 1s, and Pt 4f regions were recorded. The binding energy scales were re-calibrated based on the C 1s line of the sp² hybridized graphitic carbon, which was set to 284.5 eV. The Casa XPS software was used for peak deconvolution. Lineshapes applied were Pseudo Voigt-type (Gaussian-Lorentzian product) for symmetrical lines, and the Doniach-Sunjic asymmetric [40] function for metal lines. Analysis was made on Shirley-type backgrounds. In the following, the spectra of different elements are plotted with normalization to the intensity of the C 1s peak of the CNT support to facilitate comparison.

PtL₃-edge (11564 eV) X-ray absorption fine structure (XAFS) measurements were carried out at HASYLAB (DESY in Hamburg, Germany) on the beamline C. A double-crystal Si (111) monochromator was used, which was detuned to 50% of maximum intensity to exclude higher harmonics in the X-ray beam. RuK-edge XAFS measurements were done on CLÆSS beamline of ALBA synchrotron facility in Barcelona, Spain. A Si (311) double crystal monochromator was used for the energy scan together with a Rh-coated toroid mirror which eliminated unwanted harmonics. The spectra were recorded in the transmission mode at liquid nitrogen temperature. For the measurements, the samples were pressed in self-supporting pellets (diameter – 13 mm for HASYLAB, 5 mm for ALBA measurements) and wrapped with Kapton tape. For energy calibration, the PtL₃ edge spectrum of a Pt foil placed between second and third ionization chambers was measured together with that of the samples. The RuK edge energy range was calibrated by measuring the XANES of a rhodium foil and attributing the RhK edge energy (23220 eV) to the maximum of its first derivative. The spectra of Ru and Pt foils and of the corresponding oxides, which were used as references, were collected under the same conditions. All spectra were measured twice to ensure their reproducibility.

Analysis of the EXAFS spectra was performed with the software VIPER for Windows [39]. In the spectra of the absorption coefficient μ , a Victorian polynomial was fitted to the pre-edge region for background subtraction. A smooth atomic background μ_0 was evaluated using a smoothing cubic spline. The Fourier analysis of either the k^2 - (for PtL₃ edge) or the k^1 -weighted (for RuK edge) experimental functions $\chi = (\mu - \mu_0) / \mu_0$ was performed with a Kaiser window. The required scattering amplitudes and phase shifts were calculated by the ab initio FEFF8.10 code [40] for Ru metal hcp, RuO₂ tetragonal, Pt metal fcc, orthorhombic PtO₂ and fcc Pt-Ru alloy structures. The fitting was done in the k - and r -spaces. The shell radius r , coordination number N , Debye-Waller factor σ^2 and adjustable “muffin-tin zero” ΔE were determined as fitting parameters. The errors of the fitting parameters were found by decomposition of the statistical χ^2 function near its minimum, taking into account maximal pair correlations.

3.2.2.2 Electrochemical characterization

The electrocatalytic activity of the catalysts towards the methanol oxidation reaction (MOR) was tested in a three electrodes three compartment cell by cyclic voltammetry and chronoamperometry using an Autolab PGSTAT128N potentiostat/galvanostat controlled by the NOVA 1.8 software. A Pt wire served as counter electrode, an Ag/AgCl/KCl sat (SSC) as reference electrode and a catalyst-coated glassy carbon electrode as working electrode. The preparation of the electrodes for electrochemical measurements was reported previously [29]. The catalytic activity was evaluated in 1 M CH₃OH/0.5 M H₂SO₄ solution with chronoamperometric (CA) measurements at a fixed potential of 0.7 V vs. SSC. For these measurements, two electrodes were prepared. A CA curve was recorded for the first electrode in 1 M CH₃OH/0.5 M H₂SO₄ solution for 1 h ("initial CA"). The second electrode was first subjected to 100 potential cycles in a potential window of -0.2 to 1 V vs. SSC in 1 M CH₃OH/ 0.5 M H₂SO₄ at scan rate of 50 mV s⁻¹ after which it was rinsed carefully with N₂ saturated 0.5 M H₂SO₄ before recording a base CV in N₂ saturated 0.5 M H₂SO₄ (10 cycles, 50 mV s⁻¹). This procedure was used to detect any surface changes of the electrocatalyst during potential cycling in MeOH containing acid. The final CV cycle was taken as the characteristic CV after methanol oxidation. Afterwards, the CA curve was recorded for 1 h at 0.7 V vs. SSC in the same solution ("CA after MOR"). The catalytic activity was compared for all catalysts using the value of the steady state current from CA after 1 h expressed in mass specific current (mA mg⁻¹_{Pt}). All measurements were carried out in N₂ saturated solution prepared from deionized water and N₂ gas flow was maintained over the surface of the solution during the measurements. Before electrochemical tests all working electrodes were subjected to an electrochemical cleaning by potential cycling for 50 cycles in 0.5 M H₂SO₄ in the potential window of - 0.2 V to 1 V at a scan rate of 50 mV s⁻¹ and the final cycle was recorded as the base voltammogram.

3.2.2.3 Direct methanol fuel cell tests

(i) Membrane electrode assembly (MEA) fabrication

Both PtRu/CNT and commercial PtRu/C from Alfa Aesar (JM) samples were used as anode catalysts with metal loadings (PtRu) of 0.5 mg cm⁻² whereas commercial Pt/C (20 wt %) from ETEK was used as cathode catalyst with metal a loading (Pt) of 1 mg.cm⁻². The active area of the fuel cell electrodes was 5 cm².

For the anode catalysts layer the required amount of catalyst was dispersed in water and isopropanol in a ratio of (Catalyst (mg): H₂O (mL): ISP (mL)) equal to (1: 0.01: 0.1) and the amount of Nafion taken from Nafion solution (5 wt. %) in the mixture was controlled to be 10 wt. % of the initial weight of the catalyst. The mixture was sonicated for 20 min and the obtained catalyst ink was coated onto the gas diffusion

layer (GDL 35 BC from Sigracet) using the hand brush technique and dried using a hair drier. The metal loading in the electrode was determined from the difference in weight of the diffusion layer before and after the coating process. The cathode catalysts layer was prepared in the same manner, except that the amount of Nafion in the layer was controlled to be 30 wt. % of the Pt/C catalyst weight.

A Nafion membrane 115 was sandwiched between the two electrodes and the resulting MEA hot pressed at 130 °C for 3 min. After cooling down, the MEA was mounted into a single fuel cell (qcfFC25 from Baltic Fuel cells GmbH, Germany) to be ready for the measurements.

(ii) Single fuel cell operation and measurements

Each MEA is subjected to series of steps as detailed below. The flow rates are controlled by a fuel cell test station (SMART) from WonATech co. Ltd, Korea and IV curves, CV and Impedance measurements are measured by using IM6e potentiostat from ZAHNER Elektrik GmbH, Germany.

Activation

- 1) Passing water at 0.5 ml/min through both the anode and the cathode at a cell temperature of 80 °C for 16 h.
- 2) Recording five IV curves with 1 M CH₃OH at 0.5 ml.min⁻¹ and humidified O₂ at 50 ml min⁻¹.
- 3) Passing water at 0.5 ml/min (anode and cathode) at 80 °C for 2 h.

Steps 2 and 3 were repeated 3 times, after which even the most rof MEAs reached stable performance.

IV curves recording

The fuel cell performance was evaluated at 60 °C by recording IV curve in two modes:

- 1) CH₃OH/O₂ mode where the anode feed is 1 M CH₃OH (MOR) and the cathode feed is humidified O₂ (ORR).
- 2) CH₃OH/H₂ mode where the anode feed is 1 M CH₃OH (MOR) and the cathode feed is humidified H₂ (HER) to serve as dynamic hydrogen electrode (DHE).

In the first mode, the cell polarization during IV curves measurement is attributed to both anode and cathode polarization whereas in second mode the cell polarization is attributed to anode polarization only since the HER is known to be relatively fast. The flow of 1 M CH₃OH was set to 0.5 ml min⁻¹ whereas O₂ and H₂ flows were set to 50 ml min⁻¹.

CV and EIS measurements

CV measurements for characterization of the anode side of the MEAs were carried out in N₂/H₂ mode with N₂ atmosphere at the anode and H₂ flow at 50 ml min⁻¹ at cathode. The impedance spectra were recorded at 0.5 V for CH₃OH/H₂ mode and at 0.3 V for CH₃OH/O₂ mode in frequency range from 50 kHz to 0.1 Hz with amplitude potential of 10 mV and 5 steps per decade.

Accelerated durability test

Accelerated durability tests (ADT) were carried out in H₂O/H₂ mode with H₂O flow of 0.5 ml min⁻¹ at the anode and H₂ flow of 50 ml min⁻¹ at the cathode. ADT was carried out according to a potential cycling protocol [12] in which all MEAs were subjected to potential cycling in a potential window of 0.1 to 0.7 V vs. DHE for 5000 potential cycles.

3.3 Results

3.3.1 Structural characterization of the electrocatalysts

3.3.1.1 XPS analysis

X-ray photoelectron spectroscopy was used to analyze the surface chemical properties of the catalysts. A series of Pt4f photoelectron spectra is presented in Figure 3.1. The Pt 4f_{7/2} line position gradually shifts from 71.2 to 71.65 eV in the sequence PtRu/CNTs CR - PtRu/CNTs MW - PtRu/CNTs MW200 - PtRu/CNTs MW400 - PtRu/CNTs MW600 - PtRu/CNTs MW800. However these shifts hardly indicate an oxidation of platinum. Pt 4f_{7/2} binding energies were reported to be around 71.5 eV in Pt-Ru alloys by several authors [42,43] and the overall line shapes do not suggest the presence of oxidized Pt states. The commercial PtRu/C sample has a much higher shift and the lines themselves are broader indicating the presence of platinum also in higher oxidation state.

The analysis of the ruthenium XPS lines analysis is essentially hampered by their close proximity to the C 1s line. Actually, the Ru 3d_{3/2} line is fully overlapped by the intense C 1s signal from the carbon nanotubes. However, the spectral resolution was high enough to record Ru 3d_{5/2} lines without significant influence of the C1s signals (Figure 3.2). All spectra show significant contribution of asymmetric Ru metal lines at a binding energy of ca. 280.2 eV [44]. At the same time commercial PtRu/C, PtRu/CNTs CR and PtRu/CNTs MW spectra have notable high-energy contributions at ca. 281 eV, which most likely correspond to ruthenium dioxide [45]. The Ru⁴⁺:Ru⁰ ratio was calculated to be 5.5, 0.6 and 1.7 for PtRu/C, PtRu/CNTs CR and PtRu/CNTs MW samples, respectively (Figure S13.1). At the same time the heat treatment has an influence on the Ru:Pt ratio assessable by XPS (Table 3.1), showing a strong Pt surface enrichment with increasing the heat treatment temperature.

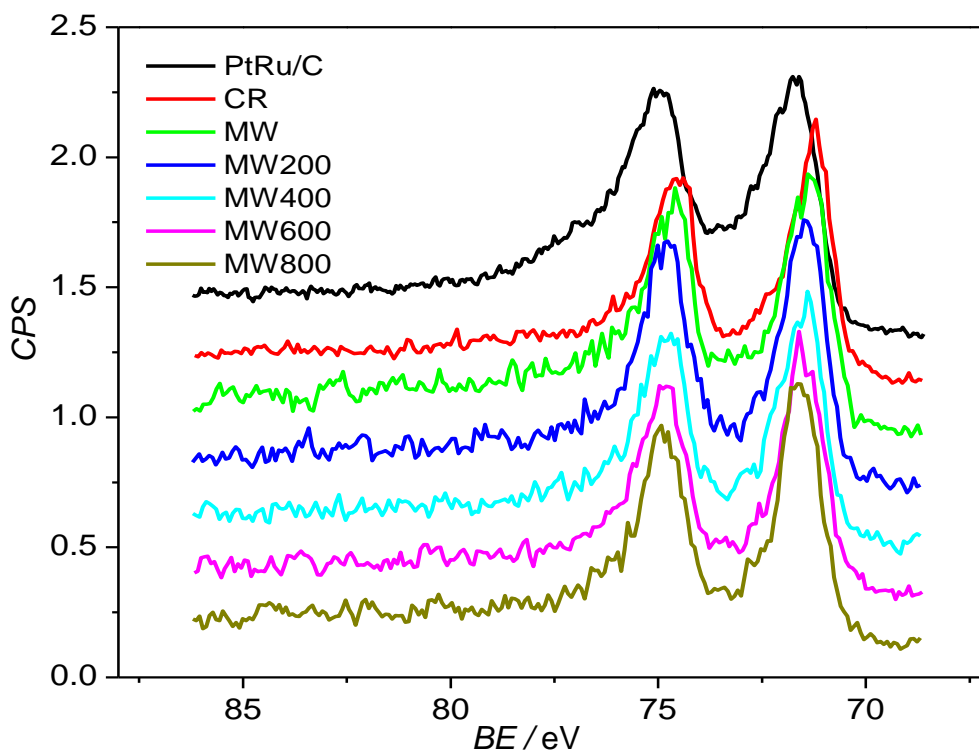


Figure 3.1: Pt 4f X-ray photoelectron spectra of PtRu/CNTs and PtRu/C catalysts.

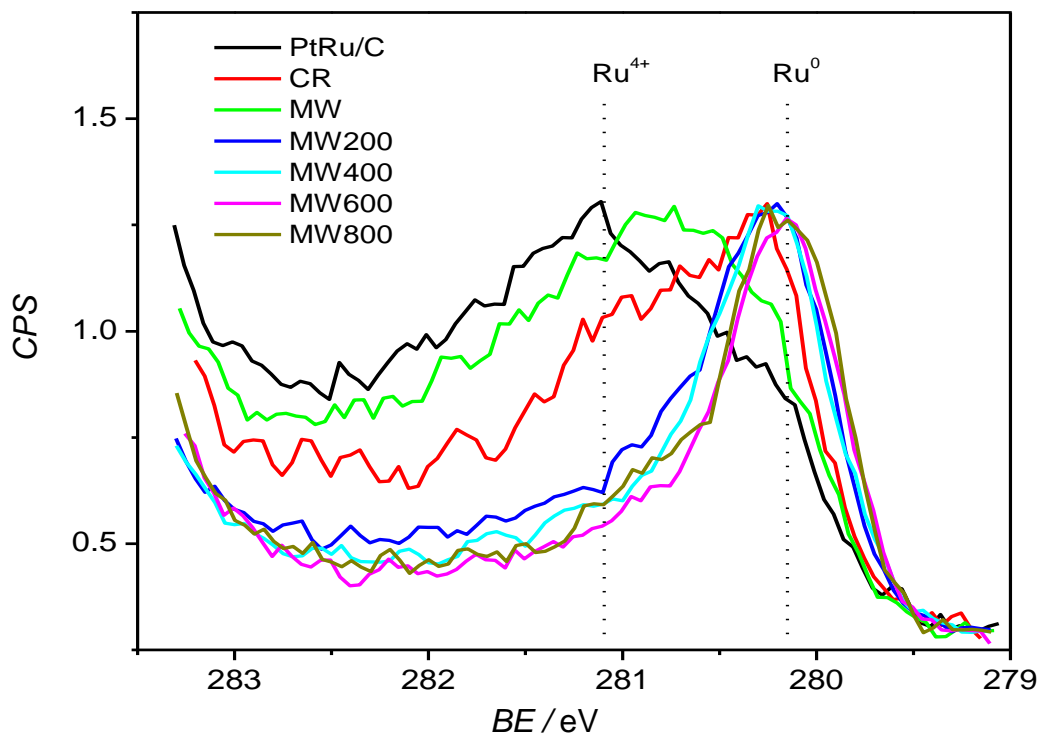


Figure 3.2: Ru 3d_{5/2} photoelectron lines of PtRu/CNTs and PtRu/C catalysts.

Table 3.1: Ru: Pt and Ru⁴⁺ : Ru⁰ ratios as seen by XPS

Catalysts	PtRu/C	CR	MW	MW200	MW 400	MW600	MW800
Ru:Pt	0.28	0.22	0.19	0.22	0.19	0.18	0.15
Ru ⁴⁺ : Ru ⁰	5.5	0.63	1.65	-	-	-	-

3.3.1.2 X-ray Absorption Fine Structure Spectroscopy

RuK edge XANES and the k^1 weighted Fourier transformed EXAFS function are presented in Figure 3.3 and Figure 3.4 correspondingly. The main distinctive feature of RuK XANES is the post-edge structure, consisting of two peaks in case of metallic ruthenium and one broad flat peak for RuO₂. The XANES spectra of commercial PtRu/C and both non heat treated samples reproduce mostly that of ruthenium oxide. Only slight humps at ca. 22142 eV and 22156 eV give hints on the presence of Ru in the metallic state. However XANES spectra of the samples heated in reducing atmosphere after synthesis represent the structure of metallic ruthenium. Additionally, the absorption edge shifts gradually towards lower energies with increasing heat treatment temperature indicating lower oxidation state. The environment of Ru in PtRu/CNTs CR and PtRu/CNTs MW samples is mainly similar – both are represented by two scattering events at 1.5 Å (oxygen) and at 2.3 Å (Ru, distances are uncorrected). However Ru-Ru peak intensity is much stronger in case of the PtRu/CNTs CR sample. PtRu/C in contrast has a lower Ru-O scattering path as seen in the EXAFS spectrum. There is a low shoulder at 2.37 Å presumably representing Ru-Ru backscattering event and relatively higher peak at 2.83 Å (all distances uncorrected). In the EXAFS spectra of the heat treated samples the well separated peak for of light backscattering event remains as a shoulder with intensity decreasing with increasing treatment temperature. The EXAFS structure is now represented by a strong peak at ca. 2.42 Å which coincides with the Ru-Ru scattering event in the Ru metal reference spectrum. Additionally, there are two lower shoulders developing at 2.06 and 2.76 Å (uncorrected) indicating the presence of platinum in coordination to ruthenium.

The PtL₃ XANES of the catalysts differ only slightly from that of the platinum foil (Figure 3.5). The first intense feature (white line, WL) of PtRu/CNTs CR and PtRu/CNTs MW samples resembles the white line of the Pt, only slightly shifted to higher energies. The latter can be ascribed to the small size of the platinum particles. The commercial PtRu/C sample catalyst shows a higher WL which does, however, not reach the height of a Pt⁴⁺ reference (Figure S13.2). PtRu/CNTs MW200, 400 and 800 samples have a slightly higher WL as compared to platinum foil. The more intense white line may indicate that platinum in the catalyst is oxidized to some extent, however, an electronic effect of alloy formation can also enhance the white line: C.-J. Zhong and coauthors [46] report minor white line intensifications for both PtNi/C and PtCo/C systems, which was attributed to the decrease of 5d orbital filling in platinum alloys

due to its hybridization with 3d states of the other transition metal. As ruthenium is largely oxidized in the commercial PtRu/C catalyst, we assign the intense PtL₃ white line to the presence of Pt ions in agreement with the XPS results. The XANES of PtRu/CNTs MW600 does not comply with the general trend of both the XAFS and the XPS results – its white line has the same intensity and position as those of the PtRu/CNTs CR and PtRu/CNTs MW samples. The Fourier transformed EXAFS spectra (Figure 3.6) are represented by a double headed peak in the 1.77 – 3.31 Å region. Its shape at the first sight resembles the shape of the first scattering peak of the platinum foil, which arises from the wave-length dependence of the Pt scattering cross section. However, with increasing treatment temperature, the ratio between the two features changes significantly, which shows that the low-distance maximum represents a lighter scatterer as well. At the highest reduction temperature, the two features are of comparable intensity. In the spectra of PtRu/CNTs MW200, PtRu/CNTs MW400 and PtRu/CNTs MW600, the scattering event at higher distance has an asymmetrical shape, pointing out that there is another element but platinum presented in first coordination shell. Opposite to expectations, the asymmetry decreases with increasing reduction temperature and is almost absent in PtRu/CNTs MW800. In the k-space EXAFS spectrum $\chi(k)$ (Figure SI3.3), phase shifts, which are most pronounced in PtRu/CNTs MW800, are obvious. This clearly indicates the presence of heteroatoms in the first coordination shell of Pt, i.e. alloy formation. The EXAFS spectrum of commercial PtRu/C is represented by three well separated peaks. The one at 1.68 Å is relatively stronger as compared to the other samples and the metallic peaks at 2.18 and 2.79 Å (all distances are uncorrected for phase shift), which confirms previous conclusions on a higher oxidation state of platinum.

Using the procedures suggested by B.-J. Hwang and co-authors, the atomic distribution and the alloying extent within the particles can be calculated from EXAFS [47]. First, pairing factors were calculated for both platinum and ruthenium, which are defined as: $P_{Pt} = CN_{Pt-Ru} / (CN_{Pt-Ru} + CN_{Pt-Pt})$ and $P_{Ru} = CN_{Ru-Pt} / (CN_{Ru-Pt} + CN_{Ru-Ru})$, where CN_{i-j} are coordination numbers of element j in the first coordination sphere of element i obtained from EXAFS fits. Pairing factors are the probability of an atom of one type to bind to an atom of the other type. The higher pairing factor for the given element highlights thus its better distribution within a nanoparticle. Dividing pairing factors observed by the pairing factors calculated for the ideally alloyed particles, one obtains the alloying extents for each particular alloy component: $J_i = P_{i,observed} / P_{i,random} \cdot 100 \%$. EXAFS fit results, pairing factors and alloying extents are presented in Table 3.2 for both RuK and PtL₃ edges. Apart from PtRu/CNTs CR and PtRu/CNTs MW samples where heteroatomic interactions could not be detected using EXAFS fitting, all other samples represent homophilic structure with atoms of the same type tending to agglomerate within one nanoparticle.

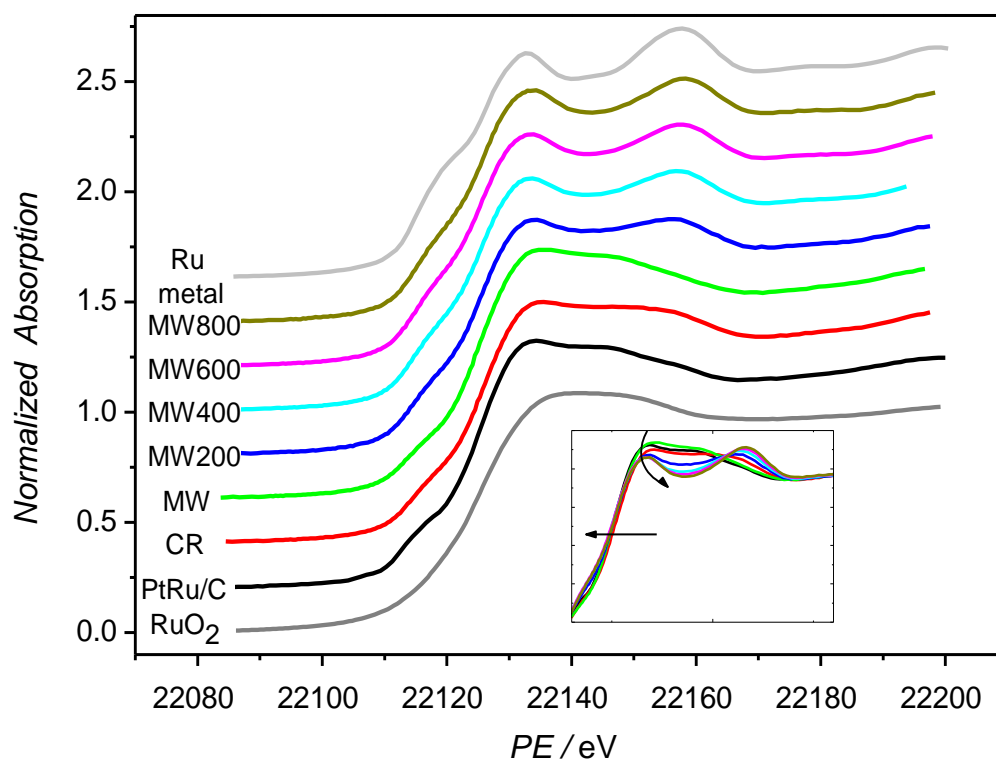


Figure 3.3: RuK XANES spectra of PtRu/CNTs, PtRu/C catalysts and Ru metal and RuO₂ as reference.

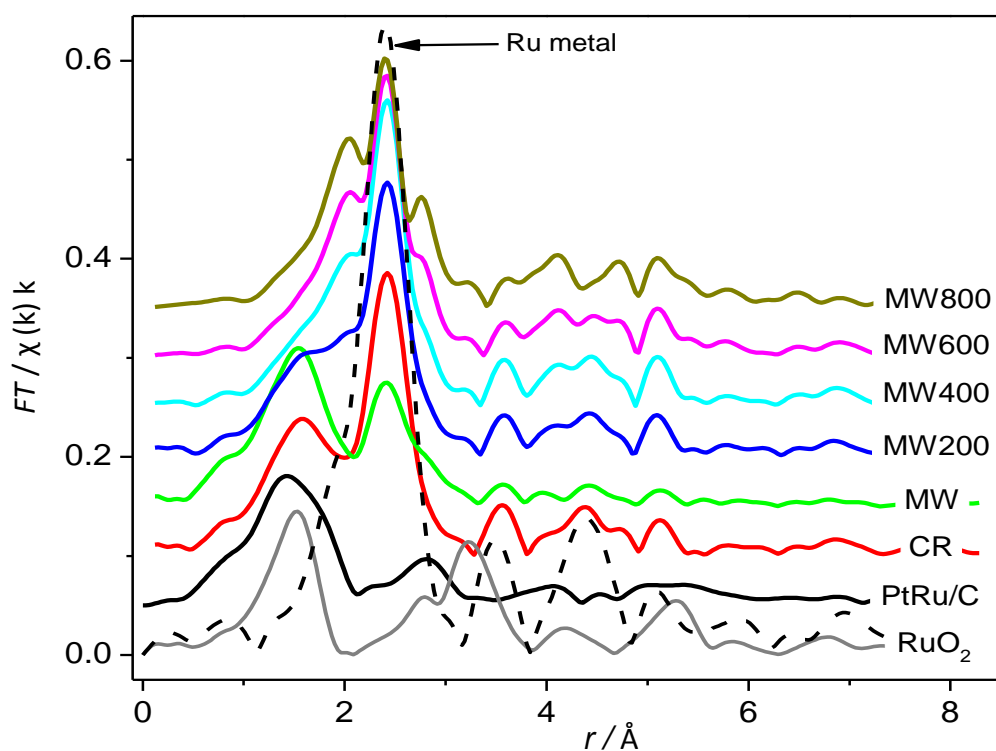


Figure 3.4: RuK FT-EXAFS spectra of PtRu/CNTs, PtRu/C catalysts and Ru metal and RuO₂ as references.

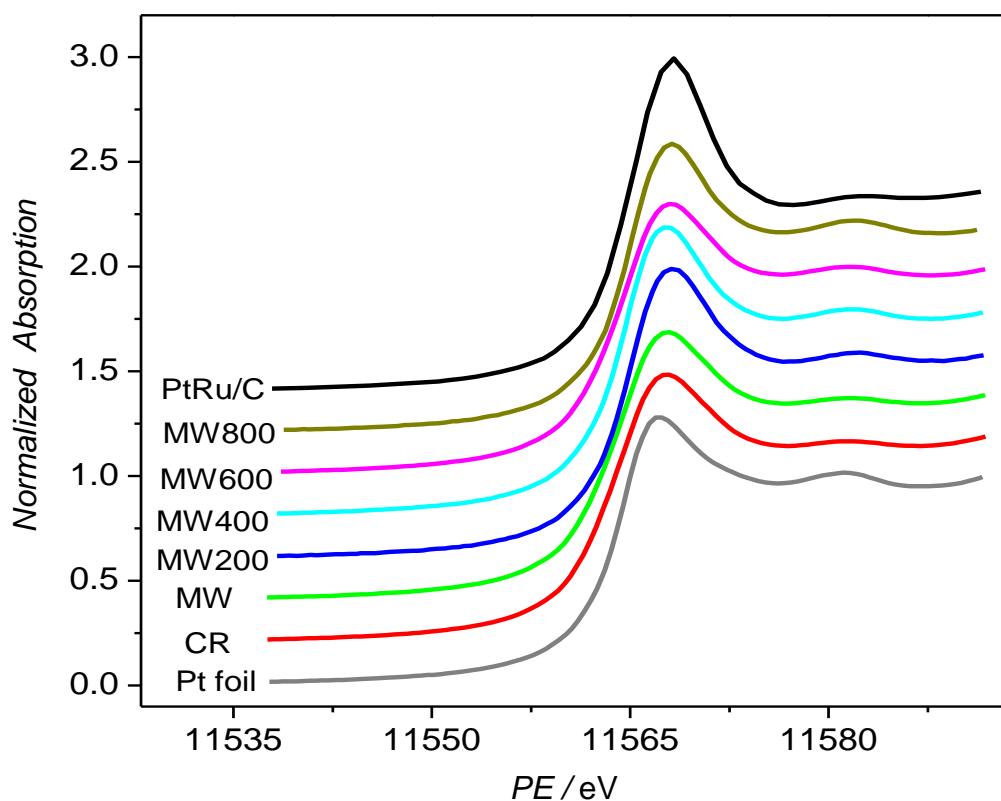


Figure 3. 5: Pt_L₃ XANES spectra of PtRu/CNTs, PtRu/C catalysts and Pt foil as reference.

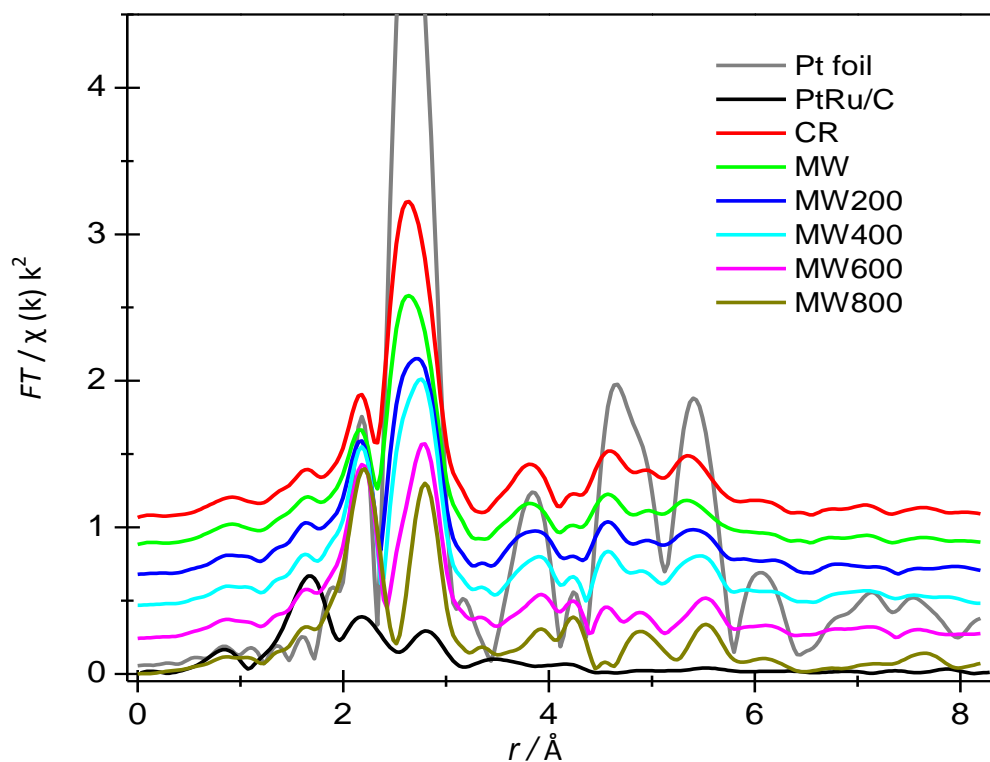


Figure 3.6: Pt_L₃ FT-EXAFS spectra of PtRu/CNTs, PtRu/C catalysts and Pt foil as reference.

Chapter 3: Structural Characterization and Performance of PtRu/CNTs in DMFCs

Table 3.2: EXAFS fit results together with paring factors and alloying extents for PtRu/CNTs and PtRu/C catalysts.

Catalysts	PtRu/C	CR	MW	MW200	MW 400	MW600	MW800
<i>PtL₃ edge</i>							
CN _{Pt-Ru}	1.0	-	-	1.3	1.8	2.1	2.7
CN _{Pt-i} *	3.7	8.5	6.3	7.9	8.1	7.8	8.2
P _{Pt, observed}	0.28	-	-	0.16	0.23	0.27	0.33
J _{Pt} **	56.5	-	-	32.8	45.1	54.8	66.4
<i>RuK edge</i>							
CN _{Ru-Pt}	4.9	-	-	1.5	2.8	4.3	3.3
CN _{Ru-i} *	7.6	5.2	2.5	8.2	10.3	11.5	11.1
P _{Ru, observed}	0.56	-	-	0.18	0.27	0.38	0.30
J _{Ru} **	130	-	-	35.5	53.5	75.3	59.5

* only metallic contributions included

** $J_{random} = 0.5$ (Pt:Ru = 1 : 1 ordered alloy)

3.3.2 Electrochemical characterization and fuel cell tests

Figure 3.7 shows voltammograms of PtRu/C and PtRu/CNTs (as prepared and heat treated at different temperature) in 0.5 M H₂SO₄ at scan rate 50 mV s⁻¹ before and after MOR. The CVs are similar to those reported in the literature for PtRu/C catalysts [25,48]. Characteristic surface features are the broad peak for hydrogen adsorption-desorption, a broad peak for oxide reduction at lower potentials and higher currents in the double layer region [25,48]. Minor difference are found for the PtRu commercial catalyst which more closely resembles that of a Pt surface, probably indicating the higher dissolution rate of Ru in the commercial catalyst compared to PtRu/CNTs.

After MOR all catalysts display a CV characteristic for a Pt surface with well-defined peaks in the hydrogen underpotential deposition (H_{upd}) region and strong peaks for oxide formation and reduction, indicating that during potential cycling under methanol oxidation Ru is lost from the surface and/or surface restructuring towards a Pt enriched surface occurs. The Pt characteristics are more pronounced in the commercial and the as-prepared catalyst, PtRu/CNTs MW. The decrease in current in the double layer region for the heat treated catalysts is lower compared to the commercial and the as-prepared catalyst. Keeping in mind the higher degree of alloying in these catalysts it can be suspected that during methanol oxidation by potential cycling in acid environment structure forms where a Pt enriched surrounds a PtRu alloy in the core.

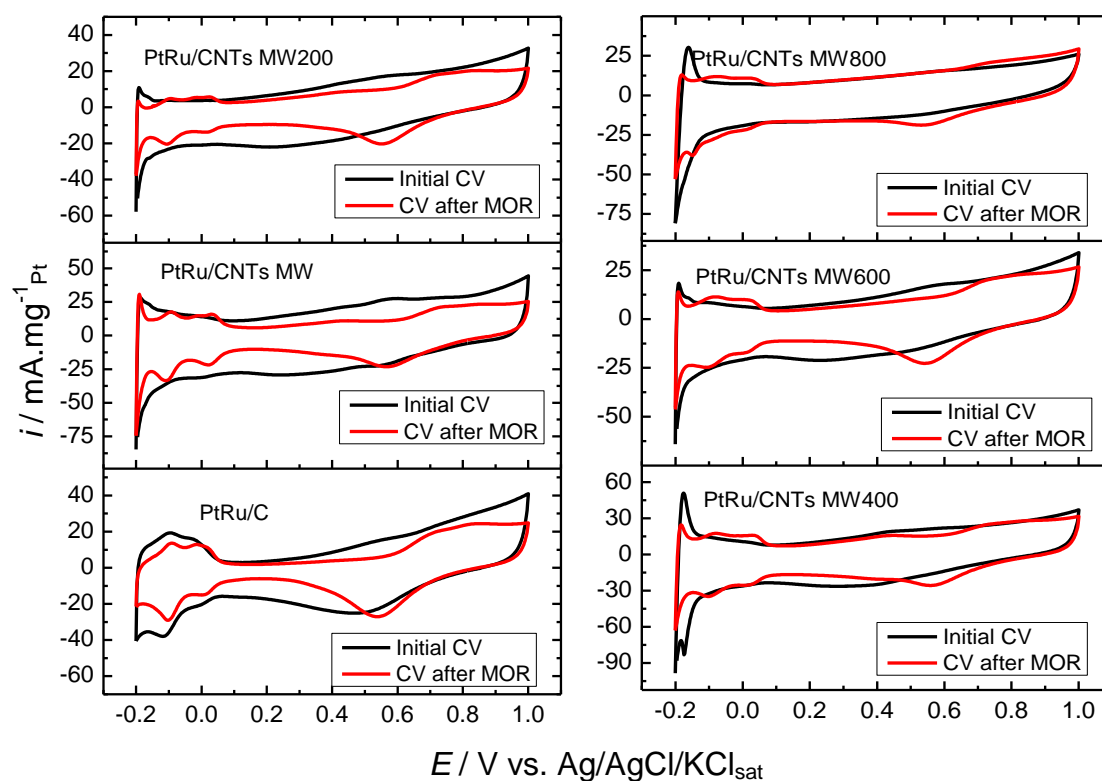


Figure 3.7: CV of PtRu/CNTs and PtRu/C catalysts in 0.5 M H_2SO_4 , scan rate 50 mV s^{-1} .

The catalytic activity for MOR was tested for all catalysts by chronoamperometry at a fixed potential of 0.7 V vs. SSC in 1 M $\text{CH}_3\text{OH}/0.5 \text{ M H}_2\text{SO}_4$ for 1 h for both the electrodes treated electrochemically for 50 cycles in 0.5 M H_2SO_4 and those cycled in MeOH containing electrolyte solution. The results are shown in Figure 3.8A and B. The catalytic activity of the fresh electrodes (initial CA measurements) depends on the extent of Pt surface available where PtRu/C with more strongly expressed Pt features (CVs Figure 3.7) shows higher catalytic activity. For the heat treated catalysts, with increase of heat treatment temperature the catalytic activity increase as a result of increasing Pt sites availability (see XPS PtRu atomic ratio, Table 3.1). On the other hand, PtRu/CNTs MW as-prepared exhibits higher activity than the catalyst PtRu/CNTs MW200 and PtRu/CNTs MW400, probably attributable to fast dissolution of Ru species and liberation of Pt sites for MOR during testing [25].

Importantly, Figure 3.8B shows that the catalytic activity for all catalysts is significantly enhanced after potential cycling in $\text{CH}_3\text{OH}/\text{H}_2\text{SO}_4$ solution with PtRu/CNTs MW800 showing only slight enhancement. The PtRu/C commercial catalyst and PtRu/CNTs MW600 show almost similar activity which is the highest among all catalysts. These results are in good agreement with cyclic voltammetry studies shown in our previous work [29]. However while the commercial catalyst shows highest activity in the beginning of potential cycling, variation of activity with cycle number

indicated a slight increase in current for all prepared catalysts (except PtRu/CNTs MW800 which showed almost constant activity with cycling) whereas the commercial catalyst lost activity with potential cycling [29]. In the present study, the activity was evaluated from the steady state current for the initial CA and for CA after MOR. An enhancement factor was extracted by dividing the mass current for CA after MOR (I_a) by the mass current for the initial CA measurements at the steady state (I_i). The data is shown in Table 3.3.

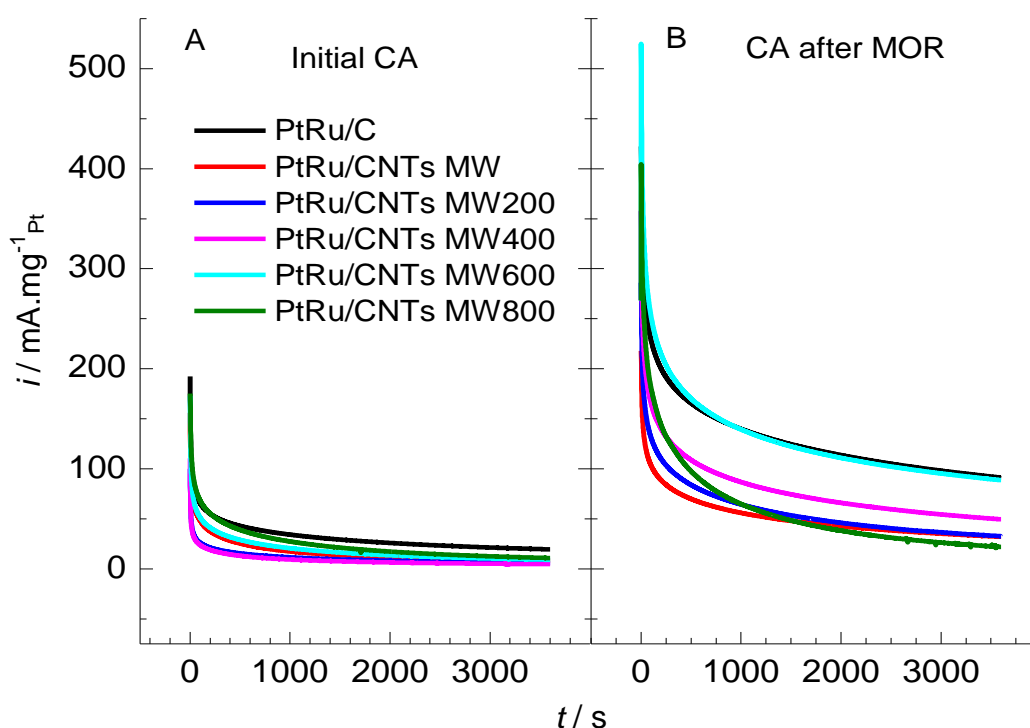


Figure 3.8: CA of PtRu/CNTs and PtRu/C catalysts at 0.7 V in 1M CH₃OH/0.5 M H₂SO₄. A) initial electrode, B) after MOR for 100 cycles in the same solution.

Three catalysts have been selected for further evaluation in single direct methanol fuel cell tests: the commercial PtRu/C catalyst, the as prepared PtRu/CNTs MW catalyst and the catalyst heat treated at 600 °C; PtRu/CNTs MW600. Before presenting the results of direct methanol fuel cells, the voltammetric behaviour in half cell tests of these selected catalysts in 1 M CH₃OH/0.5 M H₂SO₄ before and after potential cycling will be demonstrated, as shown in Figure 3.9 [29]. The behaviour of the catalyst at cycle number 20, at which the catalyst reaches its steady state, and the behaviour at cycle number 100 are compared. The deterioration of activity is more pronounced in the commercial catalyst and the as-prepared sample whereas the heat treated catalyst shows significant stability and enhanced activity for MOR after potential cycling. To quantitative this behaviour, the mass specific current at 0.5 V (i.e., close to the onset potential) and at the peak potential was extracted. The results are represented

Chapter 3: Structural Characterization and Performance of PtRu/CNTs in DMFCs

graphically in Figure 3.9D and E. The enhanced activity and stability of the heat treated catalyst are clearly seen.

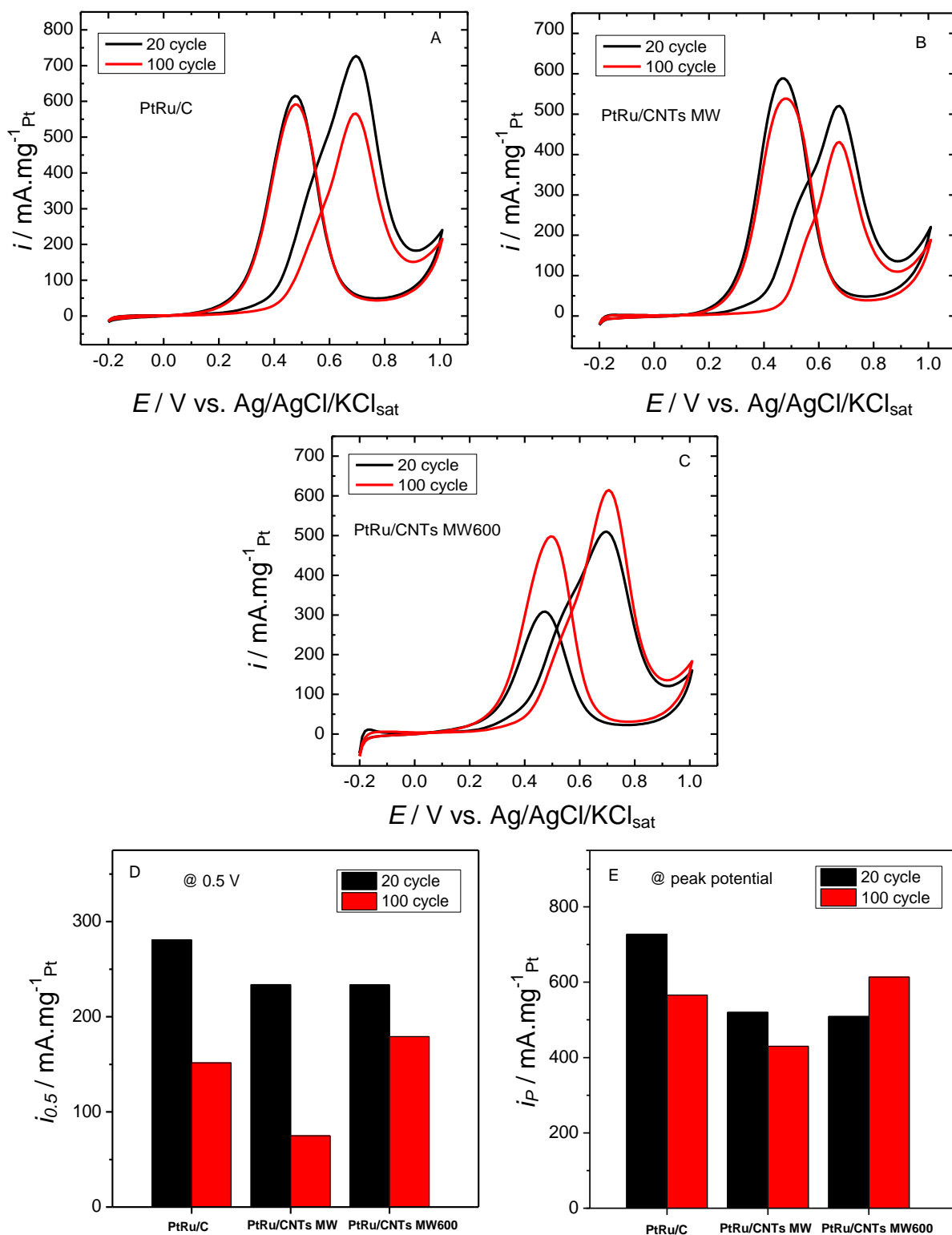


Figure 3.9: CV of PtRu/CNTs and PtRu/C catalysts in 1 M $\text{CH}_3\text{OH}/0.5$ M H_2SO_4 (A,B,C) and variation of the mass current at cycles number 20 and 100 extracted at 0.5 V D) and at peak potential E).

Chapter 3: Structural Characterization and Performance of PtRu/CNTs in DMFCs

Table 3.3: Electrochemical activity evaluated from chronoamperometry measurements

Catalysts	steady state current	steady state current	Enhancement Factor (I_a/I_i)
	$\text{mA} \cdot \text{mg}_{\text{Pt}}^{-1}$	$\text{mA} \cdot \text{mg}_{\text{Pt}}^{-1}$	
	Initial CA	CA after MOR	
PtRu/C	19.4	91.20	4.7
PtRu MW	08.3	32.00	3.8
PtRu MW200	05.9	32.60	5.4
PtRu MW400	04.6	49.50	10.7
PtRu MW600	09.1	88.60	9.7
PtRu MW800	10.8	21.85	2.0

For direct methanol fuel cells measurements, three membranes electrode assemblies (MEAs) were fabricated from the selected catalysts, PtRu/C, PtRu/CNTs MW and PtRu/CNTs MW600 and the MEAs hereafter called MEA1, MEA2 and MEA3; respectively.

IR corrected galvanostatic polarization curves for $\text{CH}_3\text{OH}/\text{H}_2$ and $\text{CH}_3\text{OH}/\text{O}_2$ for the three MEAs are presented in Figure 3.10 and 3.11. For $\text{CH}_3\text{OH}/\text{H}_2$ measurements before and after the durability test, the trend in performance in the activation region is $\text{MEA2} > \text{MEA3} > \text{MEA1}$. Although there are only marginal differences before durability, the differences after durability are more significant. From the CVs in Figure 3.9 a different order of activity would have been expected. However, CV measurements of the MEAs (Figure 3.12) indicate that the better performance of MEA2 is due to larger electrochemical surface area (ECA). It is noted that the MEA2 and MEA3 exhibited higher loss at higher current region (the mass transfer region).

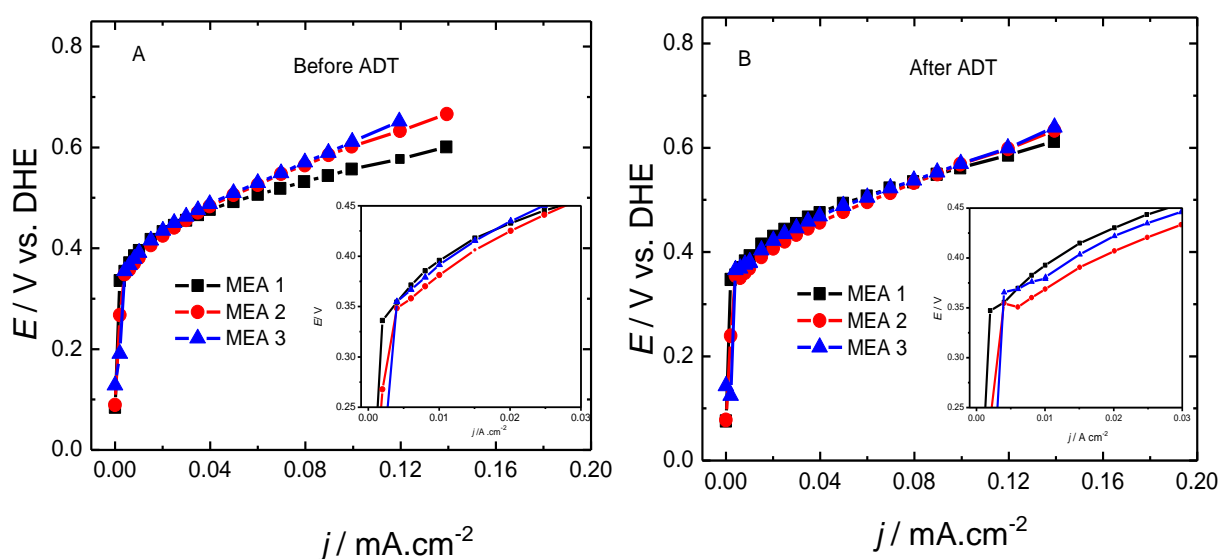


Figure 3.10: IR corrected $\text{CH}_3\text{OH}/\text{H}_2$ polarization curves for MEA1, MEA 2 and MEA 3 A) before and B) after ADT.

The direct methanol fuel cell performance ($\text{CH}_3\text{OH}/\text{O}_2$ mode) before and after accelerated durability test (ADT) for all MEAs is shown in Figure 3.11, where IR corrected polarization (I-V) curves are displayed. During the initial test (Figure 3.11A), MEA2 and MEA3 provide a higher OCV of 0.785 V and 0.780 V, respectively, whereas MEA1 shows an OCV of 0.707 V. Importantly, in the activation region, MEA2 shows the highest activity among all MEAs, in agreement with the results of $\text{CH}_3\text{OH}/\text{H}_2$ mode. Again, at higher current density region, i.e. in the mass transfer-controlled region, MEA2 and MEA3 exhibit also lower activity than MEA1, similar to the $\text{CH}_3\text{OH}/\text{H}_2$ mode and probably a result of the higher thickness of the anode catalyst layers of MEA2 and MEA3 [49].

After ADT, the MEA2 shows a slightly decrease in the OCV (0.770 V) which is still higher than that of MEA1 which shows a non-significant improvement (0.715 V) after ADT. The OCV of MEA3 after ADT is 0.710 which is close to MEA1 (Figure 3.11B). However, Figures SI3.5A, B and C demonstrate that after ADT the activity of MEA1 is deteriorated to a higher extent than in MEA2 whereas the MEA3 shows improvement in its activity, in agreement with the above CV measurements. For quantitative evaluation, the current density at two voltages (0.4 and 0.3 V) is determined for all MEAs before and after ADT. Also, a relative performance factor defined as the current density after ADT related to the one before ADT at a specific voltage is extracted (see Figures 3.11C and D). MEA1 retained a 57.5 % and 65.3 % of its initial activity after ADT at 0.4 and 0.3 V, respectively. MEA2 retrained 82.1 % and 89.3 % whereas the MEA3 exhibited an improvement in the current density after ADT with additional 43.5 % and 27.8 % of its initial activity at 0.4 and 0.3 V, respectively. In Summary, in line with earlier CV measurements [29] higher activity and stability of MEAs fabricated from the prepared catalyst with the highest stability for the heat treated sample can be observed compared to the commercial catalyst despite its exhibited higher activity in the initial performance (before ADT). To further access the behaviour of the catalysts and MEAs during fuel cell tests, in situ-CV were recorded for all MEAs as shown in Figure SI3.4. After ADT the hydrogen adsorption desorption behaviour is shifted to higher potentials. This behaviour indicates the Ru dissolution under potential cycling and additional Pt surface liberation [12]. This shift is more pronounced in MEA2 which indicate that the Ru dissolution in MEA2 is faster than in the others MEAs.

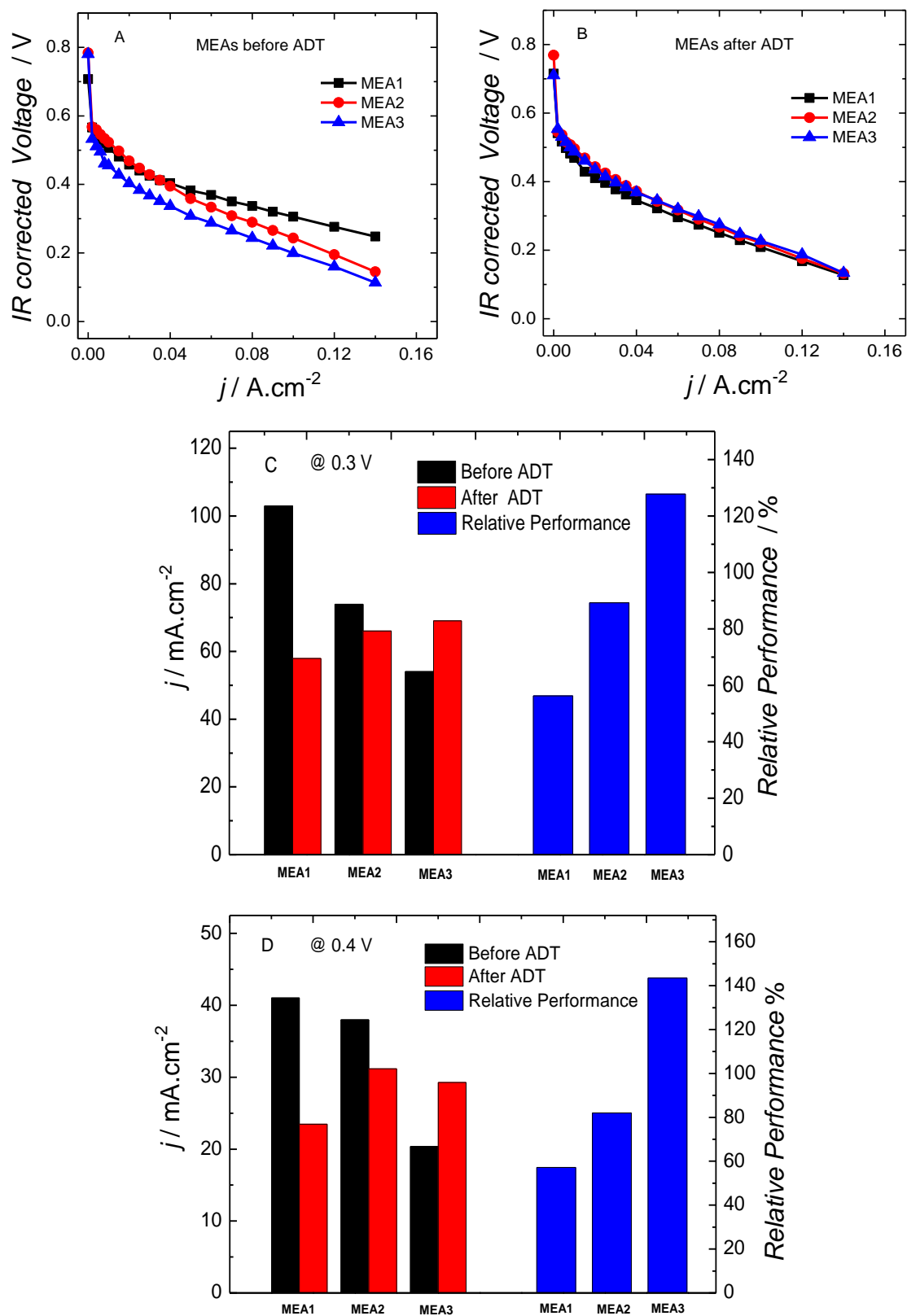


Figure 3.11: *i*-V performance curves for MEAs in direct methanol fuel cell A) before and B) after ADT, and performance and relative performance of MEAs at C) 0.3 V and at D) 0.4 V.

Still unexplained remains the higher loss for MEA2 and MEA3 at higher currents, where the performance is predominantly controlled by mass transport and ionomer resistance in the catalyst layer. At first sight, mass transport limitations at the anode might be responsible for this behaviour since the thicknesses of the catalyst layers are 8 μm , 63 μm and 51 μm for MEA1, MEA2 and MEA3 respectively. The large difference between the thicknesses is due to higher metal content and denser support material in the commercial catalyst as compared to the prepared catalysts. However, to further access this issue, Figure 3.13 shows the galvanostatic polarization curves for MEA1 and MEA2 after the durability test for the oxygen reduction reaction (ORR) obtained by subtracting the $\text{CH}_3\text{OH}/\text{H}_2$ curve from $\text{CH}_3\text{OH}/\text{O}_2$ curve. The ORR in DMFC is significantly influenced by the rate of CH_3OH crossover. It can be seen that the ORR for MEA1 and MEA2 are similar indicating that in both the MEAs the rate of crossover is similar. This also suggests that CH_3OH transport limitation must be similar in both MEAs. Thus the lower performance at higher current might be due catalyst layer resistance which is affected by the ionomer content. It is reported that the introduction of the optimum ionomer content into the catalyst layer can increase the three phase contact between reactants, electrolyte and the catalyst surface making the catalyst layer more active and facilitate the proton transport throughout the entire layer which finally would improve the cell performance especially in the high current region [50,51]. The ionomer used in all three electrodes was kept at 10 wt. % w.r.t catalyst. However due to the much higher thickness of the PtRu/CNT catalyst layers the ionomer continuity is likely to break more often than in case of the PtRu/C catalyst layer. This will result in higher losses especially in the high current region. Therefore the optimum ionomer content for PtRu/C and PtRu/CNT electrodes may not be similar due to large difference in catalyst layer thickness and it is desired to optimize the ionomer content for layers containing CNT-supported catalysts which should be taken into consideration in further studies.

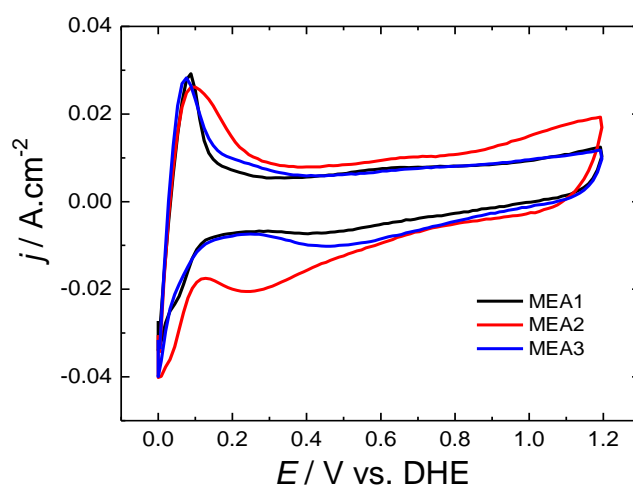


Figure 3.12: In situ CV curves for MEA1, MEA2 and MEA3 measured after ADT.

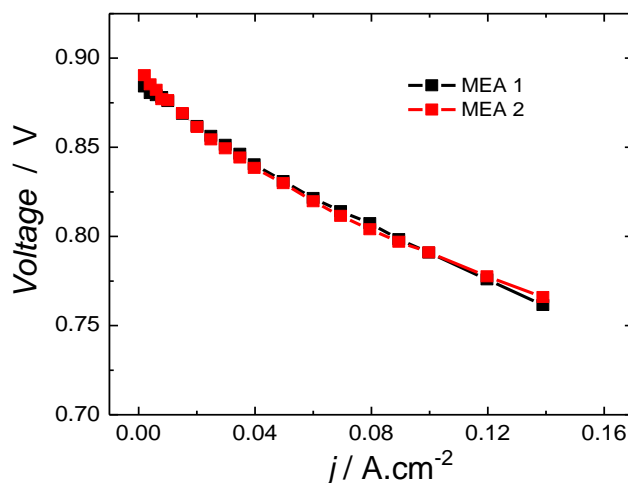


Figure 3.13: ORR polarization curves after ADT for MEA1 and MEA2 obtained by subtracting curves of $\text{CH}_3\text{OH}/\text{H}_2$ from $\text{CH}_3\text{OH}/\text{O}_2$.

Another technique suitable to access stability and degradation behaviour of MEAs is the electrochemical impedance spectroscopy (EIS). EIS of all MEAs before and after ADT is shown in Figure S13.6 in the form of Nyquist plots, displaying the typical semicircle. The tiny arc at lower frequency with formation of an inductive loop is corresponding to the oxidation of methanol intermediates, mainly (CO_{ads}), at higher potential [12,52]. The intercept of the real axis at higher frequency is corresponding to the bulk ohmic resistance (R_{ohm}) which is the sum of the ionic and electronic resistance of the cell components, i.e. in case of negligible electronic resistance it refers only to membrane resistance (R_{M}) [53]. The difference between the real axis intercept values at the higher and lower frequency of the arc is corresponding to the charge transfer resistance (R_{ct}) [54,55]. The R_{M} for MEA1 increased to some extent after ADT whereas the R_{M} for MEA2 and MEA3 was stable with no change after ADT. The increase of membrane resistance (R_{M}) in MEA1 could be attributed to the enhanced contact resistance between GDL and catalyst layer or between catalyst layer and membrane or to the higher Ru dissolution in the catalyst layer [12]. The most important observation is that the charge transfer resistance (R_{ct}) for the MEA1 and MEA2 is increased to some extent after ADT with higher increase in MEA1 indicating poorer methanol oxidation kinetics. This might be a result of higher Ru dissolution in MEA1 and MEA2 resulting from potential cycling whereas the R_{ct} for MEA3 shows a non-significant increase after ADT which confirms the good stability of the catalyst in MEA3 and enhancement of methanol oxidation kinetics even after the ADT, in agreement with results presented above.

In general, the results of electrochemical investigation of the MEAs in $\text{CH}_3\text{OH}/\text{O}_2$ and $\text{CH}_3\text{OH}/\text{H}_2$ modes demonstrate the higher activity of MEA2 and MEA3 fabricated

from the as-prepared and the heat treated catalyst; respectively, compared to MEA1 prepared from the commercial catalyst, with highest long term stability for the MEA3.

3.4 Discussion

The structural changes observed after heat treatment and during electrochemical experiments shall in the following be correlated with the performance (activity and stability) of the catalysts. Earlier investigations by XRD done to evaluate catalyst synthesis [29] already demonstrated increasing alloying with increasing heat treatment temperature. XPS and XAS studies shed additional light onto this issue. In XPS analysis, a notable fact is that the Ru $3d_{5/2}$ maximum is shifted to lower binding energies whereas the Pt 4f lines shift to higher energies as the post treatment temperature rises. These results differ from expectations for alloys based on the general assumption that XPS shifts follow the electronegativity of elements. Platinum has an electronegativity of 2.28 on the Pauling scale whereas ruthenium has 2.2. The shift to higher energies of the Pt 4f lines could be explained by the lowering of the Fermi level energy in PtRu based on rigid band theory where the energy is related to the total number of electron. According to their positions in the periodic table, the filling up of electrons in Pt is higher than Ru, i.e. a higher deficiency of electrons in Ru, and therefore when Pt is alloyed with Ru, the total number of electrons in Pt is reduced resulting in a lowering of the Fermi level energy [56]. Thus the shifts can be explained by the increasing alloying extent. According to BE shifts the alloying extent increases from PtRu/CNTs CR and PtRu/CNTs MW samples, where it is barely distinguished, to the PtRu/CNTs MW800 sample.

XAFS results support alloy formation in the heat treated catalysts. The calculation of atomic distribution and alloying extent from EXAFS spectra fitting additionally indicate a higher total CN for Ru, indicating thus a core-shell structure with a Ru-enriched core. This observation is also supported by XPS data which shows gradually increasing Pt surface enrichment with increasing post treatment temperature. These observations reveal that the heat treatment is an important step in the preparation of PtRu catalyst with alloy structure. It is remarkable that the PtRu/CNTs MW600 sample was found to have the lowest total platinum coordination number while it exhibits the highest degree of Ru alloying of 75.3. These two observations indicate the thinner Pt skin and the well-alloyed Ru-rich core as compared to the other catalysts.

The mechanism of formation of such structures could be summarised as follows. During preparation, where an ethanol/water mixture is used as reducing agent, hydrous RuO_x is expected to be formed initially by water hydrolysis of $RuCl_3$, and will not be reduced completely into metallic Ru under microwave heating (maximum temperature (85 °C) [26,29]. Thus, catalyst with higher content of RuO_2 , predominately on the surface, is produced as confirmed from both XPS and XAFS results. Upon heat

treatment at higher temperature under hydrogen atmosphere, the Ru oxide is reduced into metallic Ru which migrates into the bulk of the particle forming a true alloy of PtRu with a Pt enriched surface [37,57].

Besides the initial structures formed, under electrochemical conditions the catalyst undergoes further dynamic changes. The commercial and the as prepared catalyst lose their activities with increasing potential cycle numbers (Fig. 3.9) probably indicating dissolution of Ru (oxides). On the other hand, the heat treated samples show good stability under electrochemical conditions attributed to the more stable PtRu alloy protected by a Pt rich shell. Indeed, CA measurements demonstrate an enhancement of activity and stability of the heat treated catalysts after MOR compared to the commercial one.

In fuel cell tests the as prepared (PtRu/CNTs MW) and heat treated (PtRu/CNTs MW600) catalysts show good stability with higher stability and enhanced activity for the heat treated sample although it displays lower initial performance compared to the commercial catalyst (PtRu/C) (Figure 3.11). Also, EIS measurements indicate the lower degradation behaviour of the as-prepared and heat treated catalysts. Comparing the activity and stability for all catalysts in the three electrode cell (CV and CA measurements) with fuel cell test results, the commercial and the heat treated catalyst show the same behaviour. However, the as-prepared catalyst shows higher deterioration in its activity and stability particularly at lower potentials (Figure 3.9) in half cell measurements. These differences in activity and stability are due to the difference in the potential range used for the durability test in fuel cells and in three electrode set up. However, in both cases the potentials are higher than 0.8 V (vs. RHE); the potential until which metallic Ru is expected to be stable [58]. Thus, the dissolution of Ru is expected in both fuel cells and three electrode cells [18,59]. We assume that Ru dissolution and catalyst degradation also take place in MEA2 in the fuel cell setup, however at a much smaller rate [59].

In summary, the higher stability for the heat treated catalyst in both fuel cell set up and three electrodes set up is attributed to the favourable catalyst structure, where a well-alloyed PtRu core is surrounded (and protected) by a Pt rich shell, while oxidic Ru in the outer catalyst layers or less well alloyed Ru tend to dissolve more quickly, leading to faster catalyst degradation. Formation of a thin Pt-rich shell surrounding the PtRu alloy core under electrochemical conditions by Ru dissolution further enhances activity as evidenced from 3-electrode-setup- and fuel cell tests, maintaining the effect of Ru as promoter for MOR [60].

Figure 3.14 shows a plausible model for the structure of initially prepared catalyst followed by heat treatment (XPS evidences Pt shell formation, XAS evidences alloy formation) and finally electrochemical treatment (CV evidences formation of Pt-rich

surface) leading to the Pt enriched shell with a PtRu core, which has, as demonstrated from CV and fuel cell tests, the highest activity among the catalyst.

Elucidation of the structural change in PtRu catalysts under fuel cell operation conditions however still would benefit from in situ-studies, such as in situ-XAFS and in situ-CO stripping voltammetry, which may also shed light on additional influences on stability/activity like particle sizes and particle agglomeration.

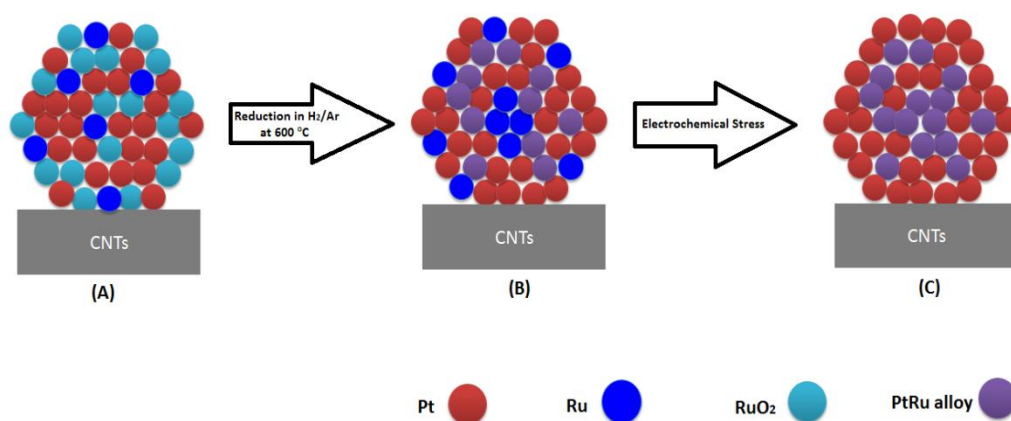


Figure 3.14: Proposed model for the as-prepared PtRu/CNTs (A), the heat treated catalysts (B) and the heat treated catalyst under electrochemical stress (C).

3.5 Conclusion

CNT-supported PtRu catalysts prepared by microwave heating initially are formed mainly as bimetallic sample without any alloy formation but with RuO₂ as the main phase of Ru. Upon heat treatment in reductive atmosphere, a PtRu alloy is formed with a Pt enriched surface and the amount of Pt on the surface increase with increasing heat treatment temperature as evidence of both XPS and XAFS results. The latter, together with earlier XRD investigations, confirms that Ru in the heat treated samples is alloyed with Pt. Compared to a commercial PtRu/C catalyst, the prepared catalysts and in particular the heat treated samples show higher activity and stability in both electrochemical testing (CV and CA) and in direct methanol fuel cells after durability test. The higher stability gained by the heat treatment results from the formation of a PtRu alloy which is supposed to be the more stable structure under electrochemical stress compared to the non-alloyed catalysts or the commercial sample. The deterioration of catalytic activity in both commercial and non-alloyed catalysts has been suggested to result from the dissolution of RuO₂, the less-stable form of Ru in an acid environment. Higher stability concurrently with high activity is achieved with PtRu alloys, which are surrounded by a thin Pt shell as a result from

Chapter 3: Structural Characterization and Performance of PtRu/CNTs in DMFCs

segregation during heat treatment and electrochemical stress. To fully access the dynamic catalyst behaviour in situ, further studies are required to established structural changes under fuel cell operation conditions in this system and gain more information about the dissolution process of Ru which will be the subject of our next studies.

References

- [1] W. Yu, M.D. Porosoff, J.G. Chen, *Chem. Rev.* 112 (2012) 5780.
- [2] C. Koenigsmann, S.S. Wong, *Energy Environ. Sci.* 4 (2011) 1161.
- [3] X. Zhao, M. Yin, L. Ma, L. Liang, C. Liu, J. Liao, T. Lu, W. Xing, *Energy Environ. Sci.* 4 (2011) 2736.
- [4] N.C. Bagkar, H.M. Chen, H. Parab, R.-S. Liu, in: H. Liu, J. Zhang (Eds.), *Electrocatalysis of Direct Methanol Fuel Cells: From Fundamentals to Applications*, Wiley-VCH, 2009, pp. 79-114.
- [5] N.V. Long, Y. Yang, C.M. Thi, N.V. Minh, Y. Cao, M. Nogami, *Nano Energy* 2 (2013) 636.
- [6] F. Taufany, C.-J. Pan, F.-J. Lai, H.-L. Chou, L.S. Sarma, J. Rick, J.-M. Lin, J.-F. Lee, M.-T. Tang, B.-J. Hwang, *Chem. Eur. J.* 19 (2013) 905.
- [7] A.S. Aricò, V. Baglio, V. Antonucci, in: H. Liu, J. Zhang (Eds.), *Electrocatalysis of Direct Methanol Fuel Cells: From Fundamentals to Applications*, Wiley-VCH, 2009, pp. 1-77.
- [8] J.C. Davis, B.E. Hayden, D.J. Pegg, *Electrochim. Acta* 44 (1998) 1181.
- [9] B.-J. Hwang, L.S. Sarma, C.-H. Chen, C. Bock, F.-J. Lai, S.-H. Chang, S.-C. Yen, D.-G. Liu, H.-S. Sheu, J.-F. Lee, *J. Phys. Chem. C* 112 (2008) 19922.
- [10] G.A. Camara, M.J. Giz, V.A. Paganin, E.A. Ticianelli, *J. Electroanal. Chem.* 537 (2002) 21.
- [11] S.K. Kamarudin, F. Achmada, W.R.W. Daud, *Int. J. Hydrogen Energy.* 34 (2009) 6902.
- [12] W. Chen, G. Sun, Z. Liang, Q. Mao, H. Li, G. Wang, Q. Xin, H. Chang, C. Pak, D. Seung, *J. Power Sources* 160 (2006) 933.
- [13] J. Guo, G. Sun, Z. Wu, S. Sun, S. Yan, L. Cao, Y. Yan, D. Su, Q. Xin, *J. Power Sources* 172 (2007) 666.
- [14] P. Joghee, S. Pylypenko, T. Olson, A. Dameron, A. Corpuz, H.N. Dinh, K. Wood, K. O'Neill, K. Hurst, G. Bender, T. Gennett, B. Pivovar, R. O'Hayre, *J. Electrochem. Soc.* 159 (2012) F768.
- [15] A.R. Corpuz, T.S. Olson, P. Joghee, S. Pylypenko, A.A. Dameron, H.N. Dinh, K. O'Neill, K.E. Hurst, G. Bender, T. Gennett, B.S. Pivovar, R.M. Richards, R.P. O'Hayre, *J. Power Sources* 217 (2012) 142.
- [16] P. Piela, C. Eickes, E. Brosha, F. Garzon, P. Zelenay, *J. Electrochem. Soc.* 151(2004) A2053.
- [17] Y. Chung, C. Pak, G.-S. Park, W.S. Jeon, J.-R. Kim, Y. Lee, H. Chang, D. Seung, *J. Phys. Chem. C* 112 (2008) 313.
- [18] E. Antolini, *J. Solid State Electrochem.* 15 (2011) 455.
- [19] M.K. Jeon, J.Y. Won, S.I. Woo, *Electrochem Solid State Lett* 10 (2007) B23.

- [20] R. Chetty, W.Xia, S. Kundu, M.Bron, T. Reinecke, W. Schuhmann, M. Muhler, *Langmuir* 25 (2009) 3853.
- [21] J.-H. Ma, Y.-Y. Feng, J. Yu, D. Zhao, B.-Q. Xu, *J. Catal.* 275 (2010) 34.
- [22] S.-Y. Huang, S.-M. Chang, C.-L. Lin, C.-H. Chen, C.-T. Yeh, *J. Phys. Chem. B* 110 (2006) 23300.
- [23] S.-Y. Huang, S.-M. Chang, K.-W. Wang, C.-T. Yeh, *ChemPhysChem* 8 (2007) 1774.
- [24] W. Wang, Y. Li, H. Wang, *Reac Kinet Mech Cat* 108 (2013) 433.
- [25] M.-S. Hyun, S.-K. Kim, B. Lee, D. Peck, Y. Shul, D. Jung, *Catal. Today* 132 (2008) 138.
- [26] K.-S. Lee, T.-Y. Jeon, S.J. Yoo, I.-S. Park, Y.-H. Cho, S.H. Kang, K.H. Choi, Y.-E. Sung, *Appl. Catal. B* 102 (2011) 334.
- [27] Y.-C. Wei, C.-W. Liu, K.-W. Wang, *ChemPhysChem* 10 (2009) 1230.
- [28] K.-H. Chang, C.-C. Hu, *J. Electrochem. Soc.* 151 (2004) A958.
- [29] A.B.A.A. Nassr, M. Bron, *ChemCatChem* 5 (2013) 1472.
- [30] R. Chetty, S. Kundu, W. Xia, M. Bron, W. Schuhmann, V. Chirila, W. Brandl, T. Reinecke, M. Muhler, *Electrochim. Acta* 54 (2009) 4208.
- [31] X. Li, J. Liu, Q. Huang, W. Vogel, D.L. Akins, H. Yang, *Electrochim. Acta* 56 (2010) 278.
- [32] Q. He, B. Shyam, M. Nishijima, X. Yang, B. Koel, F. Ernst, D. Ramaker, S. Mukerjee, *J. Phys. Chem. C* 117 (2013) 1457.
- [33] J. Tian, G. Sun, L. Jiang, S. Yan, Q. Mao, Q. Xin, *Electrochem. Comm.* 9 (2007) 563.
- [34] Y.-C. Wei, C.-W. Liu, W.-J. Chang, K.-W. Wang, *J. Alloy Compund.* 509 (2011) 535.
- [35] C.A. Menning, J.G. Chen, *J. Power Sources* 195 (2010) 3140.
- [36] T.J. Schmidt, M. Noeske, H.A. Gasteiger, R.J. Behm, P. Britz, H. Bönnemann, *J. Electrochem. Soc.* 145 (1998) 925.
- [37] G.A. Camara, M.J. Giz, V.A. Paganin, E.A. Ticianelli, *J. Electroanal. Chem.* 537 (2002) 21.
- [38] S. Doniach, M. Sunjic, *J. Phys. C: 3* (1970) 285.
- [39] K.V. Klementev, *J. Phys. D: 34* (2001) 209;
www.cells.es/Beamlines/CLAESS/software/viper.html.
- [40] A.L. Ankudinov, B. Ravel, J.J. Rehr, S.D. Conradson, *Phys. Rev. B: 58* (1998) 7565.
- [41] M.M. Bruno, A.A. Petruccelli, F.A. Viva, H.R. Corti, *Int. J. Hydrogen Energy* 38 (2013) 4116.
- [42] C. Cattaneo, M.I. Sanchez de Pinto, H. Mishima, B.A. Lopez de Mishima, D. Lescano, L. Cornaglia, *J. Electroanal. Chem.* 461 (1999) 32.
- [43] A.S. Arico, P. Creti, H. Kim, R. Mantegna, N. Giordano, V. Antonucci, *J. Electrochem. Soc.* 143 (1996) 3950.

- [44] C.D. Wagner, W.M. Riggs, L.E. Davis, J.F. Moulder, G.E. Muilenberg, *Handbook of X-Ray Photoelectron Spectroscopy*, Perkin-Elmer Corporation, Physical Electronics Division, Eden Prairie, Minn. 55344 (1979).
- [45] Appendix 5 in “*Practical Surface Analysis (Second edition)*”, D. Briggs and M.P. Seah (editors).
- [46] R. Loukrakpam, J. Luo, T. He, Y. Chen, Z. Xu, P. N. Njoki, B. N. Wanjala, B. Fang, D. Mott, J. Yin, J. Klar, B. Powell, C.-J. Zhong, *J. Phys. Chem. C* 115 (2011) 1682.
- [47] B.-J. Hwang, L.S. Sarma, J.M. Chen, C.H. Chen, S.C. Shih, *J. Am. Chem. Soc.* 127 (2005) 11140.
- [48] A.B. Kashyout, A.B. A.A. Nassr, L. Giorgi, T. Maiyalagan, B.A.B. Youssef, *Int. J. Electrochem. Sci.* 6 (2011) 379.
- [49] W. Li, X. Wang, Z. Chen, M. Waje, Y. Yan, *J. Phys. Chem. B* 110 (2006) 15353 .
- [50] T.V. Reshetenko, H.T. Kim, H. Lee, M.Y. Jang, H.J. Kweon, *J. Power Sources* 160 (2006) 925.
- [51] J.-H. Lee, D.-H. Peck, S.-K. Kim, S.-Y. Lim, D.-H. Jung, S.-H. Baeck, J.-H. Jang, *ECS Transactions* 16 (2008) 795.
- [52] J. Otomo, X. Li, T. Kobayashi, C. Wen, H. Nagamoto, H. Takahashi, *J. Electroanal. Chem.* 573 (2004) 99.
- [53] Z. Poltarzewski, P. Staiti, V. Alderucci, W. Wieczorek, N. Giordano, *J. Electrochem. Soc.* 139 (1992) 761.
- [54] T.E. Springer, T.A. Zawodinski, M.S. Wilson, S. Gottesfeld, *J. Electrochem. Soc.* 143 (1996) 587.
- [55] I.D. Raistrick, *Electrochim. Acta* 35 (1990) 1579.
- [56] H. Daimon, *PhD thesis*, Osaka University (2008) Japan.
- [57] C.-W. Kuo, I.-T. Lu, L.-C. Chang, Y.-C. Hsieh, Y.-C. Tseng, P.-W. Wu, *J. Power Sources* 240 (2013) 122.
- [58] Z. Liu, X.Y. Ling, X. Su, J.Y. Lee, *J. Phys. Chem. B* 108 (2004) 8234.
- [59] M. Inabe, *ECS transactions* 25 (2009) 573.
- [60] S. Koh, P. Strasser, *J. Am. Chem. Soc.* 129 (2007) 12624.
- [61] Z. Xu, H. Zhang, H. Zhong, Q. Lu, Y. Wang, D. Su, *Appl. Catal. B:* 111 (2012) 264.

Supporting information

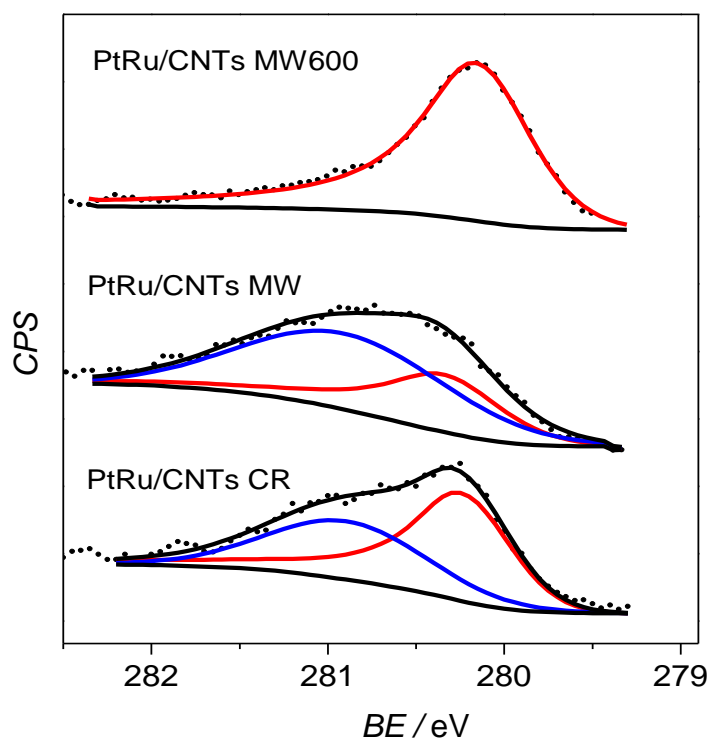


Figure SI3.1: Ru 3d_{5/2} photoelectron spectra of selected samples deconvoluted into Ru⁰ (red) and Ru⁴⁺ (blue) contributions.

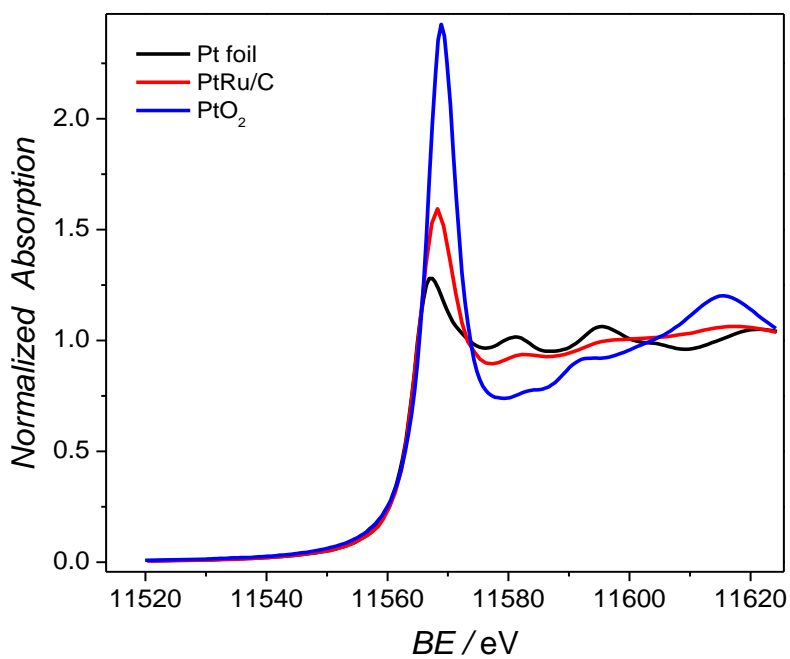


Figure SI3.2: PtL₃ XANES spectra of PtRu/CNTs compared to Pt foil and PtO₂ reference.

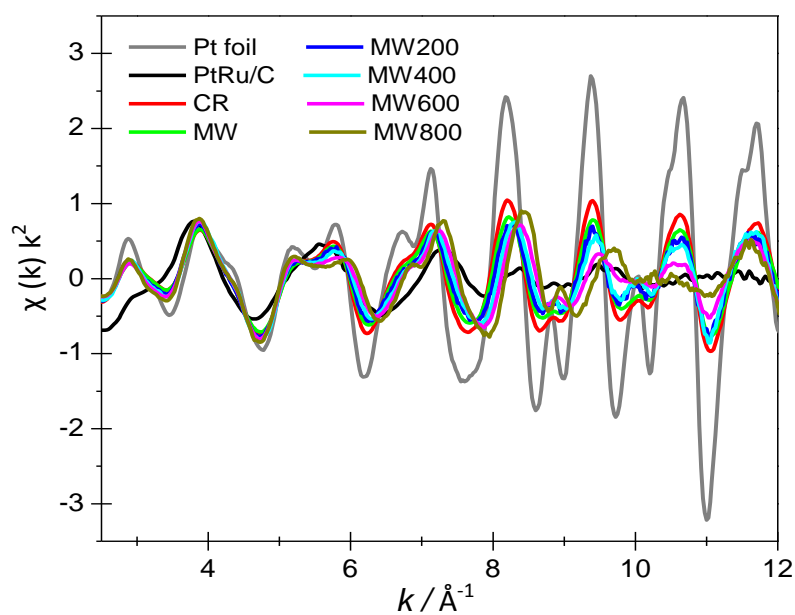


Figure S13.3: PtL_3 k-space EXAFS spectra of platinum foil, PtRu/C and PtRu/CNT catalysts.

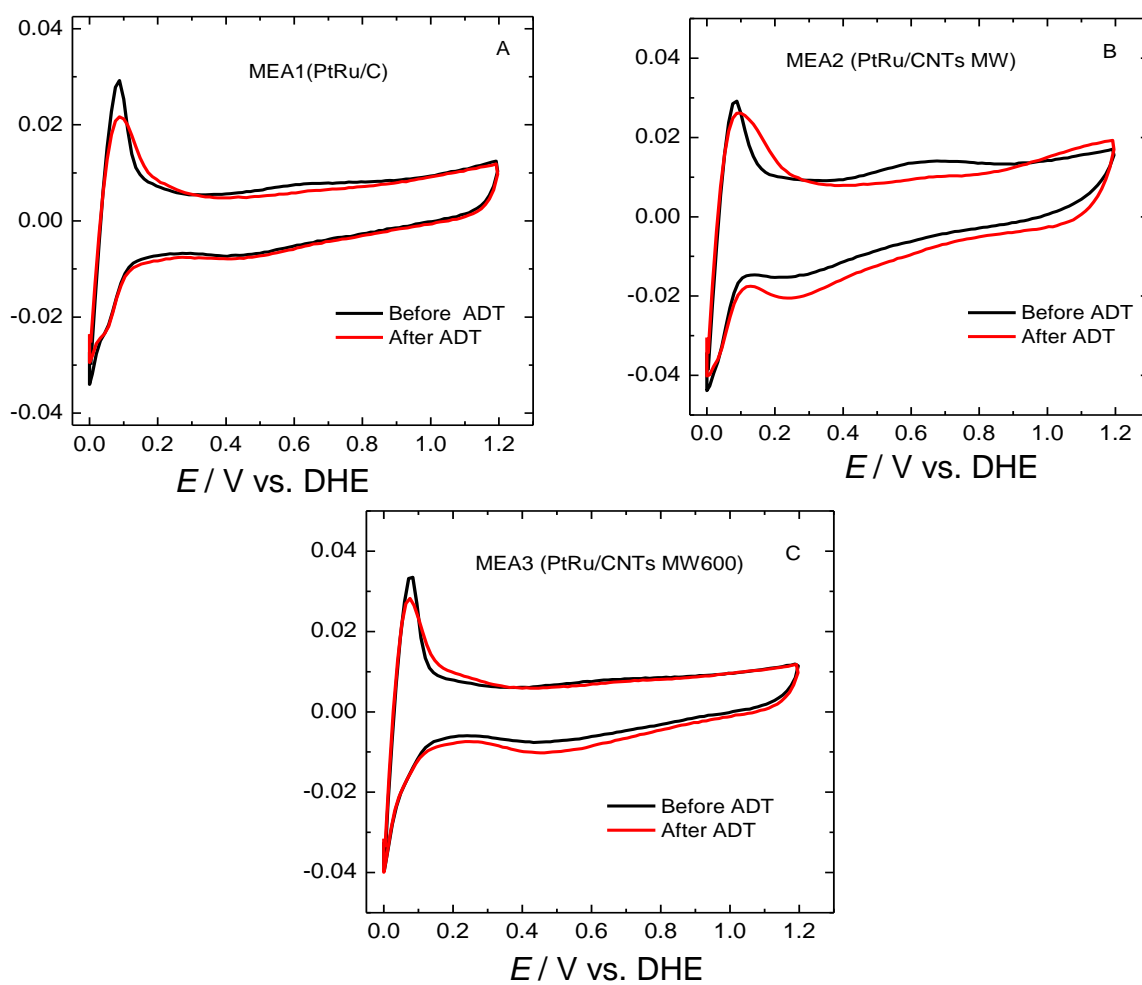


Figure S13.4: In situ CV curves for MEA1 A), MEA2 B) and MEA3 C) before and after ADT.

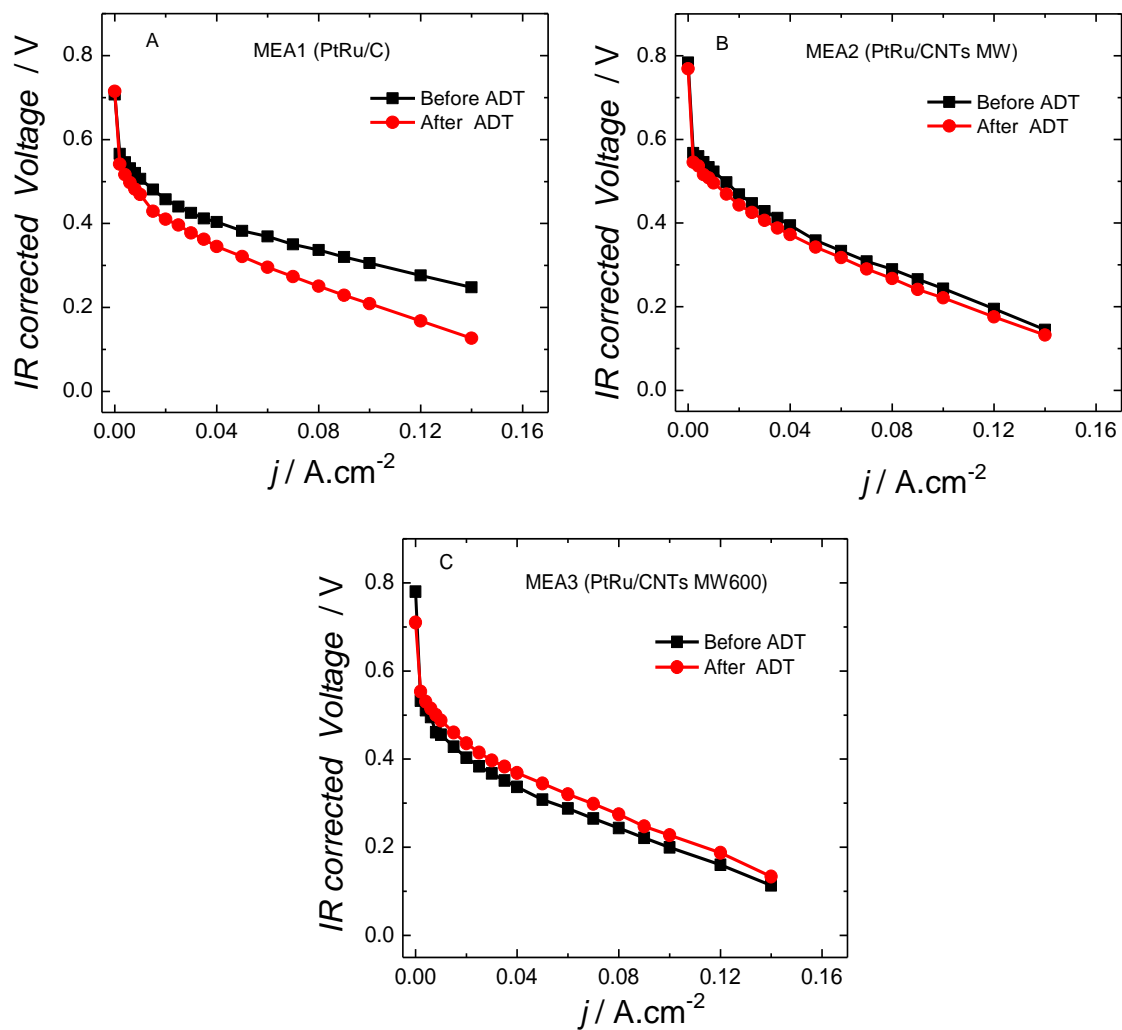


Figure S13.5: Comparison of i - V curves for all MEAs before ADT and after ADT; A) MEA1, B) MEA2, C) MEA3.

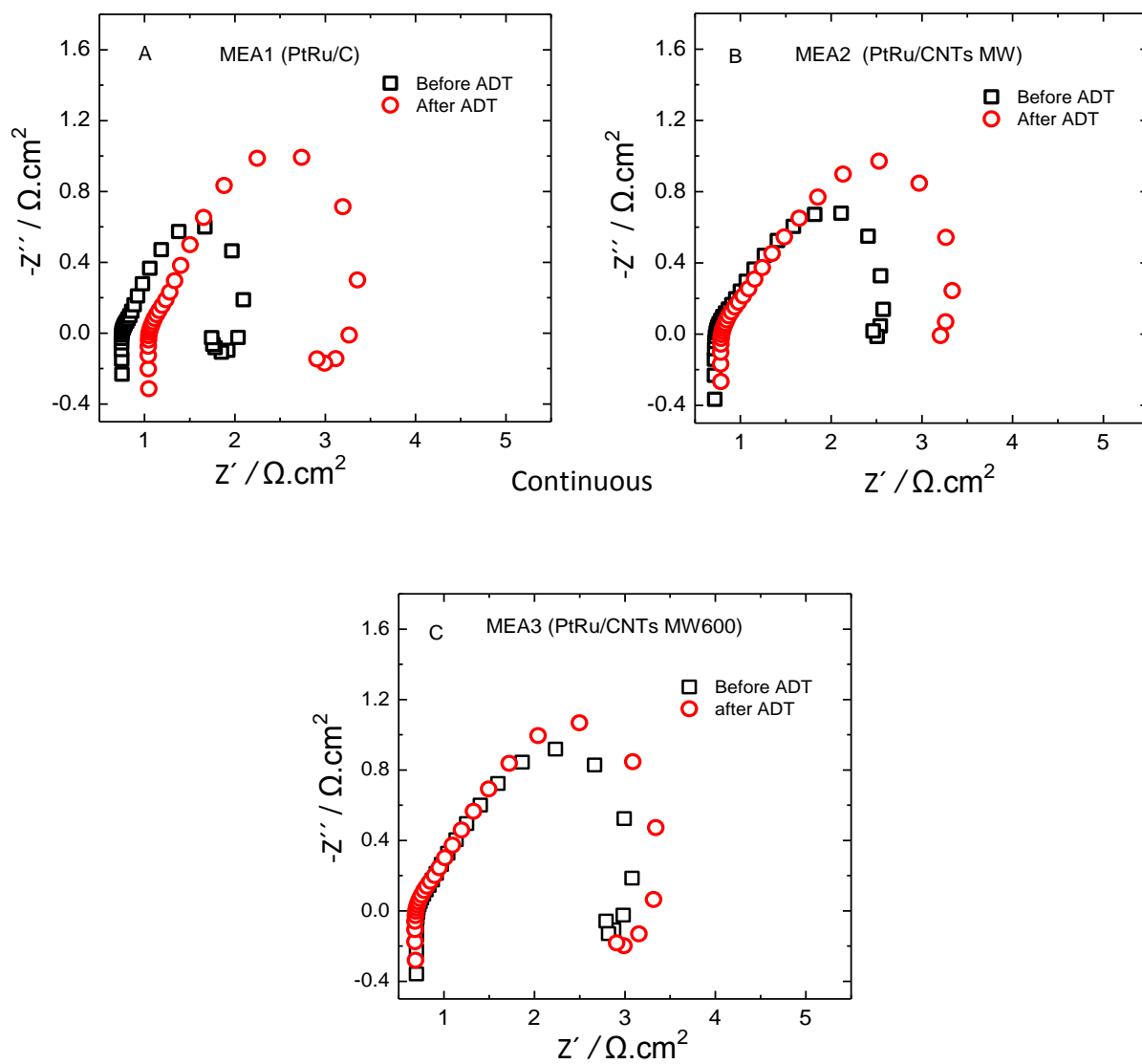


Figure SI3.6: EIS spectra (Nyquist plots) for MEA1 A), MEA2 B) and MEA3 C) before and after ADT in $\text{CH}_3\text{OH}/\text{H}_2$ mode.

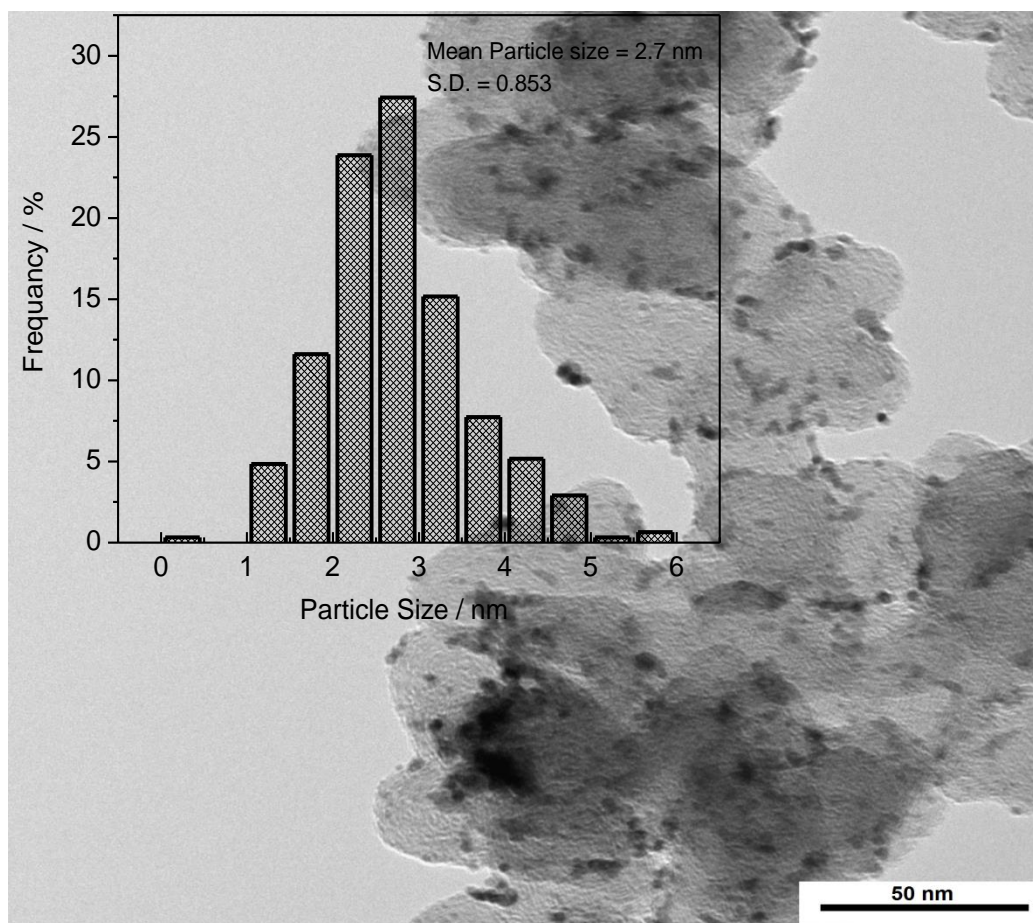


Figure SI3.7: TEM image of PtRu/C (HiSPEC[®] 5000) catalyst (30 % wt.) from Alfa Aesar (JM), inset is the corresponding histogram.

The content of this chapter has been published as
PtNi supported on oxygen functionalized carbon nanotubes: In depth structural characterization and activity for methanol electrooxidation

Abu Bakr Ahmed Amine Nassr, Ilya Sinev, Wolfgang Grünert, Michael Bron

Applied Catalysis B: Environmental 142-143(2013) 849-860

<http://www.sciencedirect.com/science/article/pii/S0926337313003962>

Reproduced with permission of Elsevier copyright® 2013

4.1 Introduction

Direct methanol fuel cells (DMFCs) working with methanol as liquid fuel have received significant attention in the last decade. DMFCs are considered as an important alternative power sources for many applications such as portable devices. Methanol as organic liquid fuel has advantageous features including easy and safe handling, storage and transportation, high energy density as well as low cost [1-3]. However, despite these benefits, DMFCs are characterized by a significantly lower power density and lower efficiency than PEMFCs operating with hydrogen because of the slow oxidation kinetics of methanol and methanol crossover from the anode to the cathode [1-3].

Pt is the best catalyst for partial methanol electrooxidation but its poisoning by CO produced as intermediate during the methanol oxidation retards the complete oxidation process and lowers the activity for methanol oxidation on the Pt electrode surface. In this regard, substantial research has been conducted to improve the activity of Pt catalysts toward methanol oxidation [4-9]. The addition of a second metal or a metal oxide as promoter for CO oxidation is considered as one of the best ways to solve the problem of CO adsorption on the Pt surface [10-21]. In bimetallic systems, Pt can initiate the methanol oxidation reaction through adsorption-dehydrogenation steps and the second metal or metal oxide can supply the oxygen species which are needed to oxidize the adsorbed CO molecules and liberate the Pt surface for further methanol adsorption/oxidation [22-25]. This mechanism is known as the bifunctional mechanism and was suggested by Wantabe et al. [25]. Another mechanism called the ligand effect or the electronic effect has been proposed, according to which the second metal modifies the electronic properties of the Pt by charge transfer processes and lowers the adsorption energy of CO onto the Pt surface [22,26-28]. A broad variety of bimetallic systems such as PtRu, PtNi, PtSn and PtCo with improved activity for methanol oxidation have been studied to replace the monometallic Pt catalysts [10-15,29-37].

Among these bimetallic catalyst systems, PtNi has the promising characteristics of being resistant to dissolution in the potential range used for methanol electrooxidation due to the stability of Ni in the Pt lattice [27,38]. A passivating role of nickel oxides has also been postulated [27]. This dissolution process is observed in various bimetallic catalyst systems like PtRu. Also, Ni is very cheap in comparison to Ru which is a precious metal [32].

PtNi catalysts supported on carbon back have been reported as active catalysts for methanol electrooxidation in alkaline and acid media [27,28,38,39]. Nickel oxyhydroxides, which form through reversible redox reaction from nickel hydroxide or present as Ni component in Ni containing catalysts, are also known to catalyze the methanol oxidation [40,41]. Furthermore, these mixed oxides, beside their corrosion resistance and stability under methanol oxidation conditions, provide mixed protonic and electronic conductivity which may facilitate the charge transfer during the oxidation process. Park et al. [27] prepared PtNi and PtRuNi catalysts and studied their electrocatalytic activity towards methanol oxidation in acid media compared to Pt and PtRu with PtNi and PtRuNi showing higher activity than Pt and PtRu. They attributed the activity enhancement to an electronic effect, where Ni modifies the electronic properties of Pt and weakens the CO adsorption on the PtNi surface, and to the presence of nickel oxides which can participate in the oxidation reaction by hydrogen spillover. The electronic effect was detected from the shift of binding energy of Pt in PtNi as measured by XPS [27]. The enhancement of methanol oxidation through hydrogen spillover by nickel oxides has been also suggested by Liang et al. [42] for carbon supported PtRuNi prepared by microwave pulsed technique followed by reductive annealing, but they also suggest that the oxyhydroxide species can participate in oxidation of CO adsorbed on Pt surface which can be considered as type of a bifunctional mechanism. Density functional theory (DFT) studies on PtNi clusters confirmed the electronic modification of Pt by charge transfer from Ni to Pt leading to weakening of the adsorption of CO on PtNi clusters as estimated from the calculation of CO adsorption energy on PtNi clusters of different compositions [28].

Despite the above observations still work is needed to improve the catalytic activity of the PtNi catalyst system and to gain further insight into catalyst structure. In the literature, little work has been devoted to carbon nanotubes supported PtNi catalysts for methanol oxidation in acid media [43]. We report in this paper on the preparation of PtNi supported on CNTs with different atomic ratio of Pt to Ni by a polyol method using ethylene glycol as reducing agent. The prepared PtNi catalysts have been characterized with physical techniques to elucidate their structural features, while their electrochemical properties have been studied with CV and CO stripping to evaluate their electrocatalytic activity toward methanol electrooxidation reaction in acid media. Furthermore, heat treatment to liberate the catalysts from possible

residual carbon species deposited during preparation resulted in significant changes in structure as well as catalytic behavior, which has been analyzed as well.

4.2 Experimental

4.2.1 Carbon nanotubes functionalization

Carbon nanotubes (CNTs) (Baytubes C 150 P) purchased from Bayer Material Science AG (Germany) were functionalized using nitric acid to introduce surface oxygen-containing groups. 500 mg of the as-received CNTs were dispersed in 100 ml of 5 M HNO₃ for 0.5 h under stirring followed by ultrasonication for 0.5 h. Then the mixture was refluxed using an oil bath at 100 °C for 6 h under stirring. After the reflux process, the mixture was left to cool to room temperature, diluted with 200 ml of deionized water and kept stirring overnight to hydrolyse the functional groups. The functionalized carbon nanotubes were separated by centrifugation and subjected to several washing cycles with deionized water until the pH of the washing water did not change anymore. Finally, the functionalized CNTs were dried in oven at 110 °C overnight and then crushed in a mortar into fine powder and stored in plastic vials until used. Throughout this paper the functionalized CNTs will be labeled FCNTs.

4.2.2 Characterization of functionalized carbon nanotubes

TPD was carried out with a Belcat B (Bel Inc., Japan) in which the FCNTs sample was heated under He gas and the released gases were detected with a mass spectrometer QMS GAM 400 (IPI; Germany). First a stream of He gas was passed over the sample for 1 h at 30 °C. Then the temperature was raised to 1000 °C with a ramp of 5 K min⁻¹ at a gas flow rate of 30 ml min⁻¹.

TGA analysis was carried out with a SDT 2960 Simultaneous DTA-TGA, TA Instruments, USA, in oxygen atmosphere to determine the thermal stability and the purity of CNTs. The sample first was heated up to 100 °C at a heating rate of 20 K min⁻¹ under nitrogen and dried at this temperature for 1 h. After cooling to 40 °C under nitrogen atmosphere, the sample was heated under oxygen atmosphere up to 800 °C at a heating rate of 5 K min⁻¹.

The textural properties (surface area, pore size and pore volume) of the CNTs before and after functionalization were determined by N₂ adsorption using a Sorptomatic 1900, Carlo ERBA. The sample was degassed at 120 °C for 24 h under vacuum followed by adsorption of nitrogen at 77 K.

The electrochemical behavior of the as-received and functionalized carbon nanotubes was tested with cyclic voltammetry in N₂-purged 0.5 M H₂SO₄ at a scan rate of 0.1 V s⁻¹ in the potential window from -0.2 to 1.0 V (Ag/AgCl/sat. KCl) for 100 cycles and the last cycle was used for comparison.

4.2.3 Preparation of electrocatalysts

PtNi electrocatalysts supported on functionalized carbon nanotubes (PtNi/FCNTs) with different nominal atomic ratios and a targeted metal loading of 20 wt% were prepared using a polyol method in which ethylene glycol (EG) served as solvent and reducing agent at the same time. Typically, 100 mg of FCNTs were dispersed in 10 ml EG under stirring for 15 min. The required volumes of 0.0197 M $\text{Ni}(\text{NO}_3)_2 \cdot 6\text{H}_2\text{O}$ and of 0.0197 M H_2PtCl_6 in EG to prepare PtNi with different nominal atomic ratios of Pt:Ni (1:1, 2:1, 3:1, 3:2) were added dropwise under stirring followed by addition of 20 ml of EG and further intense stirring for 15 min. After that, the pH of the mixture was adjusted to 11 with 2 M NaOH/EG solution and sonicated in an ultrasonic bath for 15 min. To carry out the reduction of the metal salt, the mixture was refluxed in an oil bath at 160 °C for 6 h after which it was allowed to cool down to room temperature under stirring and the solid product was separated by centrifugation. After several cycles of washing with water and centrifugation to remove residual EG and to clean the catalyst surface from undesired anions like Cl^- and NO_3^- , the catalyst was dried in an oven overnight at 80 °C, crushed in a mortar into fine powder and kept in a glass vial.

For heat treatment, 20-25 mg catalyst was weighted in a quartz boat and inserted in a horizontal high temperature oven (GERO, Germany) equipped with a quartz tube. The tube was flushed with N_2 (purity 99.999 %) for 30 min to remove oxygen before raising the temperature with a heating ramp of 10 °C min^{-1} to 200 and 400 °C, respectively. After 2 h it was allowed to cool down to room temperature under N_2 atmosphere.

During this text, the PtNi/FCNTs catalysts will be labeled according to their nominal Pt to Ni atomic ratio and heat treatment temperature. For example, PtNi(3:1)/FCNTs 200 refers to a Pt to Ni ratio of 3 to 1 and a heat treatment at 200 °C. Otherwise, PtNi/FCNTs without any label refers in general to all PtNi catalysts prepared in this work without heat treatment.

4.2.4 Characterization of electrocatalysts

4.2.4.1 Structural characterization

Bulk compositions (metal loading and elements ratio) of the catalysts were determined with inductively coupled plasma-optical emission spectrophotometry (ICP-OES, Jobin Yvon Ultima 2, Horiba). The catalysts were subjected to digestion in aqua regia under microwave heating using a microwave reactor (micro PREP 1500, MWS Vertriebs-GmbH, Leutkirch, Germany). The dissolved metals were separated from CNTs by filtration and diluted with water and then their concentrations were

Chapter 4: Ployol Synthesis of PtNi/CNTs Electrocatalysts

measured using ICP-OES. For verification, a commercial 20 % Pt/C catalyst from E-TEK was subjected to the same analysis.

X-ray diffraction measurements were done using a D8 advanced X-ray diffractometer, Bruker AXS, working with a Cu K α source ($\lambda = 0.15406$ nm) and collected for all prepared catalysts in the 2θ range from $20^\circ - 90^\circ$ at a scan rate of 2° min^{-1} .

TEM analysis was carried out with a LEO 912 (Japan) working at an acceleration voltage of 120 keV. The samples were prepared by dispersing the catalysts in ethanol and sonicating for a short time. Drops of this dispersion were deposited onto carbon coated copper grids and dried before analysis.

XPS measurements were done with a Leybold-Heraeus LH10 spectrometer equipped with an EA 10/100 multi-channel detector (Specs), with a base vacuum of 10^{-9} Torr. The data were collected at room temperature. Survey spectra were recorded with a step size of 1 eV and a sampling time of 0.1 s, whereas selected regions (Pt 4f, Ni 2p, C 1s and O 1s) were recorded with a step size of 0.1 eV and a varying sampling time. Mg K α (1253.6 eV, at 12 kV and 20 mA) radiation was used for the excitation. The major C 1s photoemission line was used as an internal standard for energy calibration, with BE = 284.5 eV. For every sample two XPS measurements were done – in the as prepared state and after sputtering for 1 h with He $^+$ ions with 2 keV energy.

Data reduction and signal shape analysis were performed using the program package CASA XPS. Prior to peak fitting, the X-ray satellites were deconvoluted out of the spectra. Atomic ratios of elements were calculated from intensity ratios using the Scofield photoionization cross-section data together with an experimentally derived response function of the spectrometer to the variation of the photoelectron kinetic energy. The Pt area was determined by simple integration employing a Shirley-type background in a preselected binding energy (BE) window.

X-ray absorption fine structure (XAFS) measurements (NiK-edge, 8333 eV, PtL3-edge, 11564 eV) were carried out at HASYLAB (DESY, Hamburg, Germany) at the beamline C using a double-crystal Si (111) monochromator, which was detuned to 65% of maximum intensity to exclude higher harmonics in the X-ray beam. The spectra were recorded in transmission mode at liquid nitrogen temperature. For the measurements ca. 120 mg of sample were pressed in a self-supporting pellet (13 mm diameter) and wrapped with Kapton tape. All spectra were measured simultaneously with the reference spectrum of a Ni or Pt foil placed between second and third ionisation chambers which allowed absolute energy calibration. The spectra of Ni and Pt foils, the corresponding oxides and platinum chloride, which were used as references, were collected under the same conditions. All spectra were measured 2 times to ensure their reproducibility.

Analysis of the EXAFS spectra was performed with the software VIPER for Windows [44]. In the spectra of the absorption coefficient μ , a Victorian polynomial was fitted to the pre-edge region for background subtraction. A smooth atomic background μ_0 was evaluated using a smoothing cubic spline. The Fourier analysis of the k^2 -weighted experimental function $\chi = (\mu - \mu_0)/\mu_0$ was performed with a Kaiser window. The required scattering amplitudes and phase shifts were calculated by the *ab initio* FEFF8.10 code [45] for Ni metal hcp, NiO cubic, Pt metal fcc, and tetragonal P/4mmm Pt-Ni alloy structures. The fitting was done in the k - and r -spaces. The shell radius r , coordination number N , Debye-Waller factor σ^2 and adjustable "muffin-tin zero" ΔE were determined as fitting parameters. The errors of the fitting parameters were found by decomposition of the statistical χ^2 function near its minimum, taking into account maximal pair correlations.

4.2.4.2 Electrochemical characterization

All catalysts were tested toward methanol electrooxidation using cyclic voltammetry (CV). The experiments were carried out in a three compartment electrochemical cell using an Autolab PGSTAT128N potentiostat/galvanostat and a Pt electrode, an Ag/AgCl/sat. KCl electrode and a catalyst coated glassy carbon (GC) electrode as counter electrode, reference electrode and working electrode, respectively. The working electrode was prepared as follows: first, the GC electrode was polished to a mirror finish using alumina suspension (1 μ m, 0.3 μ m) sequentially with a polishing cloth and then ultrasonically cleaned in a mixture of ethanol:water = 1:1 v/v and deionized water for 10 min, respectively. To prepare the catalyst inks, 2.5 mg of PtNi/FCNTs or Pt/C were dispersed in 350 μ l of a mixture of 5 wt% Nafion solution and isopropyl alcohol (1:6, v/v). The catalyst suspension was sonicated for 1 h in an ultrasonic bath and then stirred for 2 h. 5 μ l of this suspension was dropped on the surface of the previously polished GC electrode with a geometrical area of 0.155 cm² and left to dry in air at room temperature. To test electrocatalytic activity the prepared electrode was subjected to activation and surface cleaning by potential cycling for 100 cycles in an N₂ purged solution of 0.5 M H₂SO₄ at a scan rate of 0.1 V/s in the potential window of -0.2 to 1.0 V (Ag/AgCl/sat. KCl), then the activated electrode was subjected to 200 potential cycles under the same conditions in a 0.5 M H₂SO₄/1 M CH₃OH solution purged previously with N₂ for 20 min. The cycle number 20 was used to compare the electrocatalytic activities; however the development of activity with cycle number was also studied.

The electrochemical surface area (ECSA) was determined using CO stripping voltammetry in 0.5 M H₂SO₄ solution. The electrode was subjected to the same activation and cleaning procedures as mentioned above. Afterward, CO gas was purged into the cell for 20 min while keeping the potential at -0.15 V and then N₂ gas

was purged for 20 min to remove the dissolved CO in the solution and finally the stripping voltammogram was recorded in the potential window of -0.15 to 0.9 V at a scan rate of 20 mV s⁻¹ for 3 cycles. All potential in this article are measured and reported against an Ag/AgCl/sat. KCl electrode.

4.3 Results and discussion

4.3.1 Characterization of the functionalized support

To confirm the success of the functionalization process and to study the thermal stability of the functionalized carbon nanotubes, the FCNTs were characterized with temperature-programmed desorption (TPD), thermal gravimetric analysis (TGA), nitrogen physisorption and cyclic voltammetry. The results are detailed in the Supplementary Information (SI) and are summarized here only briefly.

It is well known that the main groups created by nitric acid oxidation of carbon materials are oxygen containing groups, mainly carboxylic acid, lactone, anhydride, quinone and hydroxyl groups [46-49]. These groups are decomposing at different temperatures to release CO and CO₂. Thus, desorption of these gases at defined temperatures refers to the presence of specific surface groups. TPD analysis (Figure SI4.1 in supplementary information) confirms that various kinds of oxygen containing groups have been created on the CNTs surface upon their treatment with nitric acid. These surface oxygen groups may serve as anchoring sites for metal nanoparticles and enhance their dispersion on the FCNTs surface.

The thermal stability of CNTs in oxygen atmosphere was studied using TGA analysis. Figure SI4.2 shows the TGA of as received and functionalized CNTs. The most significant observation is that the complete decomposition of the as received CNTs starts at 450 °C while for the FCNTs the complete decomposition starts at 500 °C, indicating their higher oxidative stability. This result could be explained by removal of some remnants of the metal catalyst used for CNT preparation during the functionalization with nitric acid. The presence of these metal impurities could enhance the oxidation of as received nanotubes in O₂ atmosphere. Indeed, the residue remaining after TGA is higher for the as received CNTs (1.38%) than for the FCNTs (0.18%). Furthermore, amorphous carbon species, which should be burned at much lower temperatures [50], are obviously not formed during the mild nitric acid treatment.

The electrochemical properties of functionalized and as received CNTs were tested with cyclic voltammetry as shown in Figure SI4.3. The functionalized carbon supports exhibit strong redox peaks in the forward and backward scans, which are characteristic for electroactive surface oxygen groups and assigned to hydroquinone-quinone redox couple (HQ/Q), while the as received CNTs don't show this behavior [51,52],

confirming that the functionalization process was able to create oxygen surface functional groups on the CNT surface.

4.3.2 Characterization of electrocatalysts

4.3.2.1 Structural characterization

PtNi/FCNTs, Pt/FCNTs and commercial Pt/C (E-TEK) were analyzed with ICP-OES to determine their chemical composition and metal loading, as summarized in Table 4.1. The total metal loading for the prepared PtNi/FCNTs and Pt/FCNTs electrocatalysts is less than the theoretical loading of 20 wt%. Also, the Pt to Ni atomic ratio varies from the nominal one except for PtNi(3:1).

The lower metal loading of all catalysts could be a result of the comparably high pH used during preparation, which however is necessary to accelerate the rate of reduction. The high pH leads to negative surface charge on the FCNTs which hinders the adsorption of negatively charged platinum ions (PtCl_6^{2-}) or even the negatively charged nanoparticles after their reduction due to the charge repulsion [53]. A lower metal loading however has been reported before for Pt/C and PtRu/CNTs prepared by the polyol method using EG as reducing agent at higher pH [53,54]. On the other side, as reported by Ribeiro et al. [55] a more basic environment favors Ni ion reduction. They prepared PtRuNi/C catalysts in EG at different pH and they found that at lower pH, the amount of Ni detected by EDX is very low while the metal loading was the same as in the starting precursor. With increase in the pH of the preparation media up to 11-12 the amount of Ni detected was higher but the total metal loading was 50 % of its theoretical value which agrees well with our results.

The XRD patterns of the Pt/C, Pt/FCNTs and PtNi/CNTs catalysts are shown in Figure 4.1. Pt/C (E-TEK) (Figure 4.1A) shows diffraction peaks at 2θ of 39.9° , 46.1° , and very broad and weak signals at ca. 67.4° and 81.4° , which are characteristic for the 111, 200, 220 and 311 facets of the Pt fcc structure, respectively, while Pt/FCNTs doesn't show any characteristic peaks of Pt fcc which could be attributed to a small particle size of this catalyst (see below) and/or to the lower Pt loading. All PtNi/FCNTs catalysts display only the Pt 111 peak, which is slightly shifted to higher 2θ values confirming alloying formation in PtNi catalysts due to the incorporation of smaller Ni atoms into the Pt fcc lattice [27,43,56]. Importantly, the patterns for PtNi/FCNTs don't show any diffraction peak for Ni metal or its oxides while all the catalysts show a peak at about $25^\circ 2\theta$ which is assigned to the carbon support. No attempt was made to calculate the crystallite size of the PtNi/FCNTs catalysts from XRD due to the broad, weak peaks which however point to rather small particle sizes. XRD of the heat treated PtNi(3:1)/FCNTs and PtNi(1:1)/FCNTs electrocatalysts, respectively are shown in Figures 4.1B and C.

Chapter 4: Polyol Synthesis of PtNi/CNTs Electrocatalysts

Table 4.1: Composition (from ICP) and particle size (from TEM) for Pt/C and PtNi/FCNTs.

Catalyst sample	Pt [wt%]	Ni [wt%]	Total metal loading [wt%]	Atomic ratio Pt:Ni	Particle size from TEM [nm]
Pt/C ETEK	19.0	-	19.0	-	3.1
Pt/CNTs	04.5	-	04.5	-	1.1
PtNi(1:1)/FCNTs	11.0	1.5	12.5	2:1	2.7
PtNi(2:1)/FCNTs	09.0	0.9	09.9	3:1	2.2
PtNi(3:1)/FCNTs	06.8	0.6	07.4	3:1	2.7
PtNi(3:2)/FCNTs	09.0	0.8	09.8	3.5:1	3.0
PtNi(2:1)/FCNTs 200	-	-	-	-	3.2
PtNi(3:2)/FCNTs 400	-	-	-	-	3.9

The heat treated catalysts display more intense Pt 111 peaks and a decrease in FWHM (full width at half maximum) indicating an increase in crystallite size. The 200, 220 and 311 signals are more developed for PtNi(1:1), while PtNi(3:1) still displays only the Pt 111 signal even after heat treatment. It is important to note that with increase in the heat treatment temperature, the Pt 111 peak for PtNi/FCNTs catalysts shift to lower 2θ angle compared to of the as-prepared one, especially for those catalysts heat treated at higher temperature (400 °C). This may be attributed to a phase separation between Pt and Ni as result of nickel oxides formation during the heat treatment [57]. Note that again no peaks for Ni or Ni oxides are visible, indication either absence or very small crystallite sizes/films thickness of these species.

Selected TEM images of Pt/C ETEK, Pt/FCNTs and PtNi/FCNTs and the corresponding particle size histograms are shown in Figure SI4.5. The average particle sizes calculated from counting more than 100 particles for all catalysts are listed in Table 4.1. Nanoparticles of Pt and PtNi are well dispersed on the support and are very small with a narrow particle size distribution. These morphological properties are one of the advantages of the polyol method used for the preparation of Pt/FCNT and PtNi/FCNTs in this work. Only the PtNi(3:2)/FCNTs show some agglomeration. The average particle size for Pt/FCNTs is very low (1.1 nm) in agreement with the absence of diffraction peaks in XRD patterns (see above). The PtNi/FCNTs catalysts show particle sizes in range of 2-3 nm. Upon heat treatment, the particle sizes increase while keeping their high dispersion.

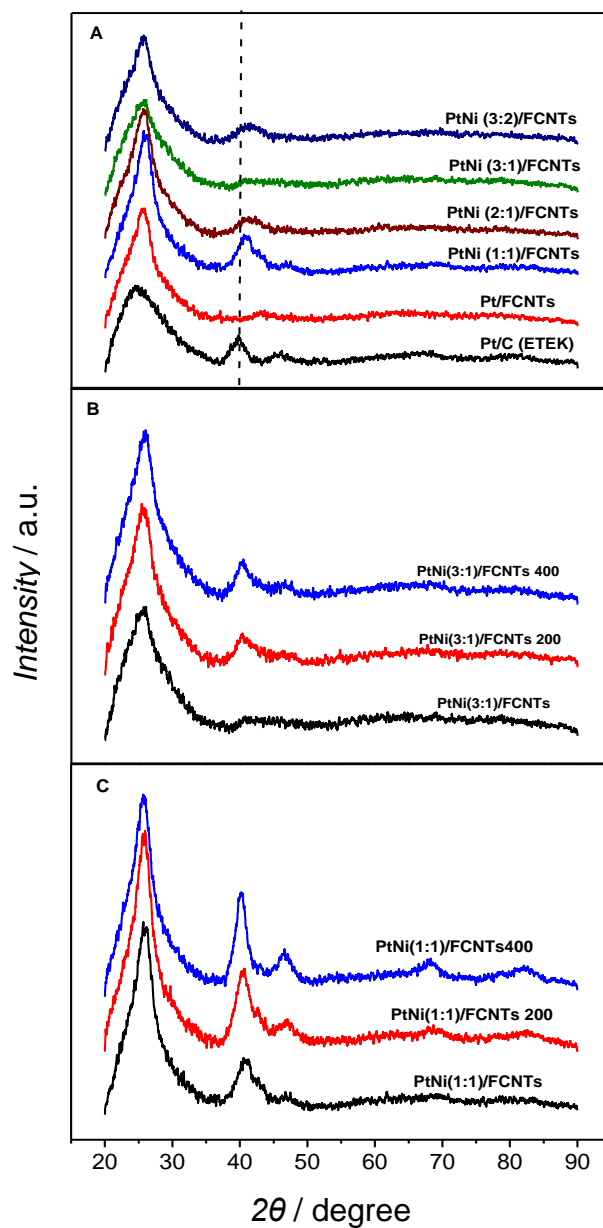


Figure 4.1: XRD patterns of Pt/C (Etek), Pt/FCNTs and PtNi/FCNTs electrocatalysts (A) , heat treated PtNi(3:1)/FCNTs (B) and PtNi(1:1)/FCNTs (C).

Pt(4f) XPS spectra are presented in Figure 4.2A. The Pt (4f 7/2) signal has a BE of 71.9 eV, which is close to the metal position (71 eV) [58,59]. This shift to higher energies is likely not related to a higher oxidation state of platinum but to initial-state or final-state effects due to small particle size [60,61]. In the bimetallic samples, the Pt (4f 7/2) binding energy is slightly lower (in average by ≈ 0.3 eV), which might indicate

Chapter 4: Ployol Synthesis of PtNi/CNTs Electrocatalysts

alloy formation. The effect is, however, near to the limits of experimental error and should not be overemphasized.

The Ni 2p spectra of selected samples are presented in Figure 4.2B and C. Although the Ni signals are weak, some conclusions on the nickel state can be derived. In all samples the Ni²⁺ state with a BE of ca. 856 eV can be detected together with its satellite approximately 6 eV higher [62]. A contribution from the Ni metallic state can also be detected in the non-heat treated samples – PtNi(1:1), (2:1) and (3:1)/FCNTs. Ni appears to be almost fully oxidized in PtNi(3:1)/FCNTs 400 and the presence of metallic state is rather unclear in PtNi(2:1)/FCNTs 200. These results support the above findings from XRD that the initially present alloy, where the Ni XPS state should be more metallic, restructures during heat treatment. However the formed Ni oxides, as detected by XPS, are in a form undetectable by XRD (i.e., small particles or thin films).

Table 4.2: Pt to Ni atomic ratios derived from XPS data

Preparation	Pt:Ni before He ⁺ sputtering	Pt:Ni after He ⁺ sputtering
2:1	10.2	12.2
2:1_200	5.5	- ^a
3:2	- ^b	19.7
3:1	12.4	12.3
3:1_400	3.5	4.7
1:1	6.0	8.7

^a Strong artifact on Ni 2p signal

^b Too weak Ni 2p signal

The Ni content detected with XPS is lower than expected from ICP analysis. The intensity of the Ni signal is very low and the 2p 1/2 line could sometimes be barely distinguished from the background noise. Taking into account that the photoionization cross section for Ni is 1.5 times higher than that of Pt it can be concluded that a low amount of nickel is accessible for the XPS analysis, i.e. in the surface region of the catalyst. A possible explanation would be that a significant part was present in big particles that give small XPS intensity, contradicting however TEM and XRD results as well as XAFS results (see below). A more likely explanation would thus be that the Ni is enriched in deeper layers. The detectable Ni amount is, however, higher after heat treatment (see Table 4.2), in line with some segregation as speculated on from XRD results.

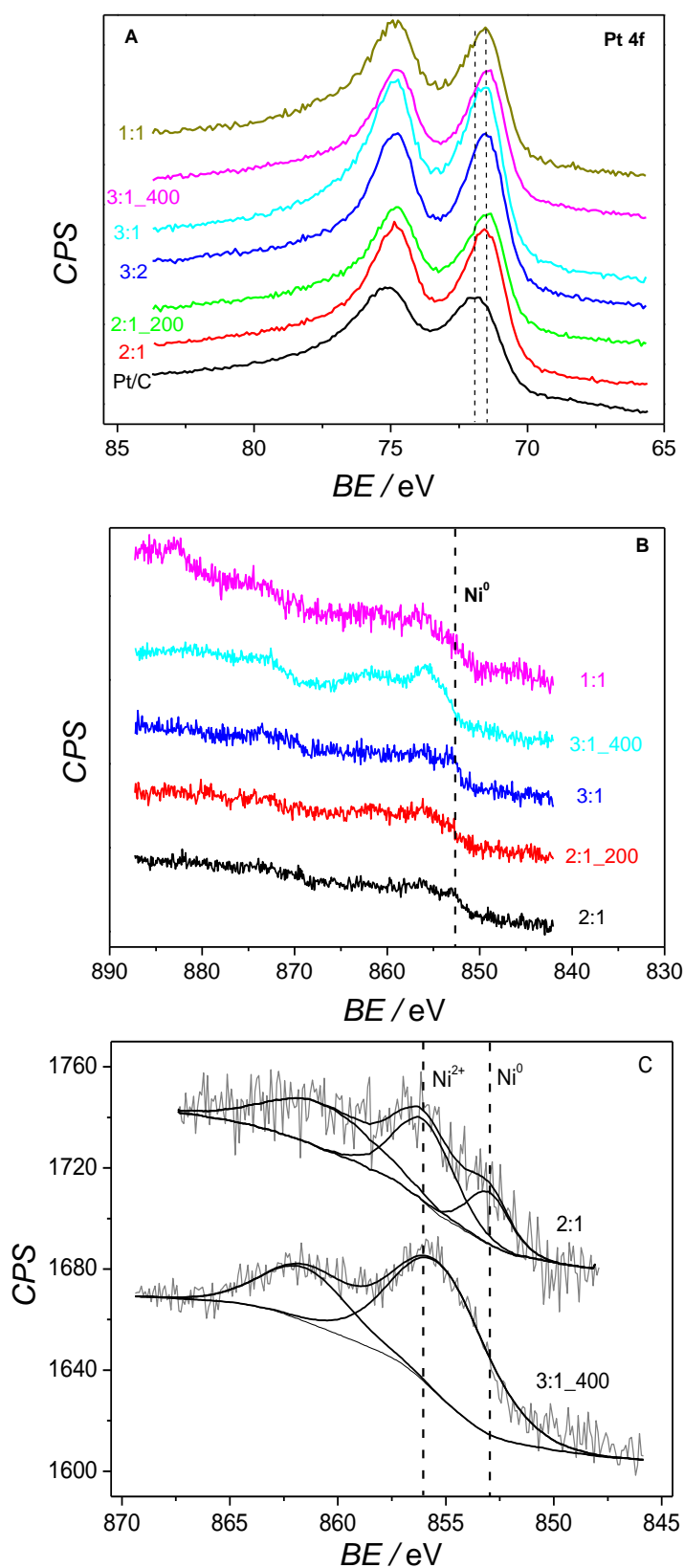


Figure 4.2: XPS spectra A) Pt 4f lines of corresponding samples; B) Ni 2p_{3/2} regions; C) Ni 2p_{3/2} lines with (PtNi(3:1)/FCNT 400) and without (PtNi(2:1)/FCNT) clearly detectable Ni⁰ contribution.

It is also remarkable that the Ni is strongly oxidized in the surface region. After sputtering (Figure S14.7) there is almost no more oxidized Ni. It is known that sputtering is reductive (preferential removal of O), at the same time Ni is also removed. Probably, together with a NiO layer on the outer surface of nanoparticles, separate highly dispersed NiO particles too small to be detected by XRD are present which are easily sputtered away.

Regarding the presence of oxides, it is not clear at the moment, if these form during catalyst preparation/heat treatment, or afterwards while handling the catalyst in air. However, the presence of oxides clearly indicates that not all Ni is in an alloy state in the catalyst.

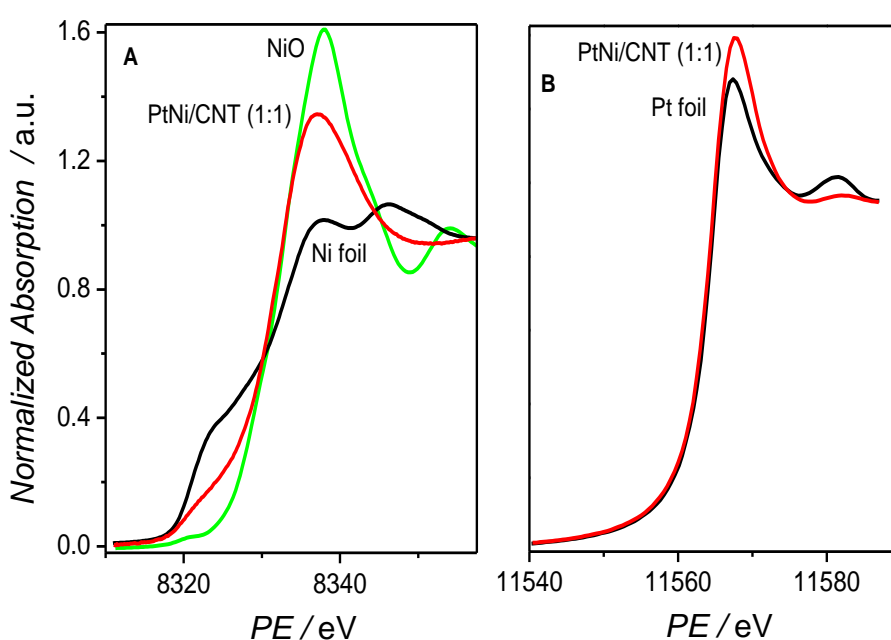


Figure 4.3: Ni K (A) and Pt L_3 (B) edge XANES spectra of the PtNi(1:1)/FCNTs catalyst and reference compounds.

Figure 4.3 shows Ni K and Pt L_3 X-ray absorption near edge structure (XANES) of PtNi(1:1)/FCNT. The catalyst spectrum resembles that of NiO with most features like edge position and white line at 8337 eV. However, there is also a shoulder similar to the pre-edge feature of the metal at 8232 eV, the white line being somehow lower than that in NiO case indicates that nickel is not totally oxidized in the sample under study. The EXAFS plot for the PtNi(1:1)/FCNT (Figure 4.4A) catalyst has a characteristic peak for Ni-O scattering at $r = 1.68 \text{ \AA}$. The second remarkable peak at $r = 2.39 \text{ \AA}$ cannot be unambiguously identified as Ni-Ni scattering event neither in Ni metallic (ref $r = 2.15 \text{ \AA}$) nor in NiO (ref $r = 2.60 \text{ \AA}$) structures. However it can indicate the appearance of a Ni-Pt scattering event.

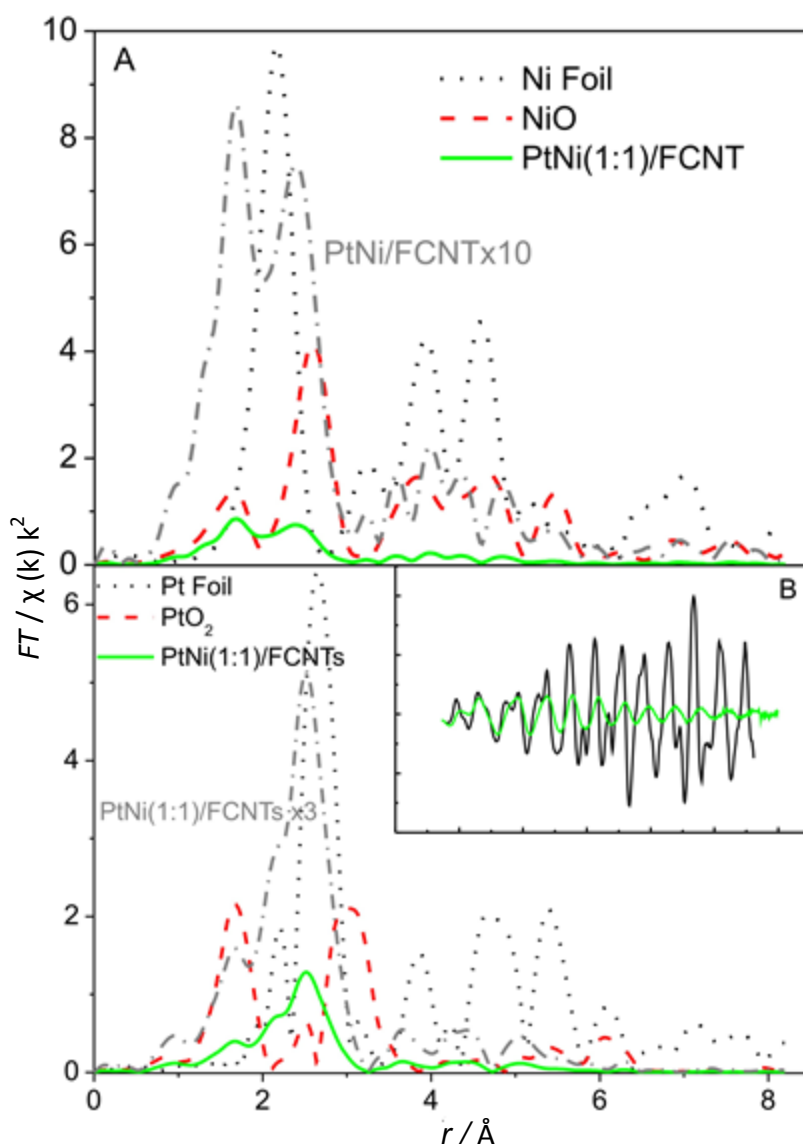


Figure 4.4: A Ni K edge real space EXAFS spectra of PtNi(1:1)/FCNTs catalyst and reference compounds B Pt L_3 real space EXAFS spectra of PtNi(1:1)/FCNTs catalyst, platinum foil and platinum oxide. Inset – the same spectra in k-space.

The catalyst Pt L_3 XANES spectrum differs slightly from that of the platinum foil (Figure 4.3). The slightly more intense white line may indicate that platinum in the catalyst is somewhat oxidized, however, an electronic effect of alloy formation cannot be ruled out. C.-J. Zhong and coauthors [63] also report minor white line intensification for both PtNi/C and PtCo/C systems. It was attributed to the decrease of 5d orbital filling in platinum alloys due to oxidation and hybridization. The r-space EXAFS spectrum (Figure 4.4B) resembles the reference platinum foil spectrum. However, the small shoulder can be detected at $r = 1.66 \text{ \AA}$ pointing on small number of light backscatterers (presumably oxygen) presented in first coordination shell of platinum atom. Additionally, the low-r component (at ca. 2.20 \AA) of the main metallic peak is

more intense than it is in the reference spectrum indicating a direct contact of Pt and Ni atoms. Moreover there is a significant difference in EXAFS functions $\chi(k)$ (see Figure 4.4B inset) consisting in a phase shift increasing to high k values. Thus there is a clear indication to the presence of another element but platinum in the first coordination shell.

4.3.2.2 Electrochemical characterization

Figure 4.5 shows selected CO stripping voltammograms for PtNi(2:1)/FCNTs, PtNi(2:1)/FCNTs 200 and PtNi(2:1)/FCNTs 400, respectively; the voltammograms of the other catalysts appeared similar.

During the first cycle of all CVs (solid line) at potentials starting from ca. 0.5 V the adsorbed CO starts to be oxidized as evidenced by the sharp CO oxidation peak. In the second cycle (dashed line) no CO oxidation peaks are observed anymore indication that CO was oxidized completely during the first cycle. All catalysts show almost the same oxidation potential for CO oxidation except the Pt/FCNTs for which the potential is shifted slightly to higher values. The electrochemical surface area (ECSA) and specific electrochemical surface area (SECSA) for all catalysts was calculated from integration the charge passed during the oxidation of CO using the following relation [64].

$$ECSA(cm^2) = \frac{Q_{CO}(mC)}{Q_0(mC.cm^{-2})} \quad (4.1)$$

$$SECSA(m^2.g^{-1}) = \frac{ECSA}{M_{Pt}} \quad (4.2)$$

Where Q_{CO} is the charge passing during the CO oxidation in mC, Q_0 is the charge required for oxidation of absorbed monolayer CO and equal to 420 ($\mu C/cm^2$) [64] and M_{Pt} is the Pt loading in the electrode.

The results are listed in Table 4.3. The specific electrochemical surface area is higher than that of Pt/C (E-TEK) for all prepared catalysts, except for the PtNi(1:1) sample which displays lower specific surface area of 29.08 m^2/g versus 47.20 m^2/g for Pt/C (E-TEK), which could be attributed to a higher Ni content in this catalyst as detected from ICP analysis.

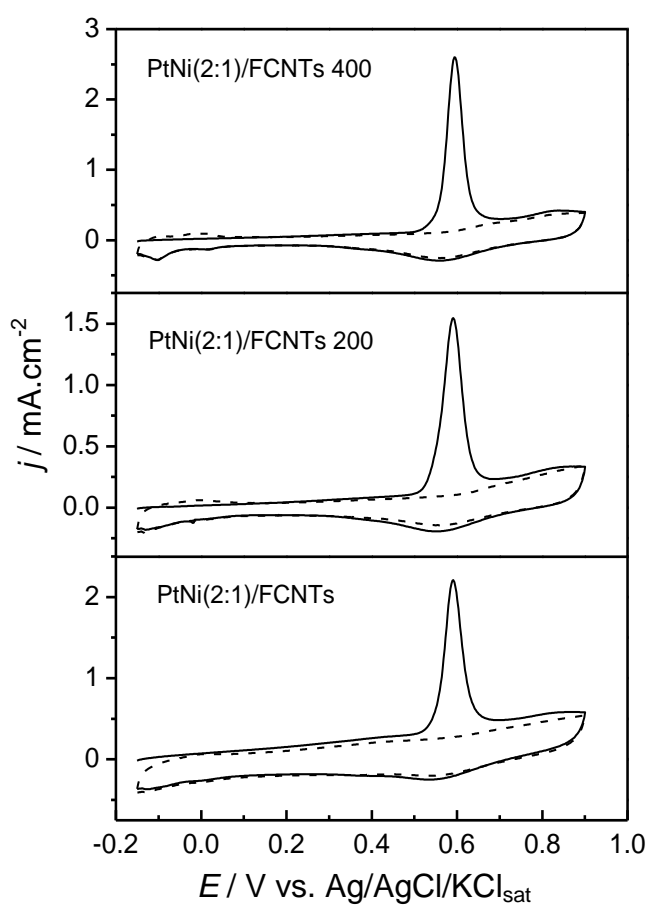


Figure 4.5: CO stripping voltammograms of selected samples.

In the as prepared catalysts with the exception of PtNi(1:1) all bimetallic samples display hardly any features for hydrogen adsorption/desorption in the second CV (after CO oxidation). However, after heat treatment, these features are much more pronounced, indicating the formation of a Pt enriched surface (see Figure 4.5). Furthermore, for almost all PtNi/FCNTs electrocatalysts the electrochemical surface area increase with increase of heat treatment temperature while the particle size also increases as shown above with TEM. Since only surface Pt is detected during ESCA measurements and Ni is not, these results support the postulation of a more Pt-rich surface after heat treatment at 400 °C.

Chapter 4: Ployol Synthesis of PtNi/CNTs Electrocatalysts

Table 4.3: Electrochemical parameters calculated from CO stripping measurements.

Catalyst	Peak potential for CO oxidation [V]	Charge Q [mC]	ECSA [cm ²]	SECSA [m ² /g]
Pt/C ETEK	0.60	1.346	3.20	47.2
Pt/CNTs	0.63	0.415	0.98	61.3
PtNi(1:1)/FCNTs as prepared	0.59	0.593	1.14	29.1
PtNi(1:1)/FCNTs 200	0.59	0.609	1.45	37.0
PtNi(1:1)/FCNTs 400	0.59	0.750	1.78	45.4
PtNi(2:1)/FCNTs as prepared	0.59	0.757	1.80	56.1
PtNi(2:1)/FCNTs 200	0.59	0.612	1.45	45.2
PtNi(2:1)/FCNTs 400	0.59	0.921	2.19	68.2
PtNi (3:1)/FCNTs asprepared	0.59	0.720	1.71	70.7
PtNi (3:1)/FCNTs 200	0.59	0.710	1.69	69.8
PtNi (3:1)/FCNTs 400	0.60	0.729	1.73	71.5
PtNi (3:2)/FCNTs asprepared	0.59	0.981	2.33	72.6
PtNi (3:2)/FCNTs 200	0.58	0.782	1.86	57.9
PtNi (3:2)/FCNTs 400	0.59	0.780	1.85	57.6

4.3.3 Structure of the catalysts

The above characterization results shall be discussed already at this part of the paper to derive a structural model of the catalyst and its changes induced by heat treatment. This model will then help to understand the results of the catalytic experiments below.

Both XPS and XAFS studies reveal that the platinum state in the catalysts under study is metallic, with clear indications of alloy formation. However, besides metallic Ni significant Ni oxide contributions are also detected, and after heat treatment oxides are the only Ni species detectable by XPS. In accordance, XRD detects the presence of alloys with the degree of alloying decreasing, however not completely vanishing, after heat treatment. Oxidic species, however, are not detected by XRD.

The difference in Pt:Ni ratio between XPS and ICP-OES results deserves special attention. While ICP-OES, analyzing the whole sample, yielded Pt:Ni ratios close to the nominal ones, XPS, restricted to the upper surface layers, indicated very high Pt:Ni ratios, the values however decreasing after heat treatment. A Ni depleted surface, with structural changes and Ni segregation however after heat treatment, is in line with this model. Thus, a PtNi alloy core surrounded by a Pt enriched shell with some Ni oxides present outside could be postulated. Further segregation occurs during heat treatment. Unfortunately the quality of XRD is not high enough to distinguish all these species due to small particle size.

The results of the electrochemical experiments are in line with these postulations. After heat treatment, Pt features are more expressed in electrochemical experiments. Heat treatment might aid in the removal of residual organic material adsorbed on the catalyst surface during the preparation process leading to an enhancement of electrochemically accessible surface (ECSA) area and development of Pt features in the CV. However, after heat treatment at 400 °C besides this simple effect of surface cleaning, characterization indicates changes in the catalyst, i.e. more oxidized Ni species and a reduction in the degree of alloying (see XRD). Obviously a Pt enriched surface or separated phases of Pt and Ni (oxides) render the voltammograms more Pt characteristic than a PtNi surface [63]. While this effect is strong in the catalyst with high Ni content (PtNi(1:1) (real ratio was 2:1), it is less pronounced in the catalysts (2:1) and (3:1) (both real ratio 3:1), where also particle growth diminishes the effect of ECSA enhancement. The decrease of electrochemical surface area upon heat treatment in the PtNi (3:2) could in line with this be attributed to agglomeration and growth of nanoparticles, as indicated by TEM and which overcompensates the other changes in the catalyst.

To further analyze the structural features of the catalyst, EXAFS functions were fitted with three shell model using backscattering amplitudes and phases theoretically calculated by ab-initio FEFF8.10 code [45]. For the NiK edge the Ni-Ni homo- and Ni-Pt heterometallic scattering contributions were used together with one metal-oxygen shell. The PtL₃ edge was fitted using Pt-Pt and Pt-Ni contributions. The fitting results, consisting of coordination number (CN), scattering distance (r), Debye-Waller factors index of power (σ^2) and muffin-tin potential adjustment (ΔE) are presented in Table 4.4 for the PtL₃ and Table 4.5 for the NiK edge respectively. It can be seen that platinum tends to form homoatomic agglomerates where every atom has ca. 5 Pt neighbors. Pt-Ni scattering events however can be also detected with the average coordination number of 1.3. The presence of Pt-Ni alloy structure is thus numerically proven. Additionally, the fact that the total coordination numbers of both Pt (6.7) and Ni (5.6) are close to each other indicates that no enclosed (like core-shell) structure has been formed. To study Pt-Ni alloying extent, the method suggested by B.-J. Hwang [65] was used. In the method, the degree of alloying is determined by calculating heteroatomic bonding probability from coordination numbers derived from the EXAFS fit procedure and relating them subsequently to the theoretical values dictated by the alloy stoichiometry. For binary alloys, 7 boundary cases were suggested, including separated and perfect alloys as well as structures of various degrees of homogeneity. The method can be applied also for our case where some Ni-O coordinations are present because it relies entirely on ratios of coordination numbers. In case of the Pt:Ni (1:1) catalyst, the relative extent of alloying of platinum (J_{Pt}) was calculated to be 60, whereas J_{Ni} is close to 100. According to the Hwang classification this indicates that Ni

atoms are tending to form homophilic structures close to the outer surface of the nanoparticles (Ni-rich shell, Pt-rich core). The latter however contradicts the low Ni 2p XPS line intensities. We suspect that the homophilic structures of nickel atoms in the alloy particles are concentrated in regions near the support so that they are shielded from the atmosphere and at the same time less visible for XPS. A structural model can be suggested as shown in Figure 4.6. This model represents both the as prepared and heat treated samples, which however differ in the amount of surface segregation. The alloyed Ni exposed to the atmosphere is oxidized. The alloy particles probably coexist with very small segregated NiO aggregates which enhance the predominance of oxidized Ni in the XPS spectra.

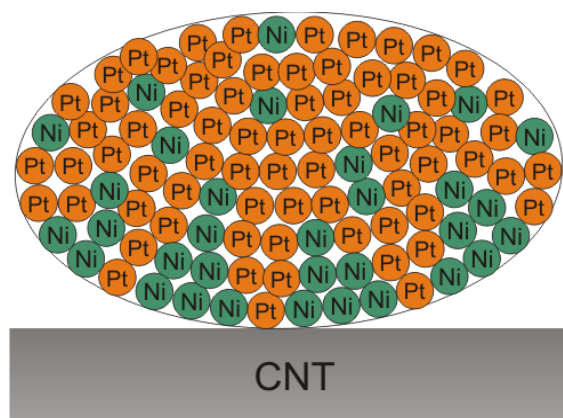


Figure 4.6: Schematic sketch of bimetallic Pt-Ni nanoparticles demonstrating that Pt and Ni are not randomly distributed in the particle, but Ni is enriched near the support and Pt towards the gas phase. Model represents both as prepared and heat treated samples, which however differ in the amount of surface segregation.

A tentative explanation for the formation of such structures might be that the positively charged Ni^{2+} ions do adsorb on the surface of the FCNTs, which are likely negatively charged at positive pH, while the negatively charged PtCl_6^{2-} -ions do not. Initially formed Ni clusters on the FCNTs surface then catalyze the further reduction of Pt and Ni and lead to the formation of a Pt-rich alloy surrounding the Ni-rich core attached to the CNT.

Table 4.4: Pt L3 edge best-fit results within two shell model.

Reference path	r (Å)	CN	$\sigma^2 \times 10^{-3}$ (Å ²)	ΔE (eV)
Pt-Ni = 2.6165	2.65±0.02	1.32±0.20	7.49±1.47	15.13±2.56
Pt-Pt = 2.6976	2.71±0.01	5.31±0.34	6.99±0.46	10.19±0.36

$\Delta R = 2.05\text{Å}$; $\Delta k = 2.77\text{-}15.83\text{Å}^{-1}$. Errors are assumed to be proportional to $k^{1.5}$, Pt-Ni distance is constrained between 2.5 and 2.7 Å

Chapter 4: Ployol Synthesis of PtNi/CNTs Electrocatalysts

Table 4.5: Ni K edge best-fit results within three shell model.

Reference path	r (Å)	CN	$\sigma^2 \times 10^{-3}$ (Å ²)	ΔE (eV)
Ni-O = 2.0842	2.04±0.01	2.19±0.30	6.74±2.03	4.43±1.37
Ni-Pt = 2.6165	2.64±0.02	2.25±1.02	8.56±2.70	-3.68±0.91
Ni-Ni = 2.6976	2.63±0.06	1.14±0.23	8.86±2.99	3.33±6.27

$\Delta R = 2.43\text{Å}$; $\Delta k = 3.35 - .83\text{Å}^{-1}$. Errors are assumed to be proportional to k .

4.3.4 Methanol electrooxidation

After having established the structure of the catalysts and the changes induced by heat treatment, it would be highly interesting to study the behavior of these materials as catalysts for the electrooxidation of methanol. Cyclic voltammograms for methanol oxidation in 0.5 M H₂SO₄ are shown in Figure 4.7, showing the typical behavior for Pt and Pt based catalysts in sulfuric acid solution containing methanol [66-71].

The ratio between the peak current in the forward (I_f) and the backward scan (I_b) is usually taken as the measure for the tolerance of the catalyst against CO poisoning with a higher I_f/I_b indicating higher tolerance. Figure 4.7 demonstrates that the catalyst with 2:1 and 3:1 nominal Pt:Ni ratios (the actual Pt:Ni ratios for these catalysts are 3:1) display a higher I_f/I_b which reflects their higher CO tolerance. On the other hand, the catalysts 3:2 and 1:1 exhibit a somewhat higher current in the reverse peak indicating a slightly higher susceptibility to CO poisoning. A Pt:Ni ratio of 3:1 might thus be optimum in terms of CO tolerance. However, the differences between these samples are comparably small. All prepared catalysts show superior CO tolerance and methanol oxidation compared to the commercial sample. In general we can say that the presence of Ni and/or its oxides has a beneficial role affecting the CO tolerance during the MOR. On the other hand, the higher CO tolerance of Pt/FCNTs indicated by the lower current in the reverse peak could be attributed to the small particles of this catalyst which would be more active for CO oxidation. Upon the heat treatment, formation of a Pt enriched surface is which observed displays methanol oxidation behavior similar to that of Pt/C ETEK with higher currents in the reverse scan (not shown).

From the CVs, the mass specific activity, which is defined as the current at the peak oxidation potential in the forward scan divided by Pt loading on the electrode, was determined. The values for mass specific activity, surface specific activity and peak potential are listed in Table 4.6.

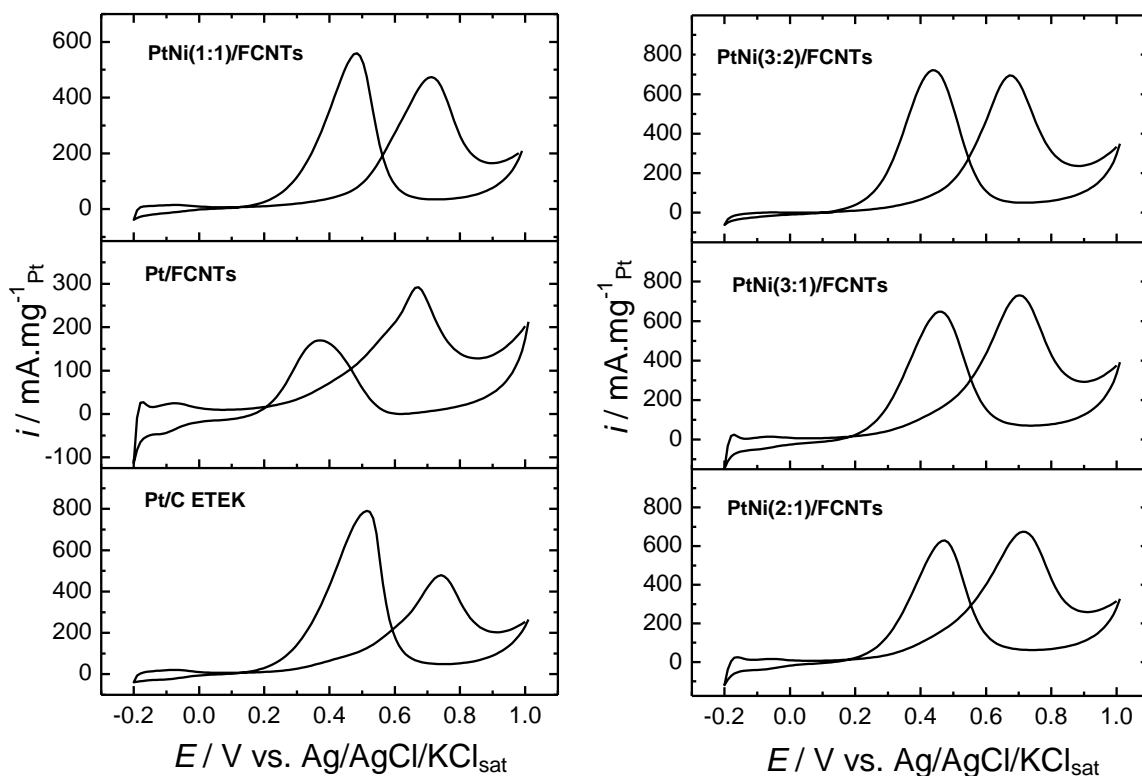


Figure 4.7: CV of Pt/C ETEK, Pt/FCNTs and PtNi/FCNTs electrocatalysts in 0.5 M H_2SO_4 / 1 M CH_3OH (scan rate 100 mV/s). The current was normalized to the mass of Pt in the electrode.

All PtNi/FCNTs show higher mass specific activity (which is relevant for fuel cell application from the viewpoint of costs) than the commercial Pt/C (E-TEK) except for PtNi(1:1), which exhibits activity very close to the commercial catalyst. However, Pt/FCNTs provide the lowest activity among all catalysts which probably can be attributed to the very small particle size of this catalysts (1.1 nm), and thus a decreased number of ensemble sites for methanol adsorption on their surface leading to lower activity as well as to strong bonding of the intermediate CO [4]. For PtNi (2:1), PtNi (3:1) and PtNi (3:2) catalysts, the activities are close to each other, which is not surprising as these catalysts possess similar atomic Pt to Ni ratios of 3:1 as determined with ICP-OES analysis, with PtNi (3:1) providing the highest activity among all catalysts. Additionally, the mass specific activities found by us are higher than those reported in the literature [72,73].

The order of activity changes if the surface specific activity is considered (i.e., the peak potential related to the surface area determined with CO stripping) (CVs see Figure 4.S16). As summarized in Table 4.6, the activity is highest in the catalyst with highest Ni content and decreases with Ni content. The virtual discrepancy between surface and mass specific activities certainly relates to the fact that the surface specific

Chapter 4: Ployol Synthesis of PtNi/CNTs Electrocatalysts

activities are related to the Pt atoms available at the surface only, which depends on particle size, Pt:Ni ratio etc. I.e., the individual Pt atoms at the surface of PtNi(1:1)/FCNT are obviously in average more active, but likely there are less of them leading to low mass specific activities. Compared to literature values, the lower SSA of our catalysts compared to literature values [72] might be due to the fact that we used CO stripping to determine surface areas whereas in the literature H adsorption desorption has been used. It is well known that the former yields higher surface areas [74] which might in part help to explain the lower SSA.

Table 4.6: Electrochemical parameters calculated from cyclic voltammetry measurements.

Catalyst	Peak potential [V]	Surface specific activity [mA/cm ²]	Mass specific activity [mA/mg _{Pt}]
Pt/C ETEK	0.742	1.00	478.2
Pt/CNTs	0.668	0.47	292.9
PtNi(1:1)/FCNTs as prepared	0.714	1.62	474.2
PtNi(1:1)/FCNTs 200	0.685	1.37	508.9
PtNi(1:1)/FCNTs 400	0.714	0.87	395.6
PtNi(2:1)/FCNTs as prepared	0.715	1.20	675.3
PtNi(2:1)/FCNTs 200	0.675	1.27	575.1
PtNi(2:1)/FCNTs 400	0.715	0.77	530.5
PtNi (3:1)/FCNTs asprepared	0.705	1.04	730.3
PtNi (3:1)/FCNTs 200	0.678	1.20	841.3
PtNi (3:1)/FCNTs 400	0.688	0.83	588.8
PtNi (3:2)/FCNTs asprepared	0.677	0.97	694.3
PtNi (3:2)/FCNTs 200	0.675	1.10	648.7
PtNi (3:2)/FCNTs 400	0.697	0.86	496.4

It is known that at least three adjacent Pt sites in the proper spatial arrangement are required in the methanol chemisorptions step [75]. Furthermore, poisoning CO has to be oxidized following either the electronic effect or the bifunctional mechanism. We assume that the arrangement of Pt to Ni on the surface of catalysts and therefore the population of Pt active site is the major factor determining the activity of PtNi catalysts for methanol oxidation also in our case. However, from our results it is hard to decide whether enhanced CO oxidation via the bifunctional mechanism or by an electronic effect occurs. The former is tentatively excluded since no early peak for CO oxidation is observed in the CO stripping voltammograms. The latter should however be taken into consideration since from the XPS results a shift in binding energy, although minor in nature, has been observed.

Other factors such as the particle size and the dispersion of the nanoparticles certainly additionally play a significant role determining catalytic activity. Also, the presence of oxygen functional groups on the surface of support could enhance the methanol oxidation on the catalysts surface through oxygen supply which facilitate the oxidation of adsorbed CO [37,46].

Heat treatment at 200 °C results in higher catalytic activity for most of the PtNi/FCNTs in terms of mass activity and peak potential than the as prepared catalyst (Table 4.6) which can be attributed to a cleaning of the catalyst surface from adsorbed organic residuals, making more active sites available for methanol oxidation. However, after treatment at 400 °C the surface and mass specific catalytic activity decreases dramatically for all catalysts. This can be attributed to the catalyst restructuring upon heat treatment as discuss above from CV, XRD, XPS and XAFS. Obviously this restructuring with the concomitant surface Pt-enrichment leads to a decrease in the population of highly active sites on the surface and probably changes the reaction mechanism [76]. Differences in CO poisoning are likely not responsible given the similar CO oxidation potentials in all catalysts.

Besides activity, stability of a catalyst is also a decisive factor in determining its suitability for real DMFC applications. The initial stability of PtNi catalysts has been studied by performing 200 repetitive cycles in 0.5M H₂SO₄/1 M CH₃OH.

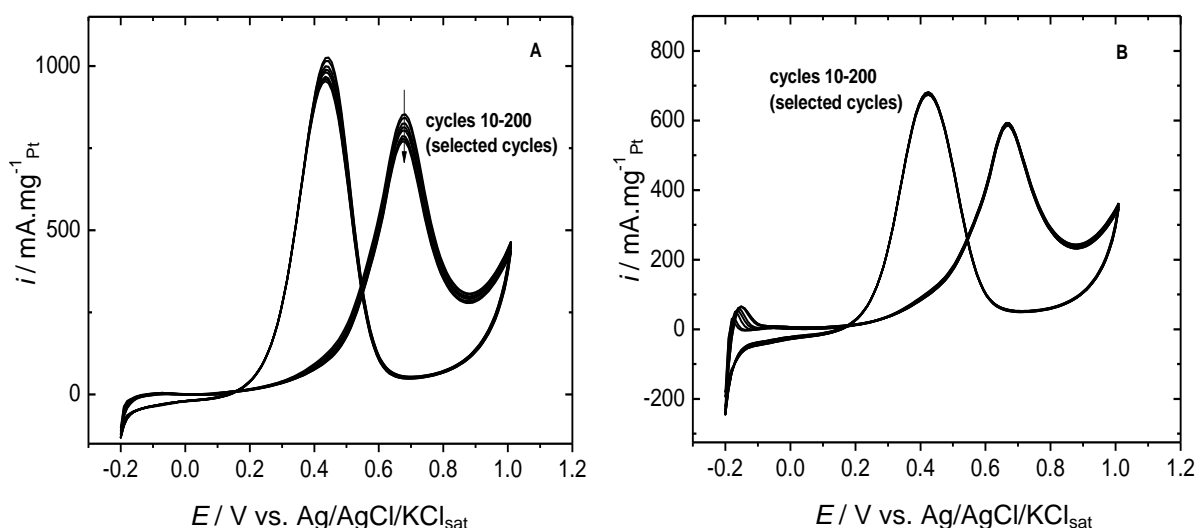


Figure 4.8: CV of PtNi(3:1)/FCNTs 200 (A) and PtNi(3:1)/FCNTs 400 (B) electrocatalysts in 0.5 M H₂SO₄/1 M CH₃OH (scan rate 100 mV/s).

Figure 4.8A shows the CV of selected cycle numbers for PtNi(3:1)/FCNTs. During the potential cycling, the current decreases slightly with increasing cycle number. Meanwhile, the CVs for PtNi(3:1)/FCNTs 400 (Figure 4.8B) show a different behavior. The characteristic peaks for hydrogen adsorption/desorption are more developed in

comparison to those for PtNi(3:1)/FCNTs and PtNi(3:1)/FCNTs 200 even in presence of methanol and these peaks further develop with increasing cycle number, in line with the observations from CO stripping showing more expressed Pt characteristics in the heat treated samples. The catalytic activity shows high stability with almost no change during the 200 cycles.

This behavior is visualized in Figure 4.9A, which shows the variation of current with the cycle number up to 200 cycles for as prepared PtNi/FCNTs. This figure indicates the long term stability for PtNi/FCNTs catalysts: PtNi (3:1) retains 92.2% from its initial current at cycle 5 after 200 cycles. On the other side, although the catalysts subjected to heat treatment at higher temperature (400 °C) showed lower activity than the as prepared ones and those after heat treatment at 200 °C, they show very high stability upon cycling up to 200 cycles. Figure 4.9B shows the variation of current with the number of cycle for the as prepared PtNi (3:1) in comparison to the heat treated one. After heat treatment at 400 °C the catalyst kept its initial activity within the limits of experimental error over 200 cycles in comparison with a retained current of 92.2% for the as- prepared one and 90 % for the one heat treated at 200 °C. Decrease in activity during cycling might be to Ni dissolution and/or restructuring, which does not occur in the already segregated samples treated at 400 °C, which are thus more stable. These features discussed above make the PtNi catalysts system with a proper surface concentration one of the most active catalysts for long term methanol fuel cells.

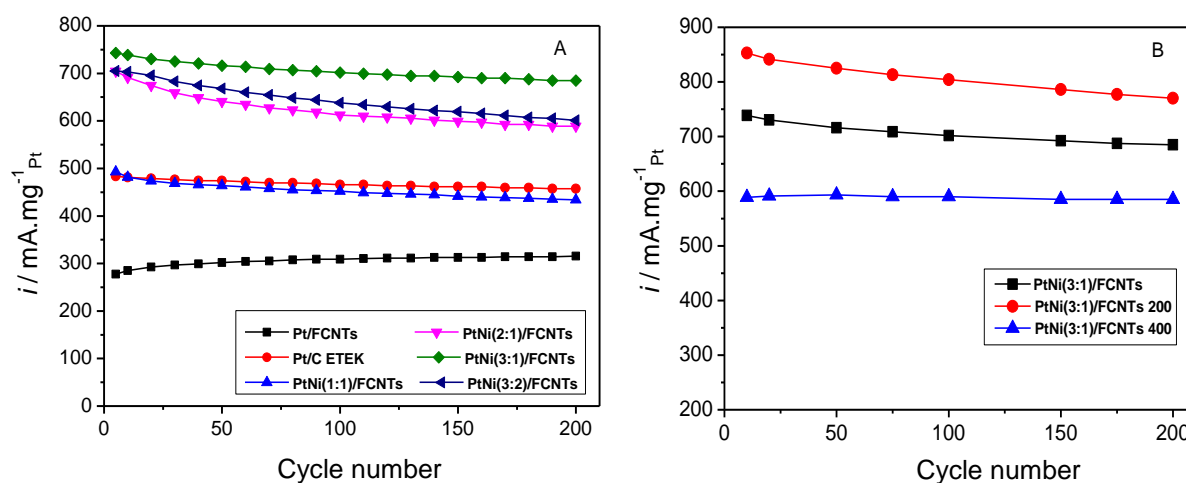


Figure 4.9: Variation of mass activity ($\text{mA}/\text{mg}_{\text{Pt}}$) with the number of cycle during the cycling potential, the data obtained for all catalysts from CV in 0.5 M H_2SO_4 /1 M CH_3OH , scan rate 0.1V/s for 200 cycle in potential window (-0.2 to 1 V, vs. Ag/AgCl).

4.4 Conclusion

PtNi/FCNTs with different Pt:Ni ratios have been prepared with ethylene glycol as reducing agent (polyol method). The catalysts display the Pt fcc structure with indications for alloy formation but also proofs for the presence of Ni oxides. Heat treatment at 400 °C in N₂ atmosphere resulted in phase separation/restructuring of the catalysts. A model is suggested where Ni-rich phases form close to the FCNTs which are surrounded by a Pt-rich alloy. It is important to mention that only the combination of advanced characterization techniques including XAS, XRD, TEM and XPS allowed to unravel the intricacies of the structures synthesized which would not have been possible from a single or two techniques alone. The highest catalytic activity was found for a Pt/Ni ratio of 3, which could be attributed to the availability and proper population of active Pt sites required for methanol adsorption in this catalyst and the easy removal of intermediate CO. Phase separation by heat treatment leads lower catalytic activity.

References

- [1] E.L. Gyenge, in: J. Zhang (Ed.), *PEM Fuel Cell Electrocatalysts and Catalyst Layers: Fundamentals and Applications*, Springer, New York, **2008**, pp. 165-270.
- [2] A.S. Aricò, S. Srinivasan, V. Antonucci, *Fuel Cells* **1** (**2001**) 133.
- [3] A. S.Aricò, V. Baglio, V. Antonucci, in: H. Liu, J. Zhang (Eds.), *Electrocatalysis of Direct Methanol Fuel Cells: From Fundamentals to Applications*, Wiley-VCh, **2009**, pp. 1-77.
- [4] Y. Tang, L. Zhang, Y. Wang, Y. Zhou, Y. Gao, C. Liu, W. Xing, T. Lu, *J. Power Sources* **162** (**2006**) 124.
- [5] R. Ganesan, D.J. Ham, J.S. Lee, *Electrochem. Commun.* **9** (**2007**) 2576.
- [6] M. Li, S. Zhao, G. Han, B. Yang, *J. Power Sources* **191** (**2009**) 351.
- [7] O.V. Cherstiouk, P.A. Simonov, E.R. Savinova, *Electrochim. Acta* **48** (**2003**) 3851.
- [8] D.-J. Guo, S-K. Cui, *J. Solid State Electrochem.* **12** (**2008**) 1393.
- [9] J. L. Lu Z. H. Li, S. P. Jiang, P. K. Shen, Lin Li, *J. Power Sources* **202** (**2012**) 56.
- [10] J. Kim, S.M. Choi, S.H. Nam, M.H. Seo, S.H. Choi, W.B. Kim, *Appl. Catal. B:* **82** (**2008**) 89.
- [11] T. Maiyalagan, T.O. Alaje, K. Scott, *J. Phys. Chem. C* **116** (**2012**) 2630.
- [12] H. Zhang, X. Xu, P. Gu, C. Li, P. Wu, C. Cai, *Electrochim. Acta* **56** (**2011**) 7064.
- [13] L. Feng, G.Gao, P. Huang, X. Wang, C. Zhang, J. Zhang, S.Guo, D. Cui, *Nanoscale Res. Lett.* **6** (**2011**) 551.
- [14] Y. Q. Wang, Z.D. Wei, L. Li, M.B. Ji, Y. Xu, P.K. Shen, J. Zhang, H. Zhang, *J. Phys. Chem. C* **112** (**2008**) 18672.
- [15] S. Papadimitriou, S. Armyanov, E. Valova, A. Hubin, O. Steenhaut, E. Pavlidou, G. Kokkinidis, S. Sotiropoulos, *J. Phys. Chem. C* **114** (**2010**) 5217.
- [16] R. Lin, C. Cao, H. Zhang, H. Huang, J. Ma, *Int. J. Hydrogen Energy* **37** (**2012**) 4648.
- [17] E. Lee, A. Manthiram, *J. Phys. Chem. C* **114** (**2010**) 21833.
- [18] D.R. Ou, T. Mori, H. Togasaki, M. Takahashi, F. Ye, J. Drennan, *Langmuir* **27** (**2011**) 3859.
- [19] B.Y. Xia, S. Ding, H.B. Wu, X. Wang, X. Wen, *RSC Advances* **2** (**2012**) 792.
- [20] P. Justin, P. H. K. Charan, G. R. Rao, *Appl. Catal. B:* **100** (**2010**) 510.
- [21] H. Yuan, D. Guo, X. Qiu, W. Zhu, L. Chen, *J. Power Sources* **188** (**2009**) 8.
- [22] H. Liu, D. Xia, J. Zhang, in: J. Zhang (Ed.), *PEM Fuel Cell Electrocatalysts and Catalyst Layers: Fundamentals and Applications*, Springer, New York (**2008**), pp. 631-654.
- [23] X. Zhao, M. Yin, L. Ma, L. Liang, C. Liu, J. Liao, T. Lu, W. Xing, *Energy Environ. Sci.* **4** (**2011**) 2736.
- [24] P.P. Lopes, K.S. Freitas, E.A. Ticianelli, *Electrocatal.* **1** (**2010**) 200.
- [25] M. Watanabe, S. Motoo, *J. Electroanal. Chem.* **60** (**1975**) 275.

- [26] T. Frelink, W. Visscher, J.A.R. van Veen, *Surf. Sci.* 335 (1995) 353.
- [27] K.-W. Park, J.-H. Choi, B.-K. Kwon, S.-A. Lee, Y.-E. Sung, H.-Y. Ha, S.-A. Hong, H. Kim, A. Wieckowski, *J. Phys. Chem. B* 106 (2002) 1869.
- [28] Q. Jiang, L. Jiang, H. Hou, J. Qi, S. Wang, G. Sun, *J. Phys. Chem. C* 114 (2010) 19714.
- [29] R. Chetty, S. Kundu, W. Xia, M. Bron, W. Schuhmann, V. Chirila, W. Brandl, T. Reinecke, M. Muhler, *Electrochim. Acta* 54 (2009) 4208.
- [30] A. B. Kashyout, A.B. A.A. Nassr, L. Giorgi, T. Maiyalagan, B.A. B. Youssef, *Int. J. Electrochem. Sci.* 6 (2011) 379.
- [31] X. Wang, H. Wang, R. Wang, Q. Wang, Z. Lei, *J. Solid State Electrochem.* 16 (2012) 1049.
- [32] E. Lee, A. Murthy, A. Manthiram, *J. Electroanal. Chem.* 659 (2011) 168.
- [33] J. Zeng, J.Y. Lee, *J. Power Sources* 140 (2005) 268.
- [34] C.-T. Hsieh, J.-Y. Lin, *J. Power Sources* 188 (2009) 347.
- [35] N.P. Lebedeva, G.J.M. Janssen, *Electrochim. Acta* 51 (2005) 29.
- [36] P. Hernández-Fernández, M. Montiel, P. Ocón, J.L.G. Fierro, H. Wangc, H.D. Abruna, S. Rojas, *J. Power Sources* 195 (2010) 7959.
- [37] R.S. Amin, K.M. El-Khatib, R.M. Abdel Hameed, E.R. Souay, M.A. Etman, *Appl. Catal. A*: 407 (2011) 195.
- [38] T.C. Deivaraj, W. Chen, J.Y. Lee, *J. Mater. Chem.* 13 (2003) 2555.
- [39] Q. Jiang, L. Jiang, S. Wang, J. Qi, G. Sun, *Catal. Commun.* 12 (2010) 67.
- [40] A.A. El-Shafei, *J. Electroanal. Chem.* 471 (1999) 89.
- [41] R. Manoharan, J.B. Goodenough, *J. Mater. Chem.* 2 (1992) 875- 887.
- [42] Y. Liang, H. Zhang, Z. Tian, X. Zhu, X. Wang, B. Yi, *J. Phys. Chem. B* 110 (2006) 7828.
- [43] S. Jiang, Y. Ma, H. Tao, G. Jian, X. Wang, Y. Fan, J. Zhu, Z. Hu, *J. Nanosci. Nanotechnol.* 10 (2010) 3895.
- [44] K.V. Klementiev, *VIPER for Windows*, freeware, K.V. Klementev, *J. Phys. D: Appl. Phys.* 34 (2001) 209. www.cells.es/Beamlines/CLAESS/software/viper.html
- [45] A.L. Ankudinov, B. Ravel, J.J. Rehr, S.D. Conradson, *Phys. Rev. B*: 58 (1998) 7565.
- [46] P. Hernandez-Fernandez, S. Baranton, S. Rojas, P. Ocon, J.-M. Leger, J.L.G. Fierro, *Langmuir* 27 (2011) 9621.
- [47] J.L. Figueiredo, M.F.R. Pereira, M.M.A. Freitas, J.J.M. Orfao, *Carbon* 37 (1999) 1379.
- [48] W. Xia, Y. Wang, R. Bergstraßer, S. Kundu, M. Muhler, *Appl. Surf. Sci.* 254 (2007) 247.
- [49] A.E. Aksoylu, M. Madalena, A. Freitas, M. Fernando, R. Pereira, J.L. Figueiredo *Carbon* 39 (2001) 175.

- [50] D.Z. Mezalira, L.D. Probst, S. Pronier, Y. Batonneau, C. Batiot-Dupeyrat, *J. Mol. Catal. A*: 340 **(2011)** 15.
- [51] W. Zhang, J. Chen, G.F. Swiegers, Z.-F. Mab, G.G. Wallace, *Nanoscale*, 2 **(2010)** 282.
- [52] R. Kannan, U. Bipinlal, S. Kurungot, V.K. Pillai, *Phys. Chem. Chem. Phys.* 13 **(2011)** 10312.
- [53] H.-S. Oh, J.-G. Oh, Y.-G. Hong, H. Kim, *Electrochim. Acta* 52 **(2007)** 7278.
- [54] L. Ren, Y. Xing, *Electrochim. Acta* 53 **(2008)** 5563.
- [55] V.A. Ribeiro, O.V. Correa, A.O. Neto, M. Linardi, E.V. Spinace, *Appl. Catal. A*: 372 **(2010)** 162.
- [56] H. Wu, D. Wexler, G. Wang, *J. Alloys Compd.* 488 **(2009)** 195.
- [57] T.-Y. Jeon, S.J. Yoo, Y.-H. Cho, K.-S. Lee, S.H. Kang, Y.-E. Sung, *J. Phys. Chem. C* 113 **(2009)** 19732.
- [58] G. Johansson, J. Hedman, A. Berndtsson, M. Klasson, R. Nilsson, *J. Electron Spectrosc. Relat. Phenom.* 2 **(1973)** 295.
- [59] S.D. Cameron, D.J. Dwyer, *Surf. Sci.* 176 **(1986)** L857.
- [60] M.G. Manson, *Phys. Rev. B* 27**(1983)** 748.
- [61] G.K. Wertheim, S.B. Diczko, S.E. Youngquist, *Phys. Rev. Lett.* 51 **(1983)** 2310.
- [62] L.A. Feldkamp, L.C. Davis, *Phys. Rev. B* 22 **(1980)** 3644.
- [63] R. Loukrakpam, J. Luo, T. He, Y. Chen, Z. Xu, P. N. Njoki, B. N. Wanjala, B. Fang, D. Mott, J. Yin, J. Klar, B. Powell, C.-J. Zhong, *J. Phys. Chem. C* 115 **(2011)** 1682.
- [64] M.V. Martinez-Huerta, S. Rojas, J.L. Gomez de la Fuente, P. Terreros, M.A. Pena, J.L.G. Fierro, *Appl. Catal. B* 69 **(2006)** 75.
- [65] B.-J. Hwang, L. S. Sarma, J.-M. Chen, C.-H. Chen, S.-C. Shih, G.-R. Wnag, D.-G. Liu, J.-F. Lee, M.-T. Tang, *J. Am. Chem. Soc.* 127 **(2005)** 11140.
- [66] H.-Y. Lee, W. Vogel, P.P.-J. Chu, *Langmuir* 27 **(2011)** 14654.
- [67] J. Prabhuram, T.S. Zhao, Z.K. Tang, R. Chen, Z.X. Liang, *J. Phys. Chem. B* 110 **(2006)** 5245.
- [68] Z. Liu, F. Su, X. Zhang, S.W. Tay, *ACS Appl. Mater. Interfaces* 3 **(2011)** 3824.
- [69] L. Ma, X. Zhao, F. Si, C. Liu, J. Liao, L. Liang, W. Xing, *Electrochim. Acta* 55 **(2010)** 9105.
- [70] Y.-Y. Chu, Z.-B. Wang, Z.-Z. Jiang, D.-M. Gu, G.-P. Yin, *Fuel Cells* 10 **(2010)** 914.
- [71] Z. Sun, X. Wang, Z. Liu, H. Zhang, P. Yu, L. Mao, *Langmuir* 26 **(2010)** 12383.
- [72] C. Xu, J. Hou, X. Pang, X. Li, M. Zhu, B. Tang, *Int. J. Hydrogen Energy* 37 **(2012)** 10489.
- [73] B. Lu, S. Xu, X. Yan, Q. Xue, *Electrochem. Comm.* 23 **(2012)** 72.
- [74] K.J.J. Mayrhofer, D. Strmcnik, B.B. Blizanac, V. Stamenkovic, M. Arenz, N.M. Markovic, *Electrochim. Acta* 53 **(2008)** 3181.

Chapter 4: Ployol Synthesis of PtNi/CNTs Electrocatalysts

- [75] H.A. Gasteiger, N. Markov, P.N. Ross Jr, E.J. Cairns, *J. Phys. Chem.* 97 **(1993)** 12020.
- [76] P. Hernandez-Fernandez, S. Rojas, P. Ocon, A. de Frutos, J.M. Figueroa, P. Terreros, M.A. Pena, J.L.G. Fierro, *J. Power Sources* 177 **(2008)** 9.

Supporting information

Characterization of FCNTs

Figure SI4.1 shows the TPD profiles of as received carbon nanotubes and functionalized nanotubes. In the profile of the functionalized nanotubes desorption of water ($m/e = 18$) can be detected at two different temperatures. The first sharp peak close to 100 °C indicates the evolution of physically adsorbed water and the second broad peak at 200 °C refers to desorption of chemically bonded water which is produced from the condensation reaction between two carboxylic groups to form the anhydride [ref. 46].

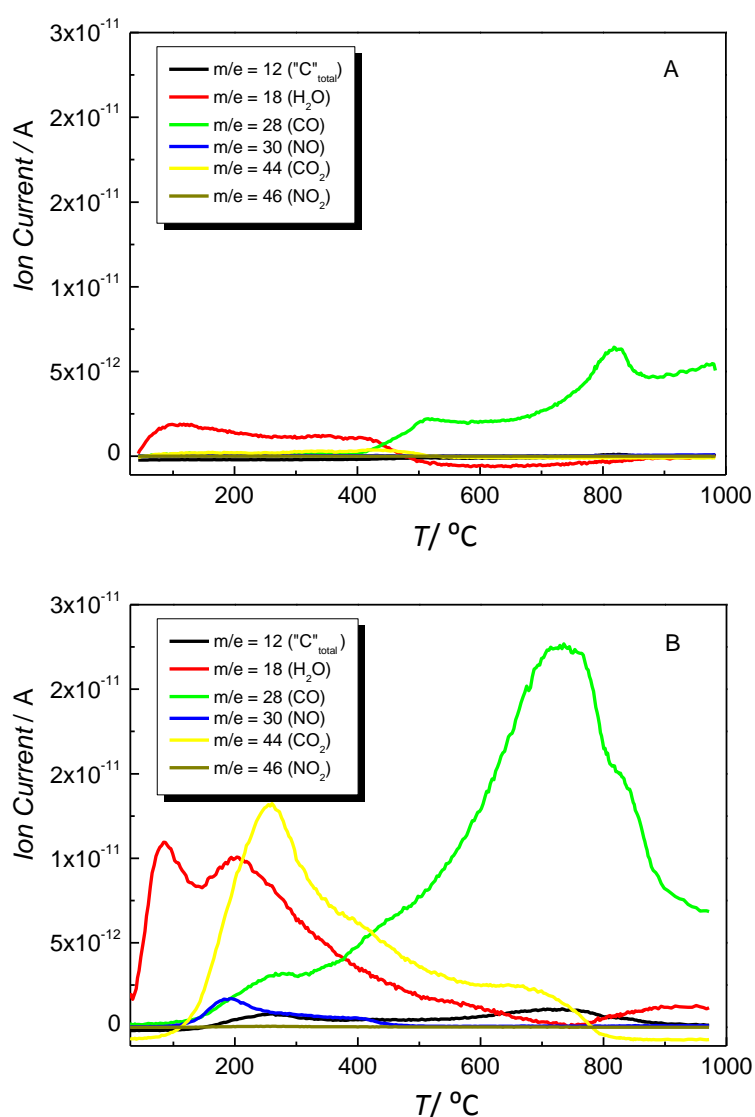


Figure SI4.1: TPD of as received (A) and functionalized (B) CNTs.

The release of CO_2 ($m/e = 44$) was detected with a sharp peak at 260°C and a shoulder at about 400°C , which indicate the decomposition of carboxylic acid at lower temperature and anhydride groups at higher temperature. The evolution of CO_2 is still detected even at temperature higher than 600°C which is attributed to decomposition of lactones [47]. On the other hand the continuous evolution of CO ($m/e = 28$) at higher temperature with an intense peak can be assigned to the presence of phenol, ether, carbonyl and quinone groups [46,47]. The peak at about 180°C for NO ($m/e = 30$) refers to nitrogen containing groups in the FCNTs. On the other hand, the TPD profile of the as received CNTs shows only the release of relative small amounts of water at lower temperatures and a small peak for CO at higher temperatures.

The thermal stability of CNTs in oxygen atmosphere was studied using TGA analysis. Figure SI4.2 shows the TGA of as received and functionalized CNTs. At a temperature of up to 100°C there is no any significant weight loss, since the samples were heated before at this temperature to prevent the inference from weight loss due to physically adsorbed water. In the temperature range from 200 to 400°C , the functionalized CNTs show a minor weight loss which could be attributed to the decomposition of surface functionalized groups while the as received CNTs don't show any weight loss in this temperature range (48), in agreement with the TPD profiles (see Figure SI4.1).

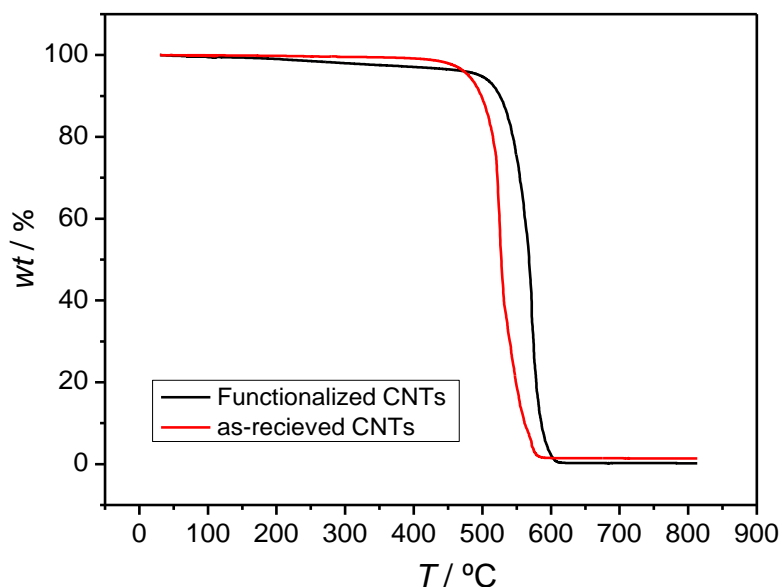


Figure SI4.2: TGA of as received CNTs and Functionalized carbon nanotubes (FCNTs) in O_2 atmosphere.

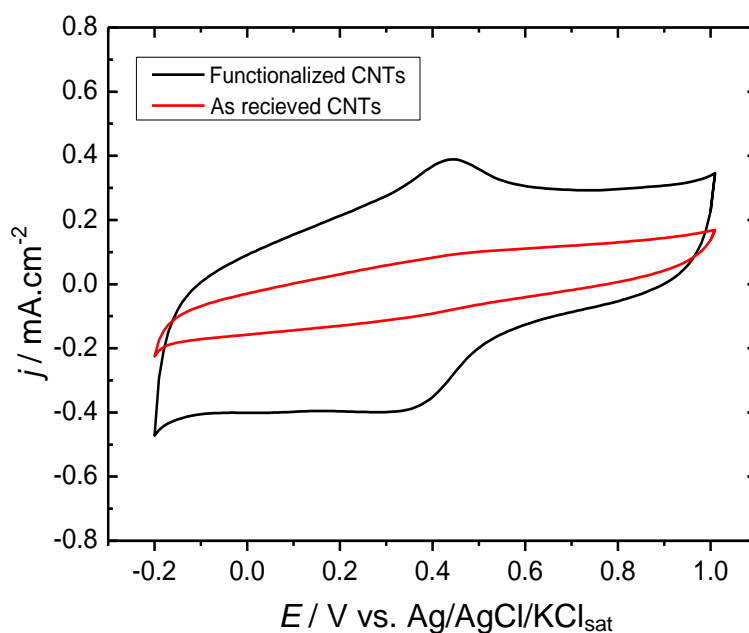


Figure SI4.3. Cyclic voltammogram for as received CNTs and nitric acid functionalized CNTs in 0.5 M H_2SO_4 (scan rate 100 mV/s).

Textural properties of the CNTs before and after functionalization have been studied with N_2 adsorption/desorption, and isotherms for as received and functionalized CNTs are shown in Figure SI4.4. The specific surface area and pore specific volume were determined using the Brunauer–Emmett–Teller (BET) method. The average pore size was determined using the Barrett–Joyner–Halenda (BJH) method. The data are summarized in Table SI4.1. The surface area increases from 249.7 m^2/g to 289.3 m^2/g upon the functionalization while pore volume and pore size almost did not change. The slight increase in surface area of FCNTs could be attributed to the introduction of surface defects. These results indicate that the mild functionalization method was able to introduce surface functional groups on the surface of CNTs while largely preserving their textural properties.

Table SI4.1: Textural properties for CNTs as obtained from BET surface area measurements.

Sample	Specific surface area [m^2/g]	Pore specific volume [cm^3/g]	Average pore size [nm]
CNTs (as received)	249.7	1.48	22.9
CNTs (Functionalized)	289.3	1.44	21.9

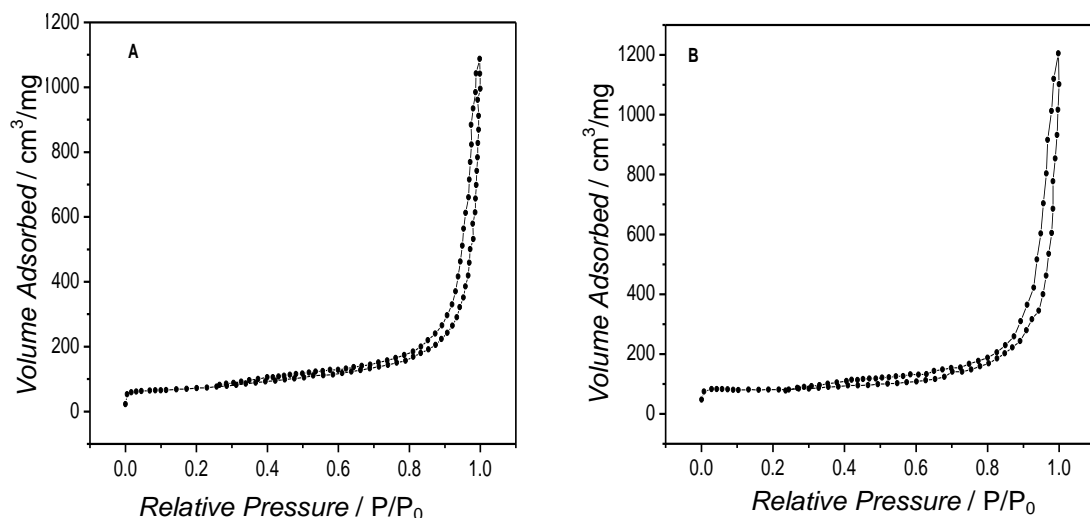


Figure SI4.4: N₂ adsorption-desorption isotherm for as received CNTs and functionalized CNTs.

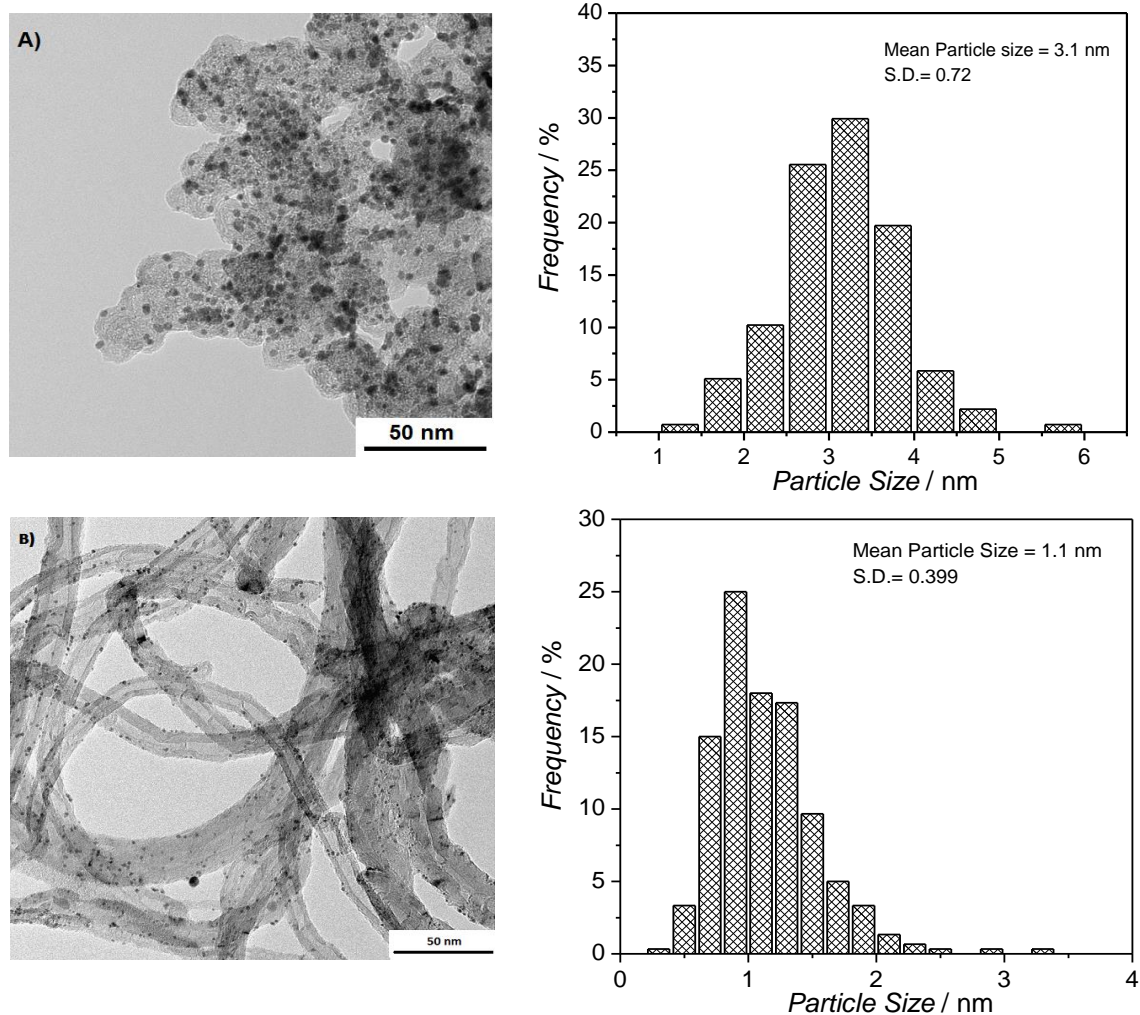


Figure SI4.5: TEM images of A) Pt/C (ETEK), B) Pt/FCNTs and C) PtNi(1:1)/FCNTs, D) PtNi(2:1)/FCNTs, E) PtNi(3:1)/FCNTs, F) PtNi(3:2)/FCNTs, G) PtNi(1:1)/FCNTs 200, H) PtNi(3:2)/FCNTs 400.

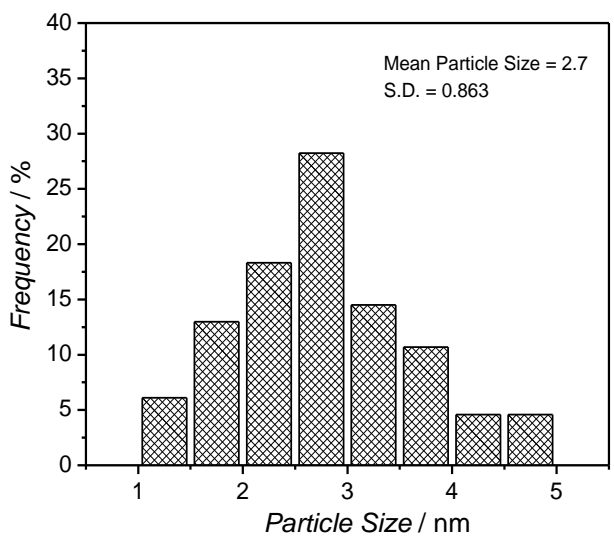
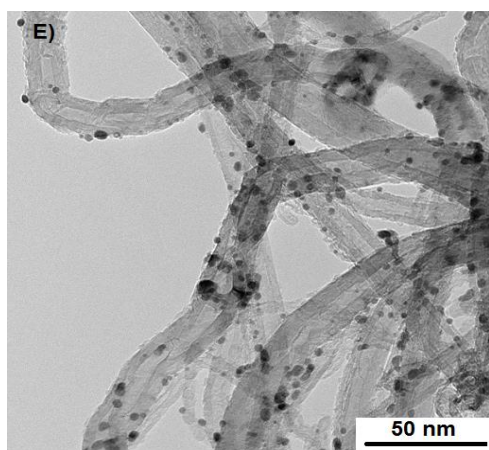
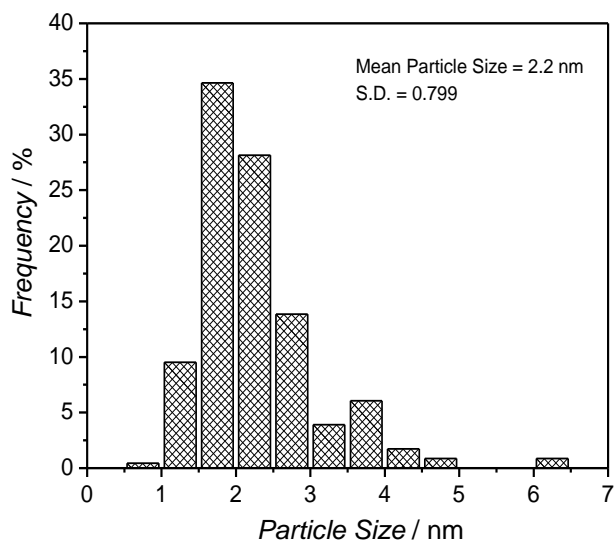
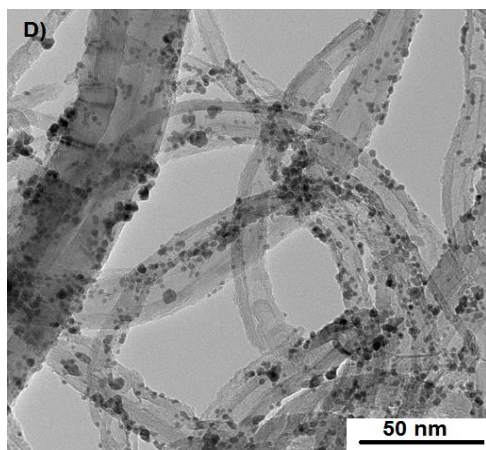
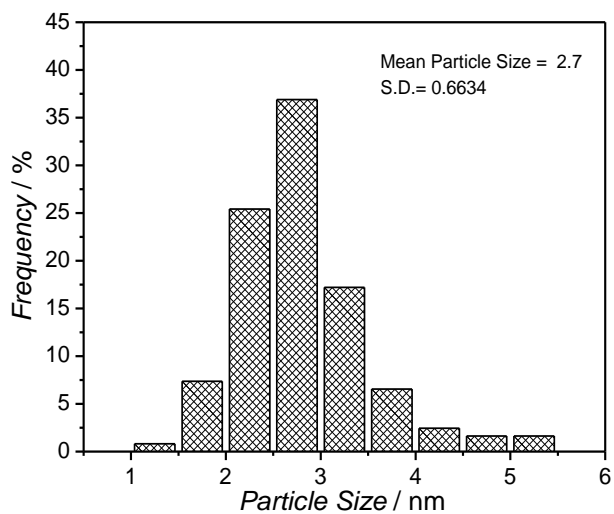
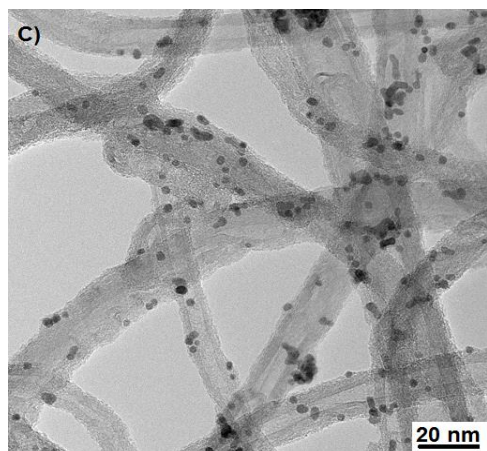


Figure SI4.5: continued

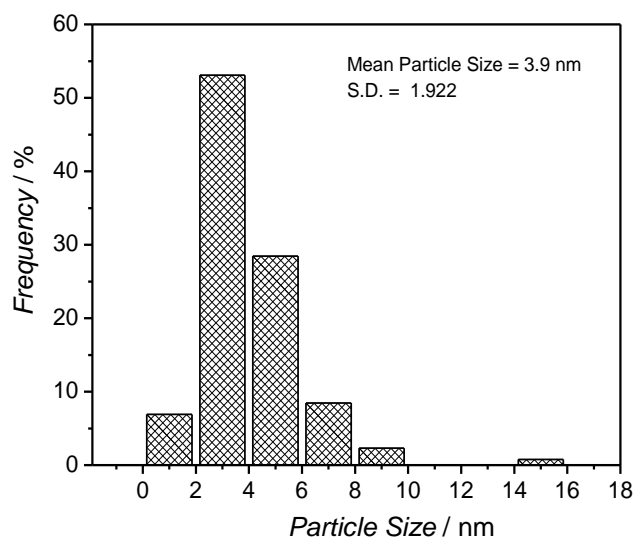
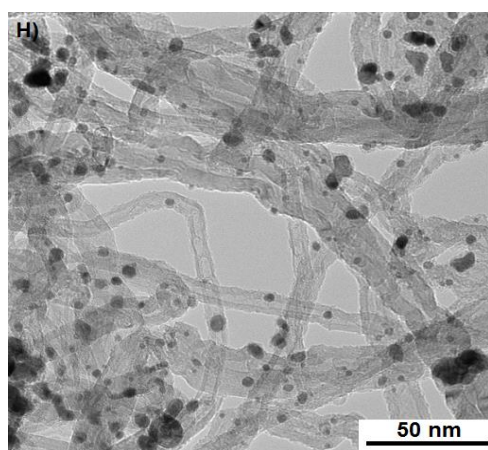
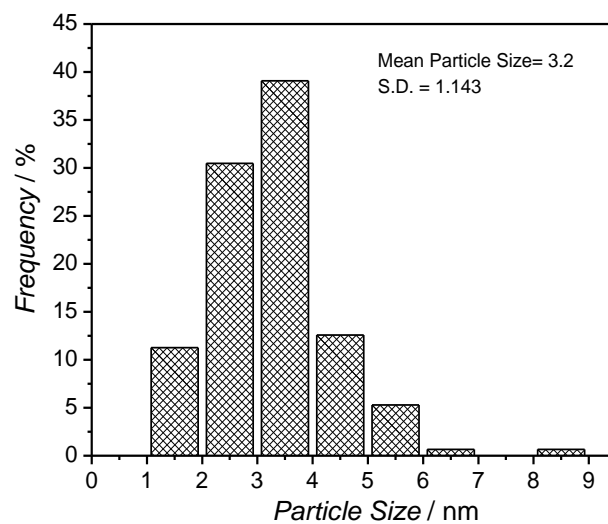
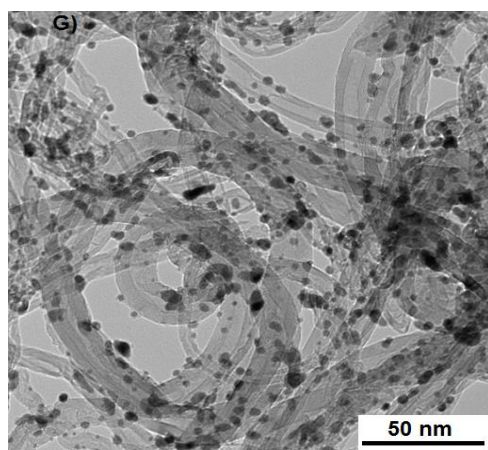
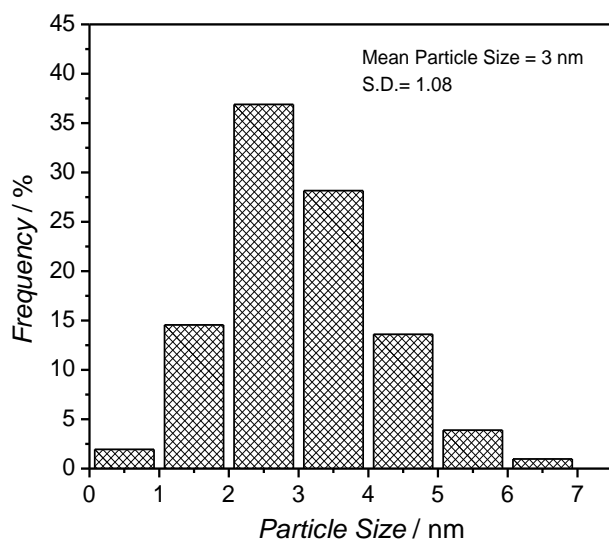
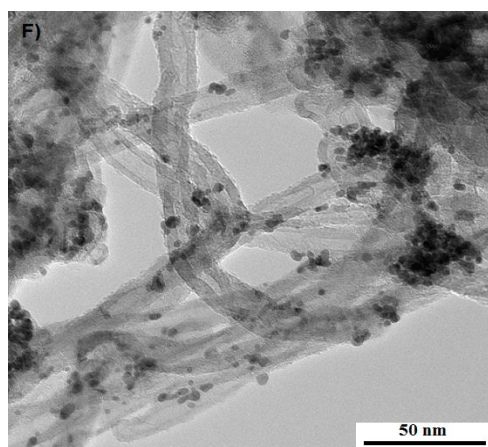


Figure SI4.5: continued

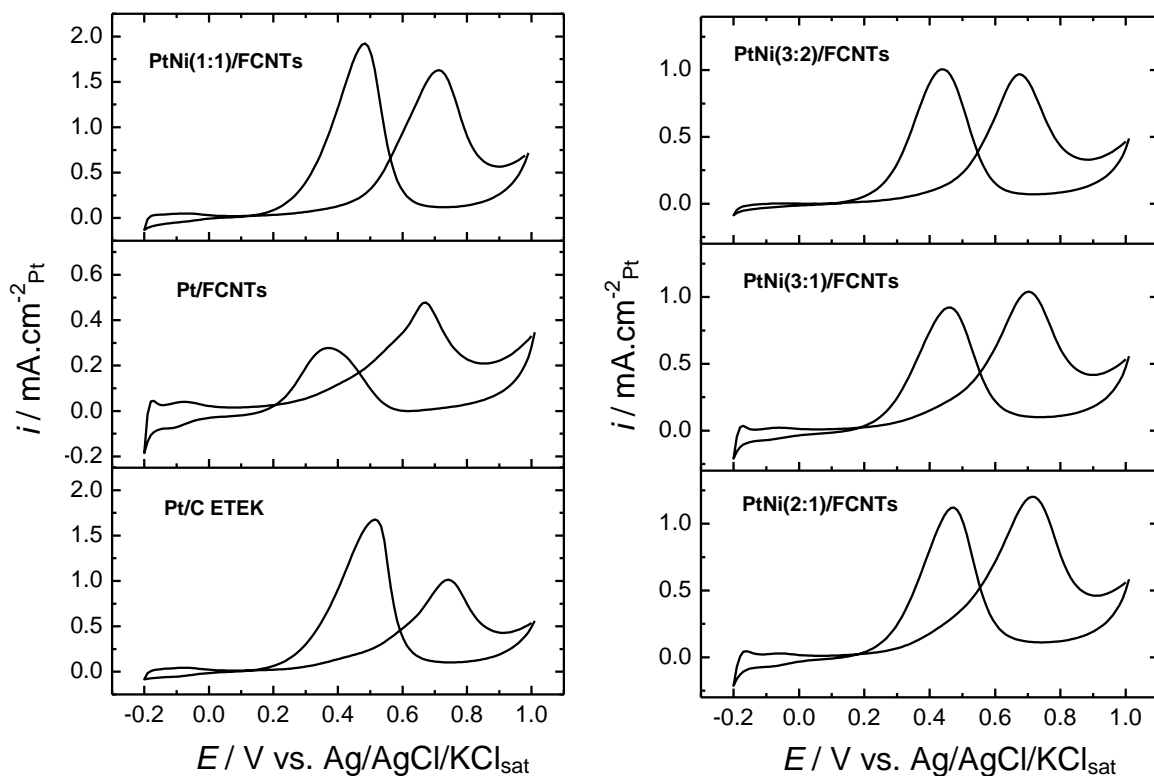


Figure SI4.6: CV of Pt/C ETEK, Pt/FCNTs and PtNi/FCNTs electrocatalysts in 0.5 M H_2SO_4 / 1 M CH_3OH (scan rate 100 mV/s). Current is normalized to electrochemical surface area of the electrode.

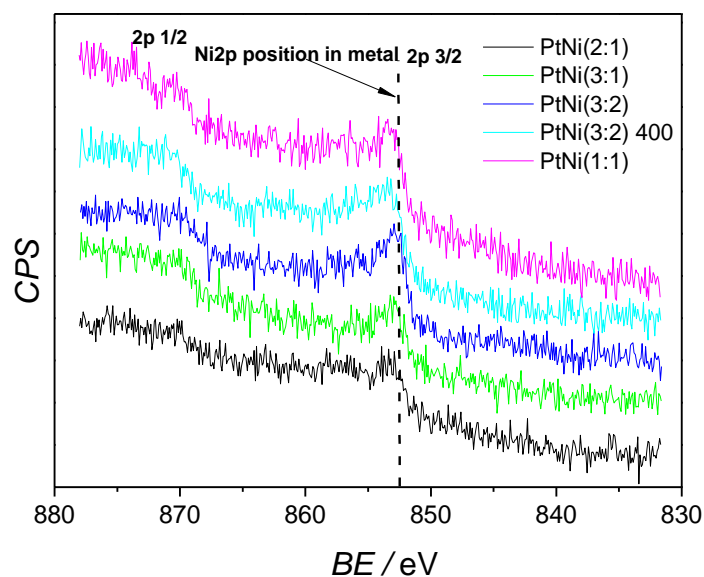


Figure SI4.7: Ni 2p X-ray photoelectron spectra of samples after He^+ sputtering.

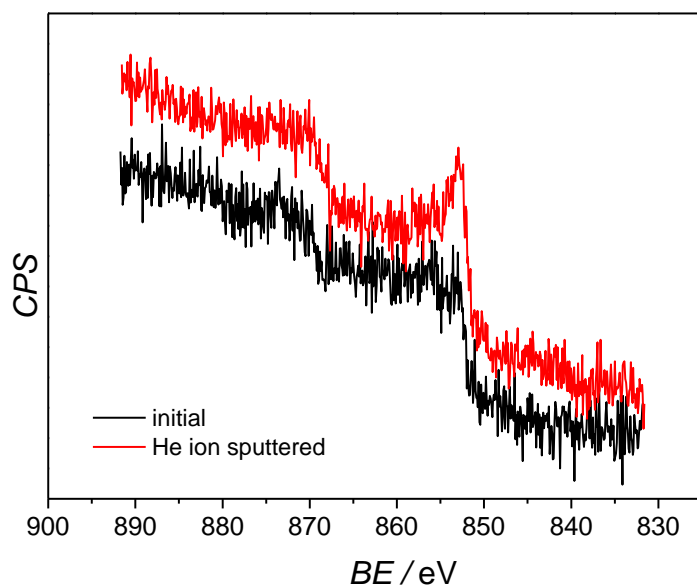


Figure SI4.8: Ni 2p X-ray photoelectron spectra of PtNi(3:2)/FCNTs sample before and after He⁺ sputtering.

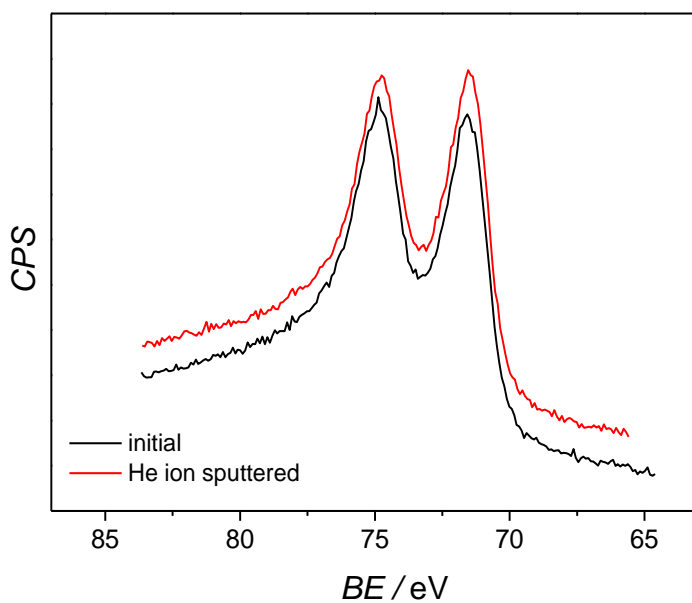


Figure SI4.9: Pt 4f X-ray photoelectron spectra of PtNi(3:2)/FCNTs sample before and after He⁺ sputtering.

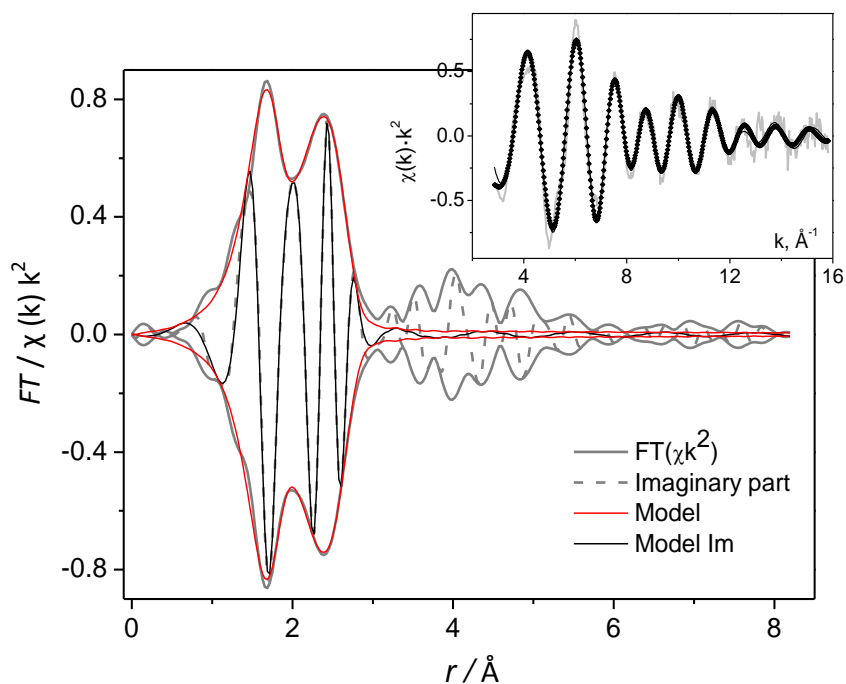


Figure SI4.10: Model fit of NiK-edge EXFAS spectrum of PtNi(1:1)/FCNTs.

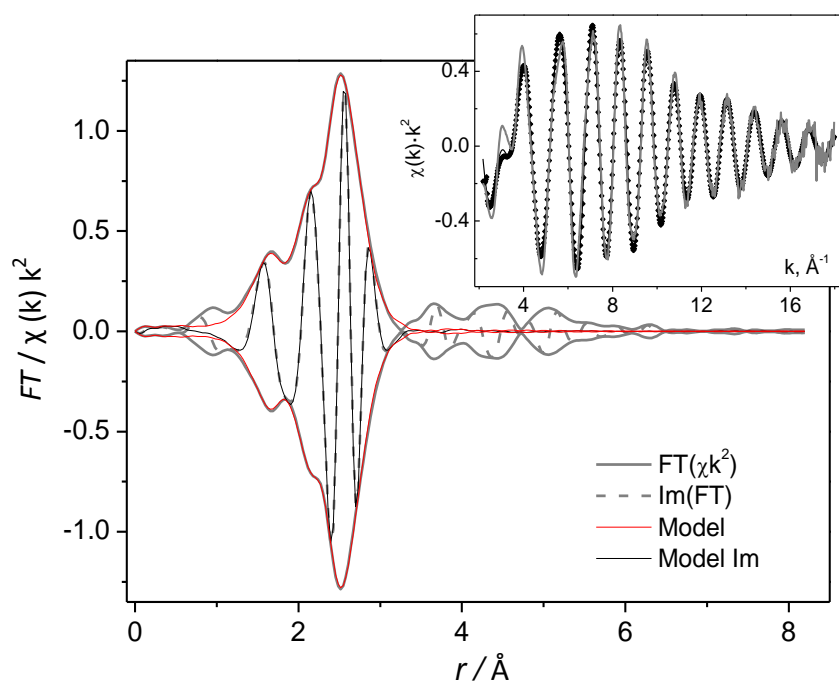


Figure SI4.11: Model fit of PtL₃-edge EXAFS spectrum of PtNi(1:1)/FCNTs.

The content of this chapter has been submitted for publication in ACS Catalysis as

Rapid microwave-assisted polyol reduction for the preparation of highly active PtNi/CNTs electrocatalysts for methanol oxidation

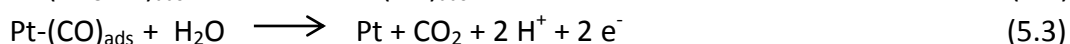
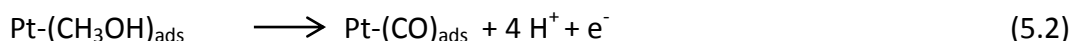
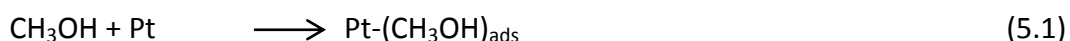
Abu Bakr Ahmed Amine Nassr, Ilya Sinev, Wolfgang Grünert, Michael Bron

5.1 Introduction

Methanol has received significant attention as fuel in low temperature fuel cells (DMFCs, direct methanol fuel cells), which are discussed as possible power sources for many portable and transportation applications ranging from mobile phones to vehicles [5,6]. Methanol has several advantages compared to hydrogen: it is easy and safe to handle, store and transport. Furthermore, it has a higher energy density than hydrogen and can be produced from biomass via syngas or through fermentation of agricultural products [1-4]. However, the electrooxidation of methanol occurring at the anode side of DMFCs is associated with poor kinetics and a resulting decrease in cell efficiency. The development of highly active anode catalysts is urgently needed to overcome these technical obstacles.

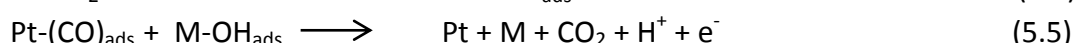
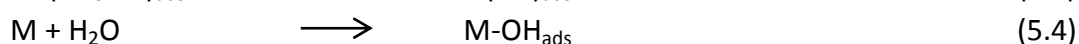
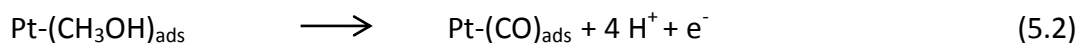
Pt is well known as the most active catalytic material for methanol oxidation but surface poisoning with CO molecules formed as an intermediate during methanol oxidation quickly deteriorates the activity of Pt electrodes when used as catalyst in direct methanol fuel cells [7]. It is well established that complete methanol oxidation is a complex multistep reaction that requires active sites for methanol adsorption and dehydrogenation as well as sites supplying oxygen-containing species for oxidation the carbonaceous intermediates formed during adsorption and dehydrogenation [8-11].

The methanol oxidation on Pt can be represented by three main steps. The first two steps involve the adsorption of methanol and its dehydrogenation to form adsorbed CO. In the third step, the adsorbed CO is oxidized with the aid of oxygen-containing species (e.g., -OH) formed on the Pt surface. The mechanism can be written by the following Equations 5.1- 5.3 [11].



Indeed, the fact that oxygen species form on the Pt surface only at higher potentials (0.7 V vs. RHE) creates a significant overpotential that limits the applicability of Pt catalysts for the methanol oxidation reaction (MOR) [8,11].

Alloying of Pt with a second metal that can supply the oxygen species at lower potentials is one strategy to decrease the poisoning of the Pt surface with CO and enhance the activity of the catalyst toward methanol oxidation [12-14]. Second metals such as M = Ru, Sn, Au, Co, Ni, or Pd [13-18] have been suggested. Moreover, oxides of transition metals have been also demonstrated to performing the same function [19-24]. The mechanism can then be represented the following Equations 5.4-5.6:



Besides this so-called bifunctional mechanism, the electronic mechanism or ligand effect has been also postulated [25,26]. It is assumed that the second metal can modify the electronic properties of Pt by changing the electron density of states of the d-band and the Fermi level energy. This electronic modification destabilizes the interaction between the CO molecules and the Pt surface and hence suppresses the Pt-CO bonding [17,26, 27].

PtNi catalysts exhibit good catalytic activity for methanol oxidation and are considered more economical than other systems owing to the lower cost of Ni [17,27-29]. The electronic mechanism of Ni in Ni containing catalysts (PtNi and PtRuNi) has been confirmed experimentally [27]. Higher activity of Ni containing catalysts was explained by electron transfer from Ni to Pt detected from shifts in the Pt 4f bind energy to lower values, resulting in a weakening of the adsorption of CO molecules onto the Pt surface. Recently a theoretical study by DFT confirmed the downshift of the Pt d-band center as a results of Ni incorporation, decreasing the interaction between Pt and CO, consistent with XPS and electrochemical results [17,26,27].

Electrocatalysis is a surface reaction that depends strongly on the surface properties of the catalyst onto which the reactants adsorb and react to give the products. Thus the structural properties of the catalysts like particle size and shape as well as interaction with the support are important factors controlling the catalytic process. The catalyst preparation methods should be tuned to yield the desired catalyst features which lead finally to the demanded higher activity. Microwave synthesis is one of the recent techniques for synthesis of catalysts with nanosized particles, high dispersion and narrow particle size distribution which meet the demanded higher catalytic activity for fuel cell applications [28,29]. The advantage of microwave preparation is the fast and homogenous heating resulting from the interaction of microwave radiation directly with the solvent molecules and the reducing agent. Short nucleation and crystallization time can be achieved resulting in small particle sizes and high dispersion. Also, the generation of localized high

temperature as a result of the fast heating enhances the rate of metal ion reduction. Moreover, the simplicity of the equipment and the short reaction time render this technique energy saving and meet economical considerations [30,31]. Despite many studies on the influence of preparation conditions on Pt and Pt-based electrocatalysts for fuel cell applications using microwave assisted synthesis [24,28,29] there was no such study on PtNi catalysts which could show how the mode of irradiation influences their structural properties and hence offers an avenue to tune their catalytic behavior.

In this study we report on the preparation of PtNi nanocatalysts supported on oxygen functionalized carbon nanotubes (FCNTs) using the microwave-assisted polyol method in which ethylene glycol (EG) is used as solvent and reducing agent at the same time. The effect of irradiation mode (continuous or pulsed irradiation), the irradiation duration under these two modes as well as aging of the catalyst prepared und continuous irradiation on catalyst structure is studied with ICP-OES, XRD, TEM, XPS and XAS. The catalytic activity of the prepared catalysts toward methanol oxidation has been evaluated and discussed in correlation to the structural properties and compared with the benchmark catalyst Pt/C from E-TEK.

5.2 Experimental work

5.2.1 Catalyst preparation

PtNi catalysts supported on functionalized carbon nanotubes (FCNTs) were prepared using microwave-assisted polyol reduction according to the following procedures. First, the as received CNTs (Baytubes C 150 P, obtained from Bayer Material Science AG, Germany) were functionalized with 5 M HNO₃ as reported elsewhere [32] to create oxygen functional groups on the surface of CNTs. 100 mg of FCNTs were dispersed under stirring in 30 ml of ethylene glycol (EG). To this dispersion, the required amounts of metal salts (Ni(NO₃)₂ · 6 H₂O and H₂PtCl₆), each dissolved in 5 ml of EG, were added dropwise in sequence under stirring and left under stirring for 30 min. The pH of the mixture was modified with 2 M NaOH/EG to pH 11 and the suspension was left stirring for 30 min. Then the solution was sonicated in an ultrasonic bath for 15 min. For metal ion reduction, the mixture was transferred into a microwave reactor (Microwave START 1500, Milestone) where it was irradiated at 700 W either continuously for a defined time or in a pulsed mode with a pulse duration of 20 s (10 s on and 10 s off) for a specific number of pulses. The microwave step was followed by aging of the catalyst under stirring overnight. Two reference samples were prepared, one without aging and one with pH modification during the aging step. The detailed preparation conditions are summarized in Table 5.1. The catalysts were separated by centrifugation (Centrifuge 4807, Eppendorf) for 20 min at 5000 rpm and subjected to 5-6 washing cycles with water before drying at 80 °C overnight. Finally, the catalysts were crushed in a mortar and stored in glass vials until used. In the

Chapter 5: Microwave-Assisted Polyol Synthesis of PtNi/CNTs Electrocatalysts

preparations, we aimed at a metal loading of 20 wt.%. The Pt/Ni atomic ratio in the precursor solution was 1.

All catalysts are labeled PtNi/CNT followed by a "C" and the irradiation duration in s for continuous irradiation and a "P " and the pulse number for pulsed irradiation. For example, PtNi/CNT_C_90 and PtNi/CNT_P_18 refer to catalysts prepared with continuous irradiation for 90 s and with pulsed irradiation for 18 pluses, respectively.

Table 5.1: Details of the preparation conditions for PtNi/CNT catalysts under microwave irradiation.

PtNi/CNT Catalysts	Irradiation Mode	Reaction Time	Aging Conditions
C_90_na	continuous	90 s	separated directly after cooling
C_90_acid	continuous	90 s	stirring overnight after pH modification ^a
C_90	continuous	90 s	stirring overnight without pH modification
C_60	continuous	60 s	stirring overnight without pH modification
C_50	continuous	50 s	stirring overnight without pH modification
C_40	continuous	40 s	stirring overnight without pH modification
P_6	pulsed	6 cycles	stirring overnight without pH modification
P_9	pulsed	9 cycles	stirring overnight without pH modification
P_12	pulsed	12 cycles	stirring overnight without pH modification
P_18	pulsed	18 cycles	stirring overnight without pH modification

^a the pH modification has been done by addition of 250 ml of 0.1 M HNO₃

5.2.2 Structural catalyst characterization

The metal loadings of both Pt and Ni on the support and their atomic ratio were determined with inductively coupled plasma–optical emission spectroscopy (ICP-OES) (JOBIN YVON ULTIMA 2, HORIBA). The samples were subjected to microwave digestion in aqua regia following the procedure in [32]. After dilution with water the metal ion concentration was measured with ICP-OES. To ensure the validity of the method a reference catalyst (20 % Pt/C from E-TEK) was subjected to the same procedure. For transmission electron microscopy (TEM) analysis, a dispersion of the catalyst sample in ethanol was prepared by sonication for 10 min and few drops of this dispersion were dropped onto a carbon coated copper grid and investigated with a LEO 912 microscope (Japan) working at an acceleration voltage of 120 keV. The crystal structure of the prepared catalysts was identified by XRD. The data was collected with a D8 advanced X-ray diffractometer, Bruker AXS, working with a Cu K α source ($\lambda = 0.15406$ nm) in the 2θ range of 20-90 ° at a scan rate of 2° min⁻¹.

X-ray photoelectron spectroscopy (XPS) measurements were carried out in an ultra-high vacuum (UHV) setup equipped with a monochromatic Al K α X-ray source ($h\nu = 1486.6$ eV), operated at 14.5 kV and 35 mA, and a high resolution Gammatdata-Scienta SES 2002 analyzer. The base pressure in the measurement chamber was maintained at about 7×10^{-10} bar. The measurements were carried out in the fixed

transmission mode with a pass energy of 200 eV resulting in an overall energy resolution of 0.25 eV. High-resolution spectra for C 1s, O 1s, Ni 2p and Pt 4f regions were recorded. The binding energy (BE) scales were re-calibrated based on the C 1s line of the sp^2 hybridized graphitic carbon, which was set to 284.5 eV. Data reduction and signal shape analysis were performed using the program package CASA XPS. Atomic ratios of elements were calculated from intensity ratios using the Scofield photoionization cross-section data together with the analyser work function provided by the manufacturer. The Pt area was determined by simple integration employing a Shirley-type background in a preselected binding energy (BE) window.

Pt L_3 -edge (11564 eV) X-ray absorption fine structure spectroscopy (XAFS) measurements were carried out at the SUPERXAS beamline of the Swiss Light Source (Paul Scherrer Institute, Villigen Switzerland). A channel-cut Si (311) monochromator was used to tune the energy of the incident beam while a Rh-coated toroid mirror was used to cut unwanted higher harmonics. The spectra were recorded in the transmission mode at ambient temperature. For the measurements, the samples were pressed into self-supporting pellets (diameter – 13 mm) and wrapped with Kapton tape. Pt L_3 -edge energy calibration was done by measuring the spectrum of a Pt foil placed between the second and third ionisation chamber together with the sample spectra. All spectra were measured twice to ensure their reproducibility.

Analysis of the Extended X-ray Absorption Fine Structure (EXAFS) was performed with the software VIPER for Windows [33]. In the spectra of the absorption coefficient μ , a Victorian polynomial was fitted to the pre-edge region for background subtraction. A smooth atomic background μ_0 was evaluated using a smoothing cubic spline. The Fourier analysis of the k^2 - weighted experimental functions $\chi = (\mu - \mu_0)/\mu_0$ was performed with a Kaiser window. The required scattering amplitudes and phase shifts were calculated by the ab initio FEFF8.10 code [33] using the models for fcc Pt metal, orthorhombic PtO_2 and fcc Pt-Ni alloy structures. The fitting was done in the k - and r -spaces. The shell radius r , coordination number CN, Debye-Waller factor σ^2 and adjustable “muffin-tin zero” ΔE were determined as fitting parameters. The errors of the fitting parameters were found by decomposition of the statistical χ^2 function near its minimum, taking into account maximal pair correlations.

5.2.3 Electrochemical measurements and electrode preparation

All electrochemical measurements were carried out using an Autolab PGSTAT 128N potentiostat/galvanostat in a three electrodes electrochemical cell with three compartments in which the reference electrode compartment was connected to the working electrode compartment through a Luggin capillary and the counter electrode compartment separated from the working electrode compartment by a glass frit. An Ag/AgCl/ KCl_{sat} electrode was used as reference electrode where the potential in this

work is referred to, whereas a platinum wire and a glassy carbon electrode ($A = 0.125 \text{ cm}^2$) were used as counter electrode and substrate for the working electrode, respectively. Before use, the glassy carbon electrode was subjected to a cleaning procedure by polishing with alumina slurry of $0.1 \mu\text{m}$ and $0.03 \mu\text{m}$ consecutively with the help of a polishing cloth and washing in an ultrasonic bath in ethanol/water and water each for 10 min, respectively.

The working electrode was prepared by dispersing 2.5 mg of the catalyst in $350 \mu\text{l}$ of a Nafion solution (5 wt.% in lower aliphatic alcohols) and isopropanol (1/6, v/v) under sonication for 1 h followed by stirring for 2 h to obtain a homogenous dispersion. $5 \mu\text{l}$ of the catalyst dispersion was drop-coated on the glassy carbon substrate and left to dry in a saturated atmosphere of isopropanol at room temperature after which the working electrode is ready for electrochemical tests.

5.2.4 CO Stripping measurements

CO stripping was used for determination of the electrochemical surface area. First, the catalyst was subjected to an electrochemical cleaning procedure by cycling the electrode in N_2 saturated $0.5 \text{ M H}_2\text{SO}_4$ for 100 cycles in a potential window of -0.2 to 1 V at a scan rate of 100 mV s^{-1} . Then CO gas was purged into the solution for 20 min while holding the electrode potential at -0.15 V to allow for the adsorption of a monolayer of CO molecules. Afterwards, dissolved CO was removed by purging the solution for 20 min with N_2 gas while keeping the electrode potential at -0.15 V . Finally, the voltammogram for CO stripping was recorded in potential window of -0.15 to 0.9 V for three consecutive cycles. The first cycle is to record the CO_{ads} stripping and the next two cycles to ensure the complete stripping of CO_{ads} during the first cycle.

5.2.5 Methanol oxidation activity

Methanol oxidation was studied on all catalysts in $1 \text{ M CH}_3\text{OH}/0.5 \text{ M H}_2\text{SO}_4$ using cyclic voltammetry and chronoamperometry. The prepared and previously electrochemically cleaned electrode was cycled in a potential window from -0.2 to 1 V at 100 mV s^{-1} for 200 cycles. The catalytic activity for all catalysts was compared at the twentieth cycle but the development of the catalysts activity during the potential cycling was also monitored. The methanol oxidation at constant potential of 0.7 V was studied by chronoamperometry in $1 \text{ M CH}_3\text{OH}/0.5 \text{ M H}_2\text{SO}_4$ for 1 h. A fresh electrode was prepared for this measurement and was subject to the same electrochemical cleaning procedure as described above before recording the CA curve.

5.3 Results and discussion

5.3.1 Structural characterization

5.3.1.1 Metal loading determination by ICP

The metal loadings of the prepared catalysts were determined by ICP analysis and the results are shown in Table 5.2. Generally the metal loading and the atomic ratios of the two components depend on the microwave irradiation mode and the irradiation duration. A clear dependence of metal loading on irradiation time is observed for the samples prepared under continuous irradiation. The amount of Pt increases from ca. 2 % to ca. 10 % when the time is increased from 40 to 90 seconds. Lower irradiation times of 40 and 50 s lead to comparably low amounts of Ni of ca. 1% and this value increases to 2 % with irradiation times of 60 s or higher. It should be noticed that the temperature of the reaction mixture during the microwave irradiation increased from 170 °C to 190 °C when the irradiation time increased from 50 s to 60 s. The enhancement of Ni loading by increasing the irradiation time can be explained either by a larger rate of metal ion reduction at higher temperature or by the formation of higher amounts of Pt nanoparticles which may serve as seeds for Ni ion reduction [37-39]. With further increasing the irradiation time from 60 s to 90 s a slight decrease in Ni loading was observed whereas Pt loading showed a slight increase. This behavior probably results from the galvanic displacement of Ni by Pt ions. Aging under stirring, which was intended to allow the PtNi particles to deposit on the support, has only a slightly beneficial effect on metal loading. Equally aging under pH modification has been attempted to promote the deposition of the nanoparticles onto the carbon support [35]. Obviously, pH modification has an adverse effect on both the Pt and the Ni loading: they decreased after this step compared to the catalyst aged without pH modification (PtNi/CNT_C_90) or even the catalyst separated directly after the reduction process (PtNi/CNT_C_90_na).

The decrease of metal loading as result of pH modification in particular for Ni could be attributed to the dissolution of Ni in acid conditions [36]. The decrease of Pt loading after pH modification is more difficult to explain since dissolution of Pt is not expected under these conditions. The actual reason for the decreased Pt loading is not clear for us at the moment.

As expected, for the catalysts prepared under pulsed microwave irradiation, the total metal loading increases with growing pulse number. The pulse mode provides obviously no advantage regarding the metal loading, since after 180 s of irradiation (i.e., 18 pulses) the loading is similar as after 90 s of continuous irradiation. This behavior is opposite to that reported by Song et al. [40], where the efficiency was higher in the pulsed mode than in the continuous mode and which was discussed by the authors in view of the heating rate. In general, the heating rate can be correlated

Chapter 5: Microwave-Assisted Polyol Synthesis of PtNi/CNTs Electrocatalysts

to the viscosity of ethylene glycol and its relaxation time [41,42]. Both viscosity and relaxation time influence the loss factor which is a measure of conversion of microwave radiation into heat by the irradiated molecules [43]. Differences in the observed behaviors thus probably might be attributed to different temperature profiles and experimental conditions obtained in the different microwave setups.

Table 5.2. Metal loading and atomic ratios as obtained from ICP and particle size from TEM.

PtNi/CNT Catalysts	Metal Loading [wt. %]		Atomic Ratio		Particle Size [nm]
	Pt	Ni	Pt	: Ni	
C_90_na	10	1.8	1.7	1	2.7
C_90_acid	7.6	0.7	3.1	1	3.2
C_90	10.15	2	1.5	1	3.3
C_60	9.8	2.3	1.3	1	2.8
C_50	7.4	1	2.2	1	n.d.
C_40	2.2	1.1	0.4	1	n.d.
P_6	7.5	0.75	3	1	2.5
P_9	8.1	1.6	1.5	1	4.7
P_12	10	1.85	1.6	1	2.5
P_18	10.2	2.2	1.4	1	2.7
Pt/C ETEK	19.5	-	-	-	3.1

n.d. = not determined

In general, the total metal loading determined by ICP is lower than the theoretical one which could be explained by the lower redox potential of Ni compared to Pt thus impeding the reduction of Ni by EG. It is, however, a challenge to prepare bimetallic catalysts containing non noble elements with the microwave polyol method: A high pH should enhance the reduction of Ni ions [44] but at the same time could prevent the negatively charged nanoparticles to adsorb on the support [45]. Compared to the preparation of PtNi by the conventional polyol method [32], the amount of Ni in the microwave assisted synthesis is higher indicating that the higher temperature of microwave heating favors Ni ion reduction [39].

5.3.1.2 XRD and TEM characterization

The XRD patterns for the prepared catalysts are shown in Figure 5.1A-C. Figure 5.1A shows the XRD patterns for the catalysts prepared with continuous irradiation for 90 s under different aging conditions in comparison with the commercial Pt/C catalyst. The peak near $2\theta = 25^\circ$ is assigned to graphite carbon in the supporting materials. Importantly, the diffraction peaks of the prepared catalysts are shifted to higher 2θ values (40.8°) in comparison to Pt/C (39.8°) indicating the formation of an alloy between Pt and Ni [46-48].

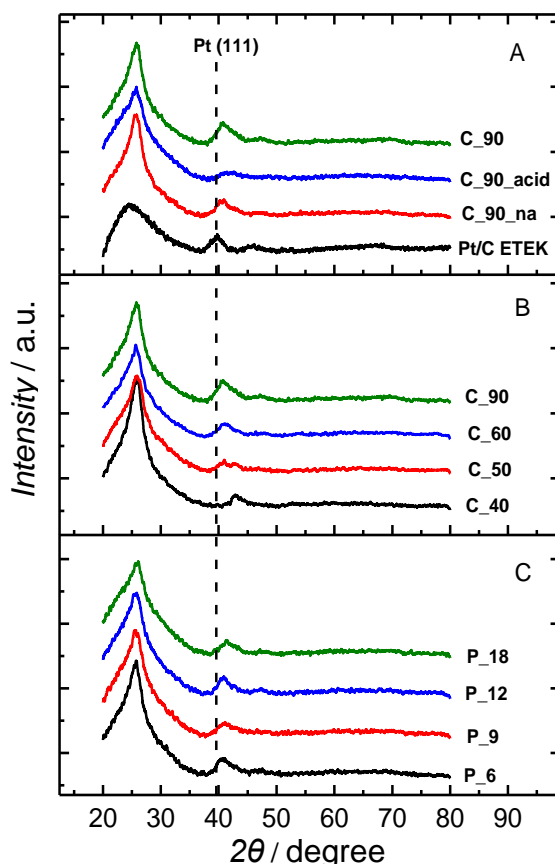


Figure 5.1: XRD patterns of PtNi/CNT electrocatalysts, A) effect of aging condition, B) effect of continuous irradiation duration, C) effect of pulse number.

The XRD patterns of catalysts prepared under continuous irradiation for different durations are shown in Figure 5.1B. PtNi/CNT_C_40 shows only a diffraction peaks at $2\theta = 43^\circ$ corresponding to the formation of NiO (200) [49,50]. Since Pt in this catalyst was detected by ICP-OES, either the amount of Pt is too low to be detected with XRD or Pt particles initially formed are too small. Initial formation of Ni species is in agreement with our previous investigations on PtNi catalyst synthesis using conventional polyol reduction, where a preferential adsorption of Ni ions on the oxidized CNT surface has been postulated [32]. Small Ni particles formed initially might be oxidized during handling in air after synthesis and are thus found as NiO in XRD. It cannot finally be ruled out that $\text{Ni}(\text{OH})_2$ precipitates during catalysts impregnation and is converted into NiO during drying. However it would then be hard to explain why these species should disappear after prolonged irradiation (see below). Upon increasing the irradiation time to 50 s, a new diffraction peak adjacent to the NiO peak develops at 2θ (40.8°) assigned to PtNi alloy formation. Further increasing the irradiation time to 60 and 90 s increases the intensity of the PtNi diffraction peak whereas the NiO peak vanishes completely probably indicating that the initially formed Ni nuclei may serve as basis for the formation of the alloy.

For the catalysts prepared in with pulsed irradiation (PtNi/CNT_P, Figure 5.1C) the pulse number has only slight effects on the crystal structure. All catalysts show a shift to higher 2θ values than that of Pt and the shift is more pronounced in the sample prepared at 18 pulses (PtNi/CNT_P_18) indicating a higher alloying extent.

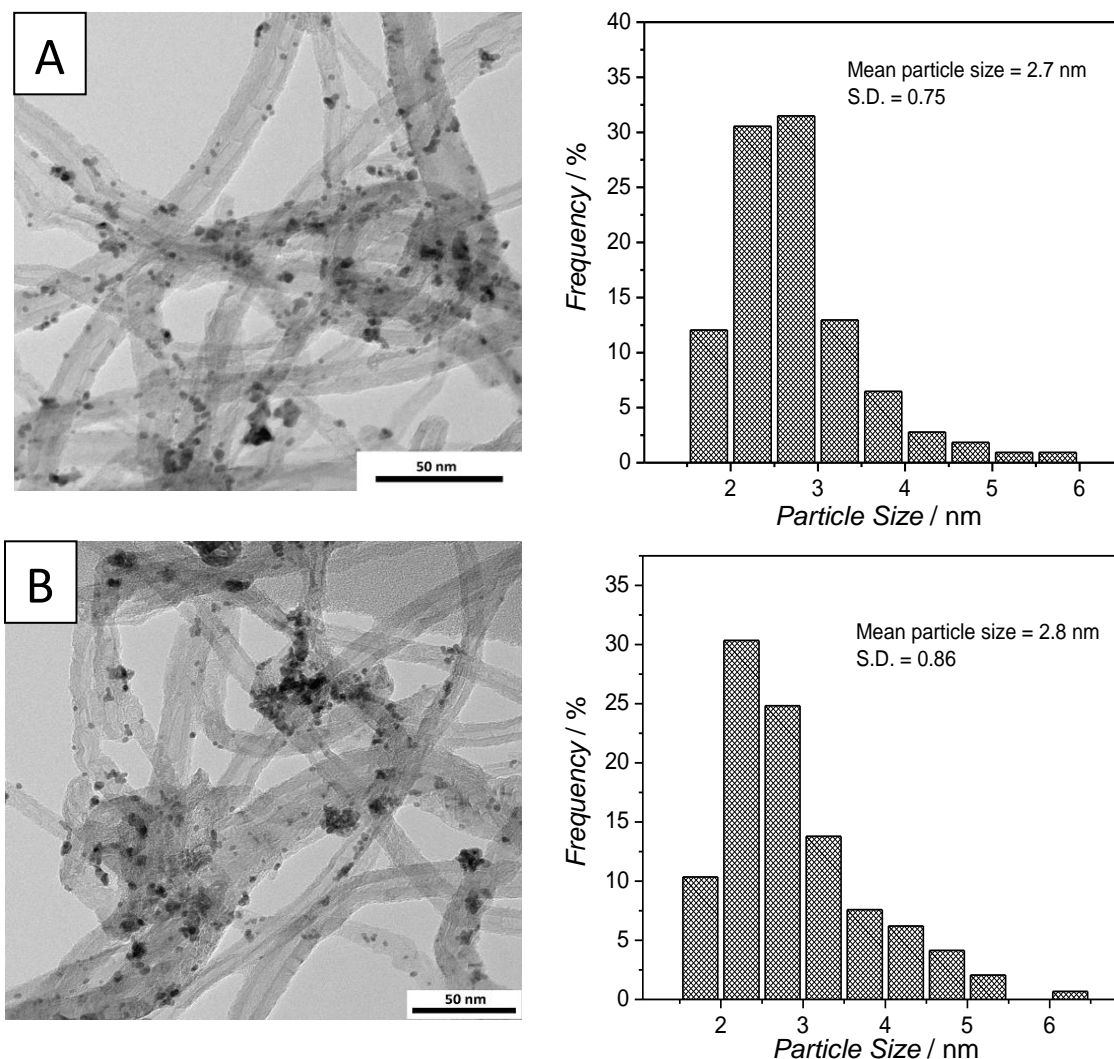


Figure 5.2: TEM images of PtNi/CNT_C catalysts, A) PtNi/CNT_C_90_na and B) PtNi/CNT_C_60.

Selected TEM images of selected catalysts are shown in Figure 5.2 and Figure 5.3, additional images can be found in the supporting information. Particle sizes determined from TEM are summarized in Table 5.2. The catalysts prepared with continuous irradiation (Figures 5.2A and B) contain small particles well dispersed on the CNT support. Increasing the irradiation time or aging the catalyst under stirring overnight (PtNi/CNT_C_90) increases the particle size from 2.7 to 3.3 nm with simultaneous appearance of regions with some agglomeration. On the other hand, acidification the reaction medium after the reduction process (PtNi/CNT_C_90_acid) followed by aging results in high dispersion of the nanoparticles on the CNTs while

keeping the same particle size (3.2 nm). It is expected that at lower pH the surface of CNTs is positively charged and therefore the negatively charged nanoparticle glyconate complexes formed during reduction can be adsorbed on the surface of the CNTs with high dispersion.

The catalysts prepared under pulsed irradiation (PtNi/CNT_P, Figure 5.3A and B) exhibit particle sizes virtually independent of the number of pulses (about 2.5 nm) except the sample PtNi/CNT_P_9 with a particle size of 4.7 nm (Figure S15.3A). Also, increasing the pulse number and therefore the irradiation time enhances the presence of agglomerated particles.

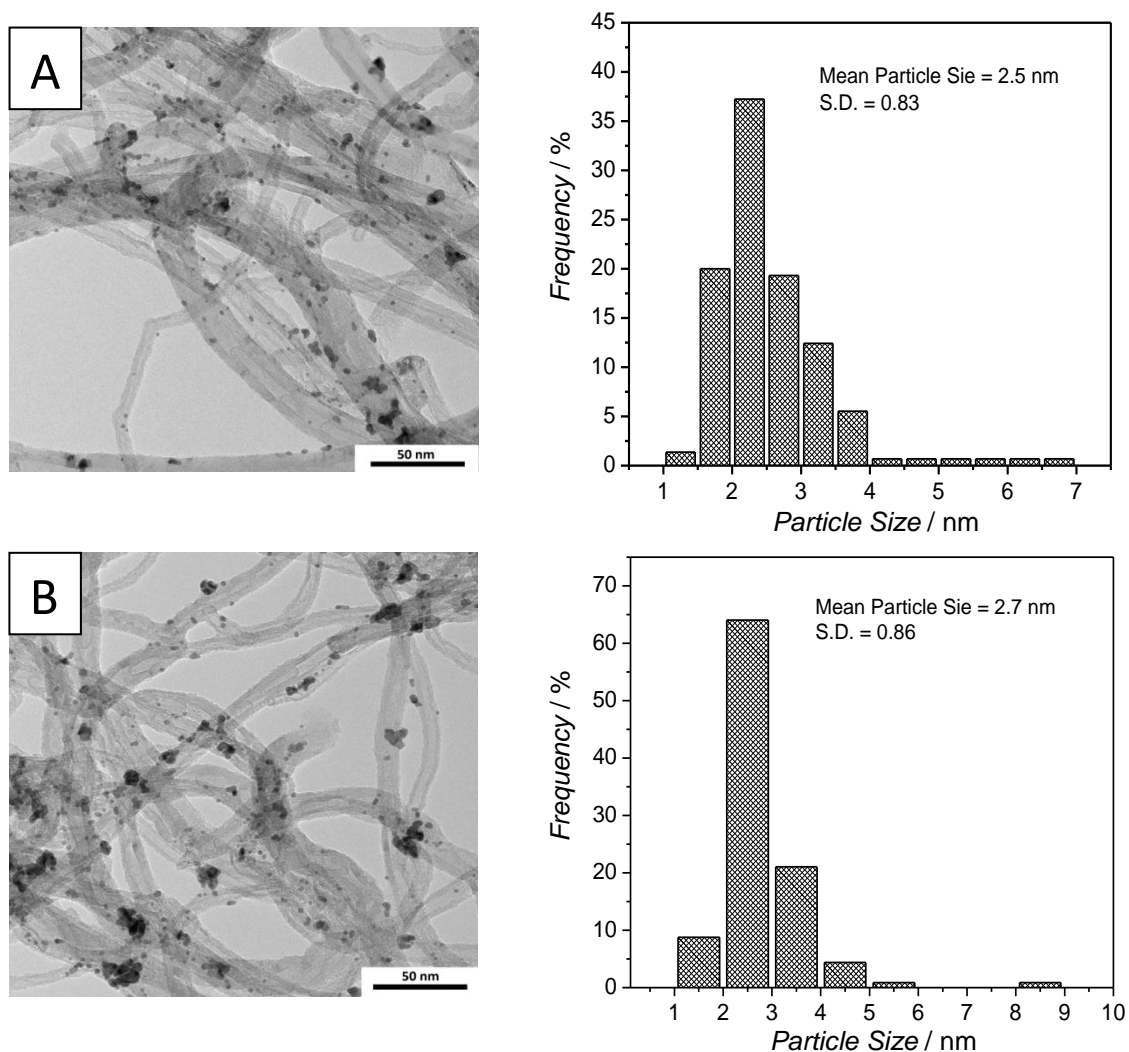


Figure 5.3: TEM images of PtNi/CNT_P catalysts, A) PtNi/CNT_P_6 and B) PtNi/CNT_P_18.

5.3.1.3 XPS and XAFS characterization

The Pt (4f) photoelectron spectra of selected PtNi catalysts compared with Pt/C are presented in Figure 5.4A. The Pt (4f 7/2) signal of the monometallic sample has a BE of 71.9 eV, which is close to the metal position (71 eV) [51,52]. This shift to higher energies is minor and likely not related to a higher oxidation state of platinum but to initial-state or final-state effects due to small particle size [53,54]. In the PtNi catalysts the Pt (4f 7/2) signal shifted to lower BE (≈ 0.4 eV) which might indicate alloy formation.

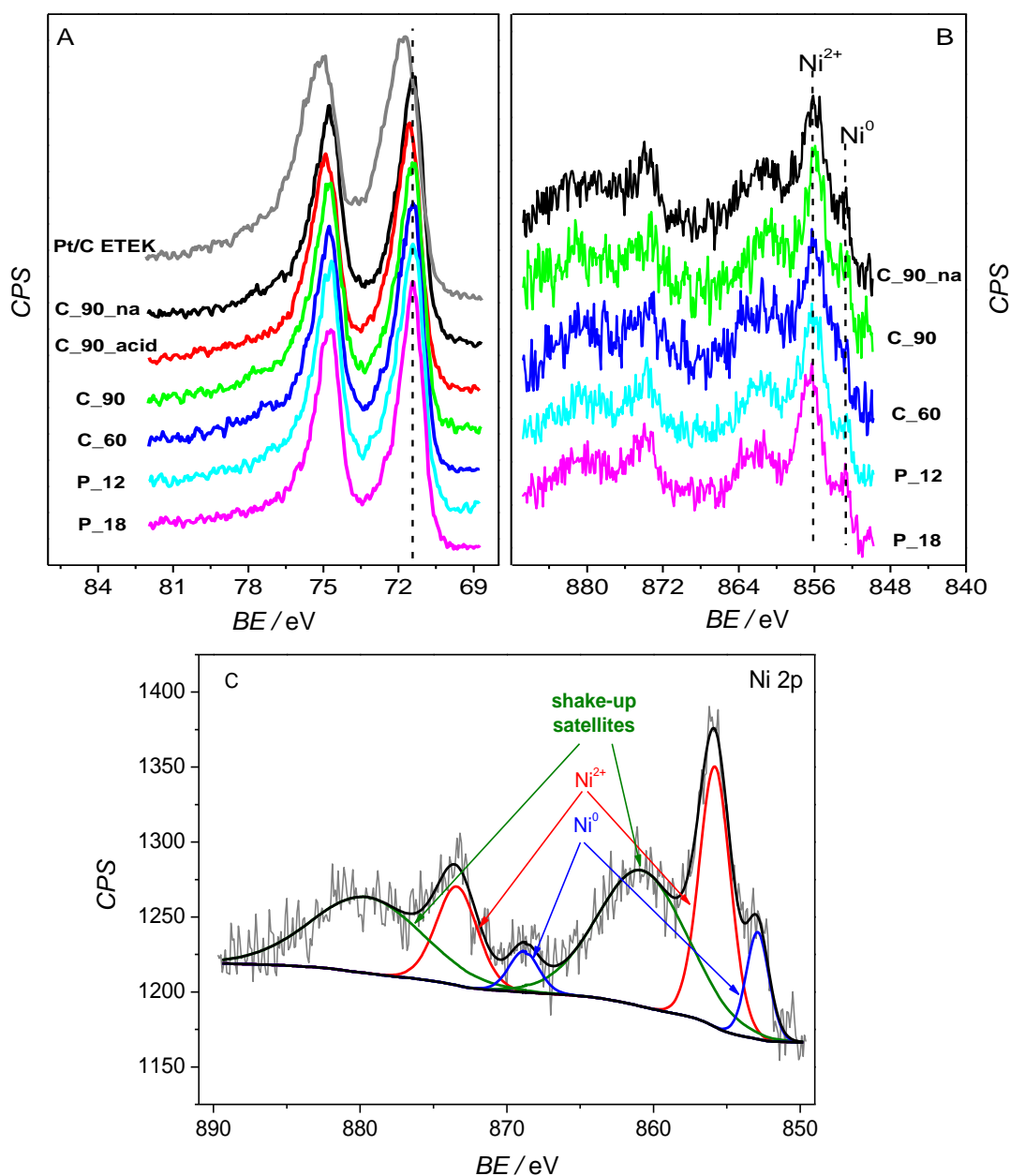


Figure 5.4: XPS spectra of PtNi/CNTs samples. A) Pt 4f signals; B) Ni 2p signals. (Ni 2p spectrum of PtNi/CNT_C_90_acid sample is not shown due to lower signal to noise ratio) and C) Ni 2p deconvolution exemplified with PtNi/CNT_C_90 sample.

The Ni 2p XPS spectra are presented in Figure 5.4B. Although the Ni signals are weak, some conclusions on the nickel state can be derived. In all samples the Ni²⁺ state with a BE of ca. 856.2 eV can be detected together with its characteristic broad shake-up satellite approximately 4 eV higher. A contribution from the Ni metallic state can also be detected in all samples. The deconvolution of the Ni 2p signal is illustrated for PtNi/CNT_C_90 in Figure 5.4C while the Ni to Pt and Ni⁰/Ni²⁺ ratios from XPS signal deconvolution are summarized in Table 5.3. It can be seen that most of the samples are severely oxidized while aging under addition of acid lead to significant increase of metallic Ni contribution accompanied by an overall decrease in nickel content. This behavior agrees well with the ICP results discussed above where the total Ni content decreases upon acid treatment due to Ni dissolution. The higher contribution of metallic Ni in PtNi/CNT_C_90_acid as detected from XPS indicates that Ni oxide species including NiO are dissolved preferentially in the acidic medium. It is quite possible that the Ni ions accessible to the acid were completely dissolved during aging, but further oxidation of surface species happened during sample storage. The surface Ni content detected with XPS is slightly lower than the bulk one measured by ICP-OES for all samples with the exception of PtNi/CNT_P_12 which may indicate a tendency of Pt to occupy the surface of the catalyst particle where Ni tends to be more concentrated near the oxidized surface support during the preparation process as reported in [32].

Table 5.3. Atomic ratios as calculated from XPS.

PtNi/CNT	C_90_na	C_90_acid	C_90	C_60	P_12	P_18
Catalysts						
Ni ⁰ /Ni ²⁺	0.09	0.29	0.11	0.05	0.08	0.16
Ni/Pt XPS	0.53	0.20	0.60	0.63	0.66	0.68
Ni/Pt ICP	0.58	0.32	0.66	0.77	0.63	0.71

The Pt L₃-edge X-ray absorption near edge structures (XANES) are shown in Figure 5.5A. The absorption at 11.564 keV corresponds to the 2p_{3/2} - 5d electronic transition of Pt metal and the amplitude of the first feature at ca. 11.569 keV, known as the white line (WL), reflects the orbital occupancy of the 5d electronic state. The WL intensity increases with decreasing occupancy in the 5d orbital. Figure 5.5A shows that the white line intensities for all samples are slightly higher than that of a Pt foil. As it was reported before [55], both oxidation state and alloying of platinum can cause changes in WL intensity. Since no significant oxidation of the platinum outer layers was detected by XPS and the presence of oxidized Pt in the bulk of the particles is highly unlikely, one can conclude that the WL intensity changes observed are an effect of Pt-Ni alloy formation. The Pt L₃-edge Fourier Transformed (FT) EXAFS spectra are depicted in Fig. 5.5B. In the spectra, signals can be discerned between 1.7 and 3.25 Å

(uncorrected), the interpretation of which requires modeling of the coordination sphere. The fact that the scattering intensity ranges down to 1.7 Å (uncorrected) shows the presence of light neighbors – oxygen or carbon – in the coordination sphere of Pt. The spectra were fitted using three different shells for next neighbors (Pt, Ni and O representing the light backscatterer), and the results are collected in Table S15.1 (see supporting information). In Figure 5.5C, a typical fit is shown to demonstrate the fit quality while the most important data (CN, r) are summarized in Table 5.4 together with platinum pairing factors P_{Pt} . The latter are calculated according to $P_{Pt} = CN_{Pt-Ni} / (CN_{Pt-Ni} + CN_{Pt-Pt})$, where CN_{i-j} are coordination numbers of element j in the first coordination sphere of element i . They allow judging on the degree of segregation and mixing in an alloy particle [56].

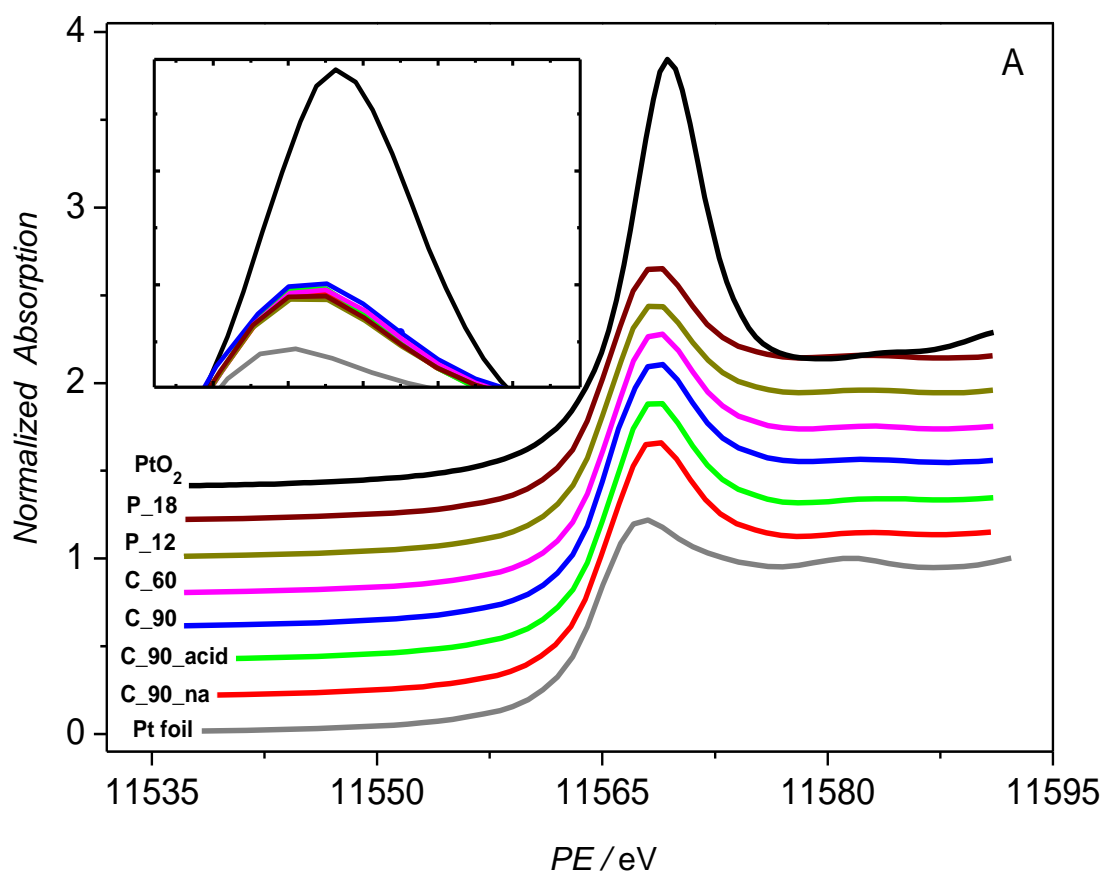


Figure 5.5: Pt L_3 -edge XANES spectra (A) of the PtNi/FCNTs together with Pt-foil and PtO_2 references, Pt L_3 -edge FT-EXAFS spectra (B) of the PtNi/FCNTs together with Pt-foil reference and their fit three shell model exemplified by PtNi/CNT_P_12 (C).

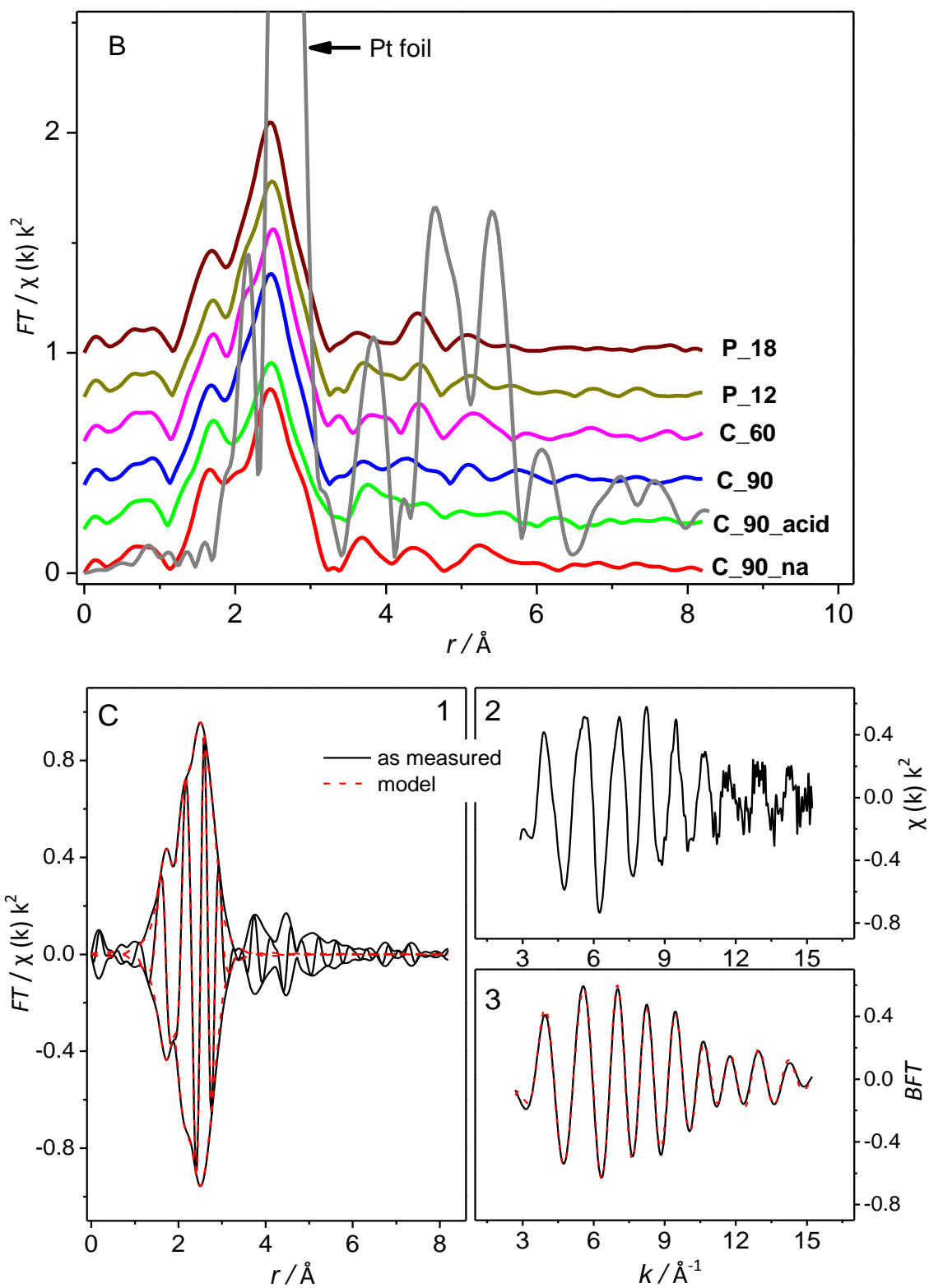


Figure 5.5: continued

Chapter 5: Microwave-Assisted Polyol Synthesis of PtNi/CNTs Electrocatalysts

Table 5.4: PtL₃ EXAFS fitting parameters – coordination numbers and distances (in brackets, in Å) along with total coordination numbers CN_{total} and platinum pairing factors P_{Pt}.

PtNi/CNTs Catalysts	C_90_na	C_90_acid	C_90	C_60	P_12	P_18
Pt-O	1.37(2.05)	1.55(2.05)	1.13(2.03)	1.19(2.04)	0.97(2.04)	1.11(2.04)
Pt-Ni	1.25(2.69)	0.98(2.69)	1.56(2.67)	1.62(2.66)	1.67(2.67)	1.60(2.68)
Pt-Pt	5.29(2.74)	4.2(2.74)	4.72(2.73)	4.57(2.74)	4.85(2.74)	4.92(2.73)
CN _{total}	6.5	5.2	6.3	6.2	6.5	6.5
P _{Pt}	0.19	0.19	0.25	0.26	0.26	0.25

In the fits, Pt-Ni CN was found to range between 1 and 1.6, which is a clear proof of alloy formation. The distance between Pt and the light scatterer “O” is consistently between 2.03 and 2.05 Å, which is significantly below the sum of covalent radii of Pt (1.39 Å) and O²⁻ (0.72 Å). This neighbor is therefore support carbon rather than oxygen. The fact that support carbon can be seen in the EXAFS spectra suggests a very small particle size or raft-like particle morphologies. The sum of CN of Pt with both metals, Pt and Ni, is consistently between 6.2 and 6.5 except for sample PtNi/CNT_C_90_acid, which was aged in acid. This also suggests extremely small average sizes of the primary particles, probably below 1 nm. The particles seen in the TEM images are most likely aggregates of such primary particles. PtNi/CNT_C_90_acid displays an even lower total coordination number, indicating an even smaller average particle size. The disagreement of this result with the TEM images may arise from the most likely polycrystalline nature of the particles seen in the microscope. Platinum pairing factors are generally very small (0.19-0.26), which indicates poor mixing between Pt and Ni. This is consistent with the results obtained with catalysts prepared by the conventional polyol route [32] where the data reported result in Pt pairing factors of ≈ 0.2 . Thus, the model of primary particles with Ni clustered near the support and Pt exposed towards the surrounding space might be valid also for catalysts made by microwave-assisted preparations.

It should be noted that our PtL_{III} edge EXAFS spectra cover only Ni species that have Pt neighbors, i.e. Ni species in or at the surface of alloy particles. The latter may be oxidized. NiO phases as detected by XRD are not seen in these measurements. As the coexistence of segregated and alloy phases would strongly complicate the interpretation of Ni K XAFS results, such data were not measured for the present series. While the segregated Ni phases are most likely dissolved in the pretreatments prior to electrochemical measurements, the Pt-related Ni atoms are more likely to survive, maybe except for surface atoms.

5.3.2 Electrochemical characterization

5.3.2.1 CO Stripping and surface area determination.

CO stripping was used to determine the electrochemical surface area of the catalysts of this study. Representative CO stripping voltammograms are shown in Figure 5.6. Peak potentials for CO oxidation are summarized in Table 5.5. CO adsorption is confirmed by the absence of hydrogen desorption peaks in the lower potential region of the first cycle. During the positive potential sweep, a shoulder at around 0.5 V followed by a signal at 0.59 V resulting from CO oxidation is visible. During the second cycle, the voltammograms don't show any peak for CO oxidation while the formation and oxidation of Hupd is clearly visible indicating that CO_{ads} was oxidized completely during the first scan. We want to emphasize that there was no significant potential shift for the CO oxidation peak on the PtNi catalysts in comparison to Pt/C (comp. Table 5.5). This behavior could be attributed to the fact that the surface of PtNi catalysts resembles a Pt surface as a result of catalyst restructuring/Ni dissolution during the pretreatment of PtNi catalysts (electrochemical treatment in acid environment for 100 cycles, comp. Figure SI5. 4A) [57].

The electrochemical surface area of the catalysts under investigation has been evaluated from the integration of the charge consumed during the CO stripping after correction for the double layer and anion adsorption related currents:

$$ECSA(cm^2_{Pt}) = \frac{Q_{CO}}{Q_0} \quad (5.6)$$

Where Q_{CO} is the integrated charge consumed during the CO_{ads} oxidation and Q_0 is the standard charge required for oxidation of a CO_{ads} monolayer on a Pt surface with a value of 420 $\mu\text{C cm}^{-2}$.

The specific electrochemical surface area (*SECSA*) ($\text{m}^2 \text{g}^{-1}_{Pt}$) was calculated by dividing the electrochemical surface area obtained from Equation 5.6 by the platinum loading in the electrode (L_{Pt}) according to the following equation:

$$SECSA(\text{m}^2/\text{g}_{Pt}) = \frac{ECSA}{M_{Pt}} \quad (5.7)$$

The calculated specific surface area of the catalysts under investigation is shown in Table 5.5. For catalysts prepared under continuous irradiation, the specific surface area increases with irradiation time. The catalyst aged in acidified media (PtNi/CNT_C_90_acid) shows slightly higher SECSA probably resulting from the dissolution of Ni and/or NiO surface species under formation of a Pt/PtNi skeleton structure. The catalyst prepared at 40 s of irradiation time (PtNi/CNT_C_40) behaves

different in CO stripping and CV showing high electrochemical surface area which might probably be attributed to the presence of only small Pt particles (see above, XRD).

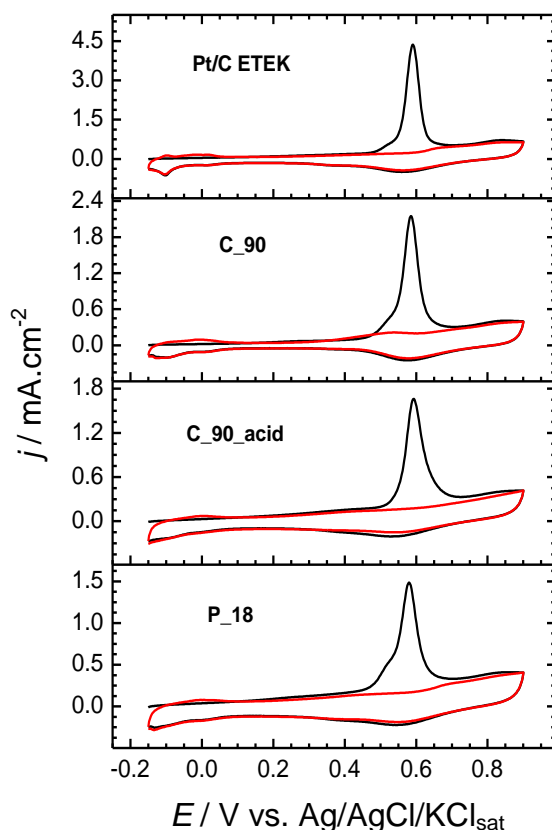


Figure 5.6: CO Stripping voltammograms of selected PtNi/CNT catalysts in 0.5 M H₂SO₄, scan rate 20 mV s⁻¹.

For the catalysts prepared with pulsed irradiation mode, the change of the SECSA was small except for the catalysts PtNi/CNT_P_9 which showed higher SECSA that could be attributed to the high dispersion and the absence of nanoparticle agglomeration in this catalyst although it has the highest particle size among all PtNi/CNT_P catalysts (Fig. SI5. 3A).

In general, with proper control of the conditions during microwave preparation, we were able to prepare PtNi/CNT catalysts in very short time with high specific electrochemical surface area comparable to that of Pt/C ETEK and to that of other PtNi/C catalysts reported in the literature [17,46,58] and higher than that of PtNi/FCNTs prepared by the conventional polyol method (SECSA of 29.1 m²g⁻¹_{Pt}) [32].

Chapter 5: Microwave-Assisted Polyol Synthesis of PtNi/CNTs Electrocatalysts

Table 5.5: Electrochemical parameters from CO Stripping and CV measurements.

PtNi/CNTs Catalysts	Peak Potential CO oxidation [mV]	SECSA [$\text{m}^2\text{g}^{-1}_{\text{Pt}}$]	Peak Potential MeOH oxidation [mV]	MSA [$\text{mA mg}^{-1}_{\text{Pt}}$]	SSA [$\text{mA cm}^{-2}_{\text{Pt}}$]	I_f/I_b
C_90_na	0.584	43.4	0.676	524.2	1.20	0.8
C_90_acid	0.593	51.1	0.673	474.6	0.93	1.0
C_90	0.585	48.1	0.688	618.5	1.28	0.78
C_60	0.580	37.1	0.679	628.8	1.69	0.75
C_50	0.590	30.3	0.669	486.7	1.60	0.78
C_40	0.590	87.9	0.660	682.2	0.77	1.1
P_6	0.586	33.7	0.670	468.9	1.39	0.81
P_9	0.582	47.1	0.675	570.2	1.20	0.86
P_12	0.589	31.3	0.673	471.0	1.50	0.82
P_18	0.580	36.1	0.679	582.9	1.62	0.81
Pt/C ETEK	0.590	45.7	0.690	482.5	1.05	0.60

5.3.2.2 Methanol oxidation activity

To evaluate the catalytic activity of the prepared catalysts toward methanol electrooxidation, they were tested in 1 M $\text{CH}_3\text{OH}/0.5$ M H_2SO_4 solution using cyclic voltammetry. Typical voltammograms are shown in Figure 5.7. In these figures, the current is given per mass of Pt. CVs showing the surface-specific currents can be found in the SI (Figure SI5.5). The CVs for methanol oxidation on PtNi catalysts resemble that of Pt/C catalysts [32,46,47,59] with a forward and a backward anodic peak. The ratio of peak current in the forward and in the backward scan (I_f/I_b) is typically considered as a measure for the poisoning resistance of a catalyst. These values are shown in Table 5.5, and it can be seen that all PtNi samples show higher poisoning resistance than the reference Pt/C E-TEK catalysts. The catalytic activities as shown in Table 5.5 were determined as mass specific activity (MSA) surface specific activity (SSA), as given by Equations 5.8 and 5.9:

$$MSA = \frac{I_{\text{peak}}}{L_{\text{Pt}}} \quad (5.8)$$

$$SSA = \frac{I_{\text{peak}}}{ECSA} \quad (5.9)$$

Table 5.5 indicates that the SSA for all PtNi/CNT catalysts is higher than that of the Pt/C sample with the exception of PtNi/CNT_C_90_acid and PtNi/CNT_C_40. The reason for the comparably lower activity of PtNi/CNT_C_90_acid might be the low Ni surface content (comp. Table 5.3). In our previous paper we have speculated on the necessity of having active sites with a certain atomic arrangement of Pt and Ni atoms and the number of such sites might be low in PtNi/CNT_C_90_acid with low Ni content. On the other hand, the I_f/I_b ratio of PtNi/CNT_C_90_acid is exceptionally higher, indicating

lower poisoning susceptibility. This could be attributed to the formation of low coordinated Pt atoms as result of acid dissolution process followed by the electrochemical pretreatment process which are considered as active sites for water activation and therefore CO removal. Similarly the catalyst PtNi/CNT_C_40 has a rather high I_f/I_b value, probably attributable to small Pt particle size. Generally, the surface specific activities of the PtNi/CNT_C and PtNi/CNT_P catalysts are within 1.2 and 1.69 mA/cm². There is a slight trend to higher SSA with higher pulse number which might be attributed to a higher Ni content in these catalysts (comp. Table 5.2). For the MSA generally it can be observed that the PtNi/CNT_P catalysts display higher activity than that of Pt/C but lower than the highly active catalysts in PtNi/CNT_C catalysts (PtNi/CNT_C_90 and PtNi/CNT_C_60) which is somehow surprising given the slightly lower particle sizes in the PtNi/CNT_P catalysts. There are several factors that influence methanol oxidation on these catalysts including particle size and shape and Ni surface and bulk atomic ratio. The intricate interplay between these factors might lead to the observed variation in MSA.

From a practical point of view, where the MSA is relevant, the continuous mode of irradiation is more effective to prepare nanoparticle catalysts by the microwave-assisted polyol method than the pulsed mode. In general, the optimized catalysts reported in this study showed higher MSA, up to 1.5 fold than that obtained with PtNi/FCNTs (1:1) catalysts prepared by us via the conventional polyol method [32] and also higher than the activity of PtNi catalysts reported recently by other groups [17,46,59].

To evaluate the stability of the catalysts during potential cycling in CV measurements, the variation of MSA with cycle number is shown in Figure SI5.6 for two selected catalysts: PtNi/CNT_C_90 and PtNi/CNT_P_18. Additionally, the values normalized to the initial current are displayed. Both catalysts display similar behavior as they show an initially decrease in the activity which declines with increasing cycle number. From the normalized currents, it can be seen that both catalysts retain almost about 82 % of the initial current value after 200 cycles.

The catalyst stability was also tested in CH₃OH/H₂SO₄ and compared to Pt/C using chronoamperometry at 0.7 V for 1 h. The chronoamperometric curves are shown in Figure 5.8. The catalysts prepared at different irradiation times (Figure 5.8A) show almost the same stability which is higher than that of Pt/C ETEK, whereas the catalysts PtNi/CNT_C_40 shows the lowest stability. As discussed above this catalyst contains high amounts of NiO which probably dissolve with time, leading to lower activity. Among the PtNi/CNT_P catalysts (Figure 5.8B) the catalyst prepared at highest pulse number (PtNi/CNT_P_18) show the highest stability whereas the other catalysts are close to Pt/C.

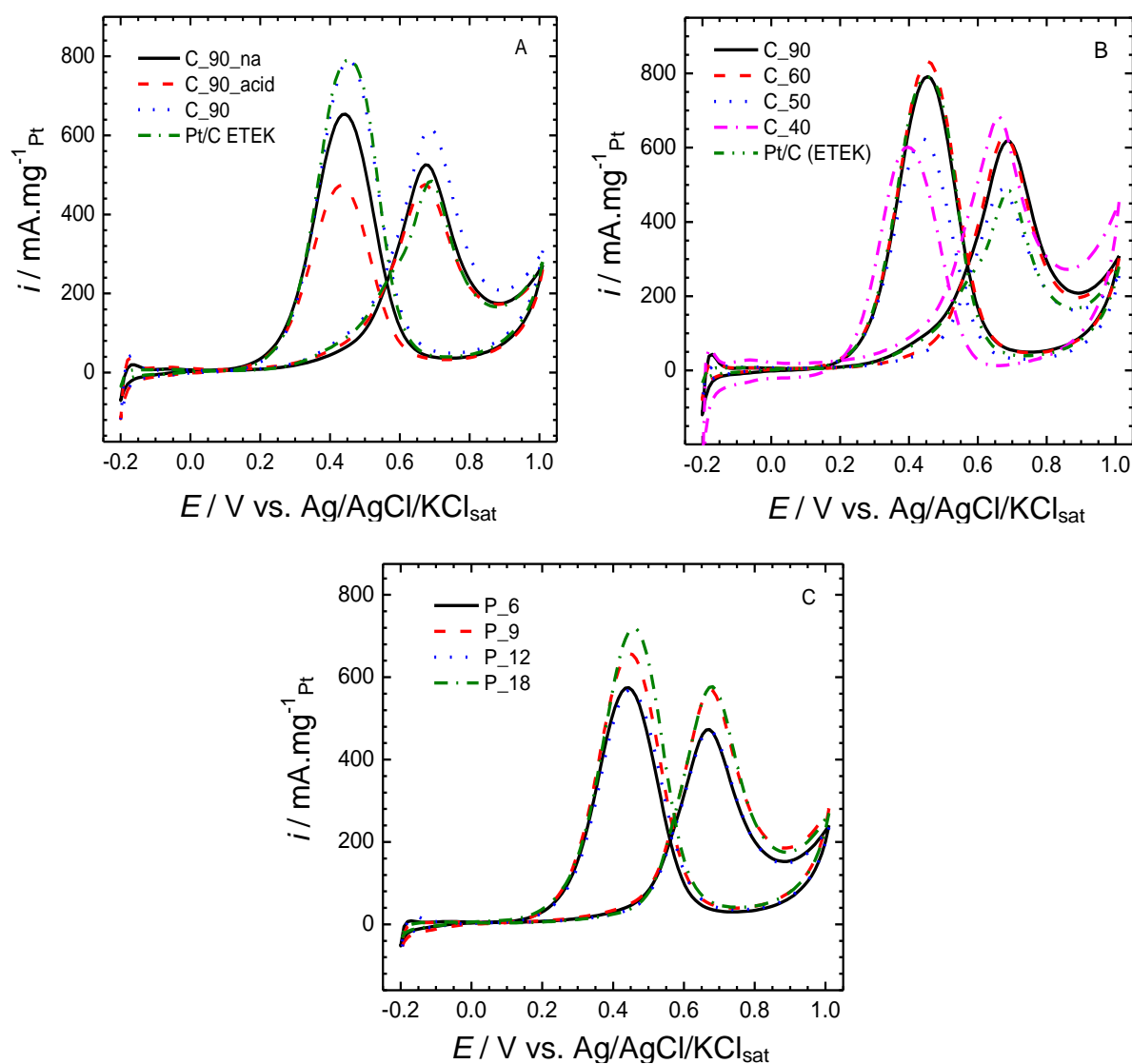


Figure 5.7: CV of PtNi/CNT catalysts in 1 M $\text{CH}_3\text{OH}/0.5$ M H_2SO_4 scan rate $100 \text{ mV}\cdot\text{s}^{-1}$, the current normalized to the Pt loading in the electrode.

Compared to the recently reported steady state currents after 1 h at the same potential (0.896 V vs. NHE) for PtNi (1:1) supported on PDDA modified carbon black, graphene and PDDA modified graphene, with currents of 4.4 , 32.7 and $64.3 \text{ mA mg}^{-1}_{\text{Pt}}$ respectively [61], our catalysts (PtNi/CNT_C_90, PtNi/CNT_C_60, PtNi/CNT_C_50, PtNi/CNT_P_18) show higher stability with steady state currents of 79.8 , 88.5 , 79.8 and $84.18 \text{ mA mg}^{-1}_{\text{Pt}}$ respectively. Pt/C E-TEK exhibits a steady state current of $55.4 \text{ mA mg}^{-1}_{\text{Pt}}$. Additionally, the chronoamperometric curves with current expressed in terms of surface specific current are shown in Figures SI5.7A and B. The same behavior as in Figures 5.8A and B is observed.

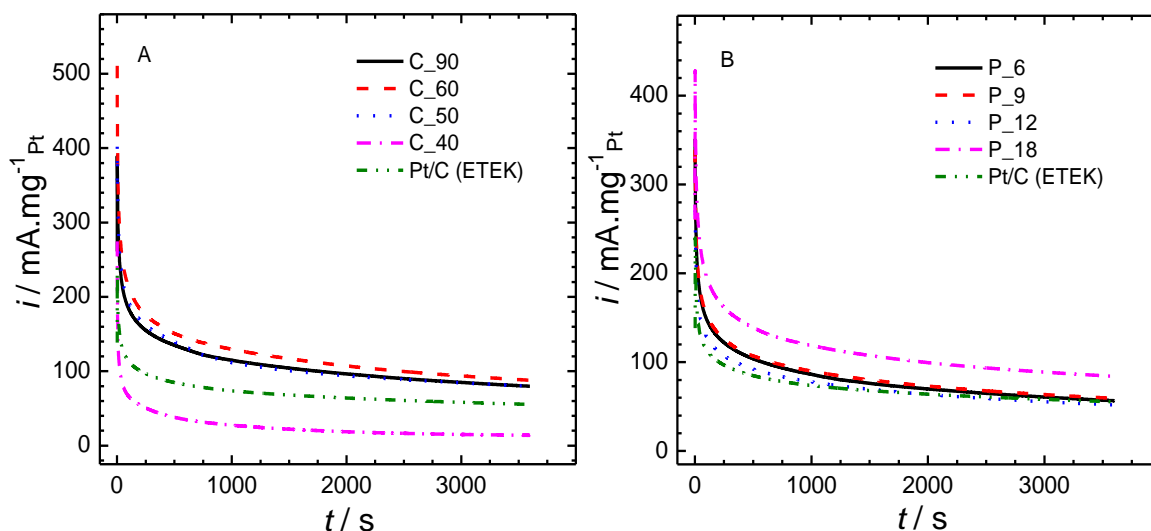


Figure 5.8: CA curves of PtNi/CNT catalysts in comparison with Pt/C ETEK in 1 M $\text{CH}_3\text{OH}/$ 0.5 M H_2SO_4 at 0.7 V; A) effect of irradiation time and B) effect of pulse number.

5.3.3 Origin of the activity enhancement in PtNi catalysts

In a bimetallic catalyst system, the catalytic activity always depends on the surface arrangement of the two active components of the system. Two mechanisms are suggested to explain the enhancement of methanol oxidation and CO tolerance in bimetallic Pt-M catalysts. The first mechanism is the bifunctional mechanism which requires that the second metal is adjacent to Pt on the surface, where the Pt catalyzes the methanol adsorption and dehydrogenation resulting in the formation of adsorbed CO intermediates and the second metal supplies the oxygen species to oxidize the adsorbed CO. The second mechanism is the electronic effect in which the second metal modifies the electronic properties of Pt, reducing CO bonding energy and enhancing CO tolerance. Based on our XPS and ICP-OES analysis, the catalysts show enriched Pt surfaces with lower amounts of Ni on the surface. The electrochemical treatment of the catalysts in acid solution before testing the catalytic activity is expected to dissolve all Ni surface species forming a structure with enriched Pt surface where PtNi alloy or PtNiO are in the subsurface as confirmed from the base voltammograms of the catalysts (Figure S15.4) [57]. Similar behavior is expected for the catalysts when treated first with acid followed by electrochemical treatment as the acid can dissolve the Ni and NiO forming an enriched Pt surface with skeleton structure of Pt/PtNi. The electrochemical treatment in acid solution afterwards results in increasing the Pt surface and formation of a thick layer with lower coordinated sites [58]. Based on these results a plausible model has been suggested for the initial structure of the catalysts and the structure after acid treatment in normal condition and/or after electrochemical treatment in Figures 5.9A-D.

From this model we can expect that the bifunctional mechanism is not suitable to discuss the enhancement of electrocatalytic activity in our PtNi catalysts. On the other hand, XRD, XPS and XAFS analyses confirmed alloy formation in PtNi as detected from Pt diffraction peak shifting in XRD, Pt 4f signal shifting in XPS and changes in the white line intensity in XANES. The increase in white line intensity and the direction of the XPS line shift seem to be contradictory, the former indicating electron deficiency, the latter electron abundance, but it should be noted that both phenomena are complex effects that are also influenced by particle size. We can clearly identify alloying in the catalyst particles, and as electrochemical techniques tend to indicate the absence of Ni from the interface with the electrolyte, the significant gain in activity should be ascribed to influences of the Ni on the active Pt atoms. These are most likely of electronic nature, lowering the electron back donation to the CO molecules and therefore suppressing the CO adsorption and poisoning on the Pt surface.

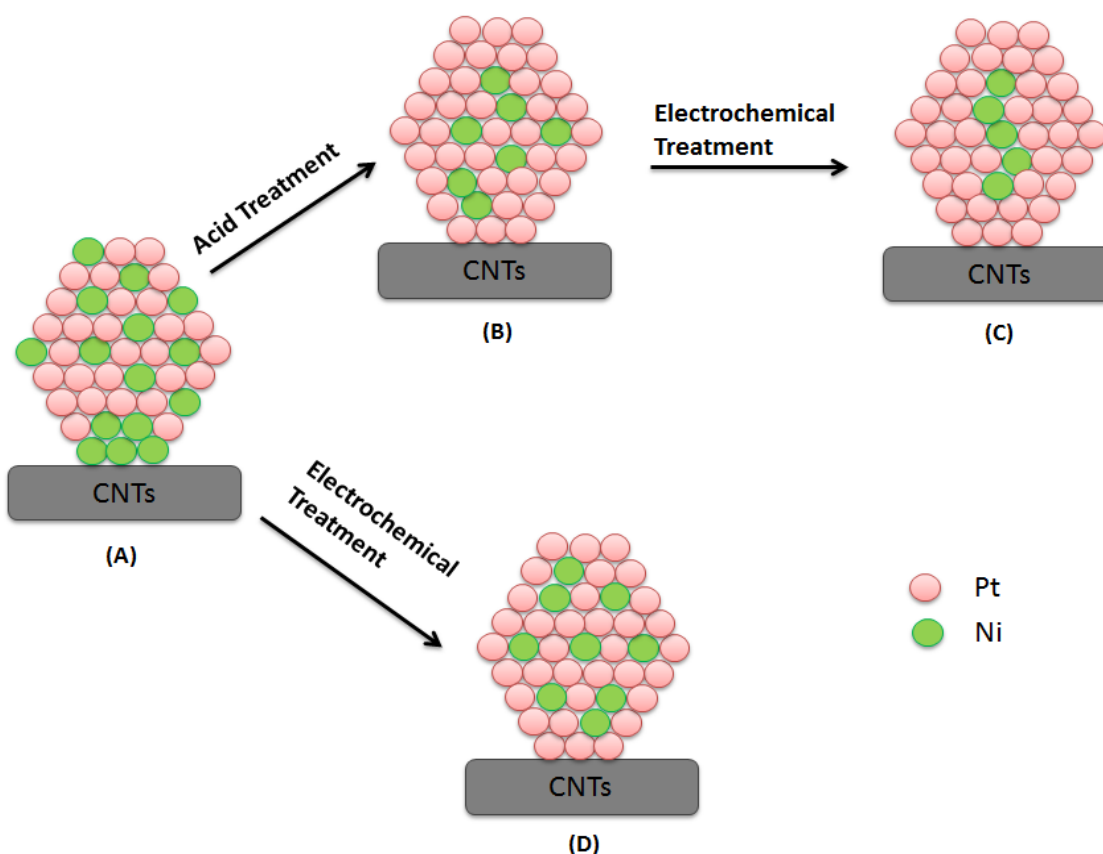


Figure 5.9: Model structures of PtNi catalysts supported on oxygen functionalized CNTs for the as prepared catalyst (A) and the catalysts after chemical (B) and/or electrochemical treatment (C) and (D) in acid environment.

5.4 Conclusions

PtNi nanocatalysts for methanol oxidation in acid media were prepared on oxygen functionalized carbon nanotubes by microwave assisted polyol reduction in two different modes of irradiation. Nanosized alloy particles well dispersed on the support were obtained. The irradiation mode (either continuous or pulsed) influences both the metal loading and the activity of the prepared catalysts where catalysts prepared under continuous irradiation show higher electrocatalytic activity. Structural characterization confirmed alloy formation and combined with the electrochemical behavior of the catalysts an electronic structure modification effect has been suggested to discuss the enhancement of activity of the prepared catalysts and their lower CO poisoning compared to benchmark Pt/C E-TEK catalyst and other PtNi catalysts reported in the literature.

References

- [1] A.S. Aricò, S. Srinivasan, V. Antonucci, *Fuel Cells* 1 **(2001)** 133.
- [2] A. S.Aricò, V. Baglio, V. Antonucci, in: H. Liu, J. Zhang (Eds.), *Electrocatalysis of Direct Methanol Fuel Cells: From Fundamentals to Applications*, Wiley-VCH, **2009**, pp. 1-77.
- [3] G.W. Huber, S. Iborra, A. Corma, *Chem. Rev.* 106 **(2006)** 4044.
- [4] C.N. Hamelinck, A.P.C. Faaij, *Energy Policy* 34 **(2006)** 3268.
- [5] R. Dillona, S. Srinivasana, A.S. Aricò, V. Antonucci, *J. Power Sources* 127**(2004)** 112.
- [6] S.K. Kamarudin, F. Achmad, W.R.W. Daud, *Int. J. Hydrog Energy* 34 **(2009)** 6902.
- [7] A. Hamnett, *Catal. Today* 38 **(1997)** 445.
- [8] S. Wasmus, A. Küver, *J. Electroanal. Chem.* 461 **(1999)** 14.
- [9] T. Iwasita, *Electrochim. Acta* 47**(2002)** 3663.
- [10] T. Iwasita, in W. Vielstich, H.A. Gasteiger, A. Lamm (Eds.) *Handbook of Fuel Cells – Fundamentals, Technology and Applications, Volume 2: Electrocatalysis*. John Wiley & Sons, **2003**, 603-624.
- [11] E. Antolini, in: H. Liu, J. Zhang (Eds.), *Electrocatalysis of Direct Methanol Fuel Cells: From Fundamentals to Applications*, Wiley-VCH, **2009**, pp. 227-255.
- [12] T. Iwasita, H. Hoster, A. John-Anacker, W.F. Lin, W. Vielstich, *Langmuir* 16 **(2000)** 522.
- [13] J.-H. Choi, K.-W. Park, I.-S. Park, J.-S. Lee, Y.-E. Sung, *J. Electrochem. Soc.* 153 **(2006)** A1812.
- [14] H.A. Gasteiger, N. Markovic, P.N. Ross Jr., E.J. Cairns, *J. Phys. Chem.* 97 **(1993)** 12020.
- [15] AB.A.A. Nassr, M. Bron, *ChemCatChem* 5 **(2013)** 1472.
- [16] E. Lee, A. Murthy, A. Manthiram, *J. Electroanal. Chem.* 659 **(2011)** 168.
- [17] C. Xu, J. Hou, X. Pang, X. Li, M. Zhu, B.Tang, *Int. J. Hydrogen Energy* 37 **(2012)** 10489.
- [18] Y.-Y. Chu, Z.-B. Wang, Z.-Z. Jiang, D.-M. Gu, G.-P. Yin, *J. Power Sources* 203 **(2012)** 17.
- [19] J. Masud, M.T. Alam, Z. Awaludin, M.S. El-Deab, T. Okajima, T. Ohsaka, *J. Power Sources* 220 **(2012)** 399.
- [20] T. Maiyalagan, B. Viswanathan, *J. Power Sources* 175 **(2008)** 789.
- [21] A. Nouralishahi, A. A. Khodadadi, A.M. Rashidi, Y. Mortazavi, *J. Colloid Interface Sci.* 393 **(2013)** 291.
- [22] P. Justin, G.R. Rao, *Int. J. Hydrogen Energy* 36 **(2011)** 5875.
- [23] C. Hu, Y. Cao, L. Yang, Z. Bai, Y. Guo, K. Wang, P. Xu, J. Zhou. *Appl. Surf. Sci.* 257 **(2011)** 7968.

- [24] D.-M. Gu, Y.-Y. Chu, Z.-B. Wang, Z.-Z. Jiang, G.-P. Yin, Y. Liu, *Appl. Catal. B*: 102 (2011) 9.
- [25] M. Watanabe, S. Motoo, *J. Electroanal. Chem.* 60 (1975) 275.
- [26] H. Igarashi, T. Fujino, Y. Zhu, H. Uchida, M. Watanabe, *Phys. Chem. Chem. Phys.* 3 (2001) 306.
- [27] K.-W. Park, J.-H. Choi, B.-K. Kwon, S.-A. Lee, Y.-E. Sung, H.-Y. Ha, S.-A. Hong, H. Kim, A. Wieckowski, *J. Phys. Chem. B* 106 (2002) 1869.
- [28] S. Harish, S. Baranton, C. Coutanceau, J. Joseph. *J. Power Sources* 214 (2012) 33.
- [29] M. Sakthivel, A. Schlange, U. Kunz, T. Turek, *J. Power Sources* 195 (2010) 7083.
- [30] S. Das, A.K. Mukhopadhyay, S. Datta, D. Basu, *Bull. Mater. Sci.* 32 (2009) 1.
- [31] G. Whittaker, *Sch. Sci. Rev.* 85 (2004) 87.
- [32] AB.A.A. Nassr, I. Sinev, W. Grünert, M. Bron, *Appl. Catal. B*: 142 (2013) 849.
- [33] K.V. Klementiev, *VIPER for Windows*, freeware, K.V. Klementev, *J. Phys. D*: 34 (2001) 209; www.cells.es/Beamlines/CLAEISS/software/viper.html
- [34] A.L. Ankudinov, B. Ravel, J.J. Rehr, S.D. Conradson, *Phys. Rev. B* 58 (1998) 7565.
- [35] H.-S. Oh, J.-G. Oh, H. Kim, *J. Power Sources* 183 (2008) 600.
- [36] J.-L. Shui, J.-W. Zhang, J.C.M. Li, *J. Mater. Chem.* 21(2011) 6225.
- [37] D. Li, S. Komarneni, *J. Am. Ceram. Soc.* 89 (2006) 1510.
- [38] T.C. Deivaraj, W. Chen, J.Y. Lee, *J. Mater. Chem.* 13 (2003) 2555.
- [39] M.K. Carpenter, T.E. Moylan, R.S. Kukreja, M.H. Atwan, M.M. Tessema. *J. Am. Chem. Soc.* 134 (2012) 8535.
- [40] S. Song, J. Liu, J. Shi, H. Liu, V. Maragou, Y. Wang, P. Tsiakaras, *Appl. Catal. B*: 103 (2011) 287.
- [41] P. Lidstrom, J. Tierney, B. Wathey, *Tetrahedron* 57 (2001) 9225.
- [42] C. Gabriel, B.S.J. Halstead, D.M.P. Mingos, *Chem. Soc. Rev.* 27 (1998) 213.
- [43] I. Bilecka, M. Niederberger, *Nanoscale* 2 (2010) 1358.
- [44] V.A. Ribeiro, O.V. Correa, A.O. Neto, M. Linardi, E.V. Spinace, *Appl. Catal. A*: 372 (2010) 162.
- [45] H.-S. Oh, J.-G. Oh, Y.-G. Hong, H. Kim, *Electrochim. Acta* 52 (2007) 7278.
- [46] B. Luo, S. Xu, X. Yan, Q. Xue, *Electrochem. Commun.* 23 (2012) 72.
- [47] X.-W. Zhou, R.-H. Zhang, Z.-Y. Zhou, S.-G. Sun, *J. Power Sources* 196 (2011) 5844.
- [48] H.J. Kim, S.M. Choi, S.H. Nam, M.H. Seo, W.B. Kim, *Catal. Today* 146 (2009) 9.
- [49] C. Yuan, X. Zhang, L. Su, B. Gao, L. Shen, *J. Mater. Chem.* 19 (2009) 5772.
- [50] L.S. Parreira, J.C. Martins da Silva, M. D’Villa -Silva, F.C. Simões, S. Garcia, I. Gaubeur, M.A.L. Cordeiro, E.R. Leite, M. Coelho dos Santos, *Electrochim. Acta* 96 (2013) 243.
- [51] G. Johansson, J. Hedman, A. Berndtsson, M. Klasson, R. Nilsson, *J. Electron Spectrosc. Relat. Phenom.* 2 (1973) 295.
- [52] S.D. Cameron, D.J. Dwyer, *Surf. Sci.* 176 (1986) L857.

- [53] M.G. Manson, *Phys. Rev. B* 27 **(1983)** 748.
- [54] G.K. Wertheim, S.B. Diczynski, S.E. Youngquist, *Phys. Rev. Lett.* 51 **(1983)** 2310.
- [55] R. Loukrakpam, J. Luo, T. He, Y. Chen, Z. Xu, P.N. Njoki, B.N. Wanjala, B. Fang, D. Mott, J. Yin, J. Klar, B. Powell, C.-J. Zhong, *J. Phys. Chem. C* 115 **(2011)** 1682.
- [56] B.-J. Hwang, L.S. Sarma, J.-M. Chen, C.-H. Chen, S.-C. Shih, G.-R. Wnag, D.-G. Liu, J.-F. Lee, M.-T. Tang, *J. Am. Chem. Soc.* 127 **(2005)** 11140.
- [57] C. Cui, M. Ahmadi, F. Behafarid, L. Gan, M. Neumann, M. Heggen, B. R. Cuenya , P. Strasser, *Faraday Discuss.* **2013**, DOI: 10.1039/C3FD20159G.
- [58] C. Wang, M. Chi, D. Li, D. Strmcnik, D. van der Vliet, G. Wang, V. Komanicky, K.C. Chang, A.P. Paulikas, D. Tripkovic, J. Pearson, K.L. More, N.M. Markovic, V.R. Stamenkovic, *J. Am. Chem. Soc.* 133 **(2011)** 14396.
- [59] X. Yu, D. Wang, Q. Peng, Y. Li, *Chem. Eur. J.* 19 **(2013)** 233.
- [60] E. Antolini, J.R.C. Salgado, E.R. Gonzalez, *Appl. Catal. B:* 63 **(2006)** 137.
- [61] B. Luo, S. Xu, X. Yan, Q. Xue, *J. Electrochem. Soc.* 160 **(2013)** F262.

Supporting information

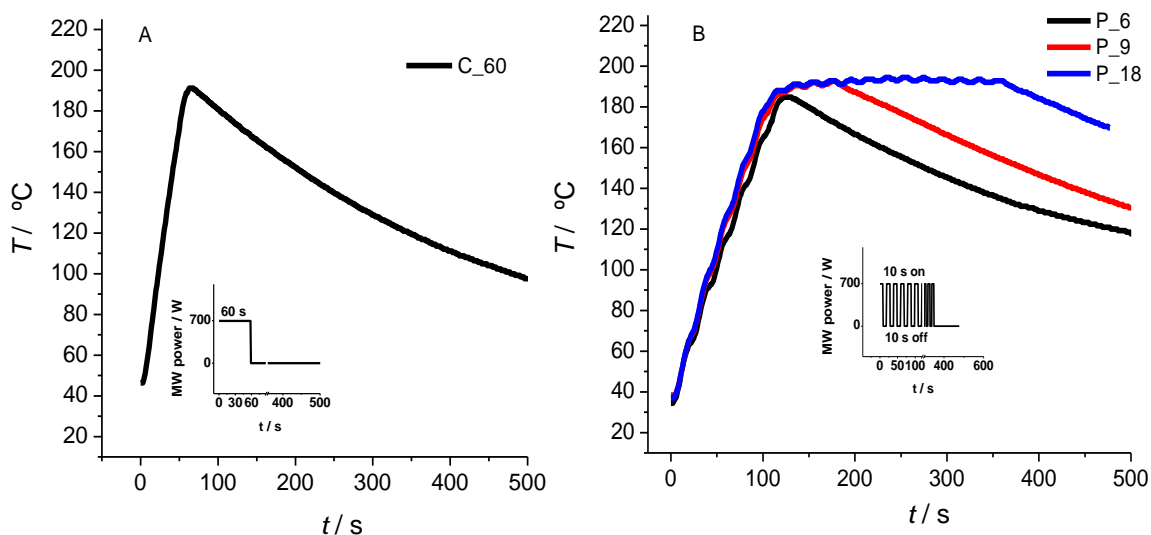


Figure SI5.1: Temperature profile of A) PtNi/CNT_C prepared under continuous irradiation mode and of B) PtNi/CNT_P prepared under pulsed irradiation mode. Inset the behaviour of irradiation mode is shown.

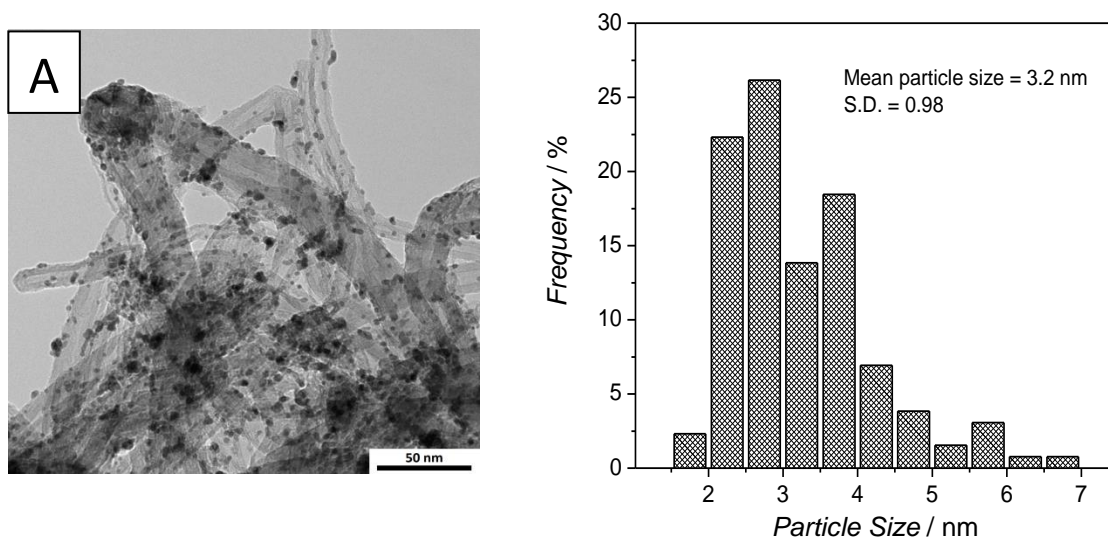


Figure SI5.2: TEM images of PtNi/CNT_C catalysts, A) PtNi/CNT_C_90_acid, B) PtNi/CNT_C_90.

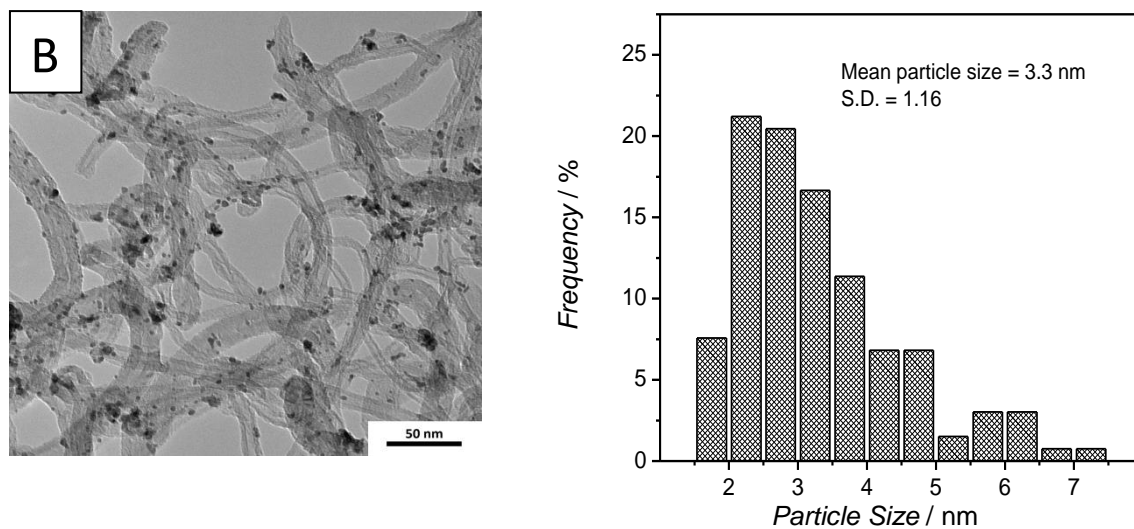


Figure SI5.2: continued

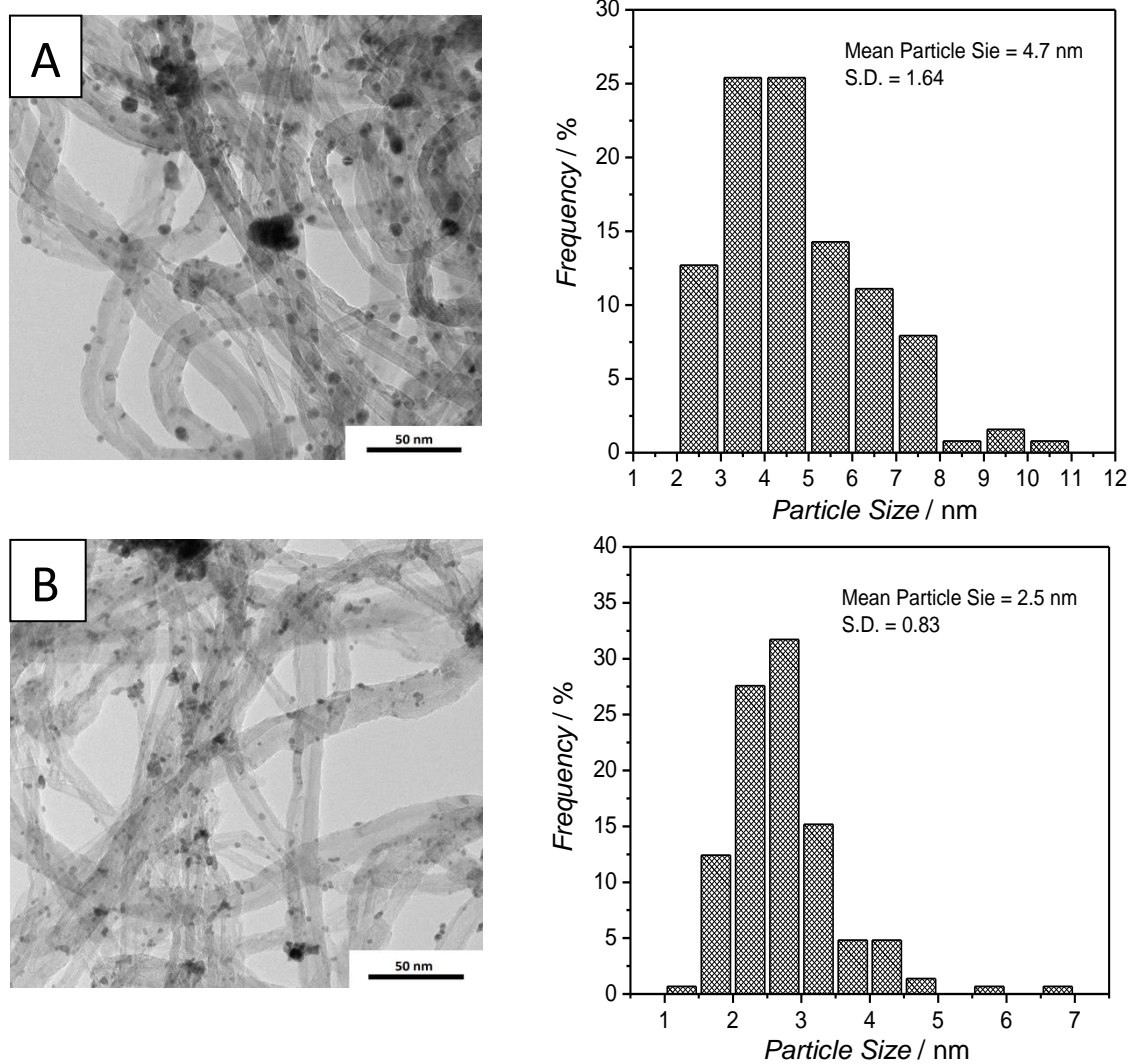


Figure SI5.3: TEM images of PtNi/CNT_P catalysts, A) PtNi/CNT_P_9, B) PtNi/CNT_P_12.

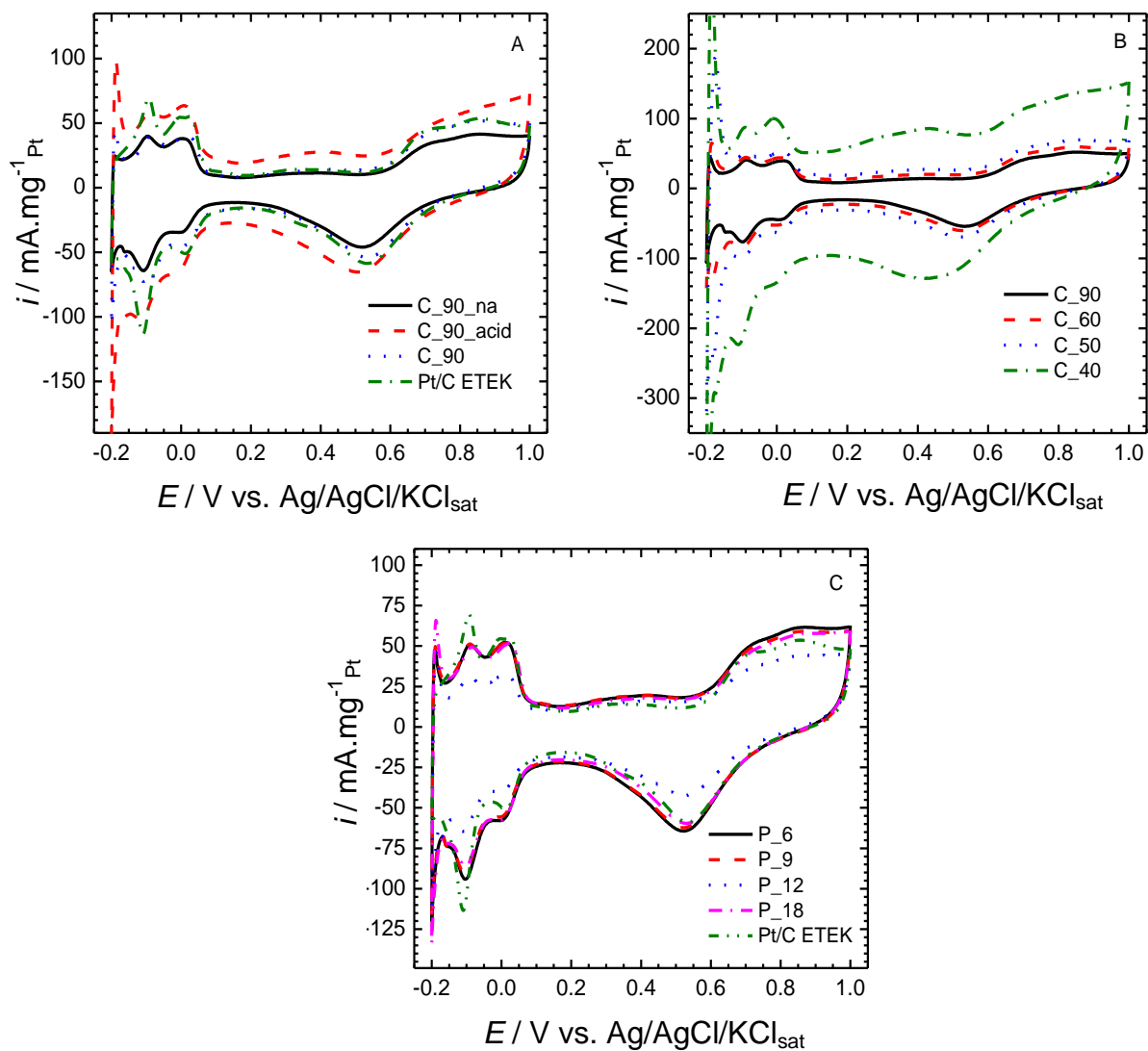


Figure SI5.4: CV of PtNi/CNT catalysts in 0.5 M H_2SO_4 scan rate $100 \text{ mV}\cdot\text{s}^{-1}$, A) aged PtNi/CNT_C catalysts, B) PtNi/CNT_C catalysts prepared at different irradiation time and C) PtNi/CNT_P catalysts.

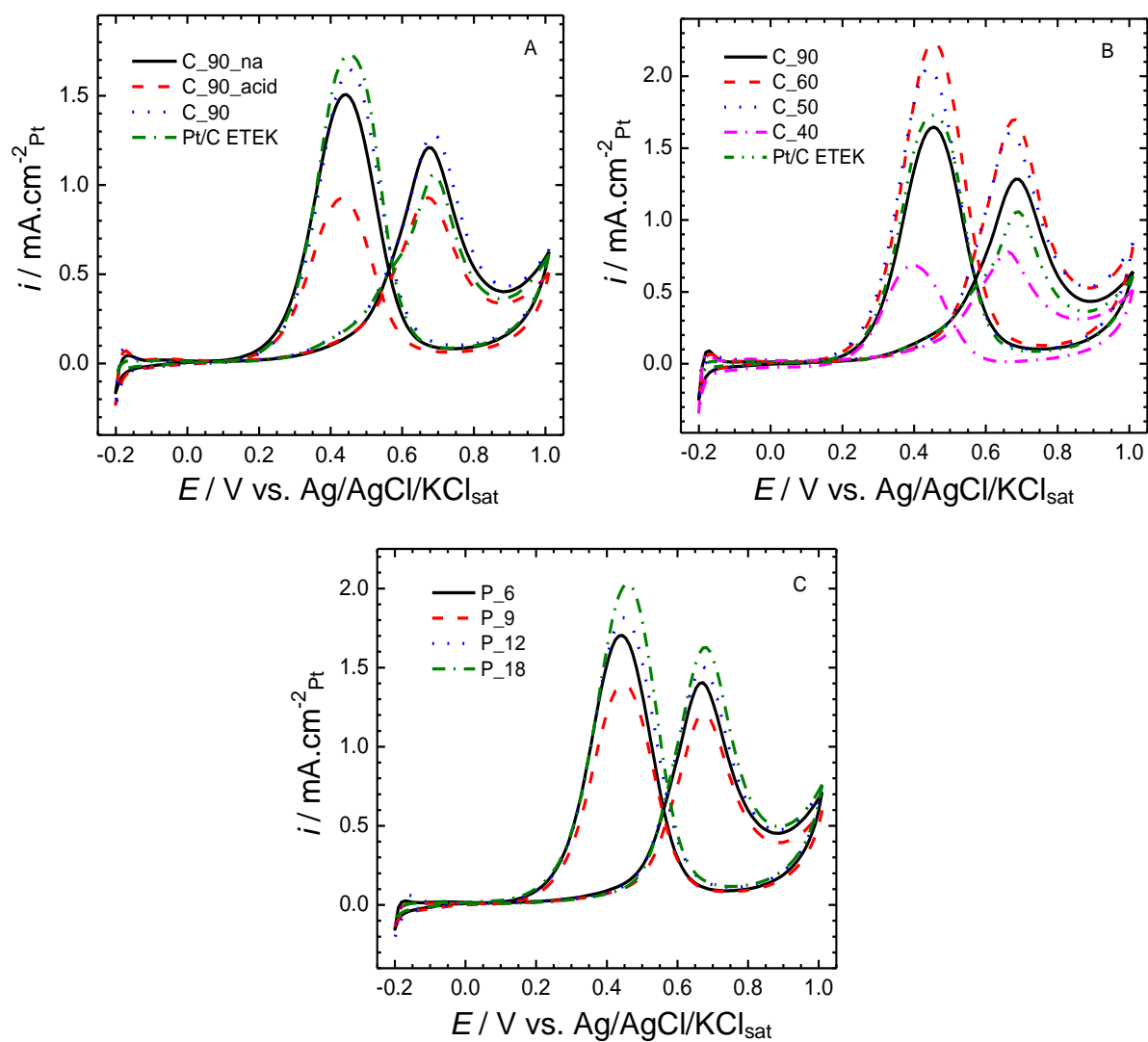


Figure SI5.5: CV for PtNi/CNT catalysts in $1 \text{ M CH}_3\text{OH}/0.5 \text{ M H}_2\text{SO}_4$ scan rate $100 \text{ mV} \cdot \text{s}^{-1}$, the current normalized to the electrochemical surface area.

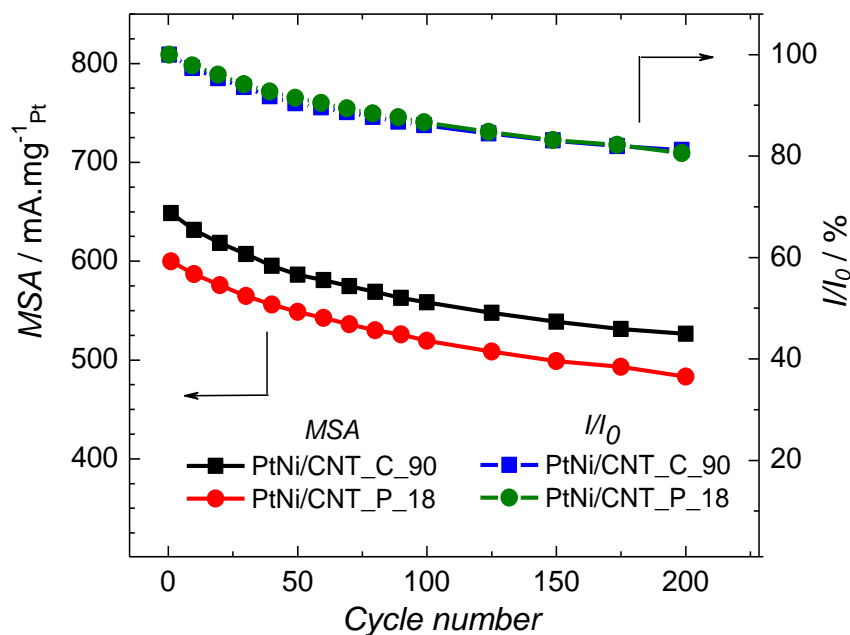


Figure SI5.6: Variation of mass specific activity and relative current against cycle number for PtNi/CNT_C and PtNi/CNT_P catalysts.

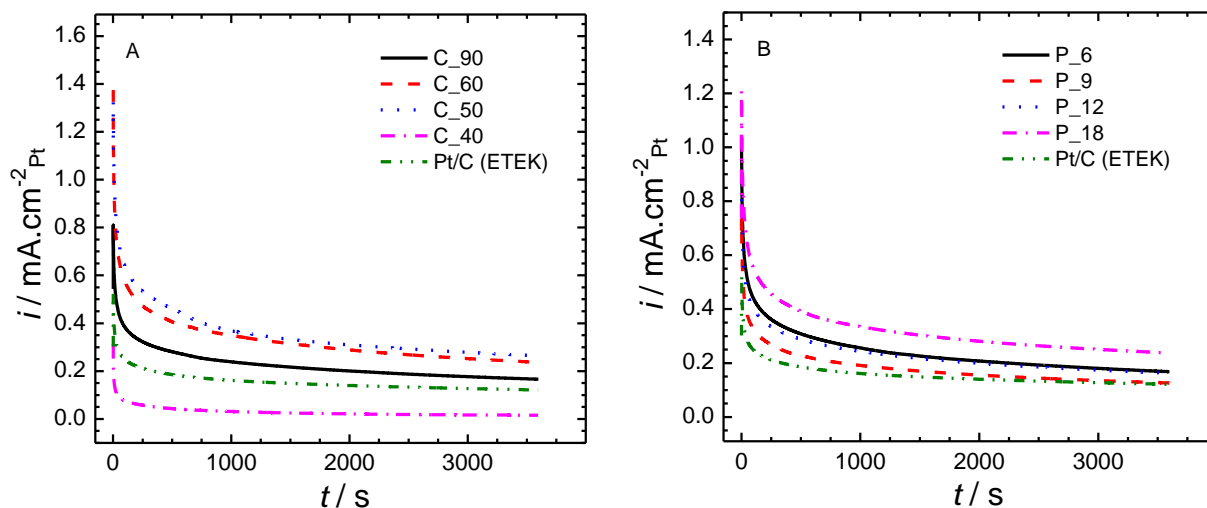


Figure SI5.7: CA curves of the PtNi/CNT catalysts in comparison with Pt/C ETEK in 1 M CH₃OH/ 0.5 M H₂SO₄ at 0.7 V; A) PtNi/CNT_C catalysts and B) PtNi/CNT_P catalysts, the current normalized to the electrochemical active surface area.

Chapter 5: Microwave-Assisted Polyol Synthesis of PtNi/CNTs Electrocatalysts

Table S15.1: Pt L_3 -edge EXAFS fit results within three shell model.

Shell	CN	R	σ^2	ΔE_0	Total metallic CN	P_{Pt}
PtNi/CNT_C_90_na						
Pt-Pt	5.29±1.45	2.74±0.02	9.5±1.53	11.41±2.51	6.54	0.19
Pt-O	1.37±0.32	2.05±0.03	8.0±3.05	16.24±5.14		
Pt-Ni	1.25±0.51	2.69±0.05	9.57±4.92	24.28±6.1		
PtNi/CNT_C_90_acid						
Pt-Pt	4.2±0.54	2.74±0.01	8.9±0.88	12.93±1.34	5.18	0.19
Pt-O	1.55±0.15	2.05±0.01	8.37±1.63	17.19±1.6		
Pt-Ni	0.98±0.25	2.69±0.02	7.52±2.39	19.21±3.6		
PtNi/CNT_C_90						
Pt-Pt	4.72±0.54	2.73±0.01	7.84±0.61	9.86±1.02	6.28	0.25
Pt-O	1.13±0.13	2.03±0.01	6.23±1.52	15.77±1.88		
Pt-Ni	1.56±0.3	2.67±0.02	9.31±1.8	15.88±2.31		
PtNi/CNT_C_60						
Pt-Pt	4.57±0.61	2.74±0.01	7.41±0.70	11.00±1.27	6.19	0.26
Pt-O	1.19±0.16	2.04±0.02	6.15±1.73	16.27±2.11		
Pt-Ni	1.62±0.33	2.66±0.02	9.63±2.15	15.66±2.57		
PtNi/CNT_P_12						
Pt-Pt	4.85±0.55	2.74±0.01	7.77±0.61	10.64±0.98	6.52	0.26
Pt-O	0.97±0.12	2.04±0.01	5.24±1.61	16.42±2.03		
Pt-Ni	1.67±0.33	2.67±9.43	9.43±1.72	15.66±2.26		
PtNi/CNT_P_18						
Pt-Pt	4.92±0.76	2.73±0.01	8.31±0.89	10.72±1.50	6.52	0.25
Pt-O	1.11±0.17	2.04±0.02	5.82±1.92	15.71±2.73		
Pt-Ni	1.60±0.40	2.68±0.02	8.02±2.14	18.03±2.88		

The content of this chapter has been published as

Electrocatalytic oxidation of formic acid on Pd/MWCNTs nanocatalysts prepared by the polyol method

Abu Bakr Ahmed Amine Nassr, Annett Quetschke, Eik Koslowski, Michael Bron

Electrochimica Acta 102(2013) 202-211

<http://www.sciencedirect.com/science/article/pii/S0013468613006129>

Reproduced with permission of Elsevier copyright® 2013

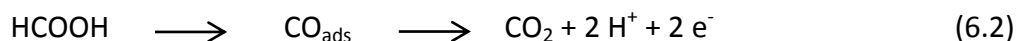
6.1 Introduction

Direct formic acid fuel cells (DFAFCs) received significant attention in the last decade as promising sources of clean energy targeted for different applications including small and portable electronics such as phones and laptop computers [1]. The direct formic acid fuel cell has a theoretical electromotive force (EMF) higher than that of a direct methanol fuel cell [1-3]. As a liquid fuel, formic acid has advantages compared to methanol as it is relatively less toxic and shows lower crossover flux through the proton exchange membrane due to its repulsion by the proton membrane terminal groups, and therefore the use of higher concentrations is possible. It is also considered as a strong electrolyte; hence it is expected to facilitate proton transport within the anode compartment of the fuel cell [2]. One major advantage of formic acid as fuel is that it can be produced from environmental waste through biomass conversion processes, as demonstrated recently [4,5].

The oxidation of formic acid on Pt catalysts mechanistically proceeds by a dual pathway [3,6-8]. One is the direct way in which formic acid is oxidized directly into CO₂ through a dehydrogenation reaction avoiding the formation of CO as poisoning intermediate; the mechanism can be represented by the following equation:



The second way is the indirect way through a dehydration reaction involving the formation of CO as intermediate followed by oxidation of this intermediate into CO₂, similar to methanol oxidation on Pt. The overall mechanisms can be represented by the following equation:



In this regards, Pt is not the best catalyst for practical formic acid fuel cell applications since the formation of CO poisoning species blocks the catalyst surface

and limits fuel cell efficiency. An approach to overcome this problem is using bimetallic system like PtRu, where the Ru can enhance the CO oxidation into CO₂ however still then CO could accumulate during long time operation and decrease the cell efficiency [2,3,8].

Pd based nanocatalysts are considered excellent catalysts for formic acid oxidation in direct formic acid fuel cells due to their higher catalytic activity where the formic acid can be oxidized directly into CO₂ according to Equation (6.1) without formation of poisoning intermediates [3,9-11]. Pd also has the advantage of lower cost than Pt and Ru and is of higher abundance than the former. Despite Pd catalysts showing promising results for the use in direct formic acid fuel cells, the detection of accumulated CO on the surface of the catalysts after several hours of operation has been reported [12-16]. Pd catalysts supported on different carbons have been investigated as promising catalysts for formic acid oxidation [17-25]. It was found that the catalytic activity of Pd nanoparticles depends on the support and its properties [25-30]. Recently, it was reported that Pd decorated functionalized carbon nanotubes prepared by sodium borohydride reduction exhibit superior activity toward formic acid oxidation for long time and at high concentration [31].

Despite these promising results, still work is needed to improve the catalytic activity of Pd/CNT catalysts and their stability for formic acid oxidation to enable their widespread application. In this work, we report on a systematic study to elucidate the effect of preparation conditions and of the support functional groups on the catalytic activity and stability of Pd catalysts supported on carbon nanotubes. The catalysts have been prepared by the polyol method with CNTs as received or functionalized under mild conditions as support and in presence and absence of citric acid. The catalysts were characterized with thermal gravimetric analysis (TGA) to determine the metal loading and their thermal behavior. The crystal structure and nanostructure of the prepared catalysts were studied with XRD and TEM analyses. Electrocatalytic activity and stability have been studied with cyclic voltammetry, CO stripping and chronoamperometry techniques.

6.2 Experimental

6.2.1 Catalyst preparation

Functionalized multiwalled carbon nanotubes (MWCNTs, Baytubes® C 150 P, purchased from Bayer MaterialScience AG, Germany) were used as support materials. The nanotubes have an outer mean diameter of 13-16 nm with a diameter distribution of 5-20 nm, an inner mean diameter of 4 nm with a diameter distribution of 2-6 nm, the number of walls is 3-15 and the length 1 - 10 μm, according to the data sheet of the producer. The BET surface area has been determined to be 250 m² g⁻¹.

Functionalization has been done according to a procedure reported elsewhere [32]. Briefly, 500 mg of the as-received CNTs were dispersed in 100 ml of 5 M HNO₃ and refluxed at 100 °C for 6 h under stirring. After adding 200 ml of water and stirring overnight the functionalized CNTs (labeled FCNTs in the following) were separated by centrifugation and washing. The presence of oxygen functional groups was confirmed by TGA and cyclic voltammetry, while the BET area increased to 290 m² g⁻¹.

In this work, Pd/CNT catalysts were prepared by the polyol method under variation of the aging time of the catalysts after reduction or the presence of citric acid as stabilizer as follows:

Route A

FCNTs (100 mg) were dispersed in 15 ml of ethylene glycol (EG) under stirring followed by sonication in an ultrasonic bath for 15 min. To this dispersion, an solution of PdCl₂ in EG (14.23 ml, 0.0165 M, containing 25 mg of Pd metal) was added and left under stirring for 15 min. The pH of the solution was adjusted with 2 M NaOH/EG solution to pH ≈ 12 and the mixture was sonicated for 15 min to aid homogeneous adsorption of the metal precursor onto the surface of the support. For the reduction of Pd ions, the reaction vessel was transferred to an oil bath and heated at 160 °C for 6 h under stirring and reflux conditions. After completing the reduction, the mixture was left under stirring to cool down to room temperature and then separated immediately with a centrifuge (Eppendorf 4807) at 5000 rpm for 20 min after which it was subjected to 5-6 washing cycles with water and subsequent centrifugation to ensure the removal of chloride ions and other impurities. Finally, the catalyst was dried in oven at 80 °C overnight and then crushed and stored in glass vial. These catalysts are labeled Pd/FCNT.

Route B

Similar to route A, except that after reduction the reaction mixture was left under stirring (“ageing”) overnight followed by separation, washing and finally drying. This type of catalyst is labeled Pd/FCNT_A, where A stands for ageing.

Route C

Similar to route A, except that the metal solution before addition to the carbon support was mixed with citric acid (CtA) in a molar ratio of CtA:Pd, 2:1. The acronym CtA for citric acid is added to the catalyst name (Pd/FCNT_{CtA}).

Route D

Similar to route B, except that the metal solution before addition to the carbon support was mixed with citric acid (CtA) in a molar ratio of CtA:Pd, 2:1. Catalyst label: Pd/FCNT_CtA_A.

In all preparation procedures, the amount of Pd metal was controlled to be 20 wt% of the catalyst. For the purpose of comparison, a Pd catalyst supported on the as received carbon nanotubes (CNTs) was prepared in the same way as route A and labeled "Pd/CNT". It was used as reference in parallel with the state of the art catalyst produced by E-TEK (20 wt% Pd/C E-TEK). This catalyst is characterized in the same way as the prepared ones and details on its properties are given within the text.

In order to remove remaining organics from the synthesis process, the catalyst samples were heat treated at 200 and 400 °C for 2 h in a horizontal furnace (GERO, Germany) equipped with a quartz tube under N₂ gas (99.999 %) atmosphere. The respective temperature is added to the catalyst name (e.g., Pd/FCNT_A_200).

6.2.2 Catalysts characterization by TGA, XRD and TEM

The thermal behavior and the metal loading of the catalysts were studied with TGA using a STA 449 FI Jupiter®, NETZSCH, Germany. About 10 mg catalyst were first heated to 100 °C with a heating rate of 20 °C m⁻¹ and kept for 1 h at this temperature under Ar atmosphere to eliminate physically adsorbed water before it was cooled down to 40 °C under the same atmosphere. This step ensures that the weight loss afterward results only from catalyst decomposition. After that the sample heated up to 800 °C with a heating rate of 5 K min⁻¹ under oxygen atmosphere (20 % O₂ in Ar gas).

Powder X-ray diffraction analysis (XRD) was done on a D8 advanced X-Ray diffractometer, Bruker AXS, working with Cu K α source ($\lambda = 0.15406$ nm) in the range of $2\theta = 20-90^\circ$ at a scan rate of 2° min⁻¹. The particle size was estimated applying the Debye–Scherrer equation using the full width at half maximum (FWHM) of the (220) peak. The FWHM was obtained by fitting the (220) peak with a Gaussian function using Origin8 software.

Transmission electron microscopy (TEM) was done on a LEO 912, Japan working at an acceleration voltage of 120 keV. For sample preparation, few mg of the catalyst were dispersed in ethanol under ultrasonication for 10 min and then some drops of the suspension were dropped onto a carbon coated copper grid. After drying in air the sample was introduced into the instrument for investigation.

6.2.3 Electrochemical characterization

Electrochemical studies have been carried out using an Autolab PGSTAT128N potentiostat/galvanostat in an electrochemical cell with three compartments in which the reference electrode compartment was connected to the working electrode compartment through a Luggin capillary and the counter electrode compartment separated from the working electrode compartment by a glass frit. An Ag/AgCl/KCl_{sat} electrode was used as reference electrode to which the potentials in this work are referred to, whereas a platinum net and a glassy carbon electrode ($r = 2$ mm) were used as counter electrode and substrate for the working electrode; respectively.

Before use, the glassy carbon electrode was subjected to a cleaning procedure by polishing with alumina slurry of $0.1 \mu\text{m}$ and $0.03 \mu\text{m}$ consecutively with the help of a polishing cloth and washing in an ultrasonic bath in ethanol/water and water each for 10 min; respectively. For preparation of the working electrode, 2.5 mg of the Pd/support catalyst were dispersed under sonication for 1 h in $350 \mu\text{l}$ of 5 wt.% Nafion solution and isopropanol (1/6, v/v) and then the dispersion was subjected to stirring overnight to get a homogenous catalyst ink. $5 \mu\text{l}$ of this ink was drop coated onto the glassy carbon electrode substrate and left in a saturated atmosphere of isopropanol at room temperature to dry after which the electrode is ready for electrochemical measurements. It was found that the overnight stirring step is very important to get a homogenous thin film of the catalyst on the electrode substrate.

The electrocatalytic oxidation of formic acid was studied according to the following procedure. First the catalyst-coated electrode was cycled in a potential window of -0.2 to 1 V at a scan rate of 50 mV s^{-1} for 10 cycles in $0.5 \text{ M H}_2\text{SO}_4$ solution. This step is considered as a cleaning step of the electrode surface. The last cycle is used to monitor the electrochemical behavior of the catalyst in $0.5 \text{ M H}_2\text{SO}_4$ solution. Then the electrochemical surface area was determined before formic acid oxidation. CO gas was purged into the cell while holding the electrode potential at -0.15 V for 15 min to form a CO_{ads} layer on the Pd surface. After purging with N_2 gas for 20 min to remove dissolved CO from the solution while keeping the potential at -0.15 V, a CO stripping voltammogram was recorded in a potential window of -0.2 to 0.9 V for three consecutive cycles. Finally, to study formic acid oxidation the electrode was transferred into another cell filled with $0.5 \text{ M HCOOH}/0.5 \text{ M H}_2\text{SO}_4$ solution and 100 cyclic voltammograms (CVs) were recorded in the potential window of -0.2 to 1 V at a scan rate of 50 mV s^{-1} and the cycle number 50 was used to evaluate the electrocatalytic activity.

To test the stability of the electrode and the oxidation current at a specific potential, chronoamperometric (CA) measurements were carried out in $0.5 \text{ M HCOOH}/0.5 \text{ M H}_2\text{SO}_4$ at 0.3 V for 1 h. For this, a fresh electrode was prepared and

subjected to the same cleaning step as above. Before all electrochemical measurements the solutions were purged with pure N₂ gas for at least 20 min and N₂ gas was maintained to purge over the solution during the measurements. In a previous study, we encountered the problem of accumulation of gas (likely CO₂) during formic acid oxidation. The accumulated gas blocks the surface of the electrode prevents further formic acid oxidation and cause noise during the measurements [25]. For this reason, in the current study, the cyclic voltammetry and chronoamperometry measurements have been carried out under hydrodynamic conditions by rotating the electrode at 900 rpm. Due to the high formic acid concentration used, no diffusion limitation was observed in our measurements confirming that electrode rotation does not influence the results.

6.3 Results and Discussion

6.3.1 TGA, TEM and XRD

TGA analysis is considered as a useful technique for the evaluation of the thermal stability and oxidation/corrosion resistance of many carbon supported electrocatalysts [33,34] and may be used to determine the metal loading of the prepared nanocatalysts. The thermogravimetric (TGA) curves of all prepared Pd/(F)CNTs nanocatalysts and of Pd/C in oxidizing atmosphere are shown in Figure 6.1. No weight loss can be detected up to 150 °C, and the catalysts show marginal weight loss up to 260 °C with a small peak at 230 °C, which may be attributed to an early decomposition of carboxylic groups on the surface of the functionalized carbon nanotubes [35] or more likely to the decomposition of carboxylic groups in citric acid and probably organic residues from the polyol synthesis. At higher temperatures all catalysts show an intense weight loss step resulting from the oxidation of the carbon support. The temperature depends on the type of the support as well as the method of catalyst preparation. Oxidation of the commercial catalyst starts at about 310 °C and is followed by a second oxidation step from 480 °C ending at 500 °C. Pd supported on as received CNTs (Pd/CNT), is as expected more stable and starts to be decomposed above 450 °C, while Pd/FCNT, prepared in the same way but with oxidized CNTs (FCNTs) as support, is even more stable and is decomposed above ca. 500 °C. Oxidation of the CNTs in nitric acid probably helps to remove metal impurities in the CNTs, which might be present from the production process and would catalyze early decomposition in oxidizing atmosphere. A similar behavior is observed for the support material only (as received CNT and FCNT, see Figure SI6.1A), indicating that the deposited Pd in Pd/CNT and Pd/FCNT does not significantly influence decomposition behaviour.

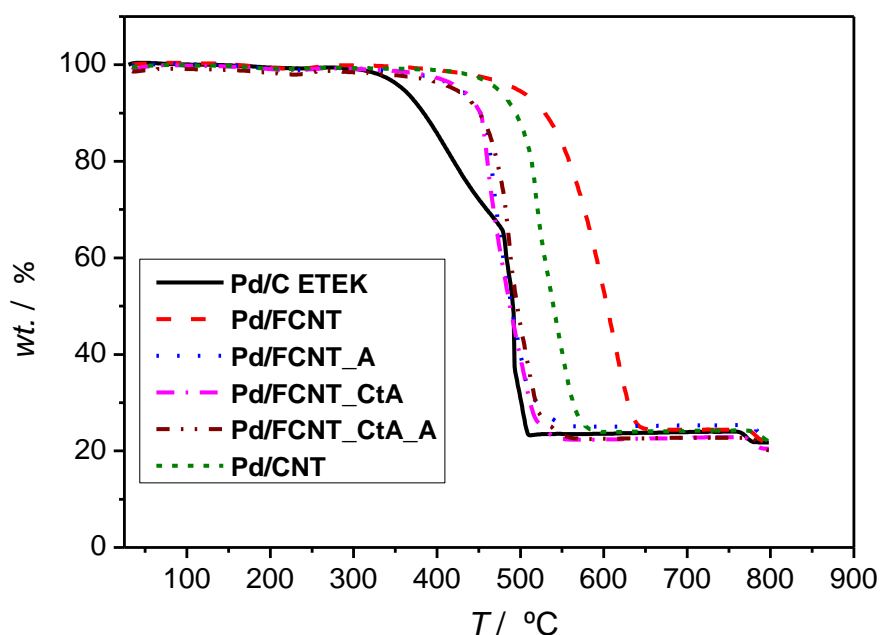


Figure 6.1: TGA curve of various CNT-supported Pd-catalysts in O_2/Ar atmosphere. Heating rate $5\text{ }^\circ\text{C min}^{-1}$.

However in this regard the comparably low stability of the catalysts prepared after ageing and/or in presence citric acid (Pd/FCNT_A, Pd/FCNT_CtA and Pd/FCNT_CtA_A) with decomposition temperatures of $410\text{ }^\circ\text{C}$ has been paid attention to since the same oxidized nanotubes as for Pd/FCNT were used. In principle it is well known that deposited nanoparticles accelerate the carbon support decomposition [33,36], thus the decomposition of these three samples at lower temperatures would be in line with the literature findings. Ageing under stirring might improve the contact between Pd nanoparticles and FCNTs, leading to improved oxidation catalysis for Pd/FCNT_A. The same argument could be put forward for the catalyst Pd/FCNT_CtA_A prepared with citric acid however comprising also an ageing step. The lower stability of Pd/FCNT_CtA and the role of citric acid are less clear in this regard. Probably citric acid promotes close contact between Pd and FCNTs and thus facilitates CNT oxidation.

After their final decomposition all catalysts show constant weight up to $770\text{ }^\circ\text{C}$ after which a sudden small weight loss is observed. This behavior has been reported before by Moore et al. [28] in their TGA analysis of Pd catalysts supported on Vulcan carbon and on diamond particles. To ensure that there is no further weight loss, the final measurement temperature has been extended for Pd/FCNT up to $1100\text{ }^\circ\text{C}$ (Figure SI6.1B). The metal loading of all catalysts can thus be determined at $800\text{ }^\circ\text{C}$ correcting the final weight to the oxide formation as suggested by Cochell et al. [37]. Results are shown in Table 6.1, indicating that the experimental Pd loading is close to the nominal one.

TEM analyses of the catalysts prepared under different conditions are shown in Figure 6.2. The dispersion of Pd nanoparticles is uneven on the CNTs support with appearance of particle agglomeration. Pd agglomeration on carbon supports has been reported in various studies [26,27,38-42]. Kumar et al. [27] attributed the formation of agglomerated Pd particles on Vulcan carbon functionalized with H_2O_2 and HNO_3 to the distortion of the support microstructure by these agents and therefore their lower BET surface area and porosity. However the mild functionalization of CNTs used in our study does not affect the textural properties of the carbon nanotubes as evidence from the characterization of CNTs before and after functionalization [32]. On the other hand, Li et al. [38] and Liang et al. [40] attributed the appearance of agglomerated Pd nanoparticles in Pd/C catalysts to the formation of $\text{Pd}(\text{OH})_x$ resulting from the modification of the pH during the catalyst preparation process. These species tend to agglomerate and after reduction form agglomerated Pd nanoparticles. This explanation could also apply in our case since a high pH was used during the polyol (EG) reduction. Even in the presence of citric acid as stabilizer (or the trivalent citrate ion in alkaline media which may form a complex with Pd ions [43]) during the preparation, agglomeration can still be observed. The interaction of OH^- species with Pd ions is obviously favored compared to the formation of a complex, leading to the formation of insoluble hydroxide $\text{Pd}(\text{OH})_x$ under these conditions, hampering to a certain amount the formation of stabilized nanoparticles and leading the formation of agglomerated Pd nanoparticles [38,40].

An important observation from TEM is that although the non-aged catalysts (Pd/FCNT, Pd/FCNT_CtA) show some individual spherical nanoparticles which can be detected from TEM images together with a high degree of agglomeration, the aged catalysts (Pd/FCNT_A and Pd/FCNT_CtA_A) show the formation of irregular particles with nanodendritic like-structure (Figure SI6.2). This behavior could be attributed to the oriented attachment mechanism where the particles of the same crystallographic orientation under loss of the stabilizer self-organize and the surface atoms get in direct contact with each other [44,45].

Heat treatment of the catalysts in N_2 atmosphere at $200\text{ }^\circ\text{C}$ does not lead to significant changes whereas treatment at $400\text{ }^\circ\text{C}$ leads to formation of large particles sizes in case of Pd/FCNT_CtA_400, however connected/agglomerated particles are still observed in the aged catalysts Pd/FCNT_CtA_A_400 (Figure SI6.3). On the other hand the commercial catalysts showed a high dispersion of nanoparticles on the carbon support and small particle size, and a low level of agglomeration. The mean particle size for the commercial catalysts was determined from TEM images to be $4 \pm 0.8\text{ nm}$ whereas for the prepared nanocatalysts despite the TEM images display some individuals nanoparticles it is impossible to precisely estimate the mean particle size due to the high extent of agglomeration.

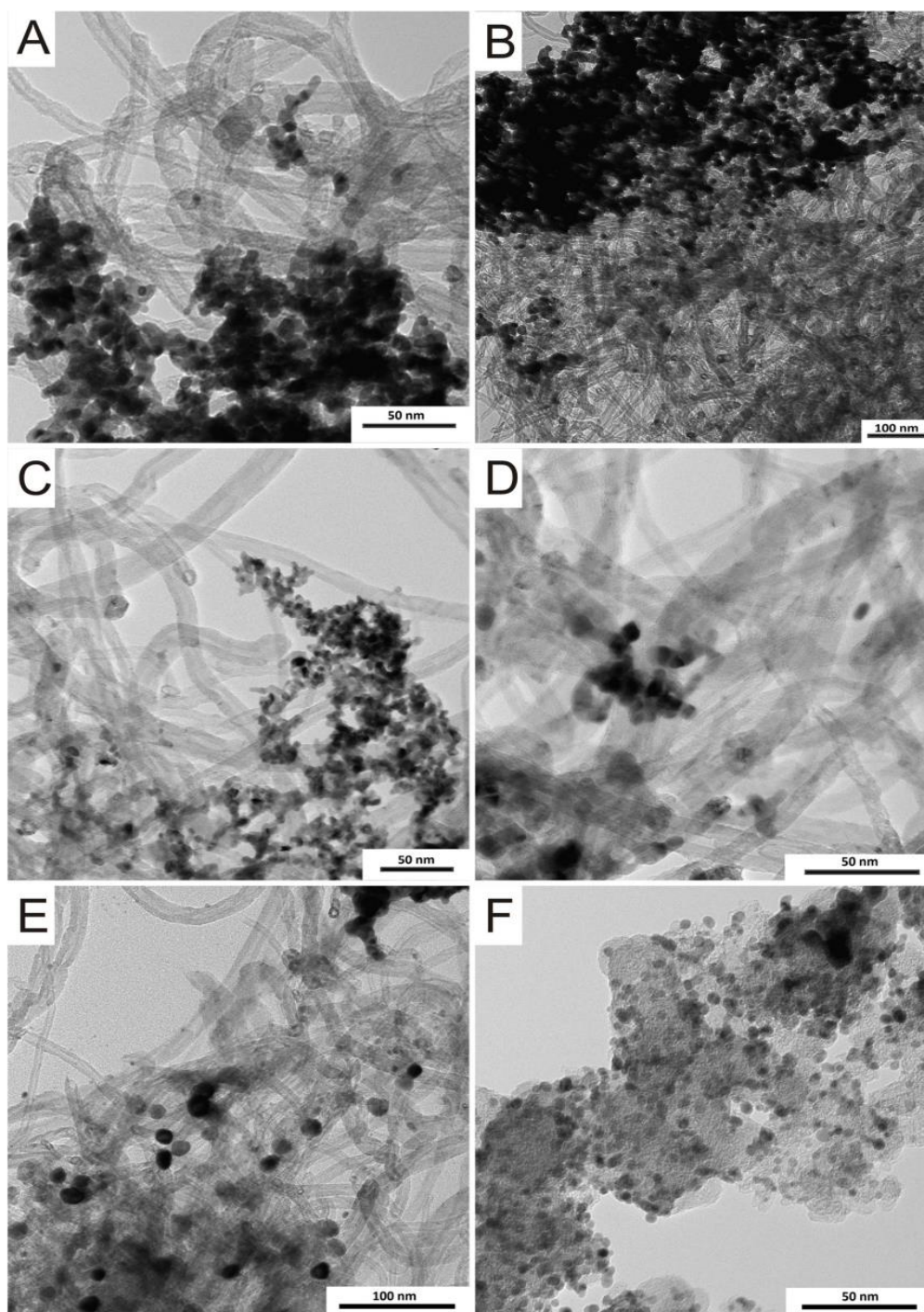


Figure 6.2: TEM images of Pd nanocatalysts, A) Pd/FCNT, B) Pd/FCNT_CtA, C) Pd/FCNT_A, D) Pd/FCNT_CtA_A, E) Pd/CNT and F) Pd/C E-TEK.

XRD patterns for the prepared nanocatalysts compared to Pd/C E-TEK are displayed in Figure 6.3, showing the expected (111), (200), (220) and (311) reflections for the Pd metal with an (fcc) lattice structure [24-27]. The peak centered at $2\theta = 25$ is assigned to the graphite plane (002) in the CNTs which is broad in case of the commercial catalyst supported on Vulcan carbon [26,27,41]. The Pd commercial catalysts display an additional peak at $2\theta = 34$ which is corresponding to PdO [46,47], which probably forms during handling in air or storage.

Heat treatment at lower temperature (200 °C) has no significant effect on the crystal structural of the catalysts as the diffraction peaks for the heat treated catalysts are nearly unchanged, however the heat treatment at 400 °C leads to significant changes as the diffraction peaks become sharper and increase in intensity which indicates a higher degree of crystallinity and/or larger particle sizes as result from catalysts sintering. Also, the heat treated catalysts at 400 °C show an additional peak at $2\theta = 33.9$ which corresponds to PdO [46,47] (Figure SI6.4A, B, and C). The formation of PdO upon heat treatment at 400 °C could be attributed to the decomposition of surface functional groups from the carbon support and also from citric acid. It is also possible that after heat treatment the catalysts are more reactive during handling in air due to removal of a stabilizing layer of EG or citrate.

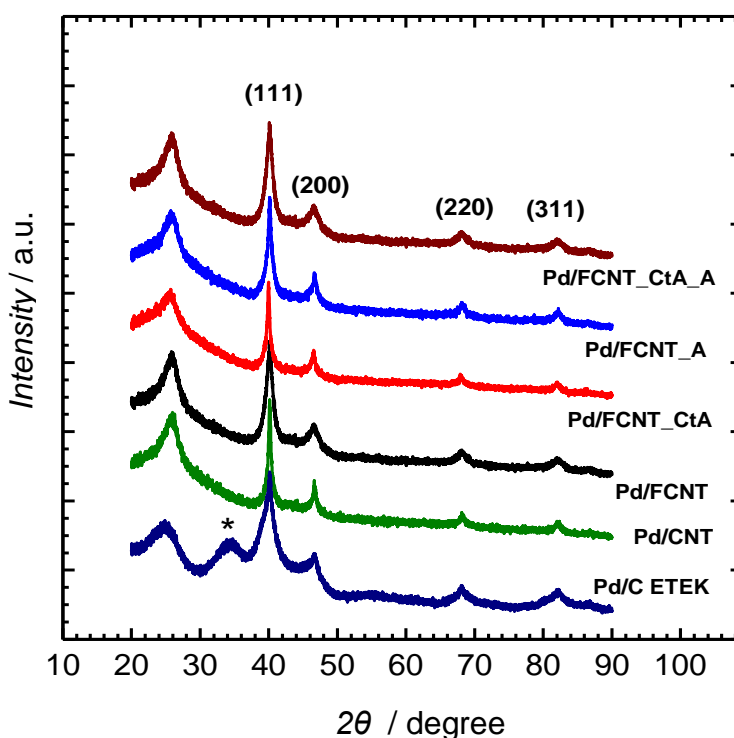


Figure 6.3: XRD patterns of the prepared Pd nanocatalysts and Pd/C ETEK.

The average crystallite size was determined using Debye-Scherrer equation [48]

$$d = \frac{0.9 \lambda}{B_{2\theta} \cos \theta} \quad (6.3)$$

Where d is the particle size, λ is the wavelength, $B_{2\theta}$ is the full width at half maximum and θ is the diffraction angle. The full width at half maximum was calculated from the diffraction peak of the (220) face, which does not overlap with signals from the carbon support. The crystallite sizes calculated for all catalysts are summarized in Table 6.1. The crystallite size of the as-prepared catalysts varies from 5-8 nm depending on the preparation route and on the carbon support (comp. Pd/CNT and Pd/FCNT). The crystallite sizes for all catalysts increase with heat treatment and the increase is more pronounced after heat treatment at 400 °C. The crystallite size for the commercial catalyst from XRD agrees well with the particle size from TEM.

Table 6.1: Structural properties of Pd nanocatalysts from TGA and XRD analyses.

Catalysts	Metal loading wt (%)	Average particle size (nm) form XRD
Pd/FCNT	19.2	5
Pd /FCNT_200	n.d	5.4
Pd/FCNT_A	19.6	6.3
Pd/FCNT_A_200	n.d	9
Pd/FCNT_CtA	17.6	6.7
Pd/FCNT_CtA_200	17.6	12.6
Pd/FCNT_CtA_400	18.9	16.1
Pd/FCNT_CtA_A	18.2	5
Pd/FCNT_CtA_A_200	18.9	6.9
Pd/FCNT_CtA_A_400	18	12.5
Pt/CNT	19.1	8
Pd /C ETEK	19.2	4.1

n.d = not determined

6.3.2 Electrochemical characterization

6.3.2.1 Surface area determination

The electrochemical features of the electrodes prepared from all Pd nanocatalysts and of Pd/C E-TEK were analyzed in 0.5 M H₂SO₄ as shown in Figure 6.4. The voltammograms depict the typical features of a Pd electrode in acid solution [20,22,23,28], which are the hydrogen adsorption-desorption at lower potentials (-0.2 to 0.1 V), the formation of oxide in the positive scan starting from potentials of 0.53 V and the oxide reduction during the negative-going scan at potential 0.63 to 0.36 V with a well-defined peak at 0.50 V [28]. The higher current associated with the hydrogen adsorption desorption and oxide reduction behavior for the catalysts Pd/FCNT and Pd/C E-TEK indicates qualitatively a higher electrochemical surface area of these catalysts. The same behavior is observed for the heat treated catalysts (Figure SI6.5),

which displays all characteristics of a Pd electrode however with decrease in the current for both the hydrogen adsorption-desorption region and oxide reduction region which indicate the decrease of active surface area as a result of increased particle size.

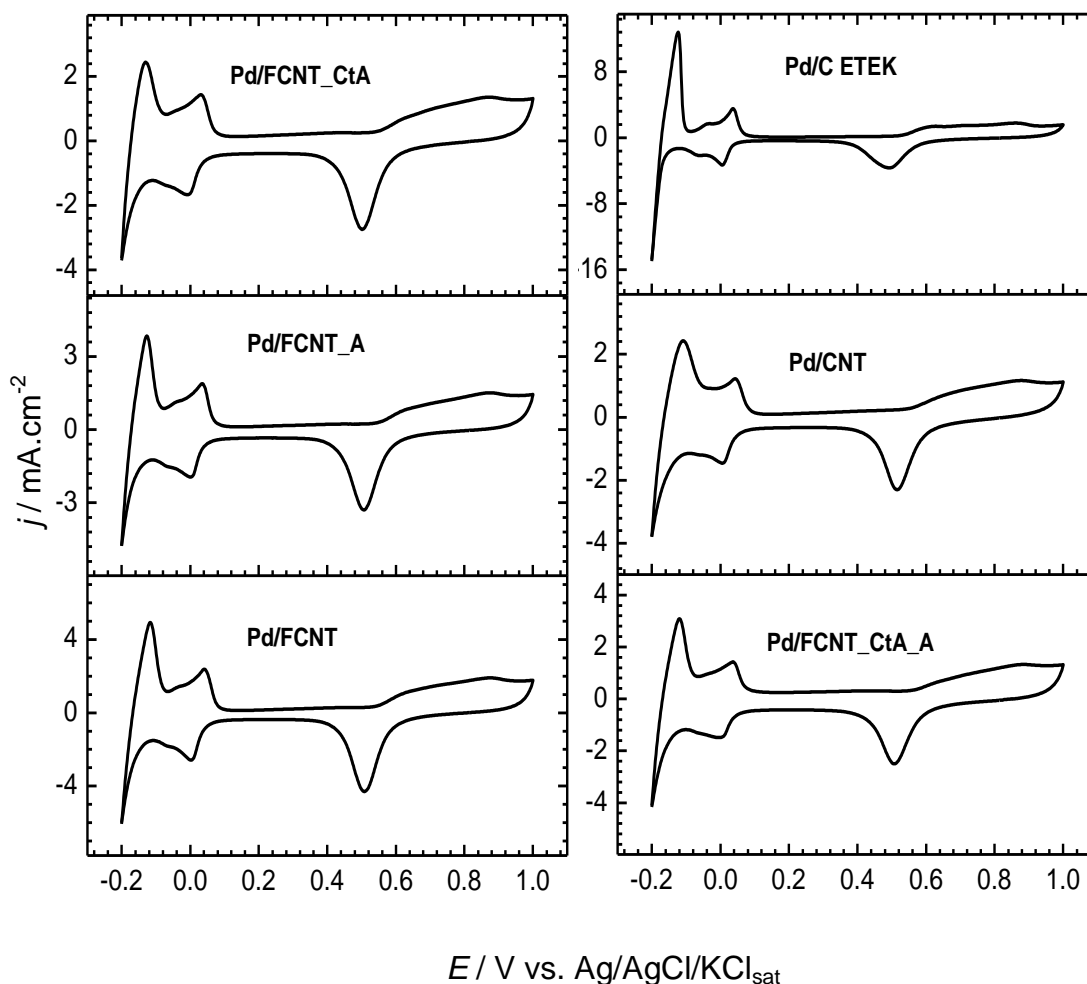


Figure 6.4: Cyclic Voltammograms of the prepared Pd nanocatalysts and Pd/C ETEK in 0.5 M H_2SO_4 (scan rate 50 mVs^{-1}) ($\omega = 0 \text{ rpm}$). Current normalized to the geometrical surface area of the electrode.

Since the hydrogen adsorption-desorption behavior on the surface of Pd is accompanied by hydrogen absorption into the Pd lattice [40,49,50], the electrochemical surface area of Pd catalysts cannot be determined by the H-upd area. Instead, we used CO-stripping for this purpose. The CO-stripping voltammograms for all electrodes prepared from Pd nanocatalysts and Pd/C E-TEK shown in Figure 6.5 are in agreement with those reported for Pd catalysts in the literature [17,20,26,28,51]. During the first cycle the hydrogen adsorption-desorption is completely suppressed as result of the adsorption of CO molecules on the surface of Pd nanoparticles. With

increasing the potential, a peak appears at 0.69 V resulting from the oxidation of adsorbed CO_{ads}. In the second cycle, the hydrogen adsorption-desorption behavior is clearly developed again indicating the complete oxidation of the adsorbed CO_{ads} molecules in the first scan. The electrochemical surface area (ECSA) was calculated from the integration of the charge associated with CO_{ads} oxidation after correction for double layer capacitance and anion adsorption according to the following equation [26,52].

$$ECSA(cm^2_{Pd}) = \frac{Q_{CO} (mC)}{Q_0(mC cm^{-2})} \quad (6.4)$$

Where Q_{CO} is the charge due to CO_{ads} oxidation and Q_0 is the charge for oxidation of a monolayer of CO on the surface of the Pd electrode and is equal to $420 \times 10^{-3} mC.cm^{-2}$. The specific electrochemical surface area (SECSA, $m^2 g^{-1}$) can be calculated by dividing the ECSA by the Pd loading in the electrode.

The calculated SECSA and the peak potential for the CO oxidation are shown in Table 6.2. Naturally the SECSA is particle size dependent and the catalysts Pd/FCNT and Pt/C E-TEK with lower particle size of 5 nm and 4.1 nm respectively exhibit the highest SECSA among all catalysts with surface areas of $55.3 m^2 g^{-1}$ and $67.8 m^2 g^{-1}$, respectively, which is 1.5 times higher than that previously reported for Pd/MWCNTs [26]. The CO oxidation peak is slightly shifted to higher values on Pd/C ETEK (0.7 V) compared to the prepared catalysts (0.69 V) which indicates a slightly higher tolerance of the prepared catalysts to CO poisoning, indirectly enhancing the oxidation of formic acid into CO₂ through the direct path way [51]. The CO-stripping voltammograms for the heat treated Pd catalysts show the same behavior with no change in the peak potential of CO oxidation indicating that CO oxidation on these catalysts is particle size independent (Figure SI6.6), while the CO oxidation charge and thus the electrochemical active surface area are certainly lower. The decrease of the electrochemical surface area is more pronounced at higher temperatures (400 °C) which agrees with the results of TEM and XRD where larger particles have been detected.

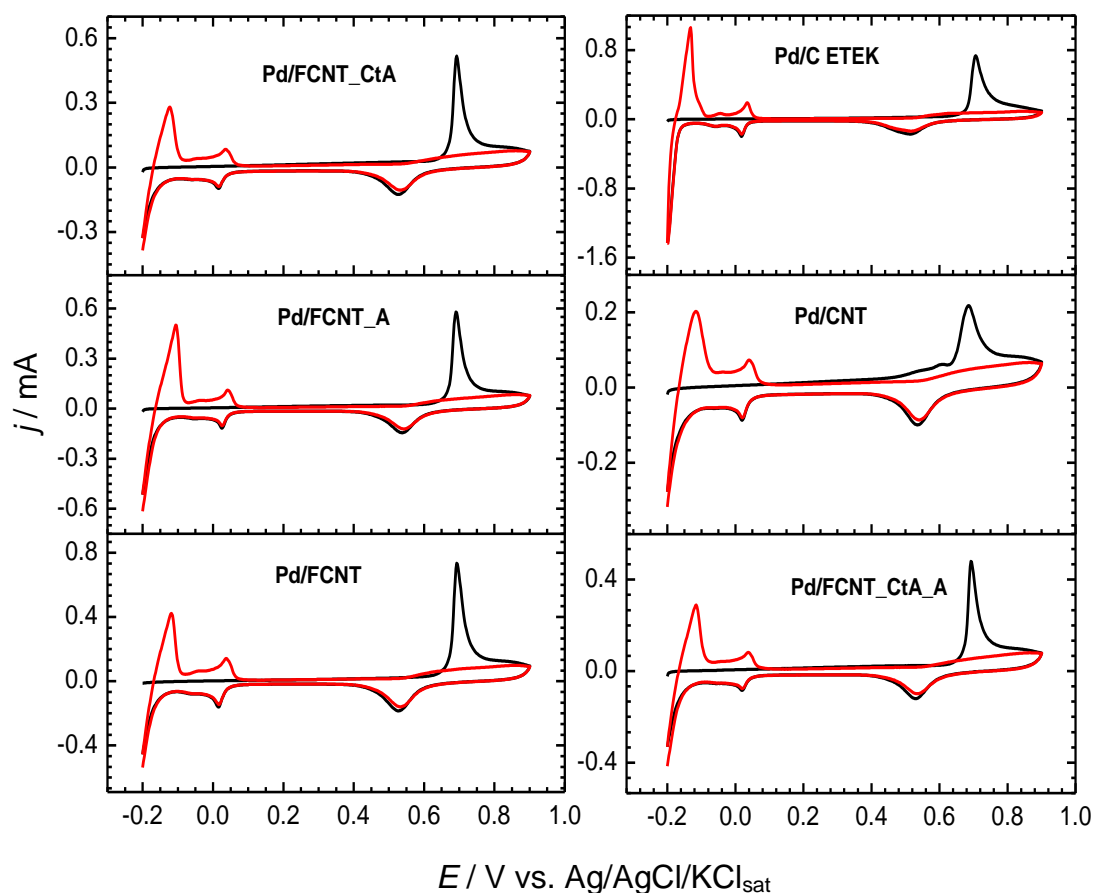


Figure 6.5: CO-Stripping voltammograms of the prepared Pd nanocatalysts and Pd/C ETEK in 0.5 M H_2SO_4 (scan rate 20 mVs^{-1}) ($\omega = 0 \text{ rpm}$), the black line represents the first scan whereas the red line represents the second one.

6.3.2.2 Formic acid oxidation

Formic acid oxidation has been studied with cyclic voltammetry in 0.5 M $\text{HCOOH}/0.5 \text{ M H}_2\text{SO}_4$ solution as shown in Figure 6.6, which reflects the general behavior for formic acid oxidation on Pd electrodes as reported in the literature [25,28-30,53]. The voltammograms show a broad peak in the forward scan after which the current decreases as result from catalysts surface deactivation due to the oxide formation. In the reverse scan the current starts to increase again as the surface of Pd is regenerated by oxide reduction.

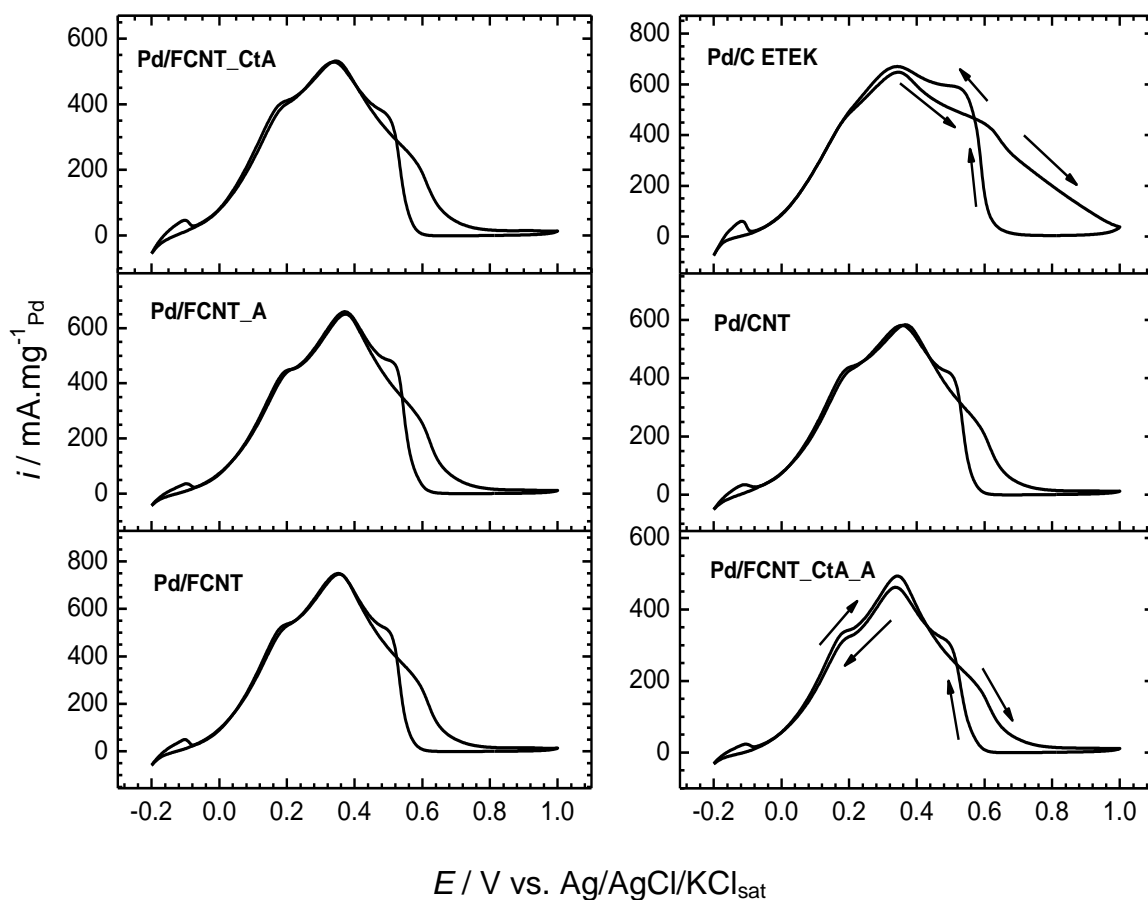


Figure 6.6: Cyclic voltammograms of the prepared Pd nanocatalysts and Pd/C ETEK in 0.5 M HCOOH/0.5 M H₂SO₄ (scan rate 50 mVs⁻¹, ω = 900 rpm).

Table 6.2: Electrochemical parameters from CO-Stripping, cyclic voltammetry and chronoamperometry measurements

Catalysts	Peak potential CO oxidation (V)	SECSA (m ² g ⁻¹ _{Pd})	MSA (mA mg ⁻¹ _{Pd})	SSA (mA cm ⁻² _{Pd})	I _{SSC} /I ₅₀₀ (%)
Pd/FCNT	0.69	55.3	746.1	1.35	50
Pd /FCNT_200	0.69	36.9	657.8	1.78	26
Pd/FCNT_A	0.69	42.5	650.0	1.52	24
Pd/FCNT_A_200	0.69	35.0	673.1	1.92	32
Pd/FCNT_CtA	0.69	40.8	532.0	1.30	45
Pd/FCNT_CtA_200	0.69	38.0	704.8	1.85	47
Pd/FCNT_CtA_400	0.69	16.0	362.1	2.56	20
Pd/FCNT_CtA_A	0.69	37.8	492.5	1.30	25
Pd/FCNT_CtA_A_200	0.69	32.8	538.8	1.63	34
Pd/FCNT_CtA_A_400	0.69	25.5	494.5	1.94	19
Pt/CNT	0.68	26.7	582.8	2.18	31
Pd /C ETEK	0.70	67.8	648.3	0.95	30

An important observation from the voltammograms is that the currents in the forward and reverse scan are identical or the forward current is higher (Pd/FCNT_CtA_A), while Pd/C E-TEK shows a lower forward current, as reported before for this catalyst [25,28]. This behavior suggests the higher tolerance of the prepared catalysts against the poisoning with intermediates formed in the forward scan at lower potentials compared with the E-TEK catalysts. The voltammograms for the heat treated catalysts show the same behavior (Figure SI6.7). The mass specific activity (MSA) expressed in current normalized to the amount of Pd in the electrode as well as the surface specific activities (SSA, i.e., current normalized to surface area) are calculated for all catalysts and are shown in Table 6.2.

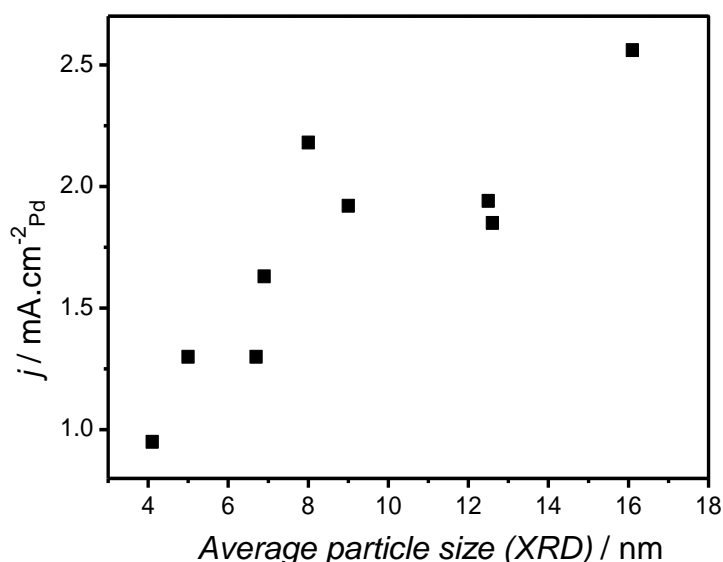


Figure 6.7: Relation between the average particle size of the Pd nanocatalysts and the surface specific activity (SSA).

The highest mass specific activities as a measure for the practical applicability of the catalysts are obtained for the catalysts with smallest particle size, which is reasonable given their higher surface area. Note that Pd/FCNT and Pd/FCNT_A exhibit higher MSA than the commercial catalyst. The comparably low activity of Pd/FCNT_CtA and Pd/FCNT_CtA_A despite their small particle size is mostly like attributed to the presence of citric acid/citrate from the synthesis on the surface of Pd. This is corroborated by the increase of catalytic activity of these catalysts upon heat treatment at 200 °C (Pd/FCNT_CtA_200 and Pd/FCNT_CtA_A_200), which might aid in the removal of these surface species. Heat treatment up to 400 °C decreases the catalytic activity which could be attributed to the increase of the particle size as detected from XRD and TEM. Furthermore the formation of PdO with heat treatment at 400 °C as detected from XRD analysis is expected to be a reason for decrease the

catalytic activity of the heat treated catalysts as PdO is not an active species for formic acid oxidation [55].

From a fundamental point of view, the surface specific activity (SSA), i.e. the activity related to the available surface area, is equally important. In our case there is a clear tendency to an increased SSA with increasing particle size, which could point to a true particle size effect. The heat treated catalysts with larger particle sizes show higher SSA, while the SSA of Pd/C E-TEK with the smallest particles is the lowest. The values of our catalysts are higher than those reported for Pd/MWCNTs [26]. A correlation of particle size with surface specific activity can be found in Figure 6.7 which shows the general trend of increasing SSA with particle size. From the above discussion it is clear that a doubtless determination of surface specific activity is difficult in our case. Thus, Figure 6.7 should be read with some caution.

6.3.2.3 Electrocatalyst stability

To get a first glimpse on the stability of the prepared nanocatalysts compared to Pd/C E-TEK, chronoamperometric measurements have been carried out at a fixed potential of 0.3 V for 1 h. The measurements have been done using a rotating disk electrode to minimize accumulation of CO₂ bubbles on the electrode surface [56]. The rotation furthermore leads to reproducible and comparable diffusion profiles, ensuring comparability of the individual experiments. The chronoamperometric curves for all catalysts are shown in Figure 6.8. The catalysts exhibit an initial strong decay of activity with time probably resulting from catalyst deactivation by adsorption of intermediates. Importantly, Pd/C E-TEK provides higher activity during the first minutes however with a stronger deterioration with time. On the other side, the prepared catalysts show good stability and higher current during the time of measurements. These results agree well with the cyclic voltammetry measurements where also the Pd/C E-TEK showed higher activity in first cycles which decreased rapidly with increasing cycle number while the prepared catalysts showed better stability. To compare and evaluate the stability of the different catalysts we suggest an indicator which is based on the value of the steady state current (I_{SSC}) divided by the initial value of the current taken at 500 s (I_{500}) after the start of measurement (this duration has been chosen to ensure that any capacitive currents have decayed). The values of the stability indicator are shown in Table 6.2 and indicate that the prepared catalysts are of better stability than the Pd/C E-TEK catalyst and the catalyst Pd/FCNT is the most stable one, maintaining 50 % of its activity compared to 30 % for the Pd/C E-TEK sample. Chronoamperometric measurements related to the SSA are shown in Figure SI6.8.

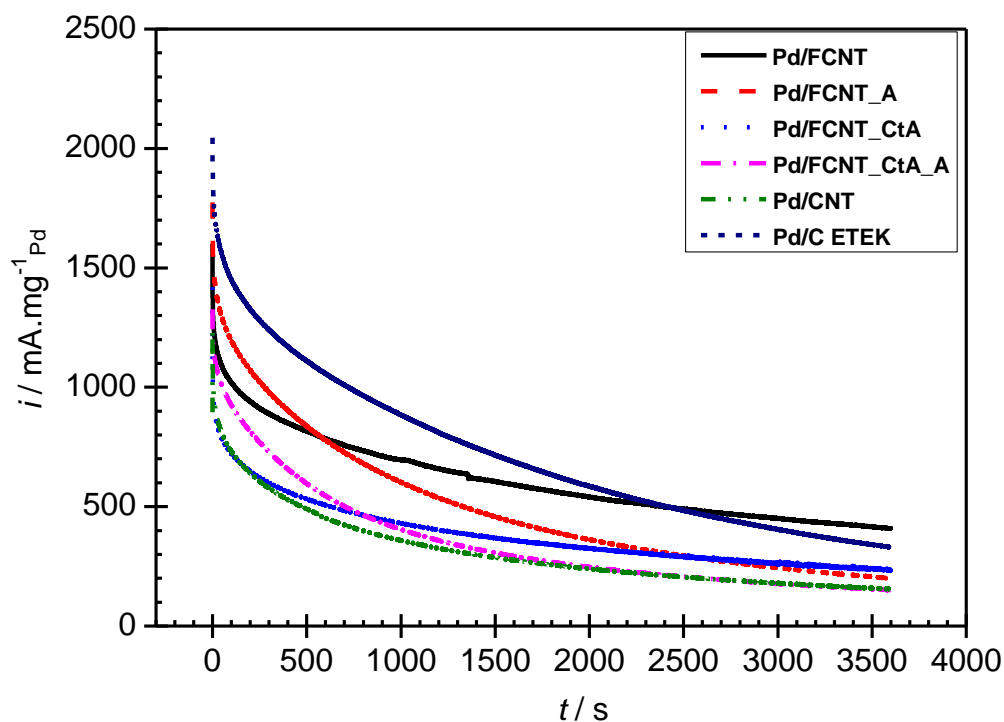


Figure 6.8: Chronoamperometric curves of the prepared Pd nanocatalysts and Pd/C ETEK in 0.5 M HCOOH/0.5 M H₂SO₄ ($\omega = 900$ rpm). Current normalized to Pd loading in the electrode.

These observations shall be discussed in view of the role of the support in improving the stability of the catalysts. The better stability of catalysts supported on functionalized CNTs could be attributed to the promotional effect of oxygenated species on the support surface as they are discussed to be able to oxidatively remove the CO-like intermediates accumulated on the electrode surface. The promotional effect of carbon support is reported by Celorrio et al. for Pd supported on activated Vulcan carbon where they showed that this promotional effect depends on the extent of functionalization and the activation of support leads to formation of small particle size which in turn enhance catalytic activity and catalyst stability [26,30].

The effect of heat treatment on the stability of the catalysts has been also studied with chronoamperometry. The curves in Figure SI6.9 show that the heat treatment at 200 °C has no significant effect on the stability of the catalysts prepared in presence of citric acid. Increase in the heat treatment to 400 °C results in a decrease of stability which agrees with the cyclic voltammetry measurements and could be explained by increasing of the particle size as results from catalysts sintering at higher temperature treatment and also formation of PdO which is expected to be the reason for deactivation of Pd catalysts toward formic acid oxidation [55].

6.4 Conclusions

Pd nanocatalysts supported on carbon nanotubes have been prepared and studied toward their activity for formic acid oxidation. The thermal stability and the catalytic activity of the catalysts depend mainly on their preparation method. While a stabilizing effect of citric acid is reported in alkaline media, in this study it was negligible due to easy formation of Pd hydroxides in presence of NaOH and the formation of agglomerated particles. Heat treatment at 200 °C enhances the activity of the catalyst prepared in presence of citric acid resulting from liberation of the catalyst surface from organic residues whereas after heat treated at 400 °C the catalysts show lower activity resulting from particle size increase. Surface specific activity seems to increase with particle size; however these results may be interfered by the presence of residues from the catalyst synthesis.

The supporting material plays an important role in catalyst preparation and therefore in catalytic activity. The catalysts prepared with functionalized carbon nanotubes showed smaller particle size and therefore higher catalytic activity and stability compared to the catalysts prepared with as-received carbon nanotubes. In summary, this systematic study shows that Pd nanocatalysts prepared using the polyol method on carbon nanotubes as carbon support exhibit higher catalytic activity for formic acid oxidation and good stability compared to commercial catalysts from E-TEK. Improvement of the activity and stability of Pd based nanocatalysts is an ongoing research topic in our group to achieve catalysts with higher activity and stability for different electrocatalytic applications.

References

- [1] C. Rice, S. Ha, R.I. Masel, P. Waszczuk, A. Wieckowski, T. Barnard, *J. Power Sources* 111 (2002) 83.
- [2] S. Ha, R. Larsen, Y. Zhu, R.I. Masel, *Fuel Cells* 4 (2004) 337.
- [3] C. Rice, S. Ha, R.I. Masel, A. Wieckowski, *J. Power Sources* 115 (2003) 229.
- [4] F. Jin, H. Enomoto, *BioResources* 4 (2009) 704.
- [5] J. Albert, R. Wölfel, A. Bösmann, P. Wasserscheid, *Energy Environ. Sci.* 5 (2012) 7956.
- [6] N. Markovic, H. Gasteiger, P. Ross, X. Jian, I. Villegas, M. Weaver, *Electrochim. Acta* 40 (1995) 91.
- [7] N.M. Marković, P.N. Ross Jr., *Surf. Sci. Rep.* 45 (2002) 117.
- [8] X. Yu, P.G. Pickup, *J. Power Sources* 182 (2008) 124.
- [9] S. Ha, R. Larsen, R.I. Masel, *J. Power Sources* 144 (2005) 28.
- [10] R. Larsen, S. Ha, J. Zakzeski, R.I. Masel, *J. Power Sources* 157 (2006) 78.
- [11] E. Antolini, *Energy Environ. Sci.* 2 (2009) 915.
- [12] H. Miyake, T. Okada, G. Samjeské, M. Osawa, *Phys. Chem. Chem. Phys.* 10 (2008) 3662.
- [13] W. Yu, P.G. Pickup, *Electrochem. Commun.* 11 (2009) 2012.
- [14] R.D. Morgan, J.L. Haan, R.I. Masel, *J. Power Sources* 195 (2010) 6405.
- [15] J.L. Haan, K.M. Stafford, R.D. Morgan, R.I. Masel, *Electrochim. Acta* 55 (2010) 2477.
- [16] M. Ren, Y. Kang, W. He, Z. Zou, X. Xue, D.L. Akins, H. Yang, S. Feng, *Appl. Catal., B*: 104 (2011) 49.
- [17] Y. Huang, J. Liao, C. Liu, T. Lu, W. Xing, *Nanotechnology*. 20 (2009) 105604.
- [18] J. Wang, G. Yin, Y. Chen, R. Li, X. Sun, *Int. J. Hydrogen Energy* 34 (2009) 8270.
- [19] V. Mazumder, S. Sun, *J. Am. Chem. Soc.* 131 (2009) 4588.
- [20] X.-M. Wang, Y.-Y. Xia, *Electrochim. Acta* 54 (2009) 7525.
- [21] S. Bong, S. Uhm, Y.-R. Kim, J. Lee, H. Kim, *Electrocatal.* 1 (2010) 139.
- [22] J. Yang, C. Tian, L. Wang, H. Fu, *J. Mater. Chem.* 21 (2011) 3384.
- [23] Y. Liang, M. Zhu, J. Ma, Y. Tang, Y. Chen, T. Lu, *Electrochim. Acta* 56 (2011) 4696.
- [24] Z.-B. Wang, G.-H. Yuan, K. Zhou, Y.-Y. Chu, M. Chen, *Fuel Cells* 11 (2011) 309.
- [25] T. Maiyalagan, AB.A. Nassr T.O. Alaje, M. Bron, K. Scott, *J. Power Sources* 211 (2012) 147.
- [26] C. Hu, Z. Bai, L. Yang, J. Lv, K. Wang, Y. Guo, Y. Cao, J. Zhou, *Electrochim. Acta* 55 (2010) 6036.
- [27] S.M.S. Kumar, J.S. Herrero, S. Irusta, K. Scott, *J. Electroanal. Chem.* 647 (2010) 211.
- [28] A. Moore, V. Celorrio, M. Montes de Oca, D. Plana, W. Hongthani, M.J. Lázaro, D.J. Fermín, *Chem. Commun.* 47 (2011) 7656.

- [29] V. Celorrio, M.G. Montes de Oca, D. Plana, R. Molinrr, M. J. Lázaro, D.J. Fermín, *J. Phys. Chem. C* 116 (2012) 6275.
- [30] V. Celorrio, M.G. Montes de Oca, D. Plana, R. Molinrr, D. J. Fermín, M. J. Lázaro, *Int. J. Hydrogen Energy*. 37 (2012) 7152.
- [31] R.D. Morgan, A. Salehi-khojin, R.I. Masel, *J. Phys. Chem. C* 115 (2011) 19413.
- [32] D.Z. Mezalira, M. Bron, *J. Power Sources* 231 (2012) 113.
- [33] O.A. Baturina, S.R. Aubuchon, K. J. Wynn, *Chem. Mater.* 18 (2006) 1498.
- [34] L. Guo, V.M. Swope, B. Merzougui, L. Protsailo, M. Shao, Q. Yuan, G.M. Swain, *J. Electrochem. Soc.* 157 (2010) A19.
- [35] W. Xia, Y. Wang, R. Bergstraßer, S. Kundu, M. Muhler, *Appl. Surf. Sci.* 254 (2007) 247.
- [36] C. Jeyabharathi, P. Venkateshkumar, J. Mathiyarasu, K.L.N. Phani, *J. Electrochem. Soc.* 157 (2010) B1740.
- [37] T. Cochell, A. Manthiram, *Langmuir* 28 (2012) 1579.
- [38] H. Li, G. Sun, Q. Jiang, M. Zhu, S. Sun, Q. Xin, *Electrochem. Commun.* 9 (2007) 1410.
- [39] H. Li, G. Sun, Q. Jiang, M. Zhu, S. Sun, Q. Xin, *J. Power Sources* 172 (2007) 641.
- [40] Y. Liang, Y. Zhou, J. Ma, J. Zhao, Y. Chen, Y. Tang, T. Lu, *Appl. Catal. B:* 103 (2011) 388.
- [41] T. Ramulifho, K.I. Ozoemena, R.M. Modibedi, C.J. Jafta, M.K. Mathe, *Electrochim. Acta* 59 (2012) 310.
- [42] K. Jukk, N. Alexeyeva, C. Johans, K. Kontturi, K. Tammeveski, *J. Electroanal. Chem.* 666 (2012) 67.
- [43] J.W. Guo, T.S. Zhao, J. Prabhuram, C.W. Wong, *Electrochim. Acta* 50 (2005) 1973.
- [44] B. Lim, M. Jiang, T. Yu, P.H.C. Camargo, Y. Xia, *Nano Res.* 3 (2010) 69.
- [45] Y.Z. Fu, Y. Yang, *Int. J. Electrochem. Sci.* 7 (2012) 106.
- [46] J.-H. Ryu, K.-Y. Lee, H.-J. Kim, J.-I. Yang, H. Jung, *Appl. Catal. B:* 80 (2008) 306.
- [47] Y.-H. Qin, Y.-B. Jia, Y. Jiang, D.-F. Niu, X.-S. Zhang, X.-G. Zhou, L. Niu, W.-K. Yuan, *Int. J. Hydrogen Energy* 37 (2012) 7373.
- [48] A.B. Kashyout, AB.A.A. Nassr, L. Giorgi, T. Maiyalagan, B.A.B. Youssef, *Int. J. Electrochem. Sci.* 6 (2011) 379.
- [49] M. Breiter, *J. Electroanal. Chem.* 81 (1977) 275.
- [50] H. Duncan, A. Lasia, *Electrochim. Acta* 52 (2007) 6195.
- [51] H. Sun, J. Xu, G. Fu, X. Mao, L. Zhang, Y. Chen, Y. Zhou, T. Lu, Y. Tang, *Electrochim. Acta* 59 (2012) 279.
- [52] X.-M. Wang, D.-D. Zhou, Q.-Q. Zou, Y.-Y. Xia, *J. Mater. Chem.* 22 (2012) 15418.
- [53] W.P. Zhou, A. Lewera, R. Larsen, R.I. Masel, P. S. Bagus, A. Wieckowski, *J. Phys. Chem. B* 110 (2006) 13393.

Chapter 6: Ployol Synthesis of Pd/CNTs Electrocatalysts

- [54] W. Zhou, J.Y. Lee, *J. Phys. Chem. C* 112 **(2008)** 3789.
- [55] D. Morales-Acosta, M.D. Morales-Acosta, L.A. Godinez, L. Álvarez-Contreras, S.M. Duron-Torres, J. Ledesma-García, L.G. Arriaga, *J. Power Sources* 196 **(2011)** 9270.
- [56] J.-Y. Wang, Y.-Y. Kang, H. Yang, W.-B. Cai, *J. Phys. Chem. C* 113 **(2009)** 8366.

Supporting information

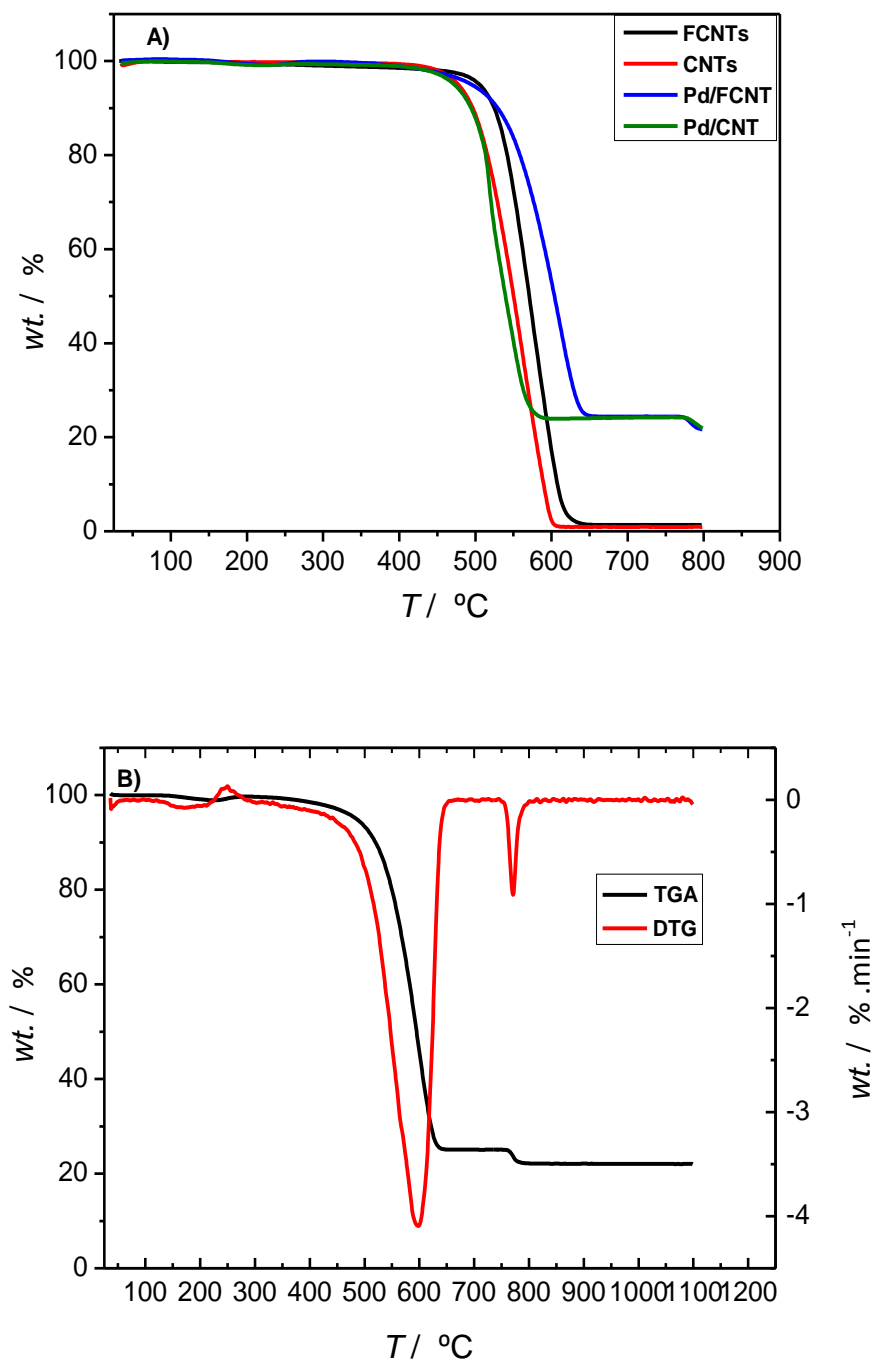


Figure SI6.1: A) TG curve of FCNTs, as-received CNTs, Pd/FCNT and, Pd/CNT B) TG-DTG curves of Pd/FCNT with heating up to 1100 °C.

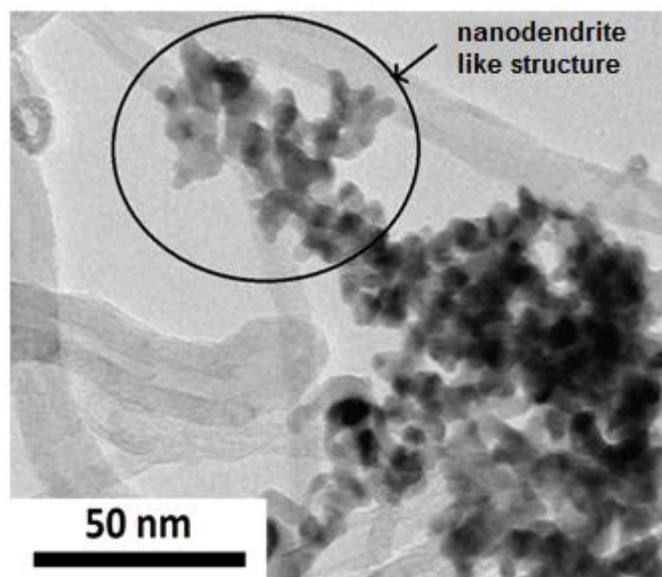


Figure SI6.2: TEM image of Pd/FCNT_A nanocatalysts, higher magnifications.

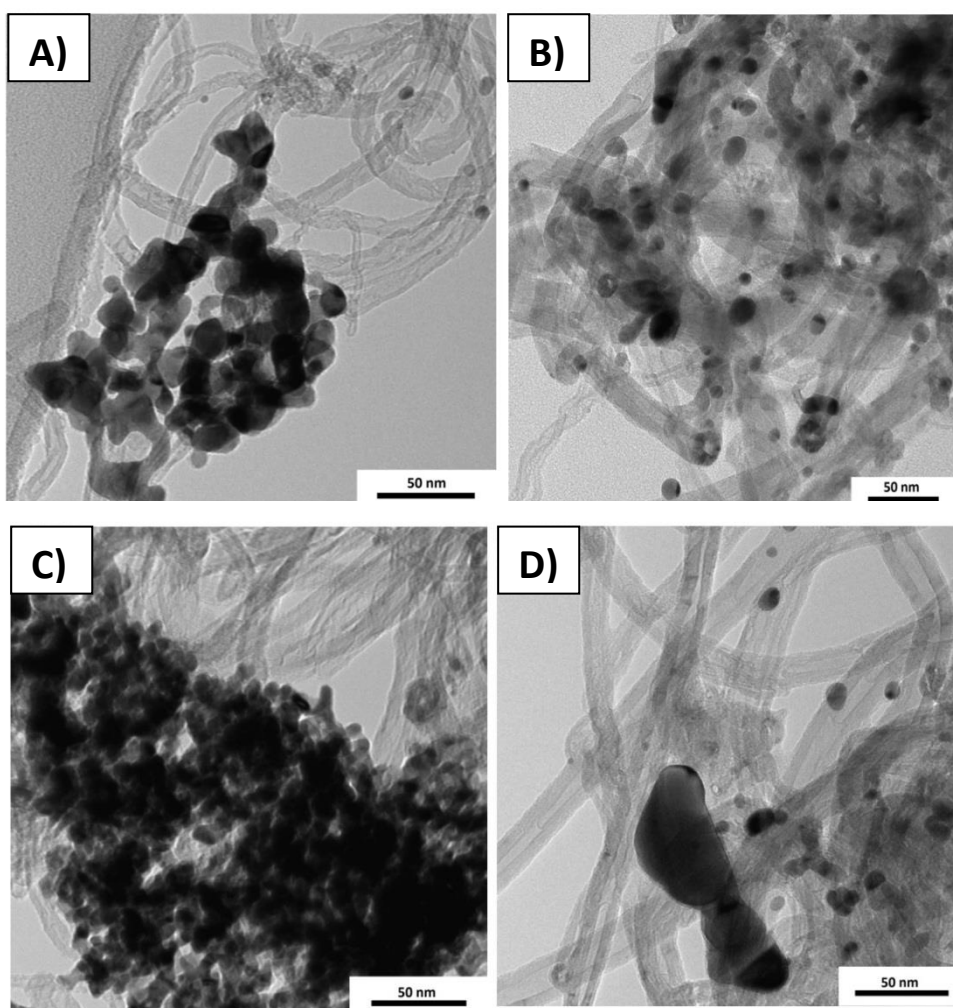


Figure SI6.3: TEM images of Pd nanocatalysts after heat treatment A) Pd/FCNT_CtA_200, B) Pd/FCNT_CtA_400, C) Pd/FCNT_CtA_A_200, and D) Pd/FCNT_CtA_A_400.

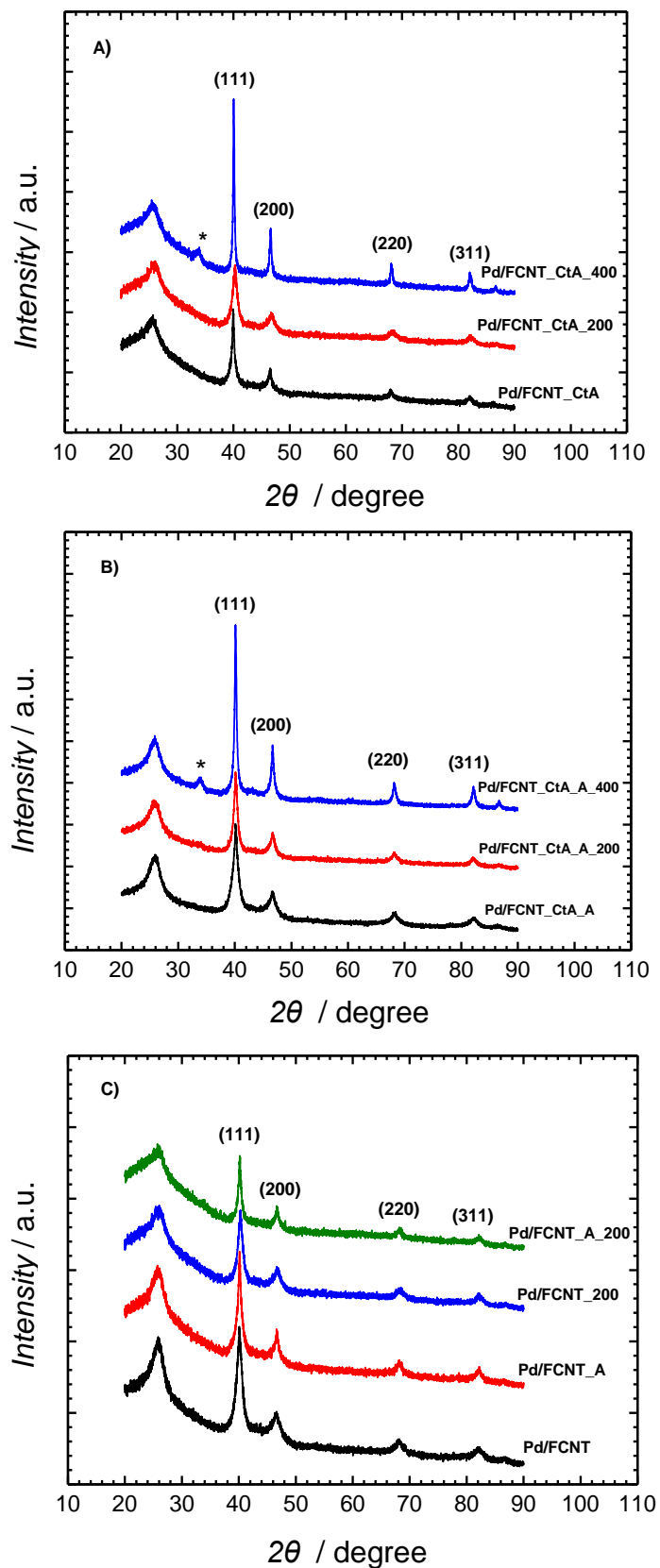


Figure S16.4: XRD patterns of Pd nanocatalysts after heat treatment.

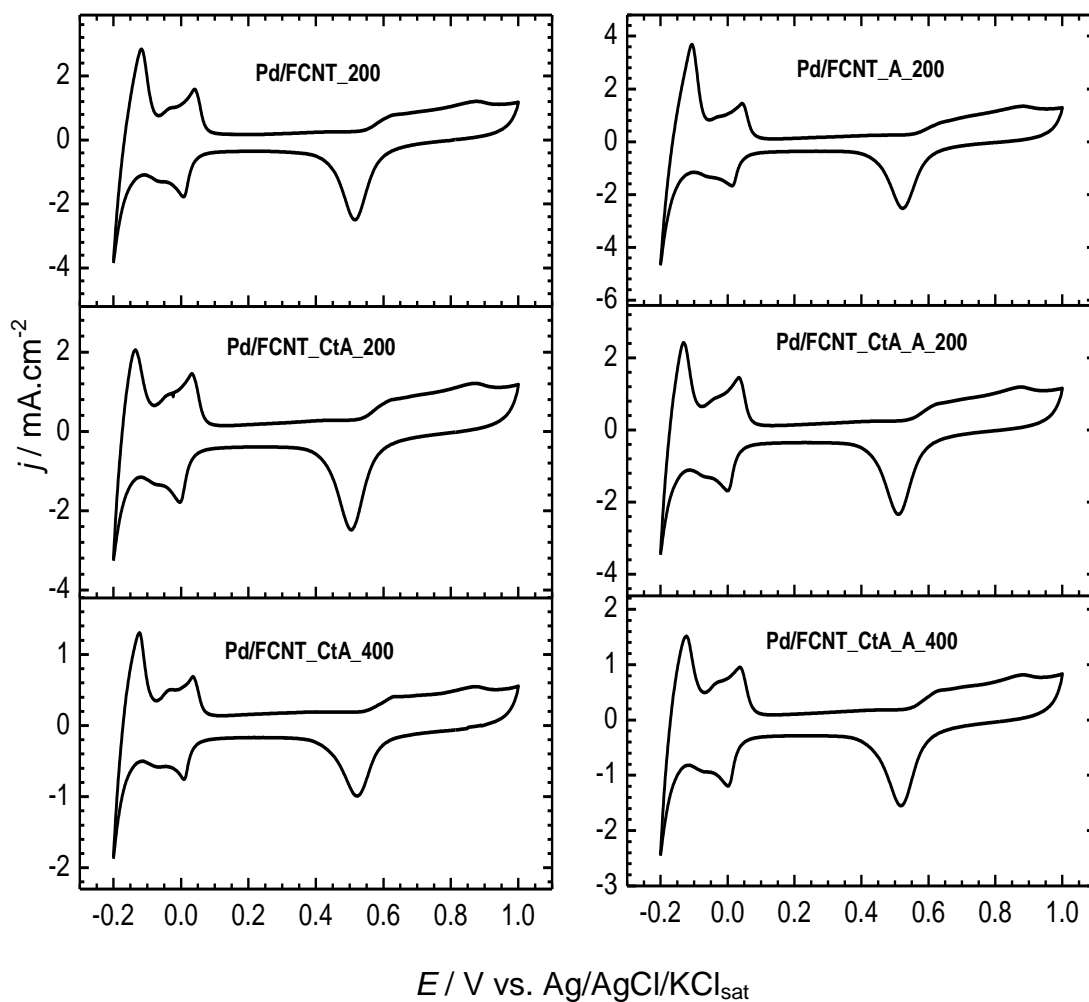


Figure SI6.5: Cyclic Voltammograms of the heat treated Pd nanocatalysts in 0.5 M H₂SO₄ (scan rate 50 mVs⁻¹) ($\omega = 0$ rpm), Current normalized to the geometrical surface area of the electrode.

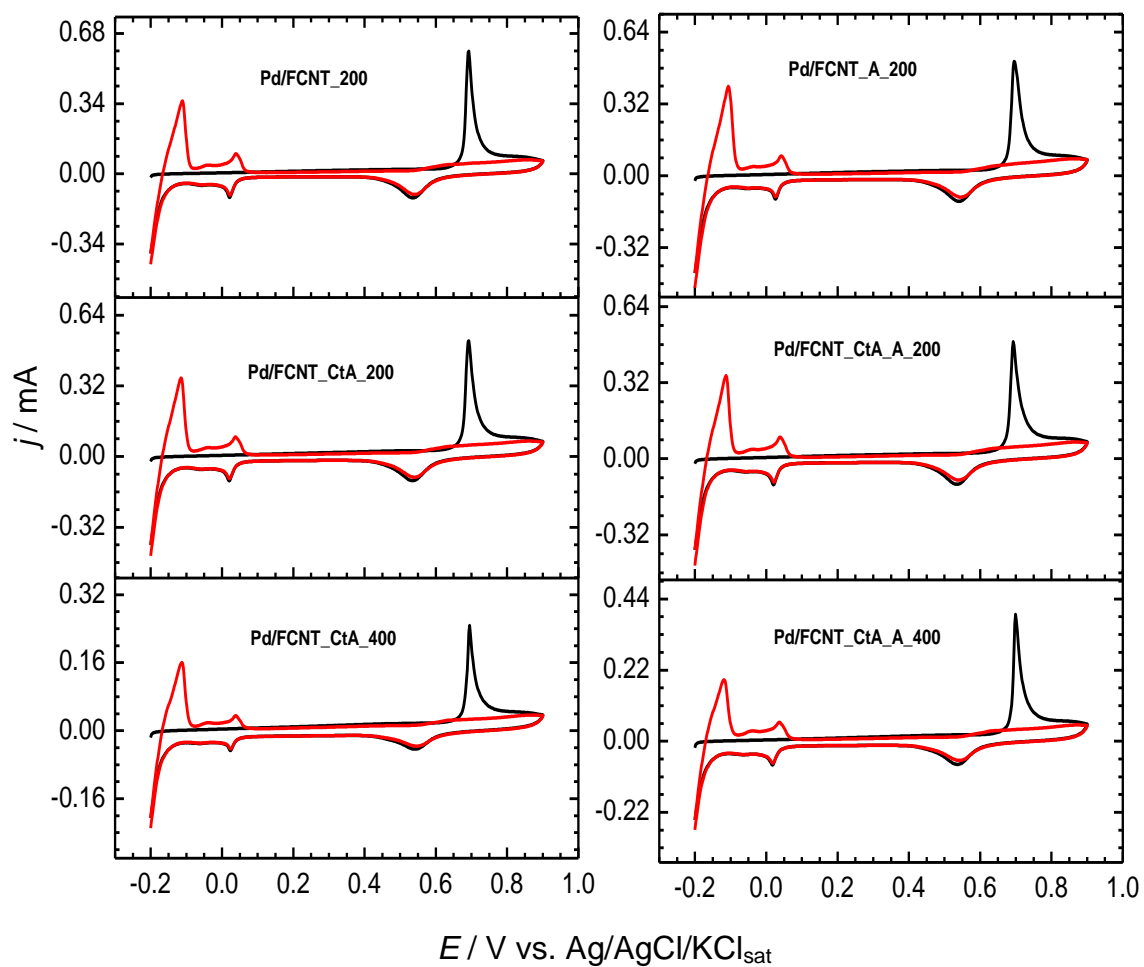


Figure SI6.6: CO-Stripping voltammograms of the heat treated Pd nanocatalysts in 0.5 M H_2SO_4 (scan rate 20 mVs^{-1}) ($\omega = 0 \text{ rpm}$), the black line represents the first scan whereas the red line represents the second one.

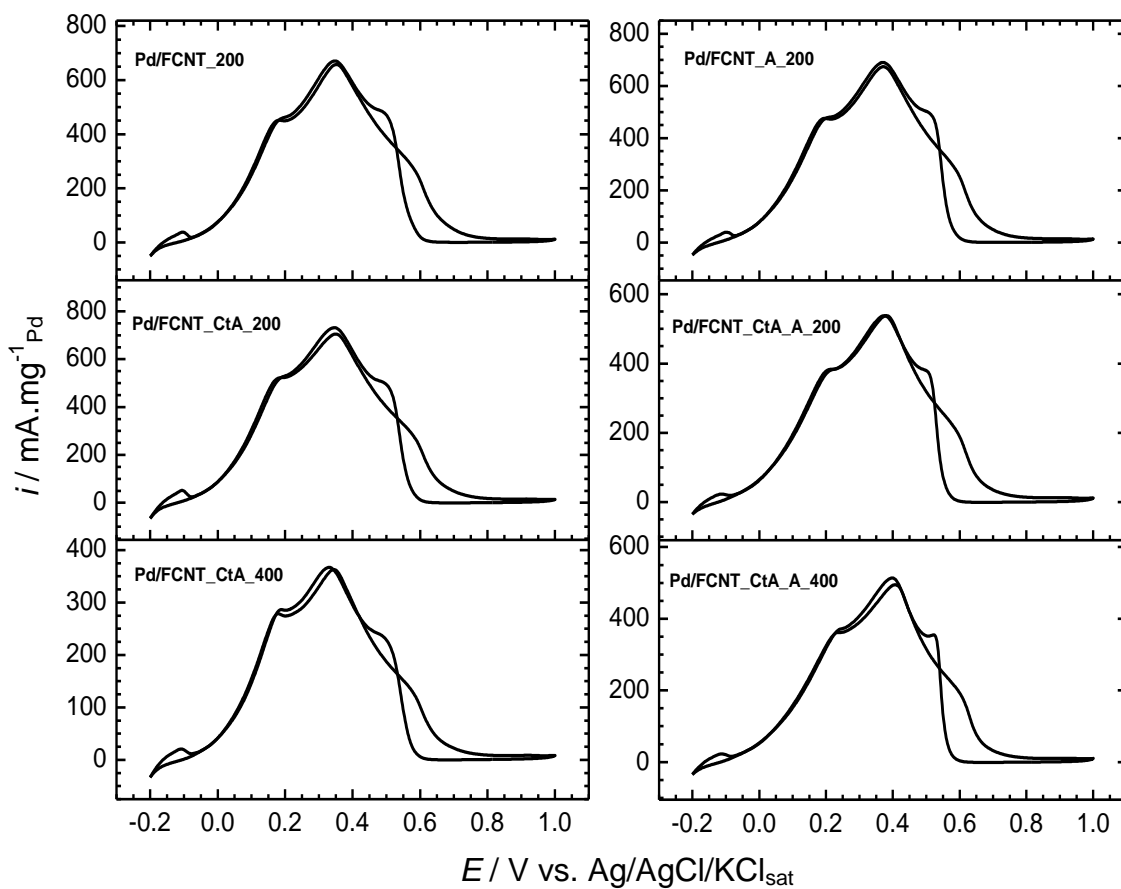


Figure SI6.7: Cyclic voltammograms of the heat treated Pd nanocatalysts in 0.5 M HCOOH/0.5 M H₂SO₄ (scan rate 50 mVs⁻¹, ω = 900 rpm).

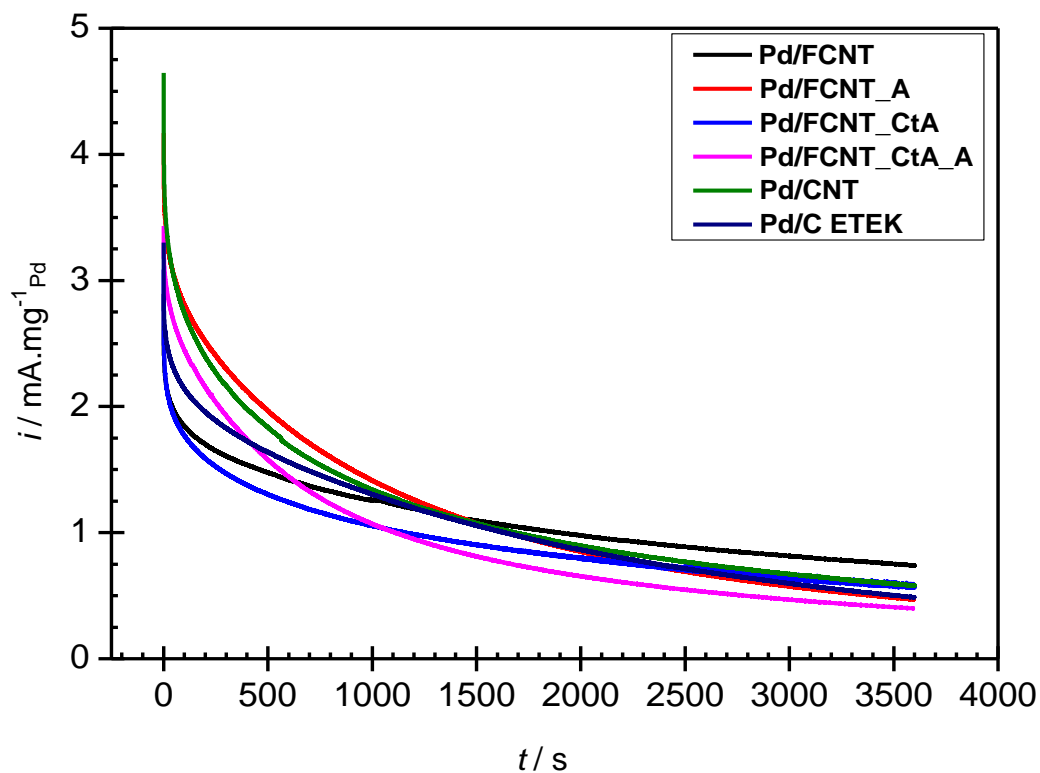


Figure SI6.8: chronoamperometric curves of the prepared Pd nanocatalysts and Pd/C ETEK in 0.5 M HCOOH/0.5 M H₂SO₄ ($\omega = 900$ rpm), the current normalized to the electrochemical surface area of Pd.

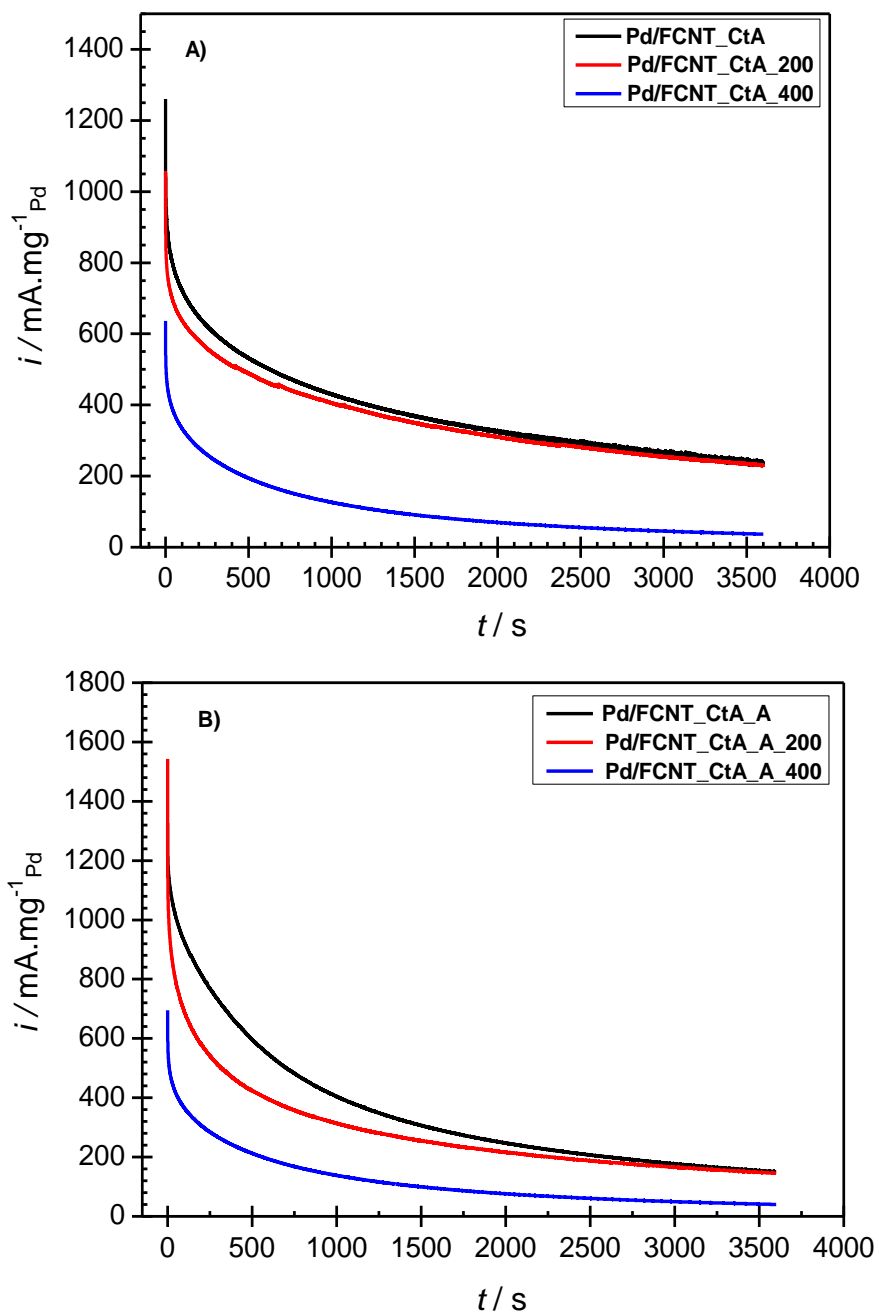


Figure SI6.9: Chronoamperometric curves of heat treated Pd nanocatalysts in 0.5 M HCOOH/0.5 M H₂SO₄ ($\omega = 900$ rpm), A) Pd/FCNT_CtA, B) Pd/FCNT_CtA_A. Current normalized to Pd loading in the electrode.

7.1 Summary

The direct oxidation of liquid fuels in fuel cells, so-called direct liquid fuel cells, has gained much attention as a promising strategy to replace the hydrogen fuel in fuel cells technology. Liquid fuels are easy to store, handle and transport compared to hydrogen. The problem associated with liquid fuels as fuel for direct liquid fuel cells is the adsorption of their oxidation intermediates on the catalyst surface leading to a decrease in the catalyst efficiency and lower cell performance.

In this thesis the development of nanostructured catalysts for methanol oxidation and formic acid oxidation has been investigated. Methanol oxidation is a multistep reaction that is associated with CO_{ads} formation which strongly adsorbs on the catalyst surface blocking further methanol adsorption and therefore decreasing the activity of the catalyst.

Pt is a well-known catalyst for methanol oxidation but its poisoning with CO decreases its efficiency. In that regard, bimetallic alloy catalysts are an established way to replace the Pt as catalyst for methanol oxidation in direct methanol fuel cells. The catalytic activity of bimetallic catalysts depends on many factors, such as alloying degree, particle size, and surface composition which depend mainly on the preparation method or the treatment steps after the preparation process. Also, the supporting material plays an important role in the stability of nanoparticle catalysts and their dispersion and hence their activities.

In this thesis, two bimetallic alloy system, namely PtRu and PtNi were prepared as electrocatalysts for methanol oxidation and characterized with structural and electrochemical tools to investigate their structural features and their electrocatalytic activity toward methanol oxidation reaction (MOR) and hence their applicability in direct methanol fuel cells.

In chapter 2 of the thesis, PtRu nanoparticles supported on functionalized carbon nanotubes were prepared by a cost effective and simple method using an ethanol/water mixture as the reductant with the assistance of microwave radiation as the heating sources. The method is very simple and the catalyst was prepared in short time compared to the conventional heating. The structural characterization showed that catalysts prepared under microwave radiation exhibit a better dispersion on the support than those prepared by conventional heating. The efficiency of the reduction process was higher under microwave irradiation and both metals were found in the catalysts in the same ratio as in the starting precursors. This indicates that the microwave irradiation facilitates the reduction of both metals at the same rate, opposite to the results from the conventional heating where the rate of Pt reduction is higher than that of Ru as a result of the more positive redox potential of Pt compared to Ru. Post heat treatment of the prepared catalysts under different heat treatment

temperatures in reductive atmosphere resulted in alloy formation between Pt and Ru which is not observed with the prepared catalysts without heat treatment as detected by XRD. The methanol oxidation on the prepared catalysts before and after heat treatment has been studied. The results demonstrated the catalytic activity of the prepared catalysts toward methanol oxidation reaction where the heat treated catalysts showed high stability during potential cycling with a catalyst treated at 600 °C exhibiting higher activity and stability compared to commercial Pt/C and PtRu/C catalysts. It has been suggested that the alloy formation upon heat treatment could be the reason for the high activity and high stability for heat treated PtRu catalyst that has been confirmed by XPS and XAS analyses in chapter 3.

In chapter 3 a full structural characterization of the as-prepared and heat treated PtRu/CNTs catalysts has been carried out using XPS and XAS (XANES and EXAFS). The results showed that the as-prepared catalysts are present in separated phase and the major Ru phase is the RuO₂. On the other hand, the RuO₂ has been reduced completely into metallic Ru in the heat treated catalysts forming an alloy of PtRu. It has been found that the alloying extent, the mixing between Pt and Ru and the surface concentration of both depend mainly on the treatment temperature as detected from XPS and XAS. Based on theoretical calculations from EXAFS analysis and XPS analysis, a structure model was developed for the as-prepared catalyst and the heated treated catalysts. A catalyst with a Ru enriched core and a Pt enriched surface is suggested as structure for the heat treated catalysts where the core and shell in the catalysts treated at lower and medium temperature are segregated whereas the core and shell in the catalysts treated at higher temperature have higher intermixing. The performance of the as-prepared catalyst PtRu/CNTs MW, the heated treated catalyst at 600 °C, PtRu/CNTs MW600 and the commercial catalysts PtRu/C from Alfa Aesar (JM) have been evaluated in a membrane electrode assembly set-up either in direct methanol single cell measurements or in anode polarization measurements. After the initial experiments in both modes, the anode catalysts have been subjected to an accelerated durability test (ADT) protocol for 5.000 cycles in the potential window of 0.1 to 0.7 V vs. DHE. Although the commercial PtRu/C catalyst showed higher performance in the single direct methanol fuel cell, after the ADT its performance preserves only less than 60% of initial performance where the as-prepared catalysts preserves more than 80% of its initial performance. On the other hand the heat treated catalyst at 600 °C after ADT showed performance enhancement by more than 30 % of its initial performance. The higher stability of the prepared catalysts in this study is attributed to the formation of PtRu alloys with a Pt shell and a core consisting of a PtRu alloy enriched with Ru in a way that it minimizes the dissolution of Ru compared to the as-prepared catalyst and the PtRu/C commercial catalyst which showed higher extent of dissolution.

In chapter 4 we developed a new catalyst system based on PtNi with the aim of using a cheaper second metal than Ru. In this study a series of PtNi catalyst with varying Pt to Ni atomic ratio has been prepared on oxygen functionalized carbon nanotubes (FCNTs) by the polyol method where ethylene glycol is used as solvent and reducing agent under conventional heating. First, the functionalization of CNTs has been carried out under mild conditions of 5 M HNO₃ to create oxygen containing groups on the surface of CNTs. The functionalization process has been studied and confirmed with different characterization tools such as TPD, TGA, cyclic voltammetry and the BET method. The prepared catalysts were characterized with structural tools such as ICP, TEM, XRD and XAS. Finally, their electrocatalytic activity has been tested toward the methanol oxidation reaction. The ICP results showed the difficulty of the complete deposition of both Pt and Ni on the CNTs using the polyol method. This is attributed to the higher pH used in the polyol method which favors the Ni reduction but at the same time prevents the reduced Pt particles to deposit on the support surface. TEM analysis confirmed the deposition of nanoparticles on the support surface with small particle size (1-3 nm) and narrow particle size distribution and high dispersion whereas XRD and XPS analysis confirmed the alloy formation between Pt and Ni while XPS additionally showed that the surface is enriched in Pt and that NiO species are present. Heat treatment in inert atmosphere induces a surface restructuring especially at a higher temperature of 400 °C. EXAFS results confirmed the alloy formation with a high alloying extent of Ni which suggests that the alloy of PtNi has a surface enriched in Ni opposite to the results from XPS. Based on these results a structural model has been postulated where the Ni atoms are tending to be concentrated in the region near the support surface and the Pt atoms are enriched on the surface of the alloy with different segregation extent depending on the heat treatment temperature.

Methanol oxidation activity of the catalysts has been evaluated and expressed in terms of mass specific activity and surface specific activity and compared to the Pt/C ETEK catalyst. All prepared catalysts showed higher activity compared to the commercial catalyst and a catalyst with Pt/Ni ratio of 3 has the highest activity. Heat treatment at 200 °C enhances the activity resulting from the removal of adsorbed species formed during the preparation step whereas the heat treatment at 400 °C has an adverse effect on the catalytic activity as results of catalyst surface restructuring that could change the position of the active sites for methanol oxidation.

The results of chapter 4 have motivated us to develop other methods to increase the activity of PtNi catalyst. In this regard, in chapter 5, PtNi catalysts supported on functionalized carbon nanotubes were prepared using a microwave assisted method where microwave irradiation heating is used instead of the conventional heating. In this study two modes of irradiation (continuous mode and pulsed mode) have been

used to reduce the metal ions of Pt and Ni in EG with different irradiation time. The effect of the irradiation modes on the catalysts structure and on their activities toward methanol oxidation reaction were studied with structural methods and electrochemical characterization methods. In both modes of irradiation the nanoparticle catalysts were deposited on the surface of the CNTs in nanosize and high dispersion with appearance of a low extent of agglomeration at long irradiation time and the metal loading increases with increasing the irradiation time. XRD and XPS confirmed the alloy formation in PtNi as detected from the peak shifting in XRD and the shifting of Pt 4f line in XPS. Additionally, XPS confirmed the presence of Ni oxide species and indicated that the surface of the catalysts is enriched with Pt which agrees with the results obtained in chapter 4. XAS analysis (XANES and EXAFS) confirmed additionally the PtNi alloy formation as detected from the increasing WL intensity in XANES spectra for all PtNi catalyst compared to the Pt reference and appearance of peaks corresponding to Pt-Pt and Pt-Ni coordination in FT-EXAFS spectra.

The electrocatalytic activity of the prepared PtNi catalysts toward methanol electrooxidation was higher for the catalysts prepared with continuous mode of irradiation in terms of mass specific activity and surface specific activity compared to the catalysts prepared under pulsed mode. Based on the XPS and XAS results, the activity of PtNi was discussed as a result of the electronic effect of Ni in PtNi catalysts modifying the electronic properties of Pt by either lowering the CO adsorption on the catalyst surface or increasing the methanol adsorption. Additionally, the role of the oxygenated carbon nanotubes support should not be neglected to affect the activity of the catalysts. The results reported in this study showed that the catalytic activity of the catalysts prepared under microwave irradiation heating exhibit a higher activity than the catalysts prepared under conventional heating reported in chapter 4.

In chapter 6 a systematic study has been carried out on Pd catalysts where different preparation routes have been suggested to prepare the Pd catalysts supported on functionalized carbon nanotubes and on as received carbon nanotubes. The general preparation has been carried out with the polyol method where the aging of Pd catalysts and their preparation in presence or absence of citric acid have been studied. The structural characterization showed that Pd nanoparticle catalysts were formed and deposited on the support surface where TEM characterization showed a high extent of agglomeration for both the catalysts prepared in absence of citric acid or in presence of citric acid.

The electrocatalytic activity of the catalysts toward formic acid oxidation was highest for the catalyst prepared in absence of citric acid without aging. The heat treatment of the catalysts prepared in presence of citric acid at 200 °C enhances their activities as a result of removing the organic residues which could adsorb on the catalysts surface.

Heat treatment at 400 °C decreases the activity of the catalysts as result of particle size increase.

Additionally, the functionalization of the carbon nanotube support has a strong effect on the catalytic activity and stability of the catalysts where the Pd supported on the functionalized CNTs showed the higher activity and stability compared to Pd catalysts supported on the as received CNTs.

7.2 Research outlook

This thesis has shown the development of promising electrocatalysts for methanol oxidation and formic acid oxidation. Still additional research in the same direction is important as stated in the following points:

- In-situ XAS measurements on membrane electrode assemblies fabricated from the as prepared PtRu/CNTs before and after heat treatment and the commercial catalysts will help to understand the mechanism of the deactivation of the catalysts and the dissolution of Ru under fuel cell operation. This study could help to establish the structure change of the catalysts during fuel cell operation, a topic which deserves further attention and research efforts.
- The PtNi electrocatalyst is a promising catalyst system to replace PtRu. In that regard, developing a preparation method by which the Pt and Ni reduction can be achieved more easily with optimum catalyst structure could promote this catalyst to replace PtRu and increase its activity.
- Using other supporting materials like reduced graphene oxide or doped supports (such as nitrogen doped CNTs and nitrogen doped graphene) could also enhance the stability of the catalysts for anode application in direct methanol fuel cells. The expected enhanced stability could arise from the stabilization effect of nitrogen atoms for the catalyst particles.
- Development of new catalysts based on other transition metal like Cu is important in the direction of cost reduction. In that regard, development of catalysts with a Pt_{shell}Cu_{core} structure using the dealloying process could be promising to develop catalysts with high electrocatalytic activity toward anodic methanol oxidation reaction with reduced cost.
- Increasing the activity of the anode catalysts for formic acid oxidation is a challenge for the development of direct formic acid fuel cells. In that regard, exploration and investigation of Pd bimetallic catalysts could enhance the activity and stability of the current Pd catalysts. Suggested systems that could work in this direction are PdNi and PdCu catalysts where also different supporting materials that could enhance the stability can be used.

Appendix

Chemicals and Materials

Name	specification	supplier
Alumina Suspension	1 μm and 0.3 μm	LECO Corporation, Germany
Citric Acid monohydrate	for synthesis, 1 kg	Carl Roth, Germany
Ethanol	$\geq 99\%$ HPLC gradient grade	Carl Roth, Germany
Ethylene Glycol	$\geq 99\%$ for synthesis, 2.5 L	Carl Roth, Germany
Formic Acid	≥ 99 p.a., ACS, 1 L	Carl Roth, Germany
Hydrogenhexachloroplatinate (IV) hydrate, $\text{H}_2\text{PtCl}_6 \cdot \text{X H}_2\text{O}$	ACS, M.Wt. 409.82, 5 g	ACROS ORGANICS, USA
Methanol	$\geq 99.98\%$ ultra LC-MS, 1 L	Carl Roth, Germany
Nafion 117 solution	5% in mixture of lower aliphatic alcohol and water, 25 mL	Sigma-Aldrich, USA
Nickel (II) nitrate hexahydrate $\text{Ni}(\text{NO}_3)_2 \cdot 6 \text{H}_2\text{O}$	99.999 % metal basis, 20 g	Sigma-Aldrich, USA
Nitric Acid, HNO_3	$\geq 65\%$ p.a. ISO, 1 L	Carl Roth, Germany
Palladium (II) chloride, PtCl_2	$\geq 99.98\%$	Sigma-Aldrich, USA
Pd/C	20 wt. % Pd on Carbon Vulcan XC-72	E-TEK, USA
2-Propanol	$\geq 99.98\%$ LC-MS grade, 1 L	Carl Roth, Germany
Pt/ C	20 wt. % Pt on Carbon Vulcan XC-72	E-TEK, USA
PtRu/ C	(HiSPEC® 5000, 20 wt% Pt and 10 wt. % Ru with Pt:Ru = 1)	Alfa Aesar (JM)
Ruthenium (III) chloride hydrate, $\text{RuCl}_3 \cdot \text{X H}_2\text{O}$	99.99 % metal basis, 5 g	Sigma-Aldrich, USA
Sodium Hydroxide, NaOH	$\geq 99\%$ p.a. ISO, Pellets, 1 Kg	Carl Roth, Germany
Sodium Borohydride, NaBH_4	99 %, 25 g	ACROS ORGANICS, USA
Sulfuric Acid, H_2SO_4	$\geq 98\%$, 1 L	Carl Roth, Germany
Ar gas		Air Liquid, Germany
CO gas	10 % in He	Air Liquid, Germany
H_2 gas	99.999%	Air Liquid, Germany
N_2 gas	99.999%	Air Liquid, Germany
Glassy Carbon rode	Sigradur® G	HTW, Germany
Reference Electrode SE	Ag/AgCl. KCl sat. SE 20	SM , Germany

Set-up and Instrumentation

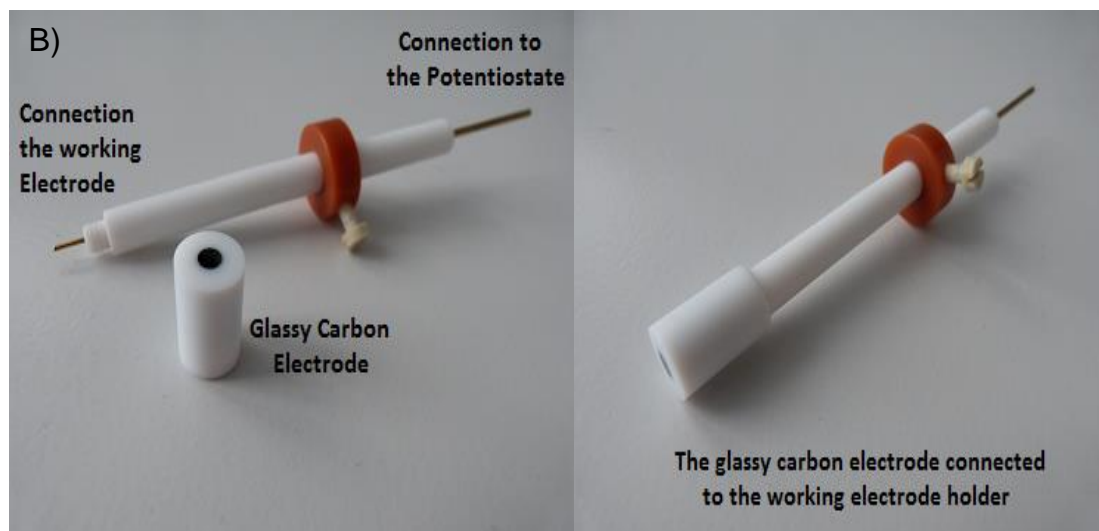
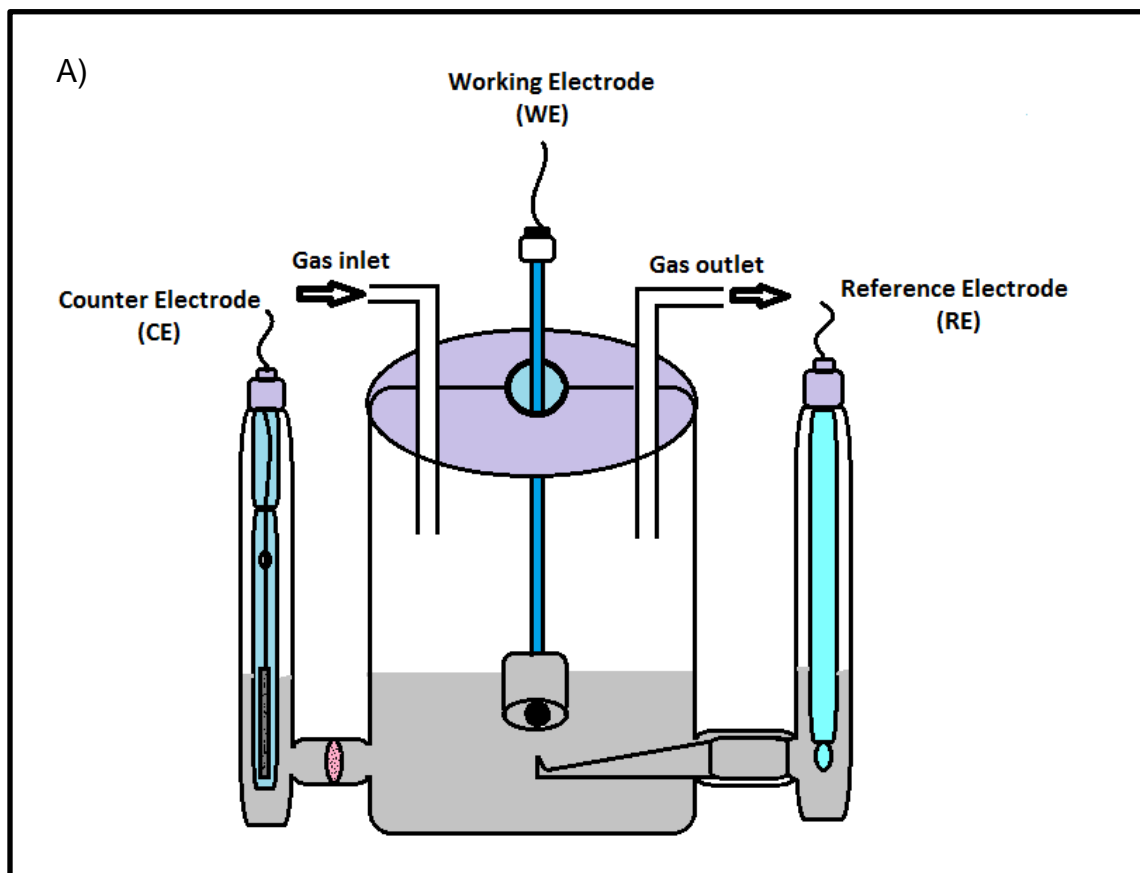


Figure A1: Schematic diagram of the set-up for the three electrodes electrochemical cell (A) and the photos for the glassy carbon working electrode and its holder (B).



Figure A2: Electrochemical set-up for electrochemical characterization at MLU Halle.

Appendix

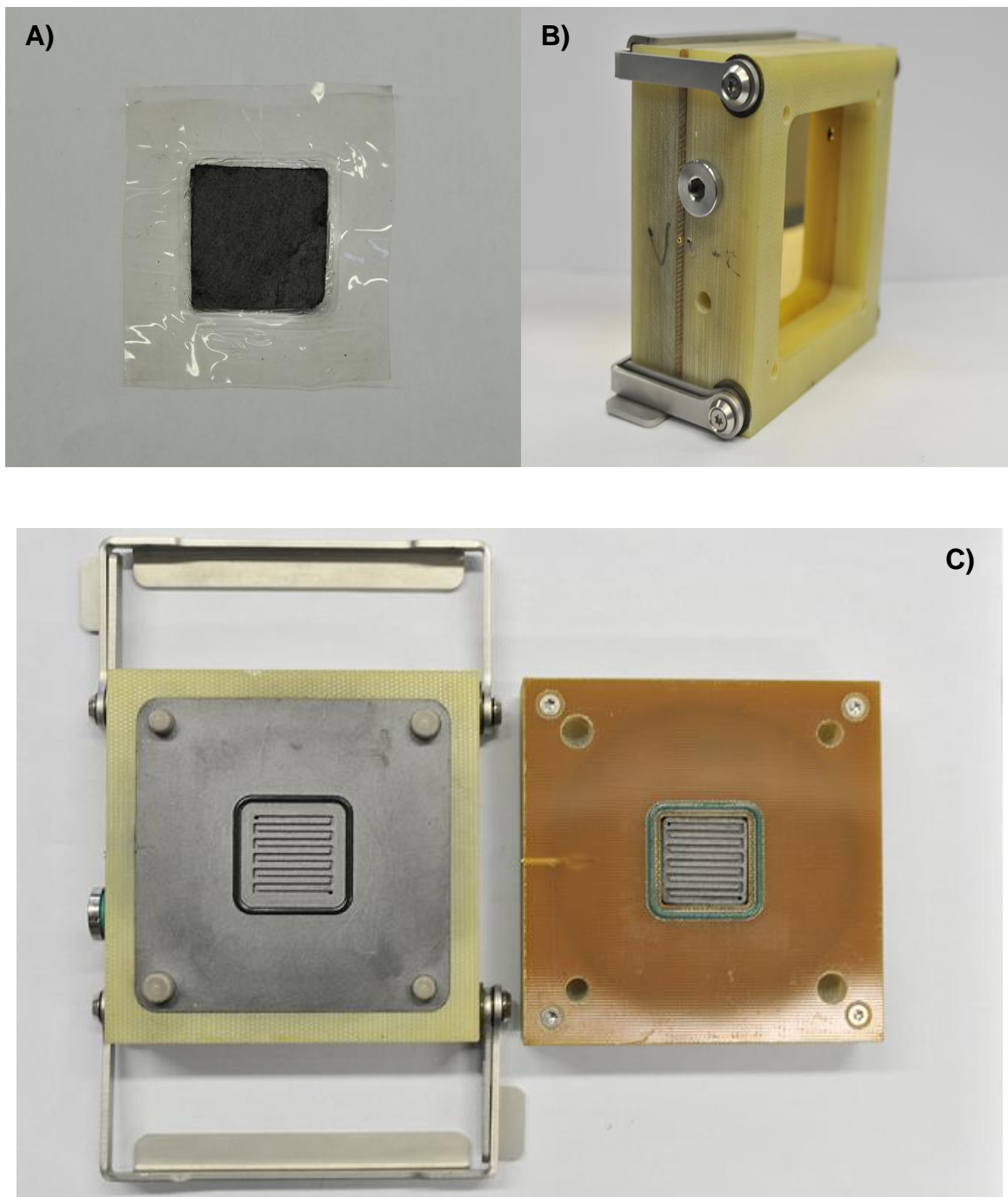


Figure A3: The photos of MEA (A), the hard components of the fuel cell (B) and the photo of the flow field for both anode and cathode sides(C).

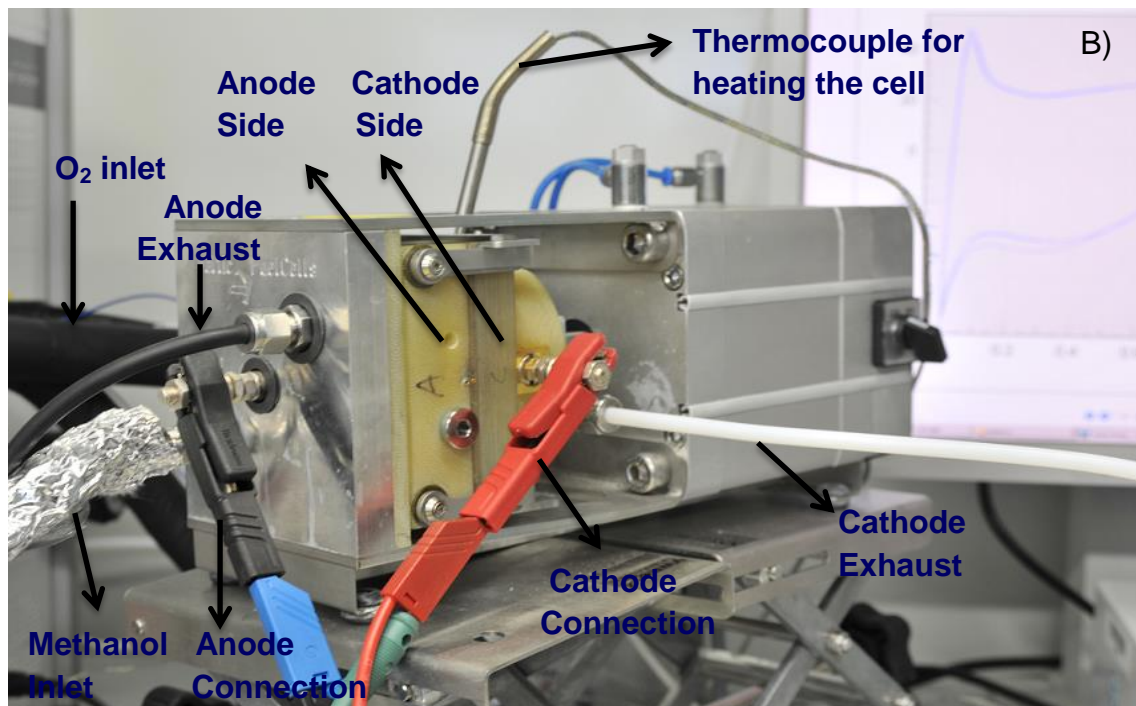
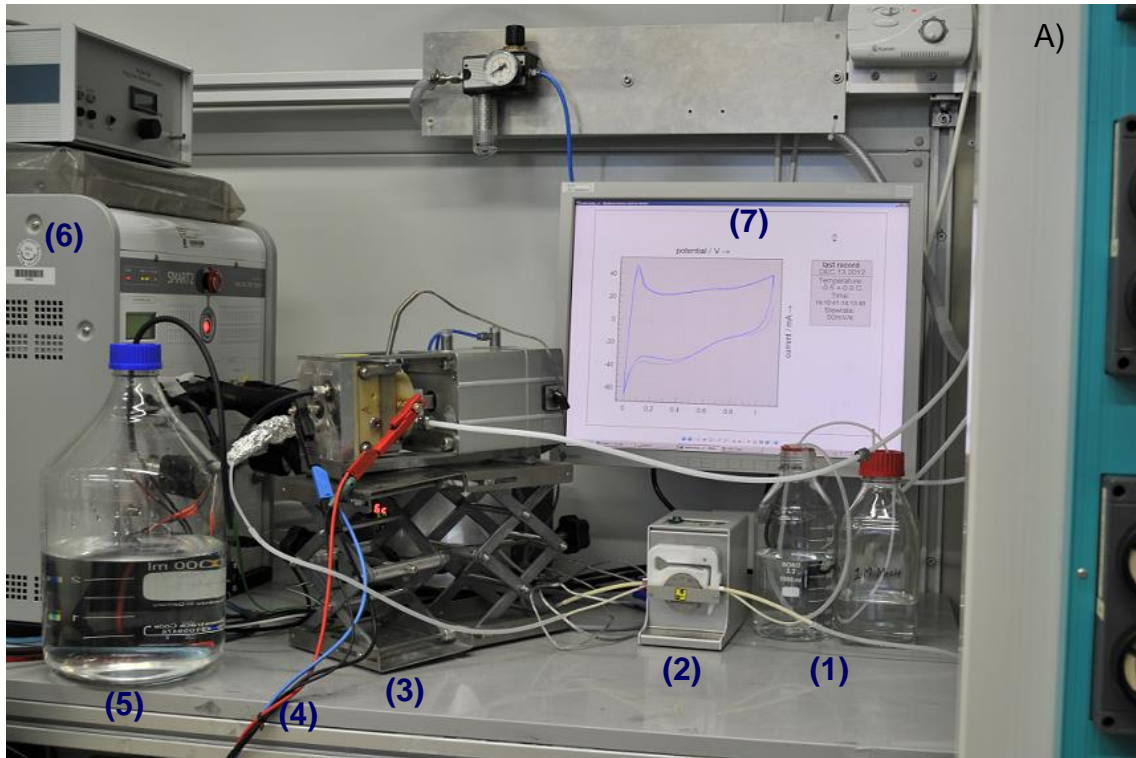


Figure A4: The photos of A) set up for DMFC measurements, 1) methanol feed solution, 2) the peristaltic pump, 3) the cell hard components and connection, 4) connection of both anode and cathode to the potentiostat, 5) the waste of the anode, 6) the fuel cell test station and 7) PC for data acquisition and B) the details of 3). The fuel cell measurements step up is available at Max Planck Institute for Dynamics of Complex Technical Systems, Magdeburg.

Publications Contribution Statement

Parts of the work presented in this thesis have been done in cooperation with other scientists. Distribution of work among the authors of the publications can be described as follows:

All catalyst syntheses including heat treatment steps have been carried out by me.

All electrochemical experiments have been carried out and were analysed by me.

Catalyst characterisation has been done in cooperation:

XRD results have been analysed by me after being recorded by Eik Koslowski at Department of Inorganic Chemistry at Martin-Luther-University.

TEM results have been analysed by me after being recorded by Annett Quetschke or Dr. Frank Heyroth at IZM of Martin-Luther-University.

XAS and XPS results have been recorded and analysed by Prof. W. Grünert and Dr. I. Sinev at Ruhr-University Bochum or at the respective synchrotron facilities. I have been involved in the discussion on the interpretation of the results.

Elemental analysis and ICP-OES has been done by the central facilities of the Chemistry Department or the Geology Department of Martin-Luther-University.

Fuel cell tests as well as interpretation of their results have been carried out by Prashant Subhas Khadke and me at MPI, Magdeburg.

All first drafts of the publications were written by me including interpretation and discussion of all results. All authors contributed to writing of the final versions of the publications.

Acknowledgment

I would like to offer my gratitude and appreciation to my research supervisor **Prof. Dr. Michael Bron**, Professor of Industrial Chemistry at Martin-Luther University Halle-Wittenberg, who gave me the opportunity to work under his supervision and to pursue my study at Martin-Luther University Halle-Wittenberg. I am greatly thankful to Prof. Bron for his support, guidance, encouragement throughout this work. His door was always open to discuss novel ideas about my research work and giving me the freedom to prove them. I am sure that I will benefit from his guidance and mentoring for the rest of my academic career.

I am sincerely indebted to **Prof. Dr. Wolfgang Grünert**, Professor of Industrial Chemistry at Ruhr University, Bochum for his fruitful collaboration and insightful discussions during my work. My gratitude and appreciation is also extended to **Dr. Ilya Sinev**, from Prof. Grünert's group for his help with XPS and XAS measurements and their data analysis, his valuable discussion, support and diligent effort to improve our joint research articles. The collaboration with Prof. Grünert's group has indeed helped strengthen my research work and made it of more value.

I offer my thanks for **Prof. Dr. Ulrike Krewer**, Professor of Process Systems Engineering, Technical University of Braunschweig who gave me the opportunity to stay at her group at the Max Planck Institute for Dynamics of Complex Technical Systems, Magdeburg for direct methanol fuel cell measurements. My thanks also go to **Prashant Subhas Khadke**, PhD student at Prof. Krewer's group for his help and assistance in direct methanol fuel cell measurements.

I would like to express my sincere gratitude for the past and present members of our group especially **Dr. Christian Kulp**, for his help and intellectual discussions during our lab meetings, **Matthias Schtimake** and **Thomas Erler**; for spending almost four years in the same office and the valuable discussion during our office hours and **Dr. Sabine Schimpf** for her help during the work and during the thesis writing. My thanks are also given to **Eik Koslowski** and **Annett Quetschke** for their technical support and our group secretary **Mrs. Anki Hassi** for her administrative support. I would also like to thank **Mr. Ronald Schollosser** from the mechanical workshop for his help with Teflon staff and mechanical support fabrication. It has been indeed a pleasant experience for me to work in such great research team. We have been all working and learning together in a very comfortable and fertile atmosphere.

I would like to thank **Dr. Frank Heyroth** from Interdisciplinary Center for Material Science (IZM) at MLU Halle for his help with TEM measurements and for accessing the TEM facilities.

Thanks are also given to the glass workshop members, for their support, help and glass materials construction.

I would like to express my gratitude and appreciation for the Ministry of Higher Education and Scientific Research (**MHESR**), Egypt and German Academic Exchange Service (**DAAD**), Germany for the scholarship in the framework of the German Egyptian Research Long-Term Scholarship (**GERLS**) program to pursue my PhD study at MLU Halle-Wittenberg.

I am indebted for **Prof. Dr. Abd El-Hady Kashyout**, Professor of Materials Science at the City of Scientific Research and Technological Application (SRTA-City), Alexandria, Egypt; who first introduced me long ago to the field of electrocatalysis for fuel cells during my master work. My thanks also go to **Prof. Dr. Mohamed Saada El-Deab**, Professor of Physical Chemistry and Electrochemistry, Faculty of Science, Cairo University, Cairo, Egypt; for his support and encouragement during my study abroad. He has also helped broaden my knowledge concerning electrochemistry and electrocatalysis prior to joining Prof. Bron's group.

I am greatly thankful for all my family members for their support and encouragement during these past years, especially my wife, my lovely daughter (**Aisha**) and my dear son (**Mohamed**) for their support and motivation that helped to reach this point of my study. The support and patience of my wife cannot be expressed in such few words.

Finally, my PhD study and this dissertation would not have been possible without the help of **ALLAH**.

Personal Information

Name: Abu Bakr Ahmed Amine Nassr

Date of Birth: 09.12.1978, Sohag, Egypt

Marital Status: Married with two children

Home address: New Borg Al-Arab City, Alexandria, Egypt

Current address: Richard-Paulick-Str. 1, 06124 Halle (Saale), Germany

E-mail contact: abu.amine-nassr@chemie.uni-halle.de
abubakramine@gmail.com



Languages

Arabic (Mother tongue), **English** (very good), **German** (good, Niveaustufe B1, CDC Köln).

Education

2010-up to now: PhD student in Industrial Chemistry at Institute of Chemistry, Martin Luther University Halle-Wittenberg, Germany
Thesis title: Development of Nanostructured Materials for PEM Fuel Cells Application
Supervisor: Prof. Dr. Michael Bron.

2004-2007: Master Student at Chemistry Department, Faculty of science, Al-Azhar University (Cairo), obtained Master Degree (M.Sc.) in Applied Physical Chemistry.

2003-2004: Master courses student for one year as partial fulfillment for Master degree at Chemistry Department, Faculty of Science, Al-Azhar University (Assuit).

1997-2001: B.Sc. in Chemistry with honor degree (85 %), Chemistry Department, Faculty of Science, Al-Azhar University (Assuit).

Employment:

2004-2007: Assistance Researcher

2007-up to now: Associate Researcher

Employer: Department of Electronic Materials, Institute of Advanced Technology and New Materials, City of Scientific Research and Technological Application, Alexandria, Egypt.

Fellowships:

2009 DAAD scholarship for PhD study in Industrial Chemistry at Martin-Luther University Halle-Wittenberg, Germany. **Starting on April 2010.**

2009 research fellowship (9 months) on TRIL programme provided by ICTP, Italy, to work on Fuel Cells Catalysts at Department of Materials and Physical Technologies, ENEA, Italy. **Starting on March 2009.**

Membership:

Member of the International Society of Electrochemistry (ISE).

List of publications:

1. A.B. Kashyout, **AB.A.A. Nassr**, L. Giorgi, T. Maiyalagan, B.A.B. Youssef, *Electrooxidation of Methanol on Carbon Supported Pt-Ru Nanocatalysts Prepared by Ethanol Reduction Method*, Int. J. Electrochem. Sci. 6 (2011) 379 – 393.
2. T. Maiyalagan, **AB.A. Nassr**, T.O. Alaje, M. Bron, K. Scott, *Three-dimensional cubic ordered mesoporous carbon (CMK-8) as highly efficient stable Pd electro-catalyst support for formic acid oxidation*, Journal of Power Sources 211 (2012) 147-153.
3. **AB.A.A. Nassr**, M. Bron, *Microwave-Assisted Ethanol Reduction as a New Method for the Preparation of Highly Active and Stable CNT-Supported PtRu Electrocatalysts for Methanol Oxidation*, ChemCatChem, 5 (2013) 1472 – 1480.
4. **AB.A.A. Nassr**, A. Quetschke, E. Koslowski, M. Bron, *Electrocatalytic oxidation of formic acid on Pd/MWCNTs nanocatalysts prepared by the polyol method*, Electrochimica Acta 102 (2013) 202-211.
5. **AB.A.A. Nassr**, I. Sinev, W. Grünert, M. Bron, *PtNi Supported on oxygen functionalized carbon nanotubes: In depth structural characterization and activity for methanol electrooxidation*, Applied Catalysis B: Environmental 142–143 (2013) 849–860.
6. **AB.A.A. Nassr**, I. Sinev, W. Grünert, M. Bron, *Rapid Microwave-assisted polyol reduction for the preparation of highly active PtNi/CNTs electrocatalysts for methanol oxidation*, submitted to ACS Catalysis.
7. **AB.A.A. Nassr**, P.S. Khadke, I. Sinev, U. Krewe, W. Grünert, M. Bron, *PtRu/CNTs as highly active and durable electrocatalysts: correlating structure with stability prepared to be submitted to Journal of Power Sources*.

Conferences:

1. A. Nassr, M. Steimecke, M. Bron, *Neue nanostrukturierte Trägermaterialien für die Elektro-katalyse*, Poster in **45. Jahrestreffen Deutscher Katalytiker**, 14. – 16. März 2012, Weimer.
2. Abu Bakr Ahmed Amine Nassr, Michael Bron, *Microwave Assisted Ethanol Reduction (MAER) as a New Method for Preparation of Highly Active and Stable Carbon Nanotubes Supported PtRu electrocatalysts for Methanol Oxidation Reaction*, Poster in **63rd Annual Meeting of the International Society of Electrochemistry**, 19-24 August, 2012 Prague, Czech Republic.

